”Cage” Nano and Micro-particles for Biomedical Applications

Xue Li

NNT : 2017SACLS316

THESE DE DOCTORAT
DE
L'UNIVERSITE PARIS-SACLAY
PREPAREE A
L'UNIVERSITE PARIS-SUD

ÉCOLE DOCTORALE N°571
SCIENCES CHIMIQUES : MOLECULES, MATERIAUX, INSTRUMENTATION ET BIOSYSTEMES

SPECIALITE DE DOCTORAT: CHIMIE

Par

Xue LI

"Cage" nano and micro-particles for biomedical applications

Thèse présentée et soutenue à Orsay, le 13/10/2017:

Composition du Jury :

M. CHAUBET Frédéric	Professeur, Inserm U1148, Institut Galilee, Université Paris 13	Rapporteur
Mme. MOTTE Laurence	Professeur, Université Paris 13	Rapporteur
M. YORK Peter	Président et scientifique en chef de Crystec Pharma	Examinateur
M. LAURENT Frédéric	Professeur, Université de Lyon 1	Examinateur
Mme. CATALA Laure	Professeur, Laboratoire de Chimie Inorganique, Université Paris-Sud	Présidente
Mme. GREF Ruxandra	Directeur de Recherche, ISMO, UMR 8214, Université Paris-Sud	Directeur de thèse

Acknowledgement

First and foremost, I would like to express my sincere gratitude to my thesis supervisor Dr. Ruxandra Gref for creating the research environment where I have performed my graduate studies. It is my honor to witness how the laboratory was set up in Orsay, Paris-Sud Université. The enthusiasm and joy she has for her research was contagious for me during my Ph.D pursuit. Her patience, motivation, and immense knowledge are also quite impressive for me. Her guidance helped me in all of my research and the writing of this thesis. I appreciate all her contributions of time, ideas, continuous support, connection with the collaborators and funding to make my Ph.D study productive. Her kindness to me and my family is more than all that I can imagine. I could not expect to have a better supervisor for my Ph.D study.

At the same time, I would like to thank Prof. Jiwen Zhang in Shanghai Institute of Materia Medica, Chinese Academy of Sciences. He provided me a great opportunity to join his team as a master student, and kindly recommended me to Dr. Ruxandra Gref as a Ph.D candidate. Without his precious support it would not be possible to conduct this research. Prof. Zhang is my co-supervisor to apply for my founding from China Scholarship Council (CSC). The experiments on CD-MOF particles were firstly started with Prof. Zhang in his group before coming to Paris-Sud université. I am grateful to the members in the team of Prof. Zhang, including Dr. Haiyan Li, Ms. Nana Lv, and Mr. Botao Liu for their kind help in finalizing the publication, titled "Composite CD-MOF nanocrystals-containing microspheres for sustained drug delivery". I thank Mr. Tao Guo for his molecular modelling of LPZ in CD-MOF.

Prof. J. Fraser Stoddart, who was awarded 2016 year's Nobel Prize in Chemistry, gave constructive comments in "Composite CD-MOF nanocrystals-containing microspheres for sustained drug delivery", since CD-MOF was firstly discovered by him.

I would also like to thank my thesis committee: Prof. Frédéric CHAUBET and Prof. Laurence MOTTE in Université Paris 13, Prof. Peter YORK in CrystecPharma, Prof. Frédéric LAURENT in Lyon 1 University and Prof. Catala Laure in Université Paris Sud, for their insightful comments and encouragement, and also for their questions which incented me to widen my research from various perspectives.

My sincere thanks also goes to my lab mates in ISMO. Firstly, Dr. Giuseppina Salzano set up the HPLC for the lab and helped me in the biological experiments including the cell toxicity

study, and confocal experiments. I am really grateful that she is very patient to show me the experiments in detail. Ms. Katie Buxton was the first internship student in the lab and she worked with me for around half a year. It was a nice memory to work with her. I thank my colleague Ms. Elisabetta Pancani for helping me with the communication on inscription issues.

Many thanks to all the collaborators in completing this thesis. Mr. Michel Terray, Mr. Laurent Lachmanski, and Mr. Samir Safi in Malvern Instruments kindly provided the Raman microscopy (Morphologi G3-ID) for the individual particle characterization, including particle morphology and Raman spectrum. Dr. Frédéric Laurent, Dr. Jérôme Josse and Ms. Virginie Tafani in École Normale Supérieure de Lyon (ENS Lyon) performed the *in vitro* efficacy experiment on Amoxicillin and calvulanate loaded nanoMOF.

Last but not the least, I would like to express my profound gratitude to my parents for their unfailing support throughout the process of researching and all my life. Although my mother was discovered to have small cell lung cancer in May, 2016, she was very strong and her continuous encouragement gave me great strength to face all of the difficulties. Thanks to my father, he raised me with a love of science and supported me for all my pursuit. Most of all, I wish to thank my husband, Jingwen QIU. He came to Orsay in September, 2016, away from his friends, jobs, and life in China. His supporting made me faithful.

Regrettably, but inevitably, the list of my gratitude will be incomplete, and I hope that those who are missing will forgive me, and will still accept my sincere appreciation of their influence on my work.

Table of Contents

Abbreviations

Ad	Adamantane
AMOX	Amoxicillin
AZT-MP	Azidothimidine monophosphate
AZT-TP	Azidothimidine triphosphate
BET	Brunauer, Emmett and Teller
BHI	Brain Heart Infusion
BTC	1,3,5 benzene tricarboxylate
Bz	Benzophenone
CAP	Captopril
CD-MOFs	Cyclodextrin-based metal organic frameworks
CD-NPs	Cyclodextrin-based nanoparticles
CD-P	β-CD-phosphates
CDs	Cyclodextrins
CFU/mL	Colony forming units per milliliter
CL	Clavulanate potassium
CT	Computed Tomography
CTAB	Cetyl trimethylammonium bromide
CUS	Coordinatively unsaturated metal sites
DCM	Dichloromethane
Dex	Dextran
Dex-Ad	Dex bearing adamantane (Ad) side units
Dex-Bz	Dex bearing Bz side units
Dex-C_{12}	Dextran (Dex) grafted with alkyl side chains
DL	Drug loading
DLS	Dynamic light scattering
DMF	N,N-Dimethylformamide
D-γ-CD	Dual-γ-CD unit
EE	The encapsulation efficiency
EP	Epichlorohydrin
EtOH	Ethanol
FA	Ferulic acid
FBS	Fetal bovine serum

GCMC	Grand Canonical Monte Carlo
Gem-MP	Gemcitabine-monophosphate
HPAC	High Performance Affinity Chromatography
HPLC	High Performance Liquid Chromatograph
IBU	Ibuprofen
^{i}PrOH	Isopropanol
IRMOF-3	Isoreticular metal organic frameworks
KOH	Potassium hydroxide
LDH	Lactate dehydrogenase leakage
LGA	Lamarckian Genetic Algorithm
LiCl	Lithium chloride
LPZ	Lansoprazole
MD	Molecular dynamics
Me_2CO	Acetone
MeOH	Methanol
MIL	Materials of Institut Lavoisier
MOFs	Metal-organic frameworks
MRI	Magnetic resonance imaging
MS	Materials Studio
MSNs	Mesoporous silica nanoparticles
MTT	3-[4,5-dimethylthiazol-2-yl]-3,5-diphenyl tetrazolium bromide
nanoMOFs	nano-scaled MOFs
NaOH	Sodium hydroxide
NPs	Nanoparticles
NTA	Nanoparticle tracking analysis
PAA	Polyacrylic acid
PBS	Phosphate buffer saline
PdI	Polydispersity
poly-CD	CD polymer
RAFT	Reversible addition−fragmentation chain transfer
RI	Refractive index
RITC	Rhodamine B isothiocyanate
S. Aureus	Staphylococcus aureus

SEC	Size exclusion chromatography
SEM	Scanning electron microscopy
TEM	Transmission electron microscopy
TGA	Thermogravimetric analysis
TL	Theoretical loading
TPT	Topotecan
TTBB	1,3,5-tri-tert-butylbenzene
TTMOFs	Tumor targeting MOFs
XRD	X-ray Diffraction
XRDP	X-ray diffraction patterns
Y	Yield of NPs
ZP	Zeta potential

General Introduction

Pharmacy has evolved regarding the specific needs of the patient. In the last five decades, the development of pharmaceutical carriers allowed the formulations to protect the fragile drugs from degradation, reduce the side effects of drugs together with allowing controlled drug release and targeted delivery [1–5]. Among all the drug delivery systems, "cage" particles recently drew special attention since they could act as "drug containers" which potentially load large amount of drugs, improve the stability of the drugs, and co-encapsulate synergetic drugs [6–8].

Cyclodextrins (CDs) are typical "cage" molecules due to their truncated cone shape with a hydrophobic cavity and a hydrophilic outer surface [9]. These unique properties enable CDs to form inclusion complexes with a variety of active molecules. They have been used as "molecule containers" to improve the solubility and bioavailability of poorly soluble drugs, stabilize drugs from light, thermal, and oxidative degradation, and mask the bitter taste of the drugs [10–12]. Therefore, self-assembled nanoparticles (NPs) composed of CDs are attractive formulations. However, since the cavity of the CDs is small, their loadig capacity is reduced to a number of drugs or portions of drugs.

Recently, a new type of porous CD-based metal organic frameworks (CD-MOFs) was synthesized [13]. They can be imagined as buildings built using CDs which act as hollow bricks. CD-MOFs contain not only the cavities of CDs, but also the big pores built up by CDs self-assemblies (Fig.1). Compared with CD-based NPs (CD-NPs), CD-MOFs have the possibility to load more drug payloads. Unfortunately, these particles immediately disassemble in aqueous media, which limits their application for oral or intravenous administration. Surface modification is therefore necessary to improve their stability in water. However, the process of surface modification leads to larger particles and reduced drug payloads.

Water-stable MOFs are a novel type of hybrid particles, showing a high potential as drug carriers. Iron trimesate MOFs, namely, MIL-100 (Fe) (MIL stands for Material of Institute Lavoisier) was among the first nanoscaled MOFs to be used for drug delivery[14]. It is a "cage" porous particle made of iron trimers connected by trimesic acid linkers. Because of their high pore volumes and surface areas, MIL-100 (Fe) particles were shown to load a large variety of drugs, such as antibiotics and anticancer drugs, which were able to efficiently penetrate within the porous MOF structures.

Therefore, three types of particles were successfully synthesized and used for the incorporation of active ingredients.

1. CD-NP was the first investigated system in this study. The advantages of these NPs lie on their "green" and simple preparation procedure. They could be obtained in pure water just by mixing two neutral polymers which instantaneously associate together. The host–guest interactions leading to inclusion complexes between hydrophobic molecules and the apolar concavities of CDs can be exploited for the formation of stable CD-NPs. A main objective was to use microfluidics to automatically prepare NPs in water media. Our interest was also focused on developing complementary techniques to well characterize the particles by in situ size measurements, and individual particle tracking (chapter 2), however, the drug loading capacity is not high (~ 5wt%).
2. Aiming at enhanced payload of drugs, CD-MOFs were synthesized because of their porous structure. Firstly, the synthesis of CD-MOFs was optimized to shorten the synthesis process and to obtain particles suitable as drug carriers (Chapter 3.1). Drugs of interest, such as lansoprazole (LPZ) were then encapsulated. Of note, methods were developed to study the morphology and chemical composition of individual particles (Chapter 3.2). In order to improve the stability of the loaded CD-MOFs in aqueous conditions and control the drug release, surface modification was performed (Chapter 3.3).
3. Since the surface modification was normally complicated and could probably reduce the drug payloads, MIL-100 (Fe) NPs were finally used as water-stable drug carrier in this study. It has been shown that they interact efficiently with phosphated drugs/coatings with high efficiencies. To gain new insights into the complex interactions taking place in the MOF/drug/coating systems, we developed a method based on Raman microscopy to track the morphology and chemical composition of individual particles (Chapter 4.1). Aiming at a drug combination delivery, co-encapsulation of two synergic antibiotics (Amoxicillin and potassium clavulanate) was successfully acheived (Chapter 4.2).

Reference

1. Lammers, T., Hennink, W. E. & Storm, G. Tumour-targeted nanomedicines: principles and practice. *Br. J. Cancer* **99,** 392–397 (2008).

2. Ganta, S., Devalapally, H., Shahiwala, A. & Amiji, M. A review of stimuli-responsive nanocarriers for drug and gene delivery. *J. Control. Release* **126,** 187–204 (2008).

3. Torchilin, V. Multifunctional and stimuli-sensitive pharmaceutical nanocarriers. *Eur. J. Pharm. Biopharm.* **71,** 431–444 (2009).

4. Torchilin, V. P. Multifunctional nanocarriers. *Adv. Drug Deliv. Rev.* **64,** 302–315 (2012).

5. Torchilin, V. P., Lukyanov, A. N., Gao, Z. & Papahadjopoulos-Sternberg, B. Immunomicelles: Targeted pharmaceutical carriers for poorly soluble drugs. *Proc. Natl. Acad. Sci. U. S. A.* **100,** 6039–6044 (2003).

6. Wei, S. *et al.* Hydroxypropylcellulose as matrix carrier for novel cage-like microparticles prepared by spray-freeze-drying technology. *Carbohydr. Polym.* **157,** 953–961 (2017).

7. Rampersaud, S. *et al.* The Effect of Cage Shape on Nanoparticle-Based Drug Carriers: Anticancer Drug Release and Efficacy via Receptor Blockade Using Dextran-Coated Iron Oxide Nanocages. *Nano Lett.* **16,** 7357–7363 (2016).

8. Bharti, C., Gulati, N., Nagaich, U. & Pal, A. Mesoporous silica nanoparticles in target drug delivery system: A review. *Int. J. Pharm. Investig.* **5,** 124 (2015).

9. Jambhekar, S. S. & Breen, P. Cyclodextrins in pharmaceutical formulations I: Structure and physicochemical properties, formation of complexes, and types of complex. *Drug Discov. Today* **21,** 356–362 (2016).

10. Bonnet, V., Gervaise, C., Djeda??ni-Pilard, F., Furlan, A. & Sarazin, C. Cyclodextrin nanoassemblies: A promising tool for drug delivery. *Drug Discov. Today* **20,** 1120–1126 (2015).

11. Katageri, a R. & Sheikh, M. a. Cyclodextrin a Gift To Pharmaceutical World. *Int. Res. J. Pharm.* **3,** 52–56 (2012).

12. Rasheed, A., Kumar C.K., A. & Sravanthi, V. V. N. S. S. Cyclodextrins as drug carrier molecule: A review. *Sci. Pharm.* **76,** 567–598 (2008).

13. Smaldone, R. A. *et al.* Metalorganic frameworks from edible natural products. *Angew. Chemie - Int. Ed.* **49,** 8630–8634 (2010).

14. Horcajada, P. *et al.* Metal-organic frameworks as efficient materials for drug delivery. *Angew. Chemie - Int. Ed.* **45,** 5974–5978 (2006).

Chapter 1: Introduction

1. "Cage" molecules: CDs

CDs were first isolated in 1891 by Villiers from the enzymatic degradation products of starch[1]. They are a family of cyclic oligosaccharides composed glucopyranose units. CDs are cage-like supramolecular with a hydrophilic outer surface and a hydrophobic central cavity. As a result of this cavity, CDs are able to form inclusion complexes with a variety of hydrophobic guest molecules, which can lead to advantageous changes in the chemical and physical properties of the included guest molecules. Therefore, CDs are widely used as "molecular cages" in the pharmaceutical to enhance the solubility, stability, and bioavailability of drug molecules[2]. They have been recognized as pharmaceutical excipients for the past 20 years.

1.1 Structure and properties

The most common natural CDs are α, β and γ-CDs, containing 6, 7 and 8 glucopyranose units respectively, attached by α-1,4-linkages (Fig.1). Due to the chair formation of the glucopyranose units, CDs are shaped like bottomless nest-shaped (truncated cone) molecules with primary hydroxyl groups extending from the narrow edge and the secondary groups from the wider edge. This makes the outer surface of CD molecules hydrophilic, whereas the lipophilicity of their inner cavity is comparable to an aqueous ethanolic solution [3].

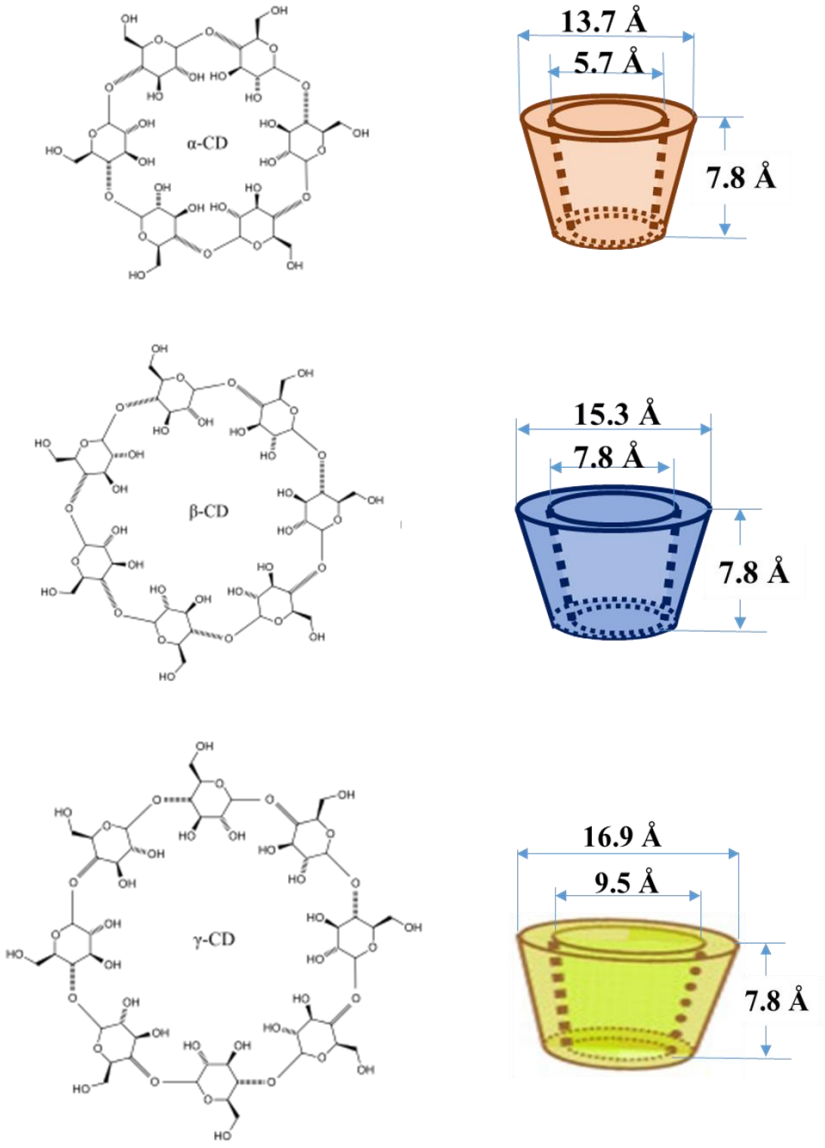

Fig.1 Structure of α, β and γ-CDs.

These unique molecular shape and structure allow CDs to act as a molecular container by trapping guest molecules in their cavity. Once the guest molecules were included, their water solubility, volatility, stability, bioavailability, and even the taste could be improved [4].

The natural CDs, in particular β-CD, have limited water solubility (18.5 mg/mL, 25°C) [2], which often results in precipitation of the inclusion complexes from the aqueous systems. Therefore, functionalized CDs were synthesized, including CD derivatives, and cross-linked CD polymers[5]. They are prepared by chemical or enzymatic reactions. The main objective of functionalization for pharmaceutical interest are: 1) to improve the solubility of the CDs and their inclusion complexes; 2) to reduce the toxicity of CDs, such as the nephrotoxicity of β-CD; 3) to improve the fitting and/or the association between the CD and its guest.

CD derivatives. New derivatives of CDs for pharmaceutical application were synthesized and currently used in pharmaceutical products, including hydroxypropyl derivatives of β-CD and γ-CD (HP-β-CD and HP-γ-CD), sulfobutylether β-CD (SBE-β-CD), and randomly methylated β-CD (RM-β-CD) [6,7]. These CD derivatives are of very high water solubility (>500 mg/mL). The main reason for this significant solubility enhancement is due to the transformation of the crystalline forms of natural CDs into amorphous mixtures of isomeric derivatives [8].

Moreover, hydrophilic derivatives of β-CD could be used in parenteral formulations showing reduced nephrotoxicity as compared to natural CDs [9].

Cross-linked CD polymer. Recently, cross-linked CD polymers were synthesized and widely used in polymeric systems, such as hydrogels, nano/microparticles, and micelles, etc. Cross-linked CD polymers were generally synthesized with cross-linker agents at controlled temperature [5,10]. Epoxides (e.g. epichlorohydrine (EP) or glycidylethers), isocyanates, aldehydes, and ketones are suitable cross-linking agents for CDs [11]. EP is considered as the most investigated agent. It posseses two reactive groups that can react with the hydroxyl groups of CDs or with other EP molecules under alkaline conditions. This reaction usually leads to microgels, which are composed of a mixture of cross-linked CDs joined by repeating glyceryl units of polymerized EP[12]. Hydrosoluble CD polymers can also be obtained if the cross-linking reaction is quenched at a certain stage [13]. Poly-β-CD synthesized by this way draw special attention in polymeric self-assembled systems because of its high solubility, and high capacity to form inclusion complexes with guest molecules [14–16].

1.2 Safety and biocompatibility of CDs

The α, β and γ-CDs were well tolerated when administered orally only a small fraction absorbed from the gastrointestinal tract [2,7]. Some CD derivatives such as HP-CD could be used safely for intravenous administration and were mainly excreted unchanged in the urine. However, β-CD showed nephrotoxicity when administered parenterally, in part, possibly due to its low aqueous solubility [2]. Lipophilic CD derivatives, such as RM-β-CD, were absorbed to a greater extent from the gastrointestinal tract and induced a toxic effet after parenteral administration [17]. Oral administration of RM-β-CD is presently limited because of its potential toxicity.

However, it is worth mentioning that the first targeted, polymer-based nanoparticle system carrying siRNA to be systemically administered to humans was based on polymeric cationic CDs [18].

1.3 Inclusion complex formation based on host-guest interactions

The inclusion complexes between CDs and guest molecules are formed mainly by hydrogen bonding, and van der Waals interactions. The release of enthalpy-rich water molecules from the CD cavity, and electrostatic interactions also contribute to the inclusion formation. As there are no covalent bonds, guest molecules in the complex are in equilibrium with free molecules in solution (Fig. 2).

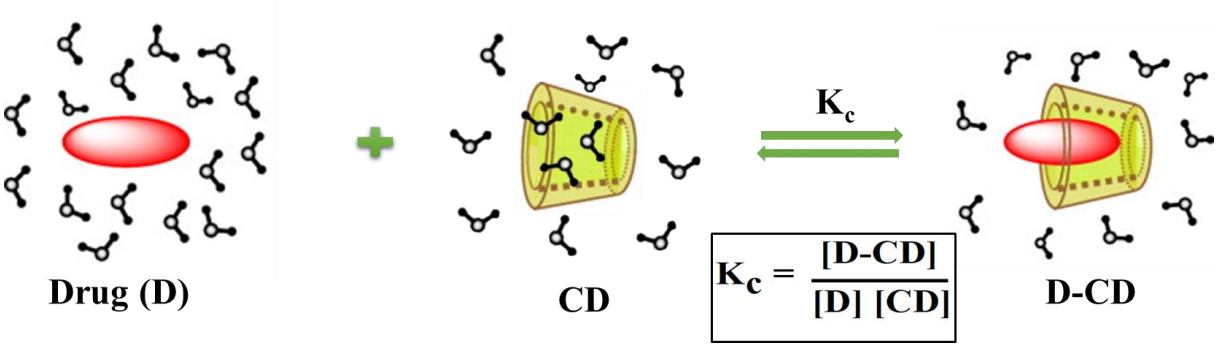

Fig. 2 The conventional inclusion complex formation when one guest molecule forms a complex with one CD molecule.

The key factor for the inclusion complex formation is the thermodynamic interaction between the chosen CDs and the drug molecules. As shown in Fig.2, the larger the K_C, the more the equilibrium will shift towards complex formation. There are four energetically favorable interactions that help increase K_C [19] : (i) the displacement of polar water molecules from the hydrophobic CD cavity; (ii) the increased number of hydrogen bonds formed as the displaced water returns to the larger pool; (iii) a reduction in the repulsive interactions between the hydrophobic guest and the aqueous environment; and (iv) an increase in van der Waals interactions and/or hydrogen bonds formation as the guest molecule inserts itself into the hydrophobic CD cavity. The first two interactions are similar in any case, but the last two interactions are up to the affinity between the guest molecule and the CD, which is dependent on the size, hydrophobicity and structure of both the guest molecules and the type of CDs.

Inclusion complexes could be formed at the molar ratios of 1:1 or 1:2 between the guest molecule and CD (Fig.3). However, as shown in Fig. 3C, CDs are also known to form non-inclusion complexes and complex aggregates capable of dissolving drugs through micelle-like structures [3].

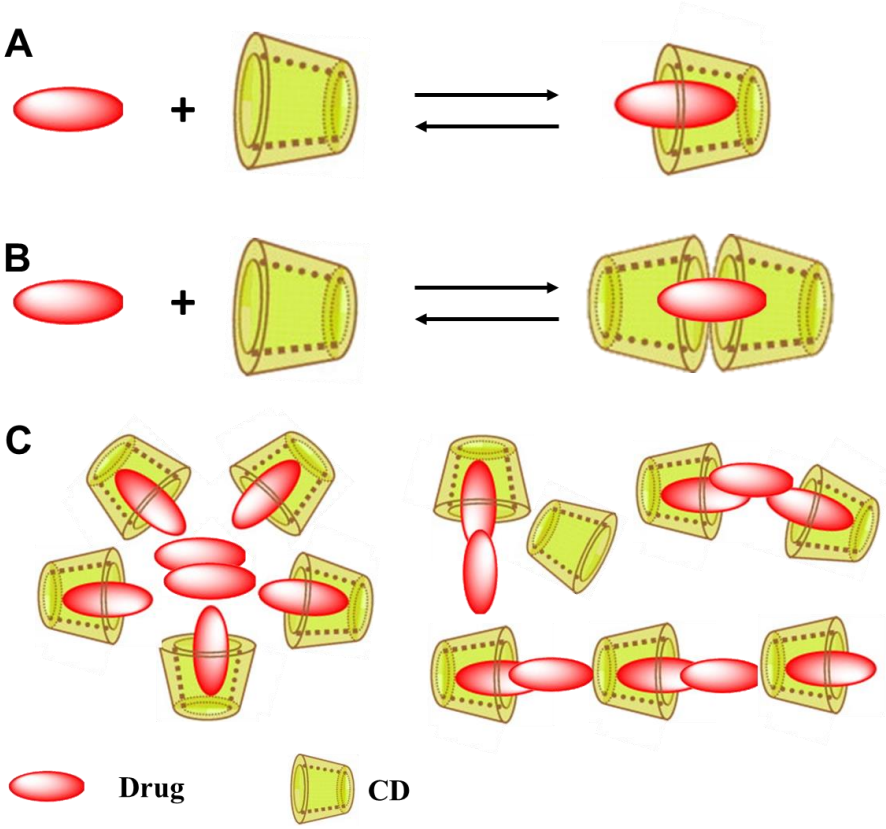

Fig.3 Types of inclusion complexes formed at the molar ratio of 1:1 (A) and 1:2 (B) between the guest molecule and CD; Non-conventional CD complexes (C).

1.4 CD-based drug-carriers

CDs are widely used in drug delivery system, including hydrogels, polymeric NPs, liposomes, niosomes, micelles, millirods, nanosponges, and supramolecular vesicles, etc[20]. They were employed almost everywhere in the pharmaceutical field, but there are only few types of drug carriers mainly composed of CDs. Herein, CD-based hydrogels and NPs driven by CD inclusion complexes and CD-based metal organic frameworks (CD-MOFs) were introduced.

CD-based hydrogels and NPs driven by CD inclusion complexes.

Supramolecular structures could be formed by simply mixing poly-CDs or polymers grafted with CDs and polymers bearing guest groups. Both hydrogels and NPs can be obtained depending on the concentration of the polymers and their architecture [21] . The inclusion complex formed between CDs in one polymer and the guest molecules in other polymer acted as knots that link the lines into nets which could further assemble into NPs or hydrogels.

The combination between β-CD-bearing polymers and adamantane (Ada)-bearing polymers were stable, due to their host–guest interaction ($K_a \sim 10^4$ –10^5 M^{-1}) [8,17,22]. Some other guest molecules were also used, such as alkyl chains, cholesterol, β-benzyl L-aspartate,

benzimidazole, and even some hydrophobic drugs [10,22,23] . It was found that polymers grafted with alkyl chains could also form stable supramolecular structures, despite the relatively low CD-alkyl chain association constant [14]. The cooperative effect of multiple complex formation played a major role on ensuring the stability of the edifices.

Drugs could be loaded in different ways. As already described, some hydrophobic drugs could be used directly as guest molecules[5]. In this case, the drugs could be conjugated in CD-bearing polymer or in another polymer. Fig. 4 A and B show the NPs formation driven by CD-drug inclusion. Alternatively, drugs could be loaded after the hydrogels/NPs formation by forming inclusion complexes with free CDs remaining unoccupied after particle formation (Fig. 4C). This strategy avoids the synthesis of drug-polymer conjugate, which can be deleterious for some fragile drugs [24]. However, the disadvantage of this type of particles lies on the low drug loading and the equilibrium between the free drug and included drug. When the particles were diluted, the equilibrium would shift to the free drug formation which leads to drug leakage.

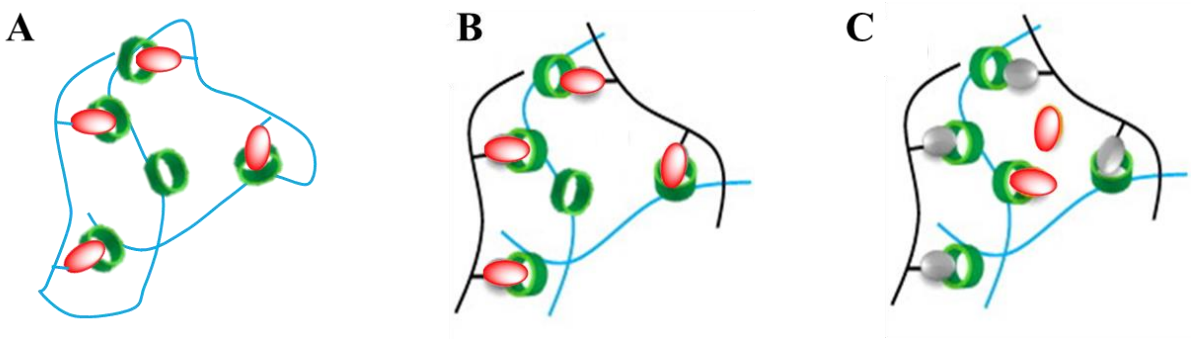

Fig. 4 Different models that represent how the drugs were loaded in the CD-based hydrogels/NPs driven by CD inclusion complexes. A, the drugs were conjugated to CD-bearing polymers; B, the drugs were conjugated on a different polymer; C, the drugs were loaded in free CDs that were not occupied by the guest molecules.

"Cage" particles: CD-based metal organic frameworks (CD-MOFs).

Although CDs are "cage" molecules, the cavity of the cage is very limited because of the dimension of the molecules. Therefore, porous "cage" particles, CD-MOFs, were recently synthesized in the group of Dr. Fraser Stoddart [25]. CD-MOFs were formed by reacting γ-CD and potassium ions employing a vapor diffusion method. In the originally reported synthesis [25], "edible" CD-MOFs were prepared by dissolving commercially available food-grade KCl or potassium benzoate and food-grade γ-CD in distilled water. The aqueous solution was filtered through cotton wool, following vapor diffusion of grain alcohol into the solution over around one week. In this process, the γ-CD molecules are linked by potassium ions to form a body-

centered cubic structure (Fig.5). They are porous particles built with cubic units which have a pore of 1.7 nm. CD-MOFs greatly improved the capability of CDs to encapsulate drug molecules[26–28].

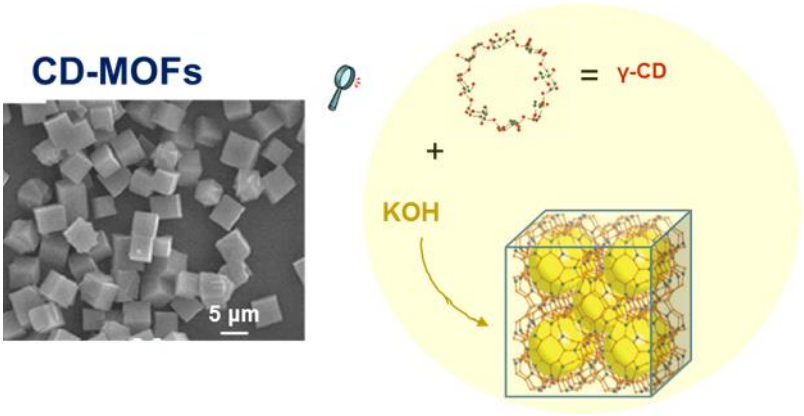

Fig.5 structure of CD-MOFs

To obtain monodispersed CD-MOFs for drug delivery, the synthesis was optimized[29]. It has been discovered that addition of cetyl trimethylammonium bromide (CTAB) leads to the preparation of smaller CD-MOFs (1-10 μm). If methanol was also added together with CTAB, nanoscale CD-MOF could be obtained (200-300 nm). All these syntheses employing vapor diffusion methods took long time (26-32 h). It was recently reported that nano-CD-MOFs (100-300 nm) were successfully obtained by a microwave-assisted method in shorter time (≤ 70 min) [30]. However, the formed CD-MOFs were polydispersed. Further optimization of CD-MOFs synthesis is still needed for their biomedical applications.

CD-MOFs have shown their capability to encapsulate molecules of interest, including ibuprofen [28], fenbufen [31], doxorubicin [32], curcumin [27], sucralose [33], ferulic acid [26], 4-phenylazophenol and rodamine B [25]. Impregnation and co-crystallization are two reported approaches for the incorporation. A high payload of 23−26 wt % was reached in the case of ibuprofen by impregnation [28]. Payload of 18.5 wt % was reached for Rhodamine B by co-crystallization [25].

However, applications of CD-MOFs as drug carriers are severely hampered since they can be easily disassociated in aqueous environment. To address this issue, the first idea was to crosslink CDs in the framework of CD-MOFs, producing CD-MOF hydrogels [29]. However, the cross-linking reaction required long time incubation (over three days) at controlled temperature (~ 65°C), which would be harmful for many of the drugs if they are already loaded. Recently, a facile method to improve their stability has been developed via the incorporation of

hydrophobic fullerene (C_{60}) in their matrices [32]. It has been shown that C_{60} (0.7 nm in diameter) can be partially trapped within the cavity of a γ-CD, forming a CD-MOF/C_{60} composite. Water-resistance of CD-MOFs could be improved since the trapped C_{60} endowed CD-MOFs with enhanced hydrophobicity. When the CD-MOF/C_{60} composite was immersed in water, C_{60} layer could effectively repel water molecules from contacting MOF surface, therefore, the stability of CD-MOFs in aqueous condition was significantly improved. This study was performed with very large CD-MOFs (more than 400 μm) and the sytem still needs further investigations for its medical application.

2. Hybrid metal–organic framework nanoparticles (MOFs)

MOFs are an intriguing class of hybrid materials obtained by the self-assembly of metallic ions or clusters and bridging organic ligands, leading to the formation of three-dimensional networks with high and regular porosities [34-38]. Taking advantage of MOF important porous surface and large pore size, versatility in terms of architecture, composition and physico-chemical properties, they have been intensively used in the last several years for a number of different applications such as catalysis, separation and gas storage and more recently, in nanomedecine.

The use of MOF materials for biomedical applications, and in particular as drug nanocarriers, requires MOFs to be scaled-down to the nanometer sizes [39] using essentially bottom-up approaches, involving controlling the MOF nucleation rate and crystallization in order to limit the MOF growth to submicronic sizes.

MOFs have high porosities together with important available BET (Brunauer, Emmett and Teller) surface areas ranging generally from 1000 up to 7000 m^2 /g [38, 40-45] higher than BET surface of mesoporous silica nanoparticles (MSNs), which is up to around 1200 m^2 /g [46]. The large nanoMOFs surface areas together with their peculiar inner environments (both hydrophilic and hydrophobic) make these materials particularly appealing for the entrapment of drugs. The active molecules cross the MOF windows to get adsorbed onto the inner surfaces and interact with metal sites and/or organic constituting ligands.

When scaling down the synthesis to the nanometer range, the outer surface properties play an increasing role, as the external surface-area-to-volume ratio is increasing. Indeed, the outer surface properties determine the nanoMOFs' colloidal stability and interactions with biological environments.

2.1 Strategies to scale-down MOFs to the nano-regime.

A large variety of methods have been developed to produce MOFs with submicronic sizes (Fig.6). They include solvothermal methods assisted or not by microwave irradiation [47,48], solvent diffusion synthesis[25], dry-gel conversion methods[49], mechanochemical [50–52] or sonochemical synthesis [53], production by reverse-phase microemulsions [54–56], electrochemical synthesis [57], preparation using a microfluidics device [58]. Besides, step-by-step [59] and high-throughput synthesis methods [60] were developed. Whatever the process, a main challenge is to control the crystallization process in order to achieve particles with uniform sizes less than one micron. Main strategies to achieve this goal consisted in adding crystal growth inhibitors, speeding the crystallization process, using nanoscale templates and downsizing the particles by mechanical or mechano-chemical methods.

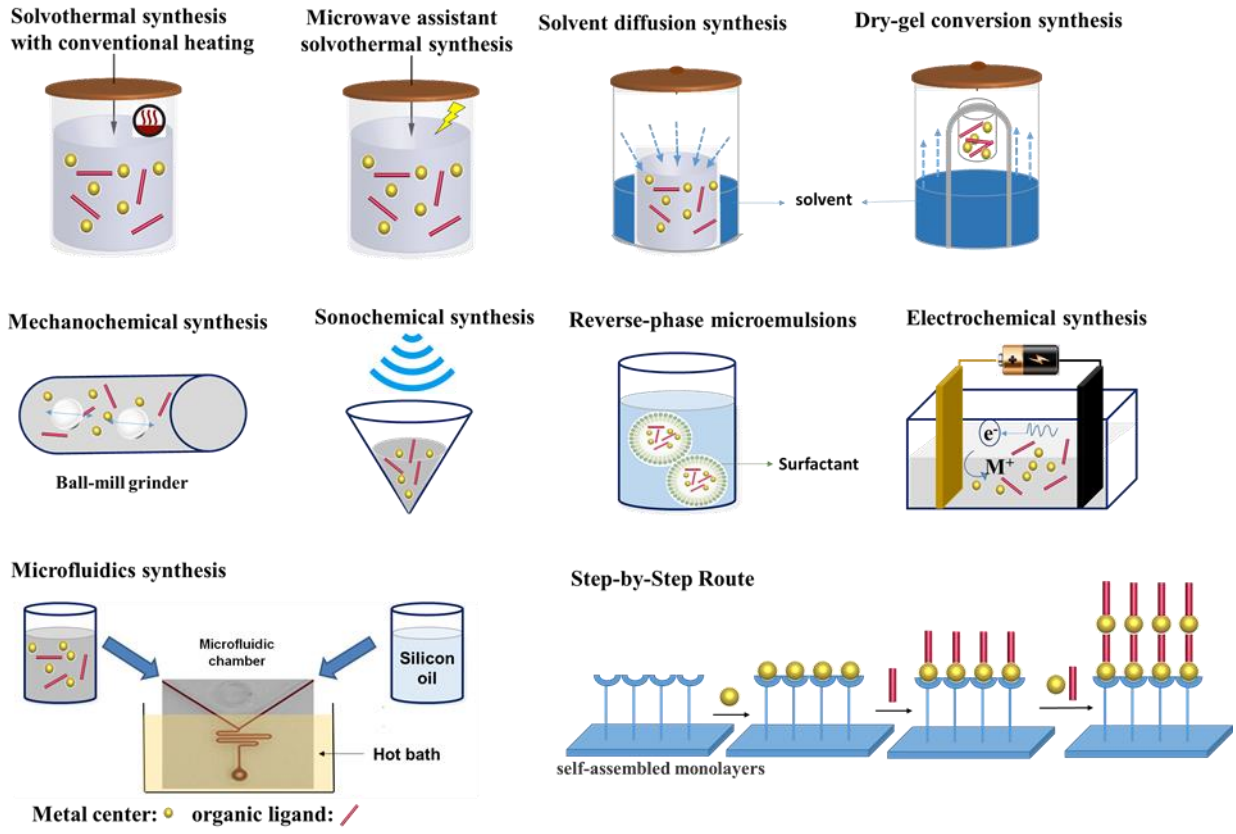

Fig.6. Overview of main synthesis methods for MOFs

Blocking or inhibiting crystal growth. Various blocking agent or acido-basic or inhibiting additives such as acetic acid, hydroxybenzoic acid and pyridine were added in the MOF synthesis to retard the nucleation growth process. For example, the size of the flexible porous iron muconate MIL-89 (MIL stands for Materials from Institut Lavoisier) could be reduced down to 30 nm by adding acetate ions in the reaction process [61]. In another study, pyridine was

used as inhibitor in the solvothermal synthesis of porous indium terephthalate particles [62]. Both the size and shape of the particles were affected by the inhibitor. In the absence of pyridine, hexagonal rods of around 1.75 μm width and 16.3 μm length were formed. Pyridine enables to reduce both width and diameters to 0.97 μm and 0.43 μm, respectively.

Luminescent nanoparticles made of terbium benzenedicarboxylate with sizes of only 4-5 nm were successfully obtained by adapting a previous method [63] using a poly(vinilpyrrolidone) as inhibitor of crystal growth [64].

Accelerating the crystallization process. An alternative methods to the use of crystal growth inhibitors, was to speed up the crystallization process. This strategy was applied to CD-MOFs prepared by solvent diffusion (Fig.6).

The chiral γ-CDs comprise eight α-1,4-linked D-glucopyranosyl residues disposed in a symmetric configuration. This allows the γ-CD building units to assemble with alkali metal ions (K^+, Na^+, Rb^+, and Cs^+) in aqueous media to form body-centered cubic CD-MOFs (Fig. 5). For example, K^+ based CD-MOFs were obtained under the form of large particles of around 200–400 μm by reacting γ-CD with KOH in aqueous solution, followed by vapor diffusion of methanol into the solution at room temperature during 2–7 days. The addition of cetyl trimethylammonium bromide (CTAB) together with an optimization of the reaction conditions enabled to reduce the reaction times and to obtain nano-scaled CD-MOF (200-300 nm) [31]. Of note, cubic particles with homogeneous sizes were obtained by using CTAB.

The reaction time was found to dramatically influence the MOF size distribution. The diameters of $Zn_3(BTC)_2 \cdot 12H_2O$ MOFs were reduced from 700 - 900 nm to 50 - 100 nm by decreasing the reaction time from 90 to around 10 min [65].

Nanoscale templates. Another promising strategy to obtained nanoscaled MOFs was the synthesis in confined spaces, using a template approach. For example, Gd-based MOF66 nanoparticles were obtained in reverse microemulsions prepared using mixtures of CTAB, isooctane, 1-hexanol and water. The morphology and size of nanoscale templates were dramatically altered by both the composition of the system and the presence of sodium salicylate, a hydrotrope [66-67].

Downsizing. Nanosized MOFs were prepared mechanochemical synthesis, consisting in a mechanical breakage of intramolecular bonds followed by a chemical transformation. First examples of the synthesis of porous MOF by this method were reported in 2006 [51]. Advantageously, mechanochemical reactions can occur at room temperature under solvent-free

conditions [68]. Nanoparticles of HKUST-1 were successfully produced in solvent free conditions [50]. Mechanochemical synthesis of MOF nanoparticles were reviewed[69]. More recently, nanosized Gd-based porous MOF has been synthesized by mechanical downsizing by ball milling the as-synthesized MOF with millimeter-scaled sizes.[70]

All these synthesis method have led to the obtention of a large variety of materials with rigid or flexible structures. Examples are compiled in Fig.7.

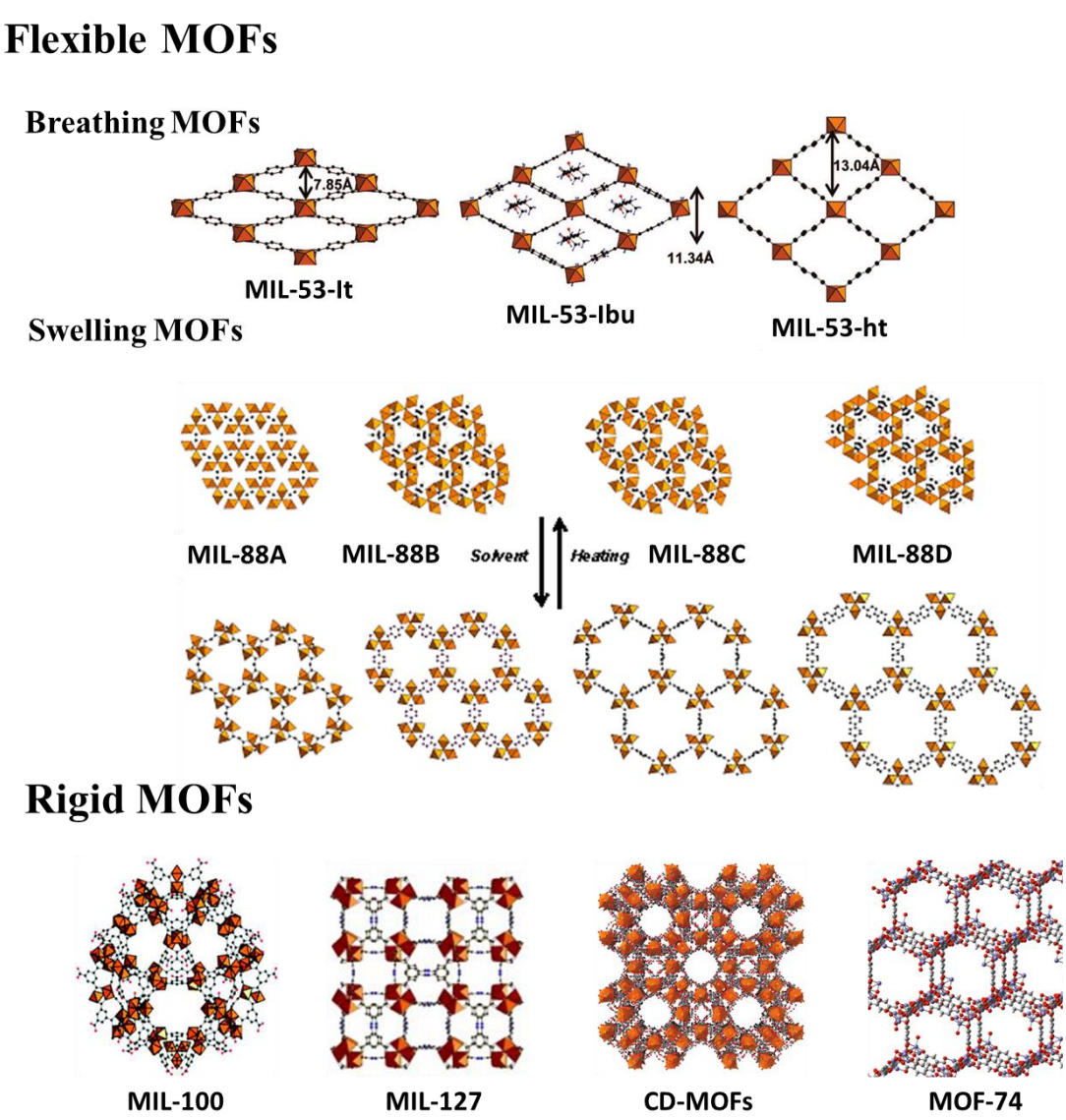

Fig.7 Overview of some representive examples of flexible and rigid of MOFs. The breathing MOFs: MIL-53-It (It=low temperature), MIL-53-Ibu (Ibu= Ibuprofen), and MIL-53-ht (ht=high temperature) are from reference 87; The swelling MOFs are from reference 45. The series of MIL-88 were prepared with iron trimer and different ligand: fumaric acid (MIL-88A), terephthalic acid (MIL-88B), 2,6-naphthalenedicarboxylic acid (MIL-88C) and 4,4′-biphenyldicarboxylic acid (MIL-88D).

2.2 Drug entrapment and release

Active molecules, mainly anticancer drugs have been successfully incorporated in the nanoMOFs using three main strategies schematized in Fig.8.

The first group of MOFs considered as potential drug delivery system is the MIL family. In particular, MIL nanoMOFs build from trivalent metal centers and polycarboxylic acid bridging ligands develop outstanding surface areas (1500-5900 m^2/g) and large pore sizes (25-34 Å) making them particularly appealing for drug entrapment [44]. For example, rigid mesoporous MIL-100 nanoMOFs, built up from trimers of iron(III) octahedra and trimesate anions, show two types of mesoporous interconnected cages accessible through microporous windows: i) large cages (~ 29 Å) delimited by hexagonal (~ 8.6 Å) and pentagonal (~ 4.8 × 5.8 Å) windows and ii) small cages (~ 25 Å) accessible exclusively by pentagonal windows [71]. MIL-100(Fe) MOFs possessed the same architecture but with larger pore openings and adsorption surfaces. They were obtained by using aminoterepthalic acid instead of trimesic acid [45].

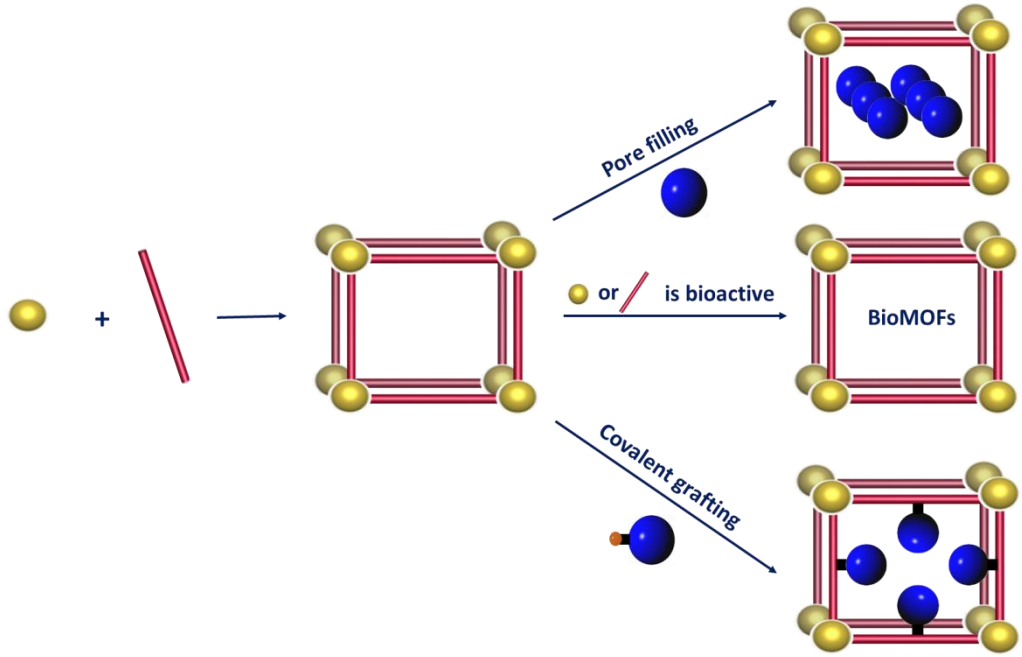

Fig.8 Drug association to hybrid MOF nanoparticles.

Drug loading by impregnation As shown in Table 1, a variety of active molecules have been successfully loaded into MIL nanoMOFs, including anti-inflammatory (ibuprofen, aspirin), antiviral (cidofovir, azidothimidine triphosphate (AZT-TP) and azidothimidine monophosphate (AZT-MP)), anticancer (busulfan, doxorubicin, ethoxysuccinato-cisplatin prodrug, gemcitabine-monophosphate (Gem-MP) and topotecan) drugs, nitric oxide, metallodrugs and

peptides. All these molecules were loaded by impregnation using preformed NPs. Advantageously, hydrophilic molecules such as azidothimidine mono-and triphosphate and gemcitabine monophosphate were entrapped simply by soaking from their aqueous solutions. The nanoMOFs acted as molecular sponges and the rapid and simple loading procedure lead to AZT-TP payloads of around 42 wt% and 21 wt% for MIL-101 and MIL-100 nanoMOFs, respectively[72]. Moreover, excellent loading efficiencies (> 95%) have been achieved, due to the high affinity of the phosphated molecules for the iron-based nanoMOFs [73,74]. It has been shown by complementary techniques that coordination took place between the unsaturated Lewis acid iron sites and the phosphate groups of the drug [74].

Table 1. Drug encapsulation in MOFs by impregnation

MOF	Metal Ion	Organic Linker	Drug	Drug Loading (%, w/w)
CD-MOF (Cs) [75]	Cs	β-CD	5-FU	151
CD-MOF (Cs) [75]	Cs	β-CD	MTX	122
CD-MOF (K) [31]	K	γ-CD	fenbufen	20
CD-MOF (K) [31]	K	γ-CD	captopril	19
CD-MOF (K) [31]	K	γ-CD	flurbiprofen	12
CD-MOF (K) [33]	K	γ-CD	sucralose	28
CD-MOF (K) [28]	K	γ-CD	ibuprofen	26
CD-MOF (Na) [76]	Na	α-CD	5-FU	9
CD-MOF (Na) [76]	Na	α-CD	MTX	38
CD-MOF (Na) [76]	Na	α-CD	silybummarianum	13
CD-MOF (Na) [76]	Na	α-CD	ferulic acid	11
CD-MOF (Na) [76]	Na	α-CD	quercetin	32
Co-BBDA [77]	Co	H_4BBDA	5-FU	15
CNZTDH [78]	Zn	TATAT	5-FU	33
CPO-27-Ni [79]	Ni	DHTPA	NO	15
Cu-BTC [80]	Cu	BTC	5-FU	45
Gd-pDBI [81]	Gd	pDBI	Doxorubicin	12
HKUST-1 [82]	Cu	BTC	ibuprofen	34
HKUST-1 [82]	Cu	BTC	anethole	38

HKUST-1 [82]	Cu	BTC	guaiacol	40
HKUST-1 [83]	Cu	BTC	Nimesulide	17
IFMC-1 [84]	Zn	H_3L	5-FU	30
Mg_2(OLZ) [85]	Mg	Olsalazine	Phenethylamine	11
MIL-53(Fe)[86]	Fe	terephthalic acid	vancomycin	20
MIL-53 (Cr) [87]	Cr	BDC	ibuprofen	20
MIL-53 (Fe) [87]	Fe	BDC	ibuprofen	20
MIL-53 (Al) [88]	Al	BDC	peptides	–
MIL-53 (Fe) [89]	Fe	BDC	busulfan	10
MIL-53 (Fe) [90]	Fe	BDC	caffeine	29
MIL-53-NH_2 (Fe) [91]	Fe	2-amino terephthalic acid	5-FU	28
MIL-88A (Fe) [89]	Fe	Fumaric acid	busulfan	8
MIL-88B (Fe) [92]	Fe	amino terephthalate	caffeine	–
MIL-89 (Fe) [89]	Fe	Muconic acid	busulfan	14
MIL-100 (Fe) [93]	Fe	BTC	topotecan	33
MIL-100 (Fe) [73]	Fe	BTC	AZT-TP	36
MIL-100 (Fe) [74]	Fe	BTC	AZT-MP	24
MIL-100 (Fe) [94]	Fe	BTC	doxorubicin	31
MIL-100 (Fe) [95]	Fe	BTC	Gem-MP	30
MIL-100(Fe) [96]	Fe	BTC	aspirin	181
MIL-100 (Cr) [97]	Cr	BTC	ibuprofen	26

MIL-100 (Cr) [88]	Cr	BTC	peptides	–
MIL-100 (Fe) [89]	Fe	BTC	busulfan	26
MIL-101 (Cr) [88]	Cr	BDC	peptides	–
MIL-101 (Cr) [97]	Cr	BDC	ibuprofen	138
MIL-100 (Fe) [98]	Fe	BTC	caffeine	50
MIL-100(Fe) [99]	Fe	BTC	RAPTA-C	42
MIL-101 (Fe) [100]	Fe	BDC	ethoxysuccinato-cisplatin	13
MIL-101 (Cr) [101]	Cr	BDC	naproxen	–
MIL-101-NH_2 (Fe) [85]	Fe	amino terephthalate	5-FU	13
MOF-74-Fe (II) [102]	Fe	DOBDC	ibuprofen	16
MOP-15 [103]	Cu	5-NH_2-mBDC	5-FU	24
NU-1000 [104]	Zr	H_4TBAPy	calcein	37
NU-901 [104]	Zr	H_4TBAPy	calcein	42
PCN-221 [105]	Zr	H_2TCPP	MTX	40
Rho-ZMOF [106]	In	H_3ImDC	Procainamide HCl	10
Tb-mesoMOF [107]	Tb	H_3TATB	Vitamins B_{12}	33
UiO-NMOFs [108]	Zr	Amino-TPDC	cisplatin	12
UiO-NMOFs [108]	Zr	Amino-TPDC	pooled siRNAs	82
UiO-66 (Zr) [109]	Zr	BDC	Caffeine	22
UMCM-1 [110]	Zn	BDC and H_3BTB	Ibuprofen	58

ZJU-800 [111]	Zr	F-H_2PDA	Diclofenac sodium	59
ZJU-101 [112]	Zr	BPYDC	Diclofenac sodium	55
ZIF-8 [113]	Zn	2-methylimidazole	Doxorubicin	20
Zn-BDC [114]	Zn	BDC	Ibuprofen	45
Zn-CDDB [115]	Zn	CDDB	5-FU	54
Zn-DDP [116]	Zn	H_4DDP	5-FU	49
Zn-TTA [117]	Zn	H_4TTA	5-FU	21

Abbreviation: AZT-TP=Azidothymidine triphosphate; AZT-MP= Azidothymidine monophosphate; Gem-MP=Gemcitabin monophosphate BTC=1,3,5-Benzene tricarboxylic acid; RAPTA-C=[Ru(p-cymene)Cl_2(pta)] ; BDC=1,4-Benzenedicarboxylic acid; DOBDC = 2,5-dioxido-1,4-benzenedicarboxylate; OLZ=Olsalazine; amino-TPDC= Aminotriphenyldicarboxylic; UiO=Universitetet i Oslo; ZJU = Zhejiang University, ZIF= zeolitic imidazolate framework; F-H_2PDA=(2E,2E′)-3,3′-(2-fluoro-1,4-phenylene)diacrylic acid; BPYDC=2,2′-bipyridine-5,5′-dicarboxylate; Zn-CDDB=[$Zn_8(O)_2$(CDDB)$_6$(DMF)$_4$(H_2O)]; CDDB = 4,4’-(9-H carbazole- 3,6-diyl)dibenzoic acid; Zn-BDC=[Zn(BDC)(H_2O)$_2$]$_n$; 5-FU=5-fluorouraci; H_3L =4,5-di(1H-tetrazol-5-yl)-2H-1,2,3-triazole); CNZTDH=[$(CH_3)_2NH_2]_2$ [Zn(TATAT)$_{2/3}$]·3DMF·H_2O; TATAT=5,5′,5′′-(1,3,5-triazine-2,4,6-triyl)tris(azanediyl)triisophthalate; H_3BTB=1,3,5-Tris(4-carboxyphenyl)benzene; 5-NH_2-mBDC= 5-NH_2-*m*-Benzenedicarboxylate; DHTPA=2,5-Dihydroxyterephthalic acid; pDBI=(1,4-bis(5-carboxy-1H-benzimidazole-2-yl)benzene); H_3ImDC=4,5-imidazoledicarboxylic acid; H_2TCPP= 5,10,15,20-tetrakis(4-carboxyphenyl)porphyrin; MTX= Methotrexate; H_4TTA = [1,1′:3′,1″-terphenyl]-3,3″,5,5″- tetracarboxylic acid; H_4DDP= 2,6-di(3′,5′-dicarboxylphenyl)pyridine; H_3TATB= triazine-1,3,5-tribenzoic acid; H_4BIBDA= 5,5'-(biphenyl-4,4'-diyl-is(methylene))bis(oxy)diisophthalic acid; H_4BBDA= 5,5'-(biphenyl-4,4'-diyl-is (methylene)) bis(oxy)diisophthalic acid; PCN= porous coordination network; HKUST= Hong Kong University of Science and Technology; MOP= Metal-organic polyhedral; UMCM= University of Michigan Crystalline Material.

In addition to MIL-family, a series of other MOFs were used as drug carriers, mainly Zn, Cu and Zr-based MOFs (Table 1). Several MOFs based on Ni, Gd, and In were also studied for drug encapsulation, with the advantages that some metal ions could confer also imaging properties. However, it has been pointed out that the toxicity of some metals could be a drawback for medical applications of some MOFs [118].

Drug release was found to be strongly dependent on the nanoMOF stability in the release media. For instance, MIL-101 nanoMOFs with poor stabilities in aqueous media released AZT-TP in a fast ("burst") manner, in contrast with the more stable MIL-100 nanoMOFs which keep their integrity over longer incubation times [72]. As a general trend, it was found that the larger the pore size, the lower the MOF stability. Drug release from highly porous nanoMOFs appeared to be related to several factors: i) drug interaction with the metal sites and ligands; ii) drug diffusion inside the open porosity of the materials; iii) nanoMOF degradation kinetics in the release media.

Moreover, it was found that in some case, drug incorporation inside nanoMOFs enabled stabilizing the matrix upon degradation. Topotecan (TPT), a hydrophilic cytotoxic drug was efficiently encapsulated in MIL-100 nanoMOFs filling the available space inside their large pores [93]. The drug molecules formed aggregates inside the pores, which in turn strongly stabilized the crystalline tridimensional networks towards degradation in physiological media. Interestingly, TPT release could be triggered by two-photon light-irradiation, opening new standpoints for further developments in stimuli-induced drug delivery. Further studies are on the way to understand the release mechanism.

Drug loading during particle synthesis A few recent examples show the possibility to load drugs in MOFs during their synthesis. Curcumin was successfully incorporated in CD-MOFs without altering their crystallinity. Interestingly, when dissolving the curcumin-loaded CD-MOFs in water, unique complexes between curcumin, CD and potassium cations were found. The stability of curcumin in these complexes was enhanced by at least 3 orders of magnitude compared to curcumin: CD complexes. It was suggested that the CD-MOFs could be useful to store and stabilize curcumin for food applications [27].

In another study, ferulic acid (FA) was strongly associated to CD-MOFs during their preparation by methanol vapor diffusion into an aqueous solution of γ-CD, KOH and FA. Differential scanning calorimetry studies indicated the formation of the stable association between FA and γ -CD in FA/CD-MOF [26].

BioMOF nanoMOFs were synthesized using the drug as a ligand to be directly linked to metal sites, thus building the tridimensional structures [119]. These so called bioMOFs could load up to 71.5 wt% of nicotinic acid. Disuccinatocisplatin was used as a linker to prepare NCP-1 [120] (NCP stands for nanoscale coordination polymer). As most drug molecules possess metal complexing groups such as carboxylates, phosphates or amines, this approach bears a high potential for the development of biocompatible drug-delivery systems, maximizing the drug loading capabilities. Of note, bioMOFs containing therapeutically active molecules as a part of the structural framework are usually synthesized with a minimum number of synthetic steps for attaining maximum drug payloads.

Some MOFs were composed of organic linkers which are not active molecules per se, but transform in physio-biological conditions to release active molecules. For instance, 1,3,5-tris(1H-1,2,3-triazol-5-yl)benzene [121] and 2,5-dihydroxyterephthalic acid [122] were used as linkers releasing NO.

Moreover, bioMOFs synthesized with active molecules as linkers could also be further used to encapsulate other drugs. Olsalazine-based porous MOF was successfully synthesized reaching 51% (w/w) drug loading. Then, phenethylamine could be impregnated into the MOFs reaching a loading of 11% (w/w) [85]

Besides, the use of biologically active metal centers as a part of the MOF structure has lately been investigated. Thus, MOFs can act as reservoirs of metal ions, providing their gradual release to achieve a sustained antibacterial action. A variety of materials have been studied so far, including as metal ions Ag [123-125], Co [126], Cu [127] and Zn [128].

2.3 Surface modification

The application of nanoparticles for drug delivery is expected to make a difference in the field of biotechnology and pharmaceutical industries in the near future, as it paves the way to achieve targeted delivery in a cell- or tissue-specific manner, with the capability to bypass biological barriers (blood-brain barriers, epithelial and endothelial barriers, etc) and to visualize the *in vivo* fate of the nanocarriers by imaging modalities. Nanoparticle surface modification is a prerequisite to achieve these goals, as the interactions between the particles and the living media take place at their interface with the complex biological systems. However, the porous structure of nanoMOFs required the development of specific coating methods which do not alter the porosity and thus the loading capacity of the nanoMOFs.

Silica coatings have been extensively used to modify the surface of both inorganic and polymer

nanoparticles [129-130]. A variety of nanoMOFs have been coated with silica shells in an attempt to stabilize them, control their degradation, increase their biocompatibility and water dispersibility and enable further functionalization with a variety of silyl-derived molecules. Silica shells were synthesized on nanoMOFs made using a variety of metals, including Gd [131], Mn [132], Tb [133], Fe [100], and Zr [134]. It was found that the silica shell significantly slowed down the nanoMOFs degradation. For example, the release of Gd^{3+} ions depended on the silica shell thickness. Silica-coated MIL-101 nanoparticles with the diameter of around 200 nm had a stability of around 14 h in PBS, while the uncoated ones readily decomposed [100]. Moreover, the silica shell also allowed to control drug release depending on its thickness. Furthermore, the surface of these core−shell structures could be further modified by grafting silyl-derived molecules through surface silanol groups to impart additional functionalities, such as targeting ligands, optical contrast agents, and sensing agents. Interestingly, by grafting a cyclic arginine-glycine-aspartate (targeting peptide), the anticancer efficacy against human colon cancer cells of Tb-based nanoMOFs was significantly increased as compared to the non-targeted MOFs [133].

Reversible addition−fragmentation chain transfer (RAFT) polymerization was used to modify the surface of Gd-based NMOFs. Polymer-coating on nanoMOFs were achieved using a trithiocarbonate RAFT agent. The coatings were attached on the MOF surfaces through vacant coordination sites on the Gd^{3+} ions. The resulting polymer-coated Gd-MOFs were demonstrated to be biocompatible and had cancer cell targeting abilities and bimodal imaging properties [134-136].

Recently, simple, fast, and ‘‘green’’ strategies for functionalization of nanoMOFs were reported. MIL-100 (Fe) was ‘‘easily’’ coated by CD molecules bearing strong iron complexing groups (phosphates) [137] or by heparin [138]. The heparin coating endowed the nanoMOFs with improved biological properties, such as reduced cell recognition, lack of complement activation, and reactive oxygen species production [138].The stable CD-based coating was further functionalized with: i) targeting moieties to increase the nanoMOF interaction with specific receptors and ii) PEG chains to escape the immune system. These results pave the way towards the design of surface-engineered nanoMOFs of interest for applications in the field of targeted drug delivery. Polysaccharides like dextran and chitosan were studied to improve the solubility, cellular adhesion and imaging properties of native MOFs [139].

Lipid coatings have recently been used to modify the surfaces of MIL-100 (Fe)[140]. Dye molecules were entrapped in the resulting MOF@lipid systems. It was shown that the lipid bilayer could: I) prevent the premature release of the dye, II) increase the colloidal stability of

the nanoparticles and III) favored a higher uptake by cancer cells as compared to uncoated particles. Amorphous MOFs or nanoscale coordination polymers, were also coated with lipid coatings [141-144]. The pH-responsive coatings have also been developed.

Doxorubicin loaded MIL-101 was functionalized with pH responsive benzoic imine bond and a redox active disulfide system. Both in vitro and in vivo results demonstrated that this system efficiently inhibited cancer cell growth while showing reduced side effects [145]. Chitosan-modified magnetic nanoMOFs loaded with doxorubicin showed pH-responsive drug release for several days. Moreover, the particles could be modified with folic acid, a target molecule, which allowed a more specific cellular internalization in folate-overexpressing cancer cells (HeLa) in comparison to normal (L929) cells [146].

2.4 *In vivo* studies

For biomedical and pharmaceutical applications, MOFs are firstly required to have toxicologically compatible features. Nine representative nanoMOFs were assessed to zebrafish embryos, including barely cytotoxic (nanoUiO-66, nanoUiO-67, and nanoCo-MOF-74, and nanoMg-MOF-74), moderately cytotoxic (nanoZIF-7, nanoMIL-100, and nanoMIL-101), and highly cytotoxic (nanoZIF-8 and nanoHKUST-1). It is found that at 120 h post fertilization, the viabilities of the embryos exposed to nanoCo-MOF-74, nanoMg-MOF-74, nanoUiO-66, nanoUiO-67, nanoMIL-100, and nanoMIL-101 were not significantly different to those of the control group (without nanoMOFs), even at highest concentration (200 µM). In contrast, nanoZIF-7, nanoZIF-8, and nanoHKUST-1 provoked significant decreases in embryo survival. NanoZIF-7 was slightly toxic at 200 µM (embryo viability 79.2%); nanoZIF-8 was more toxic at the same concentration (embryo viability 33.3%); and nanoHKUST-1 was extremely toxic even at 20 µM (viability: 0%). It was shown that the leaching of solubilized metal ions played a main role on the levels of the MOF toxicity[147].

Toxicity of iron trimesic MIL-100 (Fe) and trimesic acid were performed through intravenous administrating to rats. Around 220 mg/kg of MIL-100 and 78 mg/kg trimesic acid were intravenously injected and the results showed that the animal behavior and weight evolution of injected rats were totally normal in comparison with control group. It was concluded that this material is acceptable for drug delivery [148]. Biodistribution of MIL-100 nanoMOFs at early times (up to 24 h) or long term (from 24 h to 1 month) after administration were evaluated. The pharmacokinetic profile suggested that the nanoparticles act as a depot in the blood stream during the first hours before being cleared. Accumulation took mainly place in the liver and, in

some extent, in the spleen. Histological studies demonstrated the absence of morphological alterations due to the presence of the particles in these organs. Liver function was however slightly altered as reflected by the increased plasma aspartate aminotransferase concentrations. Finally trimesate was progressively eliminated in urine. Nevertheless, it was demonstrated that in the long-term study, these abnormalities in the iron levels were completely reversed after seven days and were not related to any toxicity signs.

Despite the paramount importance of in vivo experiments, there are only scarce examples showing in vivo data, certainly because of nanoMOFs' novelty in the biomedicine domain. Simon-Yarza et al. reported the first in vivo results with MIL-100 nanoMOFs loaded with the antineoplastic drug busulfan. Drug-loaded nanoMOFs were administered to rats and compared with the commercial Busilvex®. Large differences in serum concentration of both busulfan and the constitutive ligand (trimesate) revealed the great impact of drug encapsulation both on the drug and on nanoparticle pharmacokinetics during the first 24 h of administration[149].

Tumor targeting MOFs (TTMOFs) based on MIL-101 were successfully developed via surface modification with polymers comporting pH responsive benzoic imine bonds and redox responsive disulfide bonds. In vivo experiments showed that doxorubicin-loaded TTMOFs could effectively inhibit tumor growth with minimal side effects [145].

2.5 Imaging with MOF

Magnetic resonance imaging (MRI). MRI is a powerful and noninvasive diagnostic imaging technique allowing the detection of nuclear spin reorientations with high spatial resolution. Contrast agents are used to improve the image quality by reducing the proton relaxation times. NanoMOFs have received attention as contrast agents because of their hybrid composition consisting of metal centers and organic ligands. Moreover, as all other types of nanoparticles, they can be engineered in order to accumulate in targeted organs or tissues of interest (such as tumors) either by "passive targeting" via enhanced permeability and retention effect, or by "active targeting" using various target-ligands [150]. Firstly, Gd^{3+} -containing nanoMOFs have shown high relaxivities as T_1-weighted contrast agents. They possessed increased relaxivities as compared to the clinically used Omniscan. Gd-based nanoMOFs endowed with multimodal imaging properties were further developed. For instance, both a specific ligand and a fluorophore were grafted onto the nanoMOF surfaces enabling to achieve a tumor-targeted MRI effect [132].Multifunctional MOFs endowed with bimodal imaging properties via MRI and fluorescence microscopy were synthesized for tumor targeting and diagnostic imaging [136].A

variety of MOFs endowed with imaging properties was synthesized, including as metal ions Cu [151], Ru [134] Eu [131], and Tb [152]. Although the relaxivities of Mn^{2+}-based nanoMOFs were modest, the possibility for site-specific imaging with the help of a silica shell at the surface of nanoMOFs has been demonstrated[132] . Fe^{3+}-containing nanoMOFs possessed good T_2-weighted contrast enhancement. [72]. MRI measurements on Wistar female rats shows that the treated liver and spleen organs were darker than the normal ones, because of the preferential accumulation of the nanoMOFs in these organs. However, three months after injection, the liver and spleen returned to a similar appearance to that of the untreated rats, in accordance with the temporary accumulation of the nanoMOFs in these organs. Recently, a multifunctional nanoplatform based on isoreticular metal organic frameworks (IRMOF-3) was developed. Folic acid and the fluorescent molecule rhodamine B isothiocyanate (RITC) were both conjugated to the nanoMOF surface for cancer cell targeting and optical imaging. Paclitaxel was loaded into these magnetic nanoMOFs. The targeted nanoMOFs showed stronger T2-weighted MRI contrast towards cancer cells [153].

X-ray Computed Tomography (CT) Imaging. CT imaging is based on specimen attenuation of X-rays and can provide 3D images with excellent spatial resolution. Typical contrast agents are materials containing high Z number elements, including iodine, barium and bismuth. Currently, barium sulfate and iodinated aromatic are used clinically for intravenous and gastrointestinal tract imaging, respectively. The contrast agents for CT have the same drawbacks as for MRI, including a non-specific distribution and a fast clearance. Therefore, nanoMOFs have been developed as carriers for iodinated aromatic molecules [154]. They were prepared using tetra iodo benzene dicarboxylic acids as bridging ligands and Cu^{2+} or Zn^{2+} as metal connecting points. The efficacy of the resulting iodinated nanoMOFs for CT has been clearly demonstrated.

All the above presented studies highlight the potential of nanoscale MOFs as platforms for MRI and X-ray CT.

Conclusion

Despite an enormous amount of research in the area of nanomedicine and advanced nano-carriers drug targeting in cancer, the transition from laboratory to the market is usually very slow and unpredictable. The majority of the problems arise from effective oversight in safety- and efficacy-by-design approach for nanomedicines. “Cage” particles based on “CD” and MOFs were shown to be biocompatible and versatile materials, adapted for drug incorporation. Moreover, their “green” scalable preparation positions these materials as good candidates for

biomedical application. They are promising carriers for various drugs, including antibiotics, anticancer and anti-inflammatory drugs, etc.

CDs are recognized as “molecule containers” to form inclusion complexes with a variety of active molecules. These inclusion could not only improve the solubility and bioavailability of poorly soluble drugs, stabilize drugs from light, thermal and oxidative degradation, mask the bitter taste of the drugs, but also can be used as the driving forces to form NPs. Remarkably, the NPs spontaneously formed by CD inclusion complexes are easily formed by “green” methods, in absence of organic solvents or surfactants. While self-assembled NPs composed of CDs are attractive formulations, the stability of the formed NPs need to be studied in depth upon dilution, since the supramolecular edifices are constructed solely on the basis of non-covalent bonds. Indeed, in theory, the inclusion complexes are prone to dis-assemble upon extreme dilution, leading to the destructuring of the NPs.

CD-MOFs are a new type of porous CD-based particles, which contain not only the cavities of CDs, but also the big pores built up by CDs self-assemblies (Fig.1). Compared with CD based NPs, CD-MOFs have the possibility to load drugs with higher payloads. Given the fact that the particles disassemble in water, we foresee that a promising administration route could be pulmonary inhalation. However, with appropriate surface modification, the stability of CD-MOFs was significantly improved, which broadens their application also for potential oral and intravenous administration.

MOFs, especially biodegradable MOFs stable in aqueous media, have drawn a lot of attention as drug delivery systems. MIL-100(Fe) was considered among the most efficient material as drug carrier due to its large pore size, biocompatibility and biodegradability. A variety of drugs have been efficiently encapsulated, including anti-inflammatory (ibuprofen, aspirin), antiviral (cidofovir, AZT-TP and AZT-MP), anticancer (busulfan, doxorubicin, ethoxysuccinato-cisplatin prodrug, Gem-MP and topotecan) drugs. There are two types of cages in the structure of MIL-100(Fe), so it could be possible to load two drugs simultaneously in the same particles in theory. To the best of our knowledge, studies so far report only the incorporation of one drug in the same particles. In this context, it would be interesting try to entrap synergic drugs in the same particles to treat complex pathologies such as cancer and severe viral or bacterial infections.

By taking advantage of their specific characters such as green preparation procedure, high drug payloads, and co-encapsulation of synergic drugs, these “cage” particles, these “cage” particles

are very promising for drug delivery applications.

References

1. Crini, G. Review: A history of cyclodextrins. *Chem. Rev.* **114,** 10940–10975 (2014).
2. Stella, V. J. & He, Q. Cyclodextrins. *Toxicol. Pathol.* **36,** 30–42 (2008).
3. Loftsson, T. *et al.* Cyclodextrins in drug delivery. *Expert Opin. Drug Deliv.* **2**,335-351 (2005).
4. Del Valle, E. M. M. Cyclodextrins and their uses: A review. *Process Biochem.* **39,** 1033–1046 (2004).
5. Manakker, F. Van De, Vermonden, T., Nostrum, C. F. Van & Hennink, W. E. Cyclodextrin-Based Polymeric Materials : Synthesis , Properties Pharmaceutical/Biomedical Applications, *Biomacromolecules*. **10,** (2009).
6. Loftsson, T. & Brewster, M. E. Pharmaceutical applications of cyclodextrins: Basic science and product development. *J. Pharm. Pharmacol.* **62,** 1607–1621 (2010).
7. Szejtli, J. Introduction and General Overview of Cyclodextrin Chemistry. *Chem. Rev.* **98,** 1743–1754 (1998).
8. Harada, A., Hashidzume, A. & Takashima, Y. Cyclodextrin-based supramolecular polymers. *Adv. Polym. Sci.* **201,** 1–43 (2006).
9. Li, P. *et al.* Comparison in toxicity and solubilizing capacity of hydroxypropyl-β-cyclodextrin with different degree of substitution. *Int. J. Pharm.* **513,** 347–356 (2016).
10. Zhang, J. & Ma, P. X. Cyclodextrin-based supramolecular systems for drug delivery: Recent progress and future perspective Jianxiang. *Adv Drug Deliv Rev.* **65,** 1–39 (2014).
11. Concheiro, A. & Alvarez-Lorenzo, C. Chemically cross-linked and grafted cyclodextrin hydrogels: From nanostructures to drug-eluting medical devices. *Adv. Drug Deliv. Rev.* **65,** 1188–1203 (2013).
12. Gidwani, B. & Vyas, A. Synthesis, characterization and application of Epichlorohydrin-β-cyclodextrin polymer. *Colloids Surfaces B Biointerfaces* **114,** 130–137 (2014).
13. Renard, E., Deratani, A., Volet, G. & Sebille, B. Preparation and characterization of water soluble high molecular weight β-cyclodextrin-epichlorohydrin polymers. *Eur. Polym. J.* **33,** 49–57 (1997).
14. Gref, R. *et al.* New self-assembled nanogels based on host-guest interactions: Characterization and drug loading. *J. Control. Release* **111,** 316–324 (2006).
15. Daoud-Mahammed, S. *et al.* Cyclodextrin and polysaccharide-based nanogels: Entrapment of two hydrophobic molecules, benzophenone and tamoxifen. *Biomacromolecules* **10,** 547–554 (2009).
16. Anand, R. *et al.* β-Cyclodextrin polymer nanoparticles as carriers for doxorubicin and artemisinin: a spectroscopic and photophysical study. *Photochem. Photobiol. Sci.* **11,** 1285 (2012).
17. Rasheed, A., Kumar C.K., A. & Sravanthi, V. V. N. S. S. Cyclodextrins as drug carrier molecule: A review. *Sci. Pharm.* **76,** 567–598 (2008).

18. Zuckerman, J. E. *et al.* Correlating animal and human phase Ia/Ib clinical data with CALAA-01, a targeted, polymer-based nanoparticle containing siRNA. *Proc. Natl. Acad. Sci.* **111,** 11449–11454 (2014).

19. Jambhekar, S. S. & Breen, P. Cyclodextrins in pharmaceutical formulations I: Structure and physicochemical properties, formation of complexes, and types of complex. *Drug Discov. Today* **21,** 356–362 (2016).

20. Davis, M. E. & Brewster, M. E. Cyclodextrin-based pharmaceutics: past, present and future. *Nat. Rev. Drug Discov.* **3,** 1023–1035 (2004).

21. Venkateswarlu, N. Hydroxyethyl Cellulose : Hydrogel Based Drug Delivery. *R. R. J. P. P. S* **3,** 2320–2322 (2014).

22. Zhou, J. & Ritter, H. Cyclodextrin functionalized polymers as drug delivery systems. *Polym. Chem.* **1,** 1552 (2010).

23. Bonnet, V., Gervaise, C., Djedaini-Pilard, F., Furlan, A. & Sarazin, C. Cyclodextrin nanoassemblies: A promising tool for drug delivery. *Drug Discov. Today* **20,** 1120–1126 (2015).

24. Hoare, T. R. & Kohane, D. S. Hydrogels in drug delivery: Progress and challenges. *Polymer (Guildf).* **49,** 1993–2007 (2008).

25. Smaldone, R. A. *et al.* Metalorganic frameworks from edible natural products. *Angew. Chemie - Int. Ed.* **49,** 8630–8634 (2010).

26. Michida, W., Ezaki, M., Sakuragi, M., Guan, G. & Kusakabe, K. Crystal growth of cyclodextrin-based metal-organic framework with inclusion of ferulic acid. *Cryst. Res. Technol.* **50,** 556–559 (2015).

27. Moussa, Z., Hmadeh, M., Abiad, M. G., Dib, O. H. & Patra, D. Encapsulation of curcumin in cyclodextrin-metal organic frameworks: Dissociation of loaded CD-MOFs enhances stability of curcumin. *Food Chem.* **212,** 485–494 (2016).

28. Hartlieb, K. J. *et al.* Encapsulation of Ibuprofen in CD-MOF and Related Bioavailability Studies. *Mol. Pharm.* **14**, 1831-1839 (2017).

29. Furukawa, Y., Ishiwata, T., Sugikawa, K., Kokado, K. & Sada, K. Nano- and microsized cubic gel particles from cyclodextrin metal-organic frameworks. *Angew. Chemie - Int. Ed.* **51,** 10566–10569 (2012).

30. Liu, B. *et al.* Microwave-Assisted Rapid Synthesis of γ-Cyclodextrin Metal-Organic Frameworks for Size Control and Efficient Drug Loading. *Cryst. Growth Des.* **17,** 1654–1660 (2017).

31. Liu, B. *et al.* Optimized synthesis and crystalline stability of γ-cyclodextrin metal-organic frameworks for drug adsorption. *Int. J. Pharm.* **514,** 212–219 (2016).

32. Li, H. *et al.* Facile stabilization of cyclodextrin metal–organic frameworks under aqueous conditions via the incorporation of C_{60} in their matrices. *Chem. Commun.* **52,** 5973–5976 (2016).

33. Lv, N. *et al.* Improvement in Thermal Stability of Sucralose by γ-Cyclodextrin Metal-Organic Frameworks. *Pharm. Res.* **34**, 269-278 (2017).

34. Yaghi, O. M. *et al.* Reticular synthesis and the design of new materials. *Nature* **423,** 705–

714 (2003).

35. Férey, G. Hybrid porous solids: past, present, future. *Chem. Soc. Rev.* **37,** 191–214 (2008).

36. Eddaoudi, M. *et al.* Modular chemistry: Secondary building units as a basis for the design of highly porous and robust metal-organic carboxylate frameworks. *Acc. Chem. Res.* **34,** 319–330 (2001).

37. Kitagawa, S., Kitaura, R. & Noro, S. Functional porous coordination polymers. *Angew. Chemie - Int. Ed.* **43,** 2334–2375 (2004).

38. Férey, G., Mellot-Draznieks, C., Serre, C. & Millange, F. Crystallized frameworks with giant pores: Are there limits to the possible? *Acc. Chem. Res.* **38,** 217–225 (2005).

39. McKinlay, A. C. *et al.* BioMOFs: Metal-organic frameworks for biological and medical applications. *Angew. Chemie - Int. Ed.* **49,** 6260–6266 (2010).

40. He, C., Liu, D. & Lin, W. Nanomedicine Applications of Hybrid Nanomaterials Built from Metal-Ligand Coordination Bonds: Nanoscale Metal-Organic Frameworks and Nanoscale Coordination Polymers. *Chem. Rev.* **115,** 11079–11108 (2015).

41. Furukawa, H., Cordova, K. E., O'Keeffe, M. & Yaghi, O. M. The Chemistry and Applications of Metal-Organic Frameworks. *Science* **9,** 1230444 (2010).

42. Farha, O. K. *et al.* Metal-organic framework materials with ultrahigh surface areas: Is the sky the limit? *J. Am. Chem. Soc.* **134,** 15016–15021 (2012).

43. Senkovska, I. & Kaskel, S. Ultrahigh porosity in mesoporous MOFs: promises and limitations. *Chem. Commun. (Camb).* **50,** 7089–98 (2014).

44. Koh, K., Wong-Foy, A. G. & Matzger, A. J. A porous coordination copolymer with over 5000 m^2/g BET surface area. *J. Am. Chem. Soc.* **131,** 4184–4185 (2009).

45. Férey, G. *et al.* A chromium terephthalate-based solid with unusually large pore volumes and surface area. *Science* **309,** 2040–2042 (2005).

46. Vallet-Regí, M., Balas, F. & Arcos, D. Mesoporous materials for drug delivery. *Angew. Chemie - Int. Ed.* **46,** 7548–7558 (2007).

47. Serre, C., Millange, F., Surblé, S. & Férey, G. A route to the synthesis of trivalent transition-metal porous carboxylates with trimeric secondary building units. *Angew. Chemie - Int. Ed.* **43,** 6286–6289 (2004).

48. Jhung, S. H. *et al.* Microwave Synthesis of Hybrid Inorganic-Organic Porous Materials: Phase-Selective and Rapid Crystallization. *Chem. Eur. J.* **12,** 7899–7905 (2006).

49. Das, A. K., Vemuri, R. S., Kutnyakov, I., McGrail, B. P. & Motkuri, R. K. An Efficient Synthesis Strategy for Metal-Organic Frameworks: Dry-Gel Synthesis of MOF-74 Framework with High Yield and Improved Performance. *Sci. Rep.* **6,** 28050 (2016).

50. Pichon, A. & James, S. L. An array-based study of reactivity under solvent-free mechanochemical conditions—insights and trends. *Cryst. Eng. Comm.* **10,** 1839 (2008).

51. Pichon, A., Lazuen-Garay, A. & James, S. L. Solvent-free synthesis of a microporous metal–organic framework. *Cryst. Eng. Comm.* **8,** 211 (2006).

52. Lee, Y. R., Kim, J. & Ahn, W. S. Synthesis of metal-organic frameworks: A mini review.

Korean J. Chem. Eng. **30,** 1667–1680 (2013).

53. Carné, A., Carbonell, C., Imaz, I. & Maspoch, D. Nanoscale metal–organic materials. *Chem. Soc. Rev.* **40,** 291–305 (2011).

54. Rieter, W. J., Taylor, K. M. L., An, H., Lin, W. & Lin, W. Nanoscale metal-organic frameworks as potential multimodal contrast enhancing agents. *J. Am. Chem. Soc.* **128,** 9024–9025 (2006).

55. Sun, C.-Y., Qin, C., Wang, X.-L. & Su, Z.-M. Metal-organic frameworks as potential drug delivery systems. *Expert Opin. Drug Deliv.* **10,** 89–101 (2013).

56. Taylor, K. M. L., Jin, A. & Lin, W. Surfactant-assisted synthesis of nanoscale gadolinium metal-organic frameworks for potential multimodal imaging. *Angew. Chemie - Int. Ed.* **47,** 7722–7725 (2008).

57. Sun, Y. & Zhou, H.-C. Recent progress in the synthesis of metal–organic frameworks. *Sci. Technol. Adv. Mater.* **16,** 54202 (2015).

58. Juan-Alcaniz, J., Gascon, J. & Kapteijn, F. Metal-organic frameworks as scaffolds for the encapsulation of active species: state of the art and future perspectives. *J. Mater. Chem.* **22,** 10102–10118 (2012).

59. Shekhah, O. *et al.* Step-by-step route for the synthesis of metal-organic frameworks. *J. Am. Chem. Soc.* **129,** 15118–15119 (2007).

60. Banerjee, R. *et al*. High-Throughput Synthesis of Zeolitic Imidazolate Frameworks and Application to CO_2 Capture. *Science* **319**, 939-943 (2012).

61. Horcajada, P. *et al.* Colloidal route for preparing optical thin films of nanoporous metal-organic frameworks. *Adv. Mater.* **21,** 1931–1935 (2009).

62. Cho, W., Lee, H. J. & Oh, M. Growth-controlled formation of porous coordination polymer particles. *J. Am. Chem. Soc.* **130,** 16943–16946 (2008).

63. Theresa M. Reineke, Mohamed Eddaoudi, Michael Fehr, Douglas Kelley, & Yaghi, O. M. From Condensed Lanthanide Coordination Solids to Microporous Frameworks Having Accessible Metal Sites. *J. Am. Chem. Soc.*, **121**, 1651–1657 (1999).

64. Kerbellec, N. *et al.* Luminescent coordination nanoparticles. *New J. Chem.* **32,** 584 (2008).

65. Qiu, L.-G. *et al.* Facile synthesis of nanocrystals of a microporous metal-organic framework by an ultrasonic method and selective sensing of organoamines. *Chem. Commun. (Camb).* **5**, 3642–3644 (2008).

66. Hatakeyama, W. *et al.* Synthesis of gadolinium nanoscale metal-organic framework with hydrotropes: Manipulation of particle size and magnetic resonance imaging capability. *ACS Appl. Mater. Interfaces* **3,** 1502–1510 (2011).

67. Bhat, M. & Gaikar, V. G. Characterization of interaction between butylbenzene sulfonates and cetyl pyridinium chloride in a mixed aggregate system. *Langmuir* **16,** 1580–1592 (2000).

68. Garay, A. L., Pichon, A. & James, S. L. Solvent-free synthesis of metal complexes. *Chem. Soc. Rev.* **36,** 846 (2007).

69. Friščić, T. New opportunities for materials synthesis using mechanochemistry. *J. Mater. Chem.* **20,** 7599 (2010).

70. Kundu, T. *et al.* Mechanical downsizing of a gadolinium(III)-based metal-organic framework for anticancer drug delivery. *Chemistry* **20,** 10514–10518 (2014).

71. Horcajada, P. *et al.* Synthesis and catalytic properties of MIL-100(Fe), an iron(iii) carboxylate with large pores. *Chem. Commun.* **100,** 2820–2822 (2007).

72. Horcajada, P. *et al.* Porous metal-organic-framework nanoscale carriers as a potential platform for drug delivery and imaging. *Nat. Mater.* **9,** 172–178 (2010).

73. Agostoni, V. *et al.* Towards an Improved anti-HIV Activity of NRTI via Metal-Organic Frameworks Nanoparticles. *Adv. Healthc. Mater.* **2,** 1630–1637 (2013).

74. Agostoni, V. *et al.* Impact of phosphorylation on the encapsulation of nucleoside analogues within porous iron(iii) metal–organic framework MIL-100(Fe) nanoparticles. *J. Mater. Chem. B* **1,** 4231–4242 (2013).

75. Liu, J. *et al.* Controllable porosity conversion of metal-organic drug delivery. *Chem. Commun.* **53,** 7804–7807 (2017).

76. Sha, J. *et al.* Unprecedented α-cyclodextrin metal-organic frameworks with chirality : Structure and drug adsorptions. *Polyhedron* **127**, 396-402 (2017).

77. Wang, F. M. *et al.* A Combination of Experiment and Molecular Simulation Studies on a New Metal-Organic Framework Showing pH-Triggered Drug Release *Koord. Khim.*. **43,** 133–137 (2017).

78. Sun, C. Y. *et al.* Chiral nanoporous metal-organic frameworks with high porosity as materials for drug delivery. *Adv. Mater.* **23,** 5629–5632 (2011).

79. Rojas, S. *et al.* Metal–organic frameworks as potential multi-carriers of drugs. *Cryst. Eng. Comm.* **15,** 9364 (2013).

80. Lucena, F. R. S. *et al.* Induction of cancer cell death by apoptosis and slow release of 5-fluoracil from metal-organic frameworks Cu-BTC. *Biomed. Pharmacother.* **67,** 707–713 (2013).

81. Giménez-Marqués, M., Hidalgo, T., Serre, C. & Horcajada, P. Nanostructured metal-organic frameworks and their bio-related applications. *Coord. Chem. Rev.* **307,** 342–360 (2015).

82. Chen, Q. *et al.* Controlled release of drug molecules in metal–organic framework material HKUST-1. *Inorg. Chem. Commun.* **79,** 78–81 (2017).

83. Falcaro, P. *et al.* Application of Metal and Metal Oxide Nanoparticles@MOFs. *Coord. Chem. Rev.* **307,** 237-254 (2016).

84. Qin, J.-S. *et al.* N-rich zeolite-like metal–organic framework with sodalite topology: high CO_2 uptake, selective gas adsorption and efficient drug delivery. *Chem. Sci.* **3,** 2114-2118 (2012).

85. Levine, D. J. *et al.* Olsalazine-Based Metal-Organic Frameworks as Biocompatible Platforms for H_2 Adsorption and Drug Delivery. *J. Am. Chem. Soc.* **138,** 10143–10150 (2016).

86. Lin, S. *et al.* Porous Iron-Carboxylate Metal−Organic Framework : A Novel Bioplatform with Sustained Antibacterial Efficacy and Nontoxicity. **53,** 19248-19257 (2017).

87. Horcajada, P. *et al.* Flexible porous metal-organic frameworks for a controlled drug delivery. *J. Am. Chem. Soc.* **130,** 6774–6780 (2008).

88. Gu, Z.-Y., Chen, Y.-J., Jiang, J.-Q. & Yan, X.-P. Metal-organic frameworks for efficient enrichment of peptides with simultaneous exclusion of proteins from complex biological samples. *Chem. Commun. (Camb).* **47,** 4787–4789 (2011).

89. Chalati, T. *et al.* Porous metal organic framework nanoparticles to address the challenges related to busulfan encapsulation. *Nanomedicine* **6,** 1683–1695 (2011).

90. Ke, F. *et al.* Facile fabrication of magnetic metal–organic framework nanocomposites for potential targeted drug delivery. *J. Mater. Chem.* **21,** 3843–3848 (2011).

91. Gao, X. *et al.* Controllable Synthesis of a Smart Multifunctional Nanoscale Metal − Organic Framework for Magnetic Resonance / Optical Imaging and Targeted Drug Delivery. *ACS Appl. Mater. Interfaces*, **9**, 3455–3462 (2017).

92. Gaudin, C. *et al.* A quantitative structure activity relationship approach to probe the influence of the functionalization on the drug encapsulation of porous metal-organic frameworks. *Microporous Mesoporous Mater.* **157,** 124–130 (2012).

93. Di Nunzio, M. R., Agostoni, V., Cohen, B., Gref, R. & Douhal, A. A 'ship in a bottle' strategy to load a hydrophilic anticancer drug in porous metal organic framework nanoparticles: Efficient encapsulation, matrix stabilization, and photodelivery. *J. Med. Chem.* **57,** 411–420 (2014).

94. Anand, R. *et al.* Host-guest interactions in Fe(III)-trimesate MOF nanoparticles loaded with doxorubicin. *J. Phys. Chem. B* **118,** 8532–8539 (2014).

95. Rodriguez-Ruiz, V. *et al.* Efficient 'green' encapsulation of a highly hydrophilic anticancer drug in metal-organic framework nanoparticles. *J. Drug Target.* **23,** 759–67 (2015).

96. Singco, B. *et al.* Approaches to drug delivery: Confinement of aspirin in MIL-100(Fe) and aspirin in the de novo synthesis of metal-organic frameworks. *Microporous Mesoporous Mater.* **223,** 254–260 (2016).

97. Horcajada, P. *et al.* Metal-organic frameworks as efficient materials for drug delivery. *Angew. Chemie - Int. Ed.* **45,** 5974–5978 (2006).

98. Cunha, D. *et al.* Rationale of drug encapsulation and release from biocompatible porous metal-organic frameworks. *Chem. Mater.* **25,** 2767–2776 (2013).

99. Rojas, S., Carmona, F. J., Maldonado, C. R., Barea, E. & Navarro, J. A. R. RAPTA-C incorporation and controlled delivery from MIL-100(Fe) nanoparticles. *New J. Chem.* **40,**.5690-5694 (2016).

100. Taylor-Pashow, K. M. L., Della Rocca, J., Xie, Z., Tran, S. & Lin, W. Postsynthetic modifications of iron-carboxylate nanoscale metal-organic frameworks for imaging and drug delivery. *J. Am. Chem. Soc.* **131,** 14261–14263 (2009).

101. Hu, Y., Song, C., Liao, J., Huang, Z. & Li, G. Water stable metal-organic framework packed microcolumn for online sorptive extraction and direct analysis of naproxen and its metabolite from urine sample. *J. Chromatogr. A* **1294,** 17–24 (2013).

102. Hu, Q. *et al.* A low cytotoxic cationic metal-organic framework carrier for controllable drug release. *J. Med. Chem.* **57,** 5679–5685 (2014).

103. Wang, H.-N. *et al.* Stepwise assembly of metal-organic framework based on a metal-organic polyhedron precursor for drug delivery. *Chem. Commun. (Camb).* **47,** 7128–30 (2011).

104. Teplensky, M. H. *et al.* Temperature Treatment of Highly Porous Zirconium-Containing Metal−Organic Frameworks Extends Drug Delivery Release. *J. Am. Chem. Soc.*, **139,** 7522–7532 (2017).

105. Lin, W. *et al.* A porphyrin-based metal – organic framework as a pH-responsive drug carrier. *J. Solid State Chem.* **237,** 307–312 (2016).

106. An, J., Geib, S. J. & Rosi, N. L. Cation-triggered drug release from a porous zinc-adeninate metal-organic framework. *J. Am. Chem. Soc.* **131,** 8376–8377 (2009).

107. Chen, Y. *et al.* Investigation of the Mesoporous Metal − Organic Framework as a New Platform To Study the Transport Phenomena of Biomolecules. *ACS Appl. Mater. Interfaces* **9**, 10874–10881 (2017).

108. He, C., Lu, K., Liu, D. & Lin, W. Nanoscale metal-organic frameworks for the co-delivery of cisplatin and pooled siRNAs to enhance therapeutic efficacy in drug-resistant ovarian cancer cells. *J. Am. Chem. Soc.* **136,** 5181–5184 (2014).

109. Devautour-Vinot, S. *et al.* Ligand dynamics of drug-loaded microporous zirconium terephthalates-based metal-organic frameworks: Impact of the nature and concentration of the guest. *J. Phys. Chem. C* **118,** 1983–1989 (2014).

110. Babarao, R. & Jiang, J. Unraveling the energetics and dynamics of ibuprofen in mesoporous metal-organic frameworks. *J. Phys. Chem. C* **113,** 18287–18291 (2009).

111. Jiang, K. *et al.* Pressure-controlled drug release in a Zr-cluster-based MOF. *J. Mater. Chem. B* **4,** 6398–6401 (2016).

112. Yang, Y. Y. *et al.* A Large Capacity Cationic Metal-Organic Framework Nanocarrier for Physiological pH Responsive Drug Delivery. *Mol. Pharm.* **13,** 2782–2786 (2016).

113. Zheng, H. *et al.* One-pot Synthesis of Metal-Organic Frameworks with Encapsulated Target Molecules and Their Applications for Controlled Drug Delivery. *J. Am. Chem. Soc.* **138,** 962–968 (2016).

114. Rodrigues, M. O. *et al.* Metal organic frameworks for drug delivery and environmental remediation: A molecular docking approach. *Int. J. Quantum Chem.* **112,** 3346–3355 (2012).

115. Bag, P. P., Wang, D., Chen, Z. & Cao, R. Outstanding drug loading capacity by water stable microporous MOF: a potential drug carrier. *Chem. Commun.* **52,** 3669–3672 (2016).

116. Luo, Z. *et al.* A metal-organic framework with unusual nanocages : Drug delivery. *Inorg. Chem. Commun.* **76,** 91–94 (2017).

117. Ma, A., Luo, Z., Gu, C., Li, B. & Liu, J. Cytotoxicity of a metal – organic framework : Drug delivery. *Inorg. Chem. Commun.* **77,** 68–71 (2017).

118. Horcajada, P. *et al.* Metal Organic Frameworks in Biomedicine. *Chem. Rev.*, **112,** 1232–

1268 (2012).

119. Miller, S. R. *et al.* Biodegradable therapeutic MOFs for the delivery of bioactive molecules. *Chem. Commun.* **46,** 4526-4528 (2010).

120. Huxford, R. C. *et al.* Metal-organic frameworks as potential drug carriers. *Curr. Opin. Chem. Biol.* **14,** 262–268 (2010).

121. Neufeld, M. J., Ware, B. R., Lutzke, A., Khetani, S. R. & Reynolds, M. M. Water-Stable Metal-Organic Framework/Polymer Composites Compatible with Human Hepatocytes. *ACS Appl. Mater. Interfaces* **8,** 19343–19352 (2016).

122. Hinks, N. J., McKinlay, A. C., Xiao, B., Wheatley, P. S. & Morris, R. E. Metal organic frameworks as NO delivery materials for biological applications. *Microporous Mesoporous Mater.* **129,** 330–334 (2010).

123. Lu, X. *et al.* Silver carboxylate metal-organic frameworks with highly antibacterial activity and biocompatibility. *J. Inorg. Biochem.* **138,** 114–121 (2014).

124. Berchel, M. *et al.* A silver-based metal–organic framework material as a 'reservoir' of bactericidal metal ions. *New J. Chem.* **35,** 1000–1003 (2011).

125. Liu, Y. *et al.* Multiple topological isomerism of three-connected networks in silver-based metal-organoboron frameworks. *Chem. Commun. (Camb).* **46,** 2608–10 (2010).

126. Aguado, S. *et al.* Antimicrobial activity of cobalt imidazolate metal-organic frameworks. *Chemosphere* **113,** 188–192 (2014).

127. Chiericatti, C., Basilico, J. C., Zapata Basilico, M. L. & Zamaro, J. M. Novel application of HKUST-1 metal-organic framework as antifungal: Biological tests and physicochemical characterizations. *Microporous Mesoporous Mater.* **162,** 60–63 (2012).

128. Tamames-Tabar, C. *et al.* Cytotoxicity of nanoscaled metal-organic frameworks. *J. Mater. Chem. B* **2,** 262–271 (2014).

129. Zou, H., Wu, S. & Shen, J. Polymer / Silica Nanocomposites : Preparation, Characterization, Properties, and and Applications. *Chem. Rev.* **108,** 3893–3957 (2008).

130. Liu, S. & Han, M. Y. Silica-coated metal nanoparticles. *Chem. - An Asian J.* **5,** 36–45 (2010).

131. Rieter, W. J., Taylor, K. M. L. & Lin, W. Surface modification and functionalization of nanoscale metal-organic frameworks for controlled release and luminescence sensing. *J. Am. Chem. Soc.* **129,** 9852–9853 (2007).

132. Taylor, K. M. L., Rieter, W. J. & Lin, W. Manganese-based nanoscale metal-organic frameworks for magnetic resonance imaging. *J. Am. Chem. Soc.* **130,** 14358–14359 (2008).

133. Rieter, W. J., Pott, K. M., Taylor, K. M. L. & Lin, W. Nanoscale coordination polymers for platinum-based anticancer drug delivery. *J. Am. Chem. Soc.* **130,** 11584–11585 (2008).

134. Liu, D., Huxford, R. C. & Lin, W. Phosphorescent nanoscale coordination polymers as contrast agents for optical imaging. *Angew. Chemie - Int. Ed.* **50,** 3696–3700 (2011).

135. Rowe, M. D. *et al.* Tuning the magnetic resonance imaging properties of positive contrast

agent nanoparticles by surface modification with RAFT polymers. *Langmuir* **25,** 9487–9499 (2009).

136. Rowe, M. D., Tham, D. H., Kraft, S. L. & Boyes, S. G. Polymer-modified gadolinium metal-organic framework nanoparticles used as multifunctional nanomedicines for the targeted imaging and treatment of cancer. *Biomacromolecules* **10,** 983–993 (2009).

137. Agostoni, V. *et al.* A 'green' strategy to construct non-covalent, stable and bioactive coatings on porous MOF nanoparticles. *Sci. Rep.* **5,** 7925 (2015).

138. Bellido, E. *et al.* Heparin-Engineered Mesoporous Iron Metal-Organic Framework Nanoparticles: Toward Stealth Drug Nanocarriers. *Adv. Healthc. Mater.* **4,** 1246–1257 (2015).

139. Tanabe, K. K., Wang, Z. & Cohen, S. M. Systematic functionalization of a metal-organic framework via a postsynthetic modification approach. *J. Am. Chem. Soc.* **130,** 8508–8517 (2008).

140. Wuttke, S. *et al.* MOF nanoparticles coated by lipid bilayers and their uptake by cancer cells. *Chem. Commun.* **51,** 15752–15755 (2015).

141. Liu, D. *et al.* Coercing bisphosphonates to kill cancer cells with nanoscale coordination polymers. *Chem. Commun.* **48,** 2668 (2012).

142. Huxford, R. C., DeKrafft, K. E., Boyle, W. S., Liu, D. & Lin, W. Lipid-coated nanoscale coordination polymers for targeted delivery of antifolates to cancer cells. *Chem. Sci.* **3,** 198 (2012).

143. Liu, D., Poon, C., Lu, K., He, C. & Lin, W. Self-assembled nanoscale coordination polymers with trigger release properties for effective anticancer therapy. *Nat. Commun.* **5,** 4182 (2014).

144. He, C., Liu, D. & Lin, W. Self-assembled nanoscale coordination polymers carrying siRNAs and cisplatin for effective treatment of resistant ovarian cancer. *Biomaterials* **36,** 124–133 (2015).

145. Wang, X.-G. *et al.* A multifunctional metal–organic framework based tumor targeting drug delivery system for cancer therapy. *Nanoscale* **7,** 16061–16070 (2015).

146. Chowdhuri, A. R., Singh, T., Ghosh, S. K. & Sahu, S. K. Carbon Dots Embedded Magnetic Nanoparticles @Chitosan @Metal Organic Framework as a Nanoprobe for pH Sensitive Targeted Anticancer Drug Delivery. *ACS Appl. Mater. Interfaces* **8,** 16573–16583 (2016).

147. Ruyra, A. *et al.* Synthesis, culture medium stability, and in vitro and in vivo zebrafish embryo toxicity of metal-organic framework nanoparticles. *Chem. - A Eur. J.* **21,** 2508–2518 (2015).

148. Baati, T. *et al.* In depth analysis of the in vivo toxicity of nanoparticles of porous iron(iii) metal-organic frameworks. *Chem. Sci.* **4,** 1597–1607 (2013).

149. Simon-Yarza, M. T. *et al.* Antineoplastic busulfan encapsulated in a metal organic framework nanocarrier: First in vivo results. *J. Mater. Chem. B* **4,** 585–588 (2016).

150. Morawski, A. M., Lanza, G. A. & Wickline, S. A. Targeted contrast agents for magnetic resonance imaging and ultrasound. *Curr. Opin. Biotechnol.* **16,** 89–92 (2005).

151. Carné-Sánchez, A. *et al.* Relaxometry studies of a highly stable nanoscale metal-organic framework made of Cu(II), Gd(III), and the macrocyclic DOTP. *J. Am. Chem. Soc.* **135,** 17711–17714 (2013).

152. Yang, W., Feng, J. & Zhang, H. Facile and rapid fabrication of nanostructured lanthanide coordination polymers as selective luminescent probes in aqueous solution. *J. Mater. Chem.* **22,** 6819–6823 (2012).

153. Ray Chowdhuri, A., Bhattacharya, D. & Sahu, S. K. Magnetic nanoscale metal organic frameworks for potential targeted anticancer drug delivery, imaging and as an MRI contrast agent. *Dalton Trans.* **45,** 2963–73 (2016).

154. Dekrafft, K. E. *et al.* Iodinated nanoscale coordination polymers as potential contrast agents for computed tomography. *Angew. Chemie - Int. Ed.* **48,** 9901–9904 (2009).

Chapter 2

Spontaneous self-assembly of polymeric nanoparticles in aqueous media: new insights from microfluidics, in situ size measurements, and individual particle tracking

General Objectives and Author Contributions

CD-based nanotechnology has drawn special attention since it combines the advantage of self-assembled host-guest interactions and nanotechnology. Herein, polymeric nanoparticles driven by CD inclusion complexes were spontaneously formed in aqueous media, in the absence of organic solvents or surfactants. In order to prepare stable CD-based nanoparticles (CD-NPs), a highly soluble β-CD polymer (poly-CD) was used as the source of CDs, which was prepared by cross-linking β-CD with epichlorohydrin (EP). Benzophenone (Bz) was chosen as the guest molecule, because of its strong affinity with the cavity of β-CD and because it was well-studied in NPs made of poly-CD. Bz was grafted with dextran, forming a new polymer, namely, Dex-Bz. Poly-CD and Dex-Bz were used in this study as the two polymers for CD-NPs preparation. They are both neutral polymers, therefore, the interactions between the two polymers in water are mostly due to the host-guest interactions between β-CD and Bz, without electrostatic interactions.

To prepare and characterize these particles, complementary methods were used bringing new insights on the formation and stability of the supramolecular systems:

1) Microfluidics was used to prepare the particles by mixing the two aqueous solutions directly in the microfluidic chamber. CD-NPs with narrow size distributions were immediately formed upon contact of the two polymeric solutions.

2) *In situ* size measurements during the particle formation showed that the CD-NPs were spontaneously formed in aqueous media.

3) Individual particle tracking analysis was used to gain insights on their size distribution and concentration. Since the CD-NPs were formed by non-covalent interaction, it is important to check if the NPs disassemble upon dilution. Individual particle tracking analysis was an adapted method to prove that the particles were stable even upon extreme dilution despite their non-covalent nature.

Journal of Pharmaceutical Sciences

Volume 106, Issue 1, January 2017, Pages 395–401

Pharmaceutical Nanotechnology

Spontaneous Self-Assembly of Polymeric Nanoparticles in Aqueous Media: New Insights From Microfluidics, *In Situ* Size Measurements, and Individual Particle Tracking

Xue Li [1, 2], Giuseppina Salzano [1], Jiwen Zhang [2, *], Ruxandra Gref [1, *]

[1] *Institut des Sciences Moléculaires d'Orsay, Université Paris-Saclay, Université Paris-Sud, UMR CNRS 8214, 91400 Orsay, France*
[2] *Center for Drug Delivery Systems, Shanghai Institute of Materia Medica, Chinese Academy of Sciences, Shanghai 201203, China*

ARTICLE INFO

Article history:
Received 12 April 2016
Revised 12 September 2016
Accepted 22 September 2016

Keywords:
cyclodextrins
nanoparticles
particle size
distribution
self-assembly

ABSTRACT

Supramolecular cyclodextrin-based nanoparticles (CD-NPs) mediated by host-guest interactions have gained increased popularity because of their "green" and simple preparation procedure, as well as their versatility in terms of inclusion of active molecules. Herein, we showed that original CD-NPs of around 100 nm are spontaneously formed in water, by mixing 2 aqueous solutions of (1) a CD polymer and (2) dextran grafted with benzophenone moieties. For the first time, CD-NPs were instantaneously produced in a microfluidic interaction chamber by mixing 2 aqueous solutions of neutral polymers, in the absence of organic solvents. Whatever the mixing conditions, CD-NPs with narrow size distributions were immediately formed upon contact of the 2 polymeric solutions. *In situ* size measurements showed that the CD-NPs were spontaneously formed. Nanoparticle tracking analysis was used to individually follow the CD-NPs in their Brownian motions, to gain insights on their size distribution, concentration, and stability on extreme dilution. Nanoparticle tracking analysis allowed to establish that despite their non-covalent nature, and the CD-NPs were remarkably stable in terms of concentration and size distribution, even on extreme dilution (concentrations as low as 100 ng/mL).

Introduction

Supramolecular nanostructures mediated by host-guest interactions based on cyclodextrins (CDs) have gained increased popularity for their potential biomedical applications, particularly in drug delivery.[1-3] Drug loadings were dramatically improved when including CDs in the nanoparticles (NPs), due to complex formation between CDs and drugs.[4] As an example, the loading of prednisolone in poly(alkyl cyanoacrylate) NPs was improved 129-fold when incorporated in CDs.[5]

More recently, CD-containing NPs (CD-NPs) were prepared by a mild, solvent-free method, at room temperature and without using surfactants.[6] CD-NPs were spontaneously formed by mixing 2 aqueous solutions of (1) dextran (Dex) grafted with alkyl side chains (Dex-C_{12}) and (2) a highly soluble CD polymer (poly-CD). The alkyl side chains of Dex-C_{12} formed inclusion complexes with the CDs in poly-CD, leaving most of the CDs free for the inclusion of other molecules of interest, such as anticancer drugs, contrast agents, nitric oxide donors, and cosmetic ingredients.[1,3] Based on a similar "lock and key" concept, the first small interfering RNA delivery system in humans using CDs was developed.[7] The self-assembly of cationic poly-CDs with anionic nucleic acids gave rise to the formation of NPs to which poly(ethylene glycol) and targeting agents could be associated.[7,8]

Benzophenone (Bz) was the most studied active ingredient in the NPs made of poly-CD and Dex-C_{12}.[6,9-14] Attractive features of the Bz-loaded NPs were their one step solvent-free preparation method, the small sizes and the possibilities to be freeze-dried and reconstituted in aqueous solutions.[6,14] Bz was incorporated in the polymeric solution and it was retained in the NPs as inclusion complexes with the CDs.[13] However, because of the competition between Bz and the alkyl chains for the CD cavities, Bz loadings reached at best 2.9 wt% and there was a significant amount of free Bz in the NP suspensions.[13]

We propose here an original approach to prepare Bz-containing CD-NPs, avoiding the presence of free Bz in the suspensions. Bz was grafted to Dex, replacing the alkyl side chains. The interaction of this novel conjugate (Dex-Bz) with poly-CD, leading to CD-NP formation, was investigated by a set of complementary novel

* *Correspondence to*: Ruxandra Gref (Telephone: +33-1-69158234; Fax: +33-1-69156777) and Jiwen Zhang (Telephone: +86-21-20231980; Fax: +86-21-20231980).
E-mail addresses: jwzhang@simm.ac.cn (J. Zhang) and ruxandra.gref@u-psud.fr (R. Gref).

http://dx.doi.org/10.1016/j.xphs.2016.09.024
0022-3549/

characterization techniques. For the first time, CD-NPs were instantaneously produced in a microfluidic interaction chamber by mixing 2 aqueous solutions of neutral polymers, in the absence of any organic solvent.

Interestingly, an *in situ* method was developed to study the CD-NP formation directly in the preparation vessel. Nanoparticle tracking analysis (NTA) was used to individually follow the NPs in their Brownian motion to gain insight into their size distribution, concentration, and stability upon extreme dilution.

Experimental

Materials

Dex (40,000 g/mol) was purchased from Pharmacia (Uppsala, Sweden). β-CD was kindly provided by Roquette (Vecquemont, France). 1-Adamantyl chloride and 4-benzoylbenzoic acid were obtained from Sigma Aldrich (Saint-Quentin-Fallavier, France). MilliQ water was purified by reverse osmosis (Millipore®, Billerica, MA) and filtered using a 0.22-μm membrane (Millipore). All organic solvents were analytical grade and obtained from Thermo Fisher (Illkirch, France).

Synthesis of Modified Dextran Polymers

To synthesize Dex bearing Bz side units (Dex-Bz), 4.0 g of Dex was solubilized in 100 mL of anhydrous dimethylformamide containing 1.0 g of lithium chloride. Then, 0.46 g of 4-benzoylbenzoic acid and 31 μL of pyridine were added to the Dex solution. The reaction was carried out at 80°C for 3 h. The obtained Dex-Bz conjugate was isolated by precipitation in isopropyl alcohol. Then, Dex-Bz conjugate was further solubilized in distilled water, extensively purified by dialysis to remove unreacted Bz and finally freeze-dried overnight.

Dex bearing adamantane (Ad) side units (Dex-Ad) was obtained in a similar manner, by reacting Dex with 1-adamantanecarbonyl chloride as previously reported.[11,15] Briefly, 1.0 g of lithium chloride was dissolved in anhydrous N,N-Dimethylformamide by heating at 80°C. To this mixture, 4.0 g of Dex was added, followed by 0.5 g of 4-(dimethylamino)pyridine, 0.42 g of 1-adamantanecarbonyl chloride, and 30 μL of pyridine. The mixture was stirred for 3 h at 80°C followed by 15 h at room temperature. The polymer was then isolated by precipitation in 2-propanol. It was purified by dialysis and finally freeze-dried.

Dex-Ad and Dex-Bz were characterized by ^{1}H-NMR spectroscopy in D_2O using a Varian VXR-600 at 400 MHz and their average molar mass was determined by size exclusion chromatography (SEC) using pullulan standards. SEC studies were conducted using multiangle light scattering and refractive index detectors (SEC/multiangle light scattering/refractive index; Wyatt Technology, Santa Barbara, CA) with TSK6000PW/TSK2500PW columns, and ammonium acetate-acetic acid pH 4.5 as the eluent at a flow rate of 0.5 mL/min, using dn/dc of Dex = 0.147 mL/g. After Bz grafting, the average molar mass was shifted from 37,700 ± 400 (native Dex) to 43,400 ± 4300 g/mol (Dex-Bz), indicating the successful grafting reaction. ^{1}H NMR enabled to determine the substitution yield, showing that 5% of the Dex glucose units were effectively grafted with Bz or Ad.

Synthesis of Poly-β-CD Polymers (Poly-CD)

Poly-CD was prepared by poly-condensation of β-CD with epichlorohydrin (EP) under alkaline conditions as previously described.[6,14] Briefly, 100 g of anhydrous β-CD was dissolved in 160 mL sodium hydroxide, 33% wt/wt solution under magnetic stirring overnight. Then EP (molar ratio β-CD/EP = 10) was rapidly added to the solution heated at 30°C. The reaction was stopped in the proximity of the gelation point by adding acetone. The obtained aqueous phase was then heated at 50°C overnight. The reaction mixture was neutralized with hydrochloric acid (6 N) and ultrafiltered using membranes with a cut-off of 100,000 g/mol. The β-CD polymer was finally recovered by freeze-drying.

The β-CD content was 77% (wt/wt) as determined by ^{1}H-NMR spectroscopy analysis. Polymer average molar mass was 2.1×10^5 g/mol according to SEC measurements using pullulan standards.

Nanoparticle Preparation

The NPs of poly-CD and Dex-Bz polymers, namely poly-CD/Dex-Bz NPs, were prepared by a microfluidic technique (NanoAssemblr™ Benchtop Instrument; Precision NanoSystems, Ltd., Vancouver, BC). The mixing chamber (Fig. 1) has channels of around 100 μm. Aqueous solutions of poly-CD (5 μg/mL to 1 mg/mL) and Dex-Bz (5 μg/mL to 1 mg/mL) were obtained by dissolving the 2 polymers in MilliQ water at room temperature for 12 h. Then, the poly-CD and Dex-Bz solutions were mixed in the microfluidic mixing chamber at different volume ratios at a flow rate of 1 mL/min. The start waste and end waste indicated in the NanoAssemblr™ software were set at 0.25 and 0.05 mL, respectively. These volumes correspond to the non-steady state regime of NP formation. The NPs formed in these conditions were not further recovered for characterization purposes.

As a control, poly-CD/Dex-Bz NPs were prepared by mixing the 2 polymer solutions using a pipette at room temperature using the same experimental conditions (volume ratios and polymer concentrations).

Nanoparticle Characterization

Size Distribution and Stability

The mean diameter and the size distribution of poly-CD/Dex-Bz NPs were determined at 25°C by dynamic light scattering (DLS) at 90° angle using Zetasizer ZS 90 Instrument (Malvern Instruments Ltd., Orsay, France). Experiments were performed in triplicate. DLS enabled studying the stability of the NPs during storage at room temperature.

In Situ *Kinetic Study of NP Formation*

The kinetics of NP formations were studied *in situ* by means of a Cordouan Vasco Flex particle analyzer (Cordouan Technologies Ltd., Pessac, France) equipped with an *in situ* head detector. Samples of 100 μL of Dex-Bz solution (0.5 mg/mL) were added to 1 mL of poly-CD solution (0.5 mg/mL) every 2 min until a 1:1 volume ratio between Dex-Bz and poly-CD was reached. Size analysis of the forming NPs were performed immediately after each addition of the Dex-Bz solution to the poly-CD one.

Vasco Flex allows non-intrusive measurements of NP size distribution in indicative size range of 0.5 nm to 10 μm, and a concentration range of 10^{-5} to 5%-10% (vol/vol). The *in situ* head detects the scattered light at an angle of 170°. Size distributions were determined using the NanoQ 2.5 software with Pade-Laplace, Cumulant, and SBL inversion algorithms.

Individual Particle Tracking and NP Concentration Measurements by NanoSight

The NP concentration and stability upon dilution were investigated by NanoSight analysis (NanoSight LM10 Instrument; Malvern Instruments Ltd.), combining a conventional optical microscope with a laser to illuminate the NPs in Brownian motion in a defined volume.[16] Of main interest here, NPs could be visualized one by one,

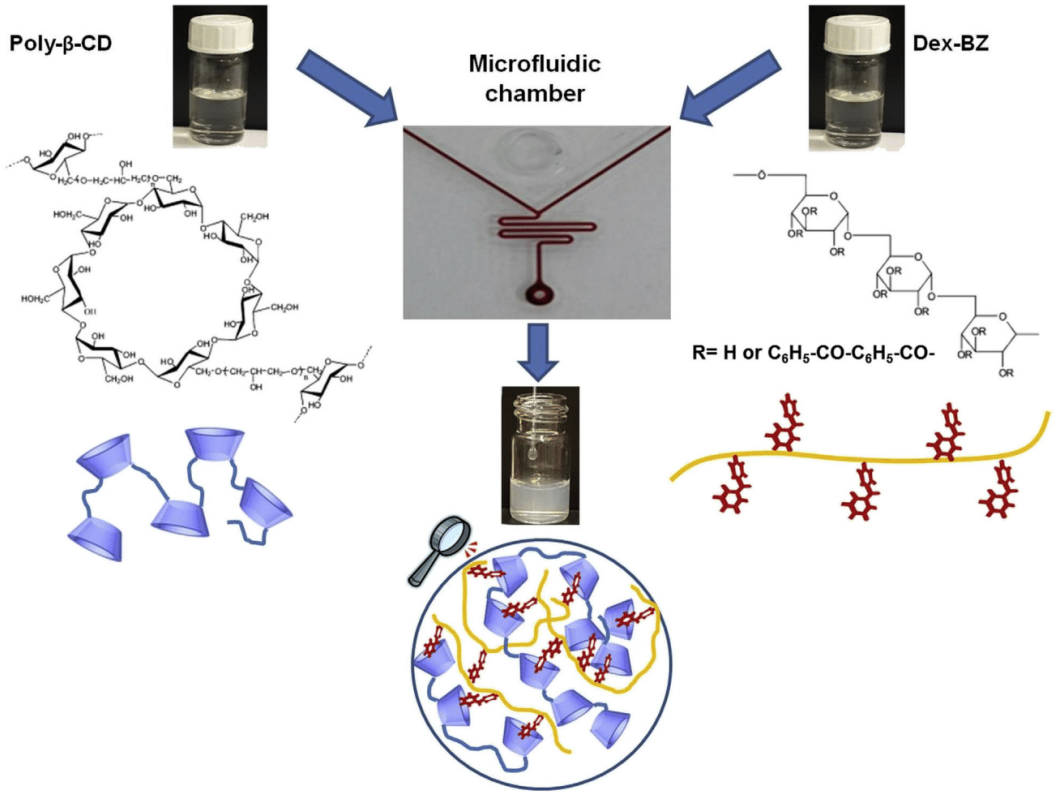

Figure 1. Schematic representation of the formation of poly-CD/Dex-Bz NPs in a microfluidic chamber. Two aqueous solutions of poly-CD (left) and Dex-Bz (right) are injected in the chamber at a defined flow rate (0.5-1 mL/min). Immediately after passage through the device, NPs are recovered and characterized.

in a concentration range between 10^6 and 10^9 particles/mL. The size distribution and concentration could be determined simultaneously. Results are expressed as means of 5 independent measurements.

Yield of NP Formation

The yield of poly-CD/Dex-Bz NP formation is defined as the ratio between the amount of formed poly-CD/Dex-Bz NPs and the amount of poly-CD and Dex-Bz polymers added in the preparation procedure. Briefly, 10 mg/mL of poly-CD/Dex-Ad NPs were prepared and kept at room temperature for 2 days until the size of NPs was stable. NPs were then centrifuged at 10,000 × *g* for 10 min. The supernatant was recovered and dried. The yield of NPs (*Y*) was calculated using the following equation:

$$Y\,(\%) = \left(1 - \frac{\text{weight of non interacted polymer}}{\text{Total weight of polymers}}\right) \times 100$$

Results and Discussion

Preparation of Poly-CD/Dex-Bz NPs by Microfluidic Device

Dex grafted with Bz moieties was successfully synthetized. After synthesis, Dex-Bz samples were extensively purified by dialysis and characterized by SEC and ^{1}H NMR spectroscopy. The average molar mass was shifted from 37,700 ± 400 (native Dex) to 43,400 ± 4300 g/mol, after Bz grafting. The increase in molar mass was a clear indication of the successful grafting reaction. ^{1}H NMR enabled to determine the substitution yield, showing that 5% of the Dex glucose units were effectively grafted with Bz. An identical substitution of 5% glucose units was obtained with Dex-Ad.

Self-assembled NPs made of poly-CD and Dex grafted with alkyl side chains were produced by mixing, using a pipette, the 2 polymer solutions.[6] It was shown by ^{1}H NMR and isothermal titration microcalorimetry experiments, as well as by molecular modeling that the hydrophobic moieties on Dex spontaneously insert in the CD cavities on poly-CD, leading to the formation of NPs in water.[6,12] Bz was also shown to form inclusion complexes with CDs and was incorporated in the NPs.[13] However, typically only up to 5 mL of suspensions loaded or not with Bz were produced. In this study, microfluidics was investigated as an alternative method to prepare larger amounts of NPs from poly-CD and Dex-Bz. These 2 polymers spontaneously associate in water, leading to NP production, presumably because of the strong CD:Bz interactions.[13] As expected, when mixing poly-CD and Dex without hydrophobic moieties, no particles were formed, proving that these moieties play a crucial role in the formation of the supramolecular structures.

The microfluidic device could allow a continuous NP production at a rate of tens to hundreds of microliters per minute. Studies in

the literature[17] describe the utility of microfluidic devices to scale up NP production.

Recently, it has been shown that NPs could be assembled by mixing an organic phase containing the solubilized biodegradable polymer and an aqueous phase.[18-21] These studies highlighted the interest of microfluidics in producing NPs by mixing 2 aqueous phases with narrow size distribution, showing spontaneous NP formation even in the confined microfluidic channels.

The microfluidic chambers were used to mix poly-CD and Dex-Bz (Fig. 1). The NPs were formed in the mixing chamber which allows for exquisite control over the mixing profile of the solutions containing the NP forming agents. [17-21] Parameters, including ratio between the different compounds, flow rate, as well as temperature can be easily and accurately controlled, which make possible to prepare libraries of NPs in a well-controlled, reproducible, and high-throughput manner.[22]

To investigate NP stability, the mean hydrodynamic diameters of the NPs are measured by DLS immediately after their formation in the microfluidic device and during their storage at room temperature up to 1 week (Fig. 2). In the first 3 h, the diameters increase from 85 to 109 nm and then tend to stabilize during storage. Indeed, there were little variations of the main hydrodynamic diameters (121 ± 11 nm) from day 2 to day 6 after formation.

As a reference, NPs were produced using the same polymer solutions, but by mixing them using a pipette, as in previous studies.[9-14] The mean diameters were slightly larger (140 ± 14 nm) than those obtained by microfluidics (132 ± 5 nm). The polydispersity of all formulations was low (PdI ≤ 0.1), showing that monomodal NPs with narrow size distribution were formed. The Dex-Bz:poly-CD volume ratios did not affect the mean diameters of the resulting NPs (Fig. 2). This ratio could be increased up to 5:1, corresponding to 4.2 wt% of Bz in the NP suspensions. The NP formation yield was around 71%. Figure 2 shows that the NPs prepared by both methods are stable (<6% size variation) over storage.

This ratio could be increased up to 5:1.

Hence, NPs were successfully produced by microfluidics irrespective of the experimental conditions (volume ratios of the 2 polymer solutions, flow rates). To the best of our knowledge, this is the first example of NP formation in "green" conditions (no organic solvent) using a microfluidic device. NPs can be prepared in a continuous manner by pumping polymer solutions from reservoirs into the microfluidic device.

Similar results were obtained with another polymer which assembles with poly-CD, Dex grafted with Ad moieties (Fig. 3). NPs produced using Dex-Ad by microfluidics and by direct mixing using a pipette had similar mean diameters, lower than 180 nm. As Bz, Ad is known to form strong inclusion complexes with β-CD (association constants of around 30,000 and 2700 /M for Ad:β-CD[23] and Bz:β-CD[12] interactions, respectively). It has been previously shown that CD-based nanoassemblies were formed by a lock and key mechanism, where interactions between the hydrophobic side chain on Dex and the hydrophobic CD cavities cooperatively contribute to establish the cohesion of the NPs.[6,24]

In Situ *Study of NP Formation*

To have a deeper insight into the formation of the NPs by self-assembly between Dex-Bz conjugate and poly-CD, *in situ* size analysis was performed during the gradual addition of Dex-Bz solution to poly-CD solution, using a VASCO-Flex™ particle size analyzer. This device offers the possibility to monitor *in situ* NP formation without withdrawing samples for analysis, as it is the case with conventional DLS (Fig. 4a). The *in situ* non-invasive technique, outlined in Figure 4b, was used to characterize the NP size distribution during the progressive addition of one polymeric aqueous phase to the other.

It was found that the size measurements conducted by conventional DLS and *in situ* VASCO-Flex provided consistent results. Typical examples are shown in Figures 4c and 4d in the case of poly-CD/Dex-Bz NPs obtained by mixing equal volumes of polymer solutions at concentration of 0.5 mg/mL. Less than 5% differences were found between the 2 techniques. The NPs were monodisperse, with PdI ≤ 0.1 in both cases.

The NPs were prepared in a glass vial by progressively adding Dex-Bz into a poly-CD solution (Fig. 4e). Results show that NPs of

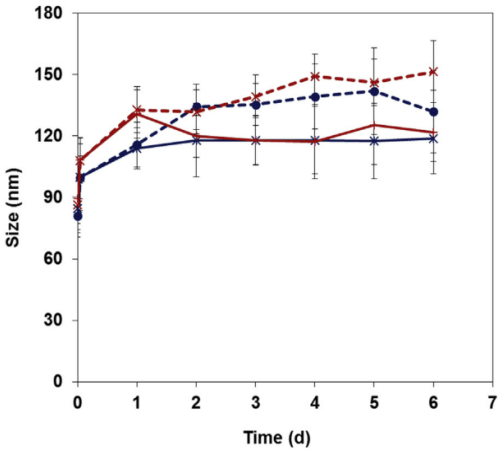

Figure 2. Mean hydrodynamic diameters of poly-CD/Dex-Bz NPs prepared using a microfluidic device (continuous line) and by mixing the polymer solutions using a pipette (dashed line). Polymer concentrations were 1 mg/mL and poly-CD:Dex-Bz volume ratios were 1:1 (blue) and 2:1 (red). The error bars are from the standard deviation values.

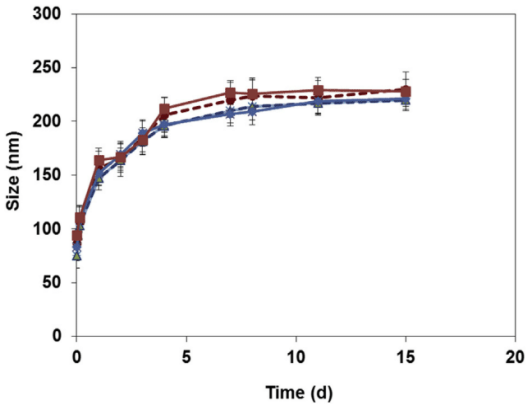

Figure 3. Mean hydrodynamic diameters of poly-CD/Dex-Ad NPs prepared using a microfluidic device (continuous line) and by mixing the polymer solutions using a pipette (dashed line). Polymer concentrations were 1 mg/mL and poly-CD:Dex-Ad volume ratios were 1:1 (blue) and 2:1 (red). The error bars are from the standard deviation values.

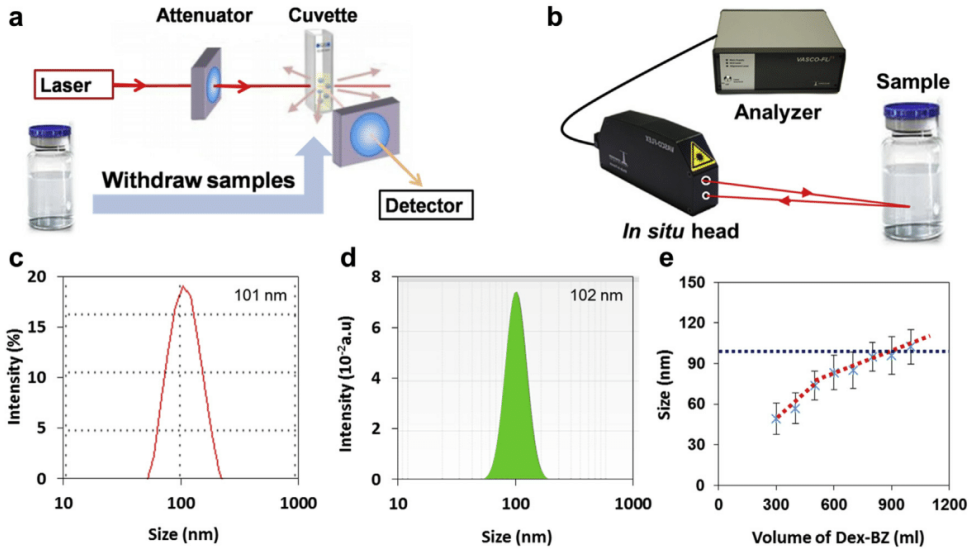

Figure 4. *In situ* measurement of NP size distribution. (a) Schematic representation of NP size distribution measurements by conventional DLS analysis. It is necessary to withdraw samples for analysis. (b) *In situ* measurements of NP size distributions directly in glass vessels. The *in situ* head detects the light scattered from the sample at an angle of 170°, and the signal is further processed by a particle analyzer. Typical size distribution results obtained by conventional DLS (c) and *in situ* measurements (d) in the case of poly-CD/Dex-Bz NPs obtained by mixing equal volumes of polymer solutions at concentration of 0.5 mg/mL. (e) Mean diameters of NPs obtained by progressive addition of Dex-Bz (0.5 mg/mL) into 1 mL of poly-CD solution (0.5 mg/mL). Results are expressed as a function of the total volume of added Dex-Bz aqueous phase. The dashed line indicates the mean diameter of NPs prepared by mixing at once 1 mL of Dex-Bz solution (0.5 mg/mL) and 1 mL of poly-CD solution (0.5 mg/mL). The error bars in (e) are from the standard deviation values.

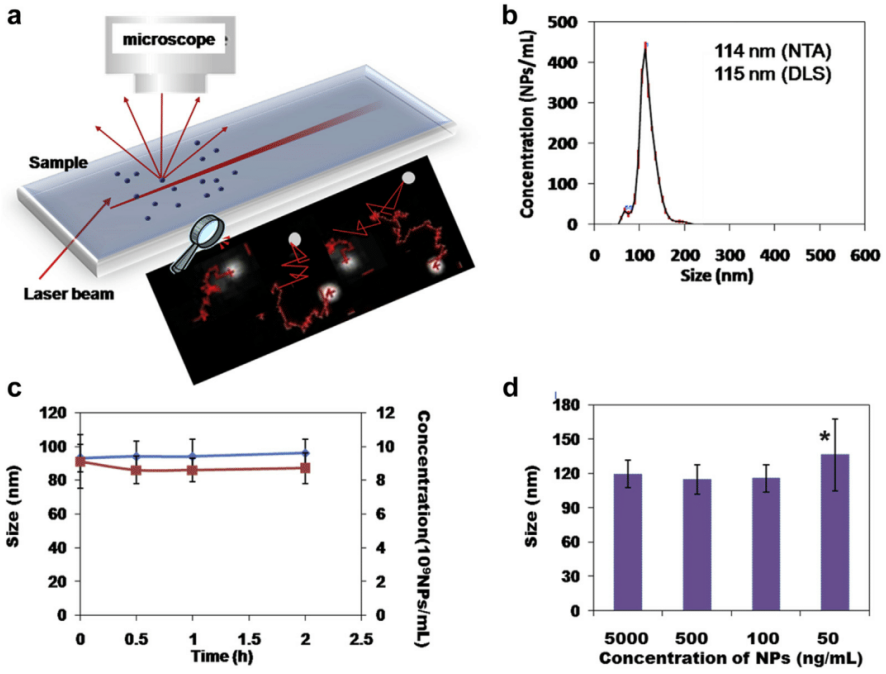

Figure 5. Poly-CD/Dex-Bz NP stability upon dilution determined by NTA analysis. (a) Schematic representation of the NTA measurements of NP diameters. (b) Typical size distribution results obtained by NTA in the case of poly-CD/Dex-Bz NPs obtained by mixing equal volumes of polymer solutions at concentration of 1.0 mg/mL. (c) Mean hydrodynamic diameters (blue) and concentration (red) of poly-CD/Dex-Bz NPs (5 μg/mL) after their formation and during storage at room temperature. (d) Mean hydrodynamic diameters of poly-CD/Dex-Bz NPs prepared at a polymer concentration of 1 mg/mL and further diluted to reach the final concentration of 5-0.05 μg/mL. The asterisk in (d) is referred to the presence of polydisperse NPs at the highest dilutions (final concentrations of 50 ng/mL). The error bars in (c) and (d) are from the standard deviation values.

around 50 nm were found since the addition of the first volume of Dex-Bz. The sizes gradually increased from 50 ± 8 to 102 ± 11 nm.

Nanoparticle Stability Upon Dilution

NPs formed by microfluidics and by mixing aqueous polymer solutions using a pipette were characterized by 2 DLS-based techniques, showing narrow size distribution and diameters of around 100 nm. They were stable upon storage at room temperature. However, DLS does not enable to determine the NP number per milliliter which is of outmost interest for the study of NP stability upon dilution. Indeed, due to the non-covalent nature of the poly-CD/Dex-Bz NPs, they could disassemble upon dilution leading to a diminution of the NP concentration. In this context, NTA was used to individually detect the NPs in their Brownian motions, to calculate their hydrodynamic diameters and their concentration (NP number/mL).

The principle of NTA is schematized in Figure 5a. An incident laser beam illuminates a small volume (20 μL) at the prism surface. In this confined region, NPs appear as white spots (Fig. 5a) and their Brownian motion was detected by means of a microscope. In the case of the poly-CD/Dex-Bz NPs produced here, the NTA results were in good agreement with the DLS ones. A typical example is presented in Figure 5b in the case of poly-CD/Dex-Bz NPs obtained by mixing equal volumes of polymer solutions at concentration of 1.0 mg/mL. Less than 5% variation was found between the 2 techniques.

Interestingly, the poly-CD/Dex-Bz NPs prepared using poly-CD and Dex-Bz solution at a concentration of 5 μg/mL were stable upon storage. There were <5% size variation upon storage at room temperature, whereas the NP concentration was $(8.7 \pm 1.4) \times 10^9$ NPs/mL with <6% variations during 2 h storage (Fig. 5c).

Noticeably, NTA could be used to track the NPs up to very low concentrations such as 50 ng/mL. NP suspensions were diluted to reach final concentrations of 5 to 0.05 μg/mL. Interestingly, Figure 5d shows that dilutions of poly-CD/Dex-Bz NPs up to 100 ng/mL did not affect their mean diameters (115 ± 14 nm, with <6% variation). Remarkably, the NP concentrations (number/mL) determined by NTA were proportional to the dilution factor. For example, the NP concentrations were $(8.7 \pm 1.4) \times 10^9$ NPs/mL at 5 μg/mL, and $(9.1 \pm 1.2) \times 10^8$ NPs/mL at 500 ng/mL. Only at concentrations lower than 50 ng/mL, NPs with polydisperse size distributions were observed. In addition, at these significantly low NP concentrations, the NP numbers per milliliter, determined by NTA, were not proportional to the dilution factor.

In a nutshell, these results show that the poly-CD/Dex-Bz NPs did not disassemble upon dilution up to a concentration of 100 ng/mL, despite their non-covalent nature.

The stability of the NPs upon dilution plays an important role on their potential applications. In the case of intravenous administration, the NPs would be highly diluted in the bloodstream. The stability of the poly-CD/Dex-Bz NP formulations paves the way for possible *in vivo* studies. It will be interesting to investigate how dilution in more complex biological media will influence NP stability.

In addition, given the capacity of Bz to absorb and dissipate ultraviolet radiations, Bz is widely used in a variety of personal care products such as nail polish, sunscreen lotions or creams, lipcare products, shampoo, and fragrances. However, Bz has been shown to penetrate the skin and cause photosensitivity, eczema, and other severe side effects.[11,14-17] Moreover, Bz has a poor water solubility making its incorporation in cosmetic formulations challenging.[14] Stable poly-CD/Dex-Bz NPs might offer a way to prevent Bz skin penetration, together with efficiently incorporating this poorly soluble compound.

Conclusion

NPs were spontaneously formed by mixing 2 aqueous polymer solutions. A microfluidic device has been set up to produce NPs of around 100 nm, with narrow size distributions. *In situ* size measurements showed that the NPs were spontaneously formed. NTA allowed to individually track each NP in its Brownian motion, showing that despite dilution up to 100 ng/mL, the NPs were still stable in terms of mean diameters. The NP number was proportional to the dilution factor, showing that the NPs did not disassemble upon extreme dilution. With further studies, this stable nanoplatform might be used in cosmetic applications, parenteral therapies, and intravenous drug delivery.

Acknowledgments

We acknowledge Gesine Heuck (Precision NanoSystems, Inc.) and Nicolas Gonzalez (Schaefer Technologies) for helpful discussions concerning the microfluidics experiments. We thank Sylvain Boj (Cordouan) for *in situ* analysis using VASCO-Flex™ system. We are grateful to Dr. Catherine Ladavière (IMP, Lyon) for her kind help with the characterization of Dex-Bz conjugates. We acknowledge support from China scholarship council (CSC, no. 201408330166), China National Science and Technology Major Project (2013ZX09402103), and National Natural Science Foundation (81430087). We are grateful for support from the French ANR grant ANR-14-CE08-0017 and from the European Marie Curie project "Cyclon Hit" FP7-PEOPLE-ITN-2013 No 608407.

References

1. Duchene D, Cavalli R, Gref R. Cyclodextrin-based polymeric nanoparticles as efficient carriers for anticancer drugs. *Curr Pharm Biotechnol*. 2016;17:248-255.
2. Loftsson T, Brewster ME. Cyclodextrins as functional excipients: methods to enhance complexation efficiency. *J Pharm Sci*. 2012;101:3019-3032.
3. Deshayes S, Gref R. Synthetic and bioinspired cage nanoparticles for drug delivery. *Nanomedicine (Lond)*. 2014;9:1545-1564.
4. Agüeros M, Areses P, Campanero MA, et al. Bioadhesive properties and biodistribution of cyclodextrin-poly(anhydride) nanoparticles. *Eur J Pharm Sci*. 2009;37:231-240.
5. Duchene D, Ponchel G. Combined poly(alkyl cyanoacrylate)/cyclodextrin nanoparticles. *J Inclus Phen Macrocyclic Chem*. 2004;44:15-16.
6. Gref R, Amiel C, Molinard K, et al. New self-assembled nanogels based on host-guest interactions: characterization and drug loading. *J Control Release*. 2006;111:316-324.
7. Davis ME, Zuckerman JE, Choi CH, et al. Evidence of RNAi in humans from systemically administered siRNA via targeted nanoparticles. *Nature*. 2010;464:1067-1070.
8. Burckbuchler V, Wintgens V, Leborgne C, et al. Development and characterization of new cyclodextrin polymer-based DNA delivery systems. *Bioconjug Chem*. 2008;19:2311-2320.
9. Wintgens V, Nielsen TT, Larsen KL, Amiel C. Size-controlled nanoassemblies based on cyclodextrin-modified dextrans. *Macromol Biosci*. 2011;11:1254-1263.
10. Daoud-Mahammed S, Couvreur P, Bouchemal K, et al. Cyclodextrin and polysaccharide-based nanogels: entrapment of two hydrophobic molecules, benzophenone and tamoxifen. *Biomacromolecules*. 2009;10:547-554.
11. Layre AM, Volet G, Wintgens V, Amiel C. Associative network based on cyclodextrin polymer: a model system for drug delivery. *Biomacromolecules*. 2009;10:3283-3289.
12. Bouchemal K, Couvreur P, Daoud-Mahammed S, Poupaert J, Gref R. A comprehensive study on the inclusion mechanism of benzophenone into supramolecular nanoassemblies prepared using two water-soluble associative polymers. *J Therm Anal Calorim*. 2009;98:57-64.
13. Daoud-Mahammed S, Ringard-Lefebvre C, Razzouq N, et al. Spontaneous association of hydrophobized dextran and poly-beta-cyclodextrin into nanoassemblies. Formation and interaction with a hydrophobic drug. *J Colloid Interface Sci*. 2007;307:83-93.
14. Daoud-Mahammed S, Agnihotri SA, Bouchemal K, Kloeters S, Couvreur P, Gref R. Efficient loading and controlled release of benzophenone-3 entrapped into self-assembling nanogels. *Curr Nanosci*. 2010;6:654-665.
15. Wintgens V, Daoud-Mahammed S, Gref R, Bouteiller L, Amiel C. Aqueous polysaccharide associations mediated by beta-cyclodextrin polymers. *Biomacromolecules*. 2008;9:1434-1442.

16. Tong M, Brown OS, Stone PR, Cree LM, Chamley LW. Flow speed alters the apparent size and concentration of particles measured using NanoSight nanoparticle tracking analysis. *Placenta*. 2016;38:29-32.
17. Vladisavljević GT, Williams RA. Recent developments in manufacturing emulsions and particulate products using membranes. *Adv Colloid Interf Sci*. 2005;113:1-20.
18. Valencia PM, Farokhzad OC, Karnik R, Langer R. Microfluidic technologies for accelerating the clinical translation of nanoparticles. *Nat Nanotechnol*. 2012;7:623-629.
19. Karnik R, Gu F, Basto P, et al. Microfluidic platform for controlled synthesis of polymeric nanoparticles. *Nano Lett*. 2008;8:2906-2912.
20. Feng Q, Zhang L, Liu C, et al. Microfluidic based high throughput synthesis of lipid-polymer hybrid nanoparticles with tunable diameters. *Biomicrofluidics*. 2015;9, 052604.
21. Lan J, Chen J, Li N, et al. Microfluidic generation of magnetic-fluorescent Janus microparticles for biomolecular detection. *Talanta*. 2016;151:126-131.
22. Liu D, Cito S, Zhang Y, et al. A versatile and robust microfluidic platform toward high throughput synthesis of homogeneous nanoparticles with tunable properties. *Adv Mater*. 2015;27:2298-2304.
23. Granadero D, Bordello J, Pérez-Alvite MJ, Novo M, Al-Soufi W. Host-guest complexation studied by fluorescence correlation spectroscopy: adamantane-cyclodextrin inclusion. *Int J Mol Sci*. 2010;11:173-188.
24. Othman M, Bouchemal K, Couvreur P, et al. A comprehensive study of the spontaneous formation of nanoassemblies in water by a "lock-and-key" interaction between two associative polymers. *J Colloid Interf Sci*. 2011;354:517-527.

Chapter 3

Particles based on CD-MOFs and their biomedical applications

Subchapter 3.1

Optimized synthesis and crystalline stability of γ-cyclodextrin metal-organic frameworks for drug adsorption

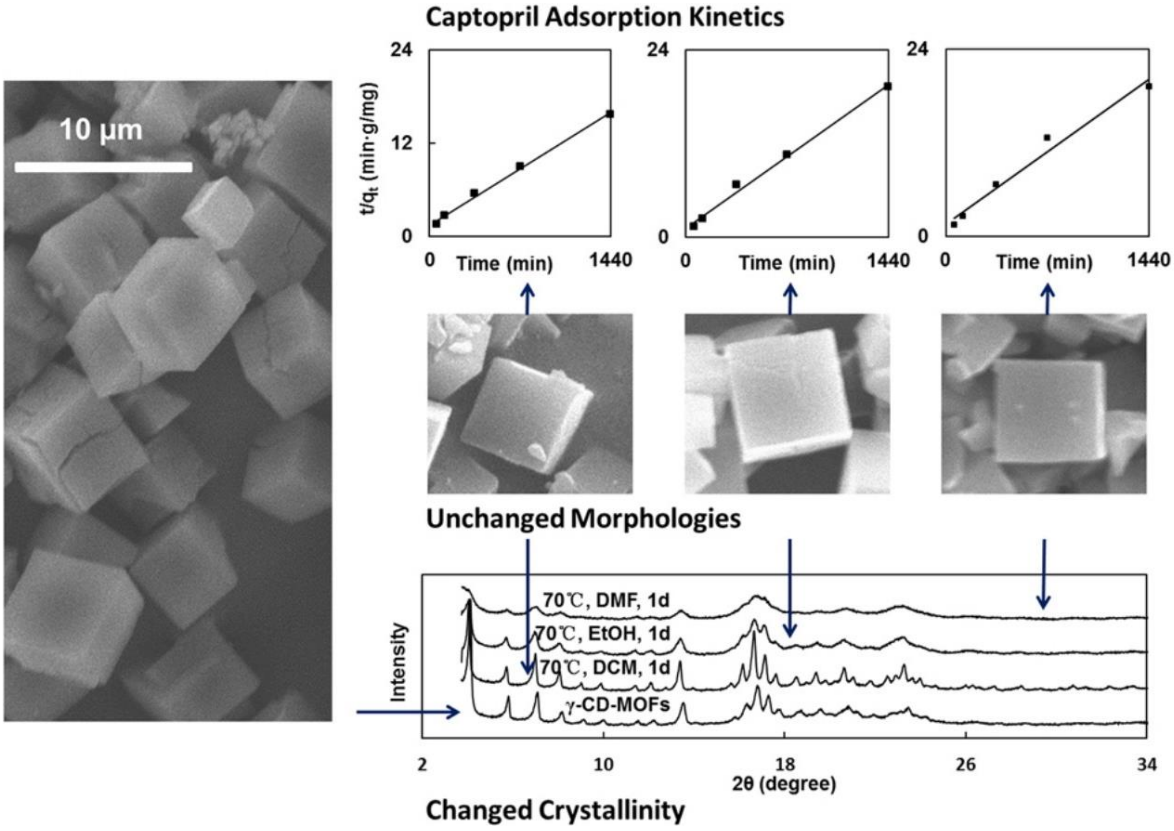

General Objectives and Author Contributions

As previously described, CD-MOFs have gained increased popularity as drug carrier since it is environment-friendly biocompatible and even "edible" MOFs. It is widely recognized that size distribution and stability are crucial parameters for drug delivery system.

In the originally reported protocols for their synthesis, the size of CD-MOF crystals was around 200-400 μm. It was then discovered that addition of cetyltrimethyl ammonium bromide (CTAB) in the preparation enabled the formation of smaller crystals (1-10 μm). However, the synthesized crystals had a large polydispersity. Moreover, the syntheses were carried out at room temperature over long time periods of time (> 24 h).

Herein, we optimized the synthesis procedure by heating at 50 °C within 6 h with pre-addition of the reaction solvent to obtain uniform cubic γ-CD-MOF crystals. The factors that affect the size of CD-MOFs were systematically investigated, including the reactant concentrations, temperatures, time, γ-CD ratios to KOH and surfactant concentrations. Subsequently, the stability of CD-MOFs were studied under conditions of high temperature (100 °C), high humidity (92.5%) and polar solvents (e.g., MeOH and DMF). Finally, drug absorption of CD-MOF was evaluated with different kinds of drugs. It is discovered that most of the drug molecules containing carboxyl groups showed relatively high adsorption (> 5%), while low adsorption (< 5%) was found for drugs with nitrogen-containing heterocyclic rings. This study pave the way towards the use of CD-MOFs for drug delivery purposes.

This study has been performed in collaboration with Dr. J. Zhang in Shanghai Institute of Materia Medica in China. X. Li contributed to perform the experiments on CD-MOFs synthesis.

International Journal of Pharmaceutics 514 (2016) 212–219

Contents lists available at ScienceDirect

International Journal of Pharmaceutics

journal homepage: www.elsevier.com/locate/ijpharm

Optimized synthesis and crystalline stability of γ-cyclodextrin metal-organic frameworks for drug adsorption

Botao Liu[a,b,1], Haiyan Li[a,c,1], Xiaonan Xu[a], Xue Li[a,d], Nana Lv[a], Vikramjeet Singh[a], J. Fraser Stoddart[c], Peter York[a], Xu Xu[b,***], Ruxandra Gref[d,**], Jiwen Zhang[a,b,*]

[a] Center for Drug Delivery System, Shanghai Institute of Materia Medica, Chinese Academy of Sciences, Shanghai 201203, China
[b] School of Chemical and Environmental Engineering, Shanghai Institute of Technology, Shanghai 201418, China
[c] Department of Chemistry, Northwestern University, 2145 Sheridan Road, Evanston, IL 60208, United States
[d] Institut de Sciences Moléculaires d'Orsay, Universite' Paris-Sud, Université Paris-Saclay, UMR CNRS 8214, 91405 Orsay Cedex, France

ARTICLE INFO

Article history:
Received 13 March 2016
Received in revised form 20 April 2016
Accepted 21 April 2016

Keywords:
Cyclodextrin-metal-organic frameworks
Synthesis
Crystalline stability
Drug adsorption

ABSTRACT

The biocompatible and renewable cyclodextrin metal-organic frameworks (CD-MOFs) have addressed a range of opportunities in molecular storage and separation sciences. The reported protocols for their synthesis, however, were carried out at room temperature over long time periods of time (24 h), producing crystals of relatively poor uniformity. In this investigation, micron sized γ-CD-MOFs were synthesized by an optimized vapor diffusion method at elevated temperature (50 °C) within 6 h, after which the size control, crystalline stability and drug adsorption behavior were investigated in detail. In this manner, uniform cubic γ-CD-MOF crystals were obtained when the reaction temperature was raised to 50 °C with pre-addition of the reaction solvent. The size of γ-CD-MOFs was adjusted efficiently by changing the reactant concentrations, temperatures, time, γ-CD ratios to KOH and surfactant concentrations, without influencing the porosity and crystallinity of the material markedly. Varing degrees of reduction in crystallinity and change in morphology were observed when the γ-CD-MOF crystals are treated under conditions of high temperature (100 °C), high humidity (92.5%) and polar solvents (e.g., MeOH and DMF). In relation to drug adsorption by γ-CD-MOFs, most of the drug molecules containing carboxyl groups showed relatively high adsorption (>5%), while low adsorption (<5%) was found for drugs with nitrogen-containing heterocyclic rings. In addition, the adsorption kinetics of captopril to standard γ-CD-MOFs matched a pseudo-second-order model rather well, whilst captopril adsorption to the damaged γ-CD-MOFs only partially matched the pseudo-second-order model. In summary, based upon the optimized synthesis and size control of γ-CD-MOFs, the crystalline stability and drug adsorption characteristics of γ-CD-MOF crystals have been evaluated as a fundamental requirement of a potential vehicle for drug delivery.

1. Introduction

Metal-organic frameworks (MOFs), also known as porous coordination polymers, have emerged as a new class of porous materials for diverse applications such as molecular recognition (Jiecheng et al., 2014; Kumar et al., 2014; Liao et al., 2014), gas storage (Ghose et al., 2015; Kumar et al., 2015; Wen et al., 2012), separation science (Kılıç et al., 2015; Li et al., 2014; Manju et al., 2014), catalysis (Li et al., 2012; Song and Lin, 2012) and drug delivery (Miller et al., 2010; Yun et al., 2013). Usually, they are highly tunable hybrid materials crafted from metal connecting points and organic bridging ligands (Li et al., 1999) with predictable extended structures.

Since the biocompatibility of materials is essential for most potential biological applications, the metals and organic bridging ligands of MOFs have to be bio-friendly. Estimated from the toxicity parameter LD_{50}, some metals such as Ca, Fe, Zn, K, and Ti are considered to be biologically acceptable (Horcajada et al., 2012)

* Corresponding author at: Center for Drug Delivery Systems, Shanghai Institute of Materia Medica, Chinese Academy of Sciences, No. 501 of Haike Road, Shanghai 201203, China.
** Corresponding author at: Institut de Sciences Moléculaires d'Orsay, (UMR CNRS 8214), Universite' Paris-Sud, Université Paris-Saclay, 91400 Orsay, France.
*** Corresponding author at: Shanghai Institute of Technology, No. 100, Haiquan Road, Shanghai 201418, China.
E-mail addresses: xuxu3426@sina.com (X. Xu), ruxandra.gref@u-psud.fr (R. Gref), jwzhang@simm.ac.cn (J. Zhang).
[1] These authors contributed equally to the manuscript.

http://dx.doi.org/10.1016/j.ijpharm.2016.09.029
0378-5173/

and therefore more attention has been paid to biomolecules as linkers of biological active MOFs for biological applications. In addition, natural linkers such as amino acids (Yang et al., 2015), nucleobases (Thomas-Gipson et al., 2015), peptides (Ikezoe et al., 2012), glutarates (Jhung et al., 2006), carbohydrates (Chen et al., 2014), oxalates (Chih-Min and Kwang-Hwa, 2009) and succinates (Cheng et al., 2010) have been reported as being suitable to bind metal ions to form functional porous MOFs.

Recently, the environmental friendly and renewable cyclodextrin (CD) metal-organic frameworks (CD-MOFs) obtained from γ-CD and potassium ions employing a vapor diffusion method have been reported (Forgan et al., 2012; Furukawa et al., 2012; Gassensmith et al., 2011; Smaldone et al., 2010). The γ-CD-MOFs are body-centered cubic structures with apertures of 7.8 Å and have large spherical voids with diameters of 17 Å, linked by coordination of the –OCCO– units located on the D-glucopyranosyl residues of γ-CD to the potassium cations. The extended frameworks of CD-MOFs are connected by numerous channels with a calculated pore volume of 54% (Smaldone et al., 2010). Among the various MOFs reported to date, γ-CD-MOFs are potential materials for gas adsorption (N_2, H_2, CO_2 and CH_4) and the sequestering of some small molecules (Rhodamine B by co-crystallization and 4-phenylazophenol by adsorption) within their pores (Smaldone et al., 2010). Taking advantage of the cavities of diameter 1.7 nm and the high local concentrations of the OH^- ions, a γ-CD-MOF-based template strategy has been developed (Wei et al., 2012) for the synthesis of silver and gold nanoparticles. The γ-CD-MOFs have also been employed to address the challenging separation and purification requirements of petrochemical feedstocks on account of the fact that their three dimensional transverse channels exhibit superior separation features and high resolutions in comparison with other extended framework materials (Holcroft et al., 2015).

On account of the weak noncovalent bonding interactions between the building blocks and metal centers, the parameters employed in the synthesis, including solvent, metal source, molar ratio of reactants, temperature and duration, have a major influence on the physiochemical properties of CD-MOFs. The preparation of pure, homogeneous and monodisperse crystals is critically important in relation to the potential applications of MOFs. Among the studies devoted to the preparation and application of CD-MOFs (Joong et al., 2011; Khan and Kang, 2011; Stock and Biswas, 2012), the crystalline stability of the materials also showed their effectiveness in the generation of families of porous materials. Very few systematic studies, however, have focused on the chemical, thermal and hydrothermal stabilities of MOFs or γ-CD-MOFs (Cychosz and Matzger, 2010).

In this investigation, γ-CD-MOF crystals were obtained by an optimized vapor diffusion method within a short production time, and the characterization, stability and drug adsorption performance were investigated. The γ-CD-MOF crystals prepared under conditions with different reactant concentrations, temperatures, time, molar ratios of γ-CD to KOH, solvents and surfactants were optimized with reference to their shape and size. The crystalline stability of the γ-CD-MOF crystals produced under different processing conditions was probed primarily using PXRD and SEM. Furthermore, preliminary studies were carried out on the adsorption of 21 drugs to γ-CD-MOFs as well as their adsorption behavior.

2. Experimental

2.1. Materials and reagents

γ-cyclodextrin was obtained from Maxdragon Biochem Ltd (China). Potassium hydroxide (KOH), cetyl trimethyl ammonium bromide (CTAB), methanol (MeOH), absolute ethanol (EtOH), isopropanol (^{i}PrOH), acetone (Me_2CO), dichloromethane (DCM) and *N,N*-dimethylformamide (DMF) were of analytical grade and purchased from Sinopharm Chemical Reagent Co. Ltd (China). All drugs (>99.5% purity) were purchased from Dalian Meilun Biotech Co., Ltd (China). Pure H_2O (18.4 MΩ cm), used in all experiments was purified by a Milli-Q system (Millipore, Milford, MA, USA). All other chemicals were of analytical grade.

2.2. Synthesis of γ-CD-MOFs

The γ-CD-MOF crystals were obtained by a modified vapor diffusion method. The crystals were prepared (Fig. S1) by reacting γ-CD (162 mg, 0.125 mmol) with 200 mM KOH in 5.0 mL aqueous solution. The solution was filtered through a 0.45 μm organic filter membrane into a glass tube with the pre-addition of 0.5 mL EtOH/MeOH/Me_2CO followed by vapor diffusion of EtOH, MeOH or Me_2CO into the solution at 50 °C for 6 to 24 h. In order to create the small sized γ-CD-MOF crystals, the supernatant was transferred into another glass tube and CTAB (8 mg mL^{-1}) was added quickly so as to trigger the rapid precipitation of crystalline material. The suspension was incubated at room temperature for 3 h. Finally, the precipitate was harvested and washed three times with ^{i}PrOH and dried at 50 °C overnight. In this manner, γ-CD-MOF crystals of about 5–10 μm in size were obtained. In parallel experiments, the morphology and size of the γ-CD-MOF crystals were modulated by altering the different parameters particularly time (t), temperatures (T), the concentration of γ-cyclodextrin (C_{CD}), molar ratio of γ-CD to KOH (R), solvents and the concentration of CTAB (C_{CTAB}). The resulting samples were identified as F1–F13. The conditions employed in the controlled preparation of these samples are summarized in Table 1.

2.3. Characterization

Morphological characterization of γ-CD-MOF crystals was carried out by the scanning electron microscopy (SEM, S-3400N, Hitachi). The specimens were immobilized on a metal stub with double-sided adhesive tape and coated with a thin gold film, before being observed under magnification. Considering the high regularity of γ-CD-MOF crystals and the sizes of γ-CD-MOFs were measured with the Image Pro Plus 6.0 software (Media Cybernetics, USA) combined with the SEM images.

The crystallinity of the samples was characterized by powder X-ray diffraction (PXRD) analysis. Diffraction patterns of the γ-CD-MOF crystals were detected with a Bruker D8 Advance diffractometer (Bruker, Germany) at ambient temperature, with tube voltage of 40 kV and a tube current of 40 mA in a stepwise scan mode (8° min^{-1}). Diffraction data for the thermal and the samples were collected on an X/Pert Pro 3040/60 diffractometer (PANalytical,

Table 1
Summary of synthesis conditions.

Samples	t (h)	T (°C)	C_{CD} (mM)	R	Solvents	C_{CTAB} (mg mL^{-1})
F1	6	50	25	1:8	MeOH	8
F2	6	50	12.5	1:8	MeOH	8
F3	6	50	50	1:8	MeOH	8
F4	6	40	25	1:8	MeOH	8
F5	6	60	25	1:8	MeOH	8
F6	12	50	25	1:8	MeOH	8
F7	24	50	25	1:8	MeOH	8
F8	6	50	25	1:6	MeOH	8
F9	6	50	25	1:10	MeOH	8
F10	6	50	25	1:8	Me_2CO	8
F11	6	50	25	1:8	EtOH	8
F12	6	50	25	1:8	MeOH	4
F13	6	50	25	1:8	MeOH	16

Holland). All the samples were irradiated with monochromatized CuKα radiation and analyzed over a 2θ angle range of 3–40°.

The N_2 adsorption-desorption isotherms of the crystal samples were measured with a liquid N_2 bath (−196 °C) using a porosimeter (TriStar 3000 V6.05 A, USA). In order to remove any interstitial solvents, the samples were activated by immersing them in DCM for three days and dried under vacuum at 50 °C for 12 h. Known amounts of samples (e.g. 150–200 mg) were loaded into the BET sample tubes and degassed under vacuum (10^{-5} Torr) at 100 °C for 5 h. The BET model was applied to measure the specific surface areas of the samples.

FT-IR spectra of samples (γ-CD and γ-CD-MOFs) were obtained using an FT-IR spectrometer (Nicolet Continuum XL, Thermo Fisher Scientific). Briefly, the sample and potassium bromide were mixed well with a ratio of 1:10 followed by being compressed into a disk. 128 scans were carried out in wavenumber 400–4000 cm^{-1} at a resolution of 4 cm^{-1}.

Thermogravimetric analysis (TGA) of γ-CD-MOF crystals was performed using a thermal analysis system (NETZSCH 209F3 240-20-382-L, USA) at a heating rate of 10 °C min^{-1} under nitrogen. Samples were weighed (approx. 5 mg) in a hanging aluminum pan and the weight loss percentage of the samples was monitored from 30 to 400 °C.

2.4. Stability tests

For thermal stability investigations, γ-CD-MOF crystals (prepared with the condition of F1, 200 mg) were placed in a sealed glass vial for predefined time periods (2, 4, 6, 18, 24 h) at 60, 80 and 100 °C. The stabilities in different solvents were assessed by immersing 200 mg of the γ-CD-MOF powders (F1) in DCM, ^{i}PrOH, absolute EtOH, Me_2CO, MeOH and DMF of 10 mL at 70 °C for 24 h. The stability of γ-CD-MOF crystals (F1) at different humidities was measured under relative humidities (RH) of 75% and 92.5% over a period of 1, 3, 5 and 10 d. Subsequently, the crystalline stabilities of all samples were characterized by SEM and PXRD.

2.5. Drug adsorptions

The adsorption profiles of captopril (CAP) as well as those of 20 other drugs exhibited by γ-CD-MOF crystals (prepared using condition of F1) using the impregnation approach were investigated. Impregnation was performed by shaking (150 rpm) a suspension (2 mL) of γ-CD-MOFs (30 mg) and drugs (10 mg mL^{-1}) in EtOH for 72 h at 25 °C. The drug-loaded γ-CD-MOF crystals were collected by centrifugation, washed with an equivalent volume of incubation solvent three times and dried at 35 °C overnight under vacuum. The adsorption behavior of CAP by γ-CD-MOF crystals were further investigated systematically.

The remained CAP and other 20 drugs in the supernatant were separately determined by HPLC with suitable chromatography conditions. All details are provided in the Supporting information (S1).

3. Results and discussions

3.1. Optimized synthesis of micron sized γ-CD-MOFs

A vapor diffusion method has been reported (Smaldone et al., 2010) for the synthesis of γ-CD-MOFs, prepared by dissolving γ-CD (1.30 g, 1 mmol) along with KOH (0.45 g, 8 mmol) in aqueous solution (20 mL), followed by vapor diffusion with MeOH at ambient temperature over the period of a week to produce γ-CD-MOFs as cubic crystals of 40–500 μm in size. A modified method with the addition of CTAB and a controlled incubation time about 26–32 h has been reported (Furukawa et al., 2012) to produce the micron- and nano-meter size crystals, yet it does not provide MOFs of sufficient quality in relation to the particle size and size distributions in a controlled manner.

In our research, we found that the nucleation could be accelerated and uniform cubic γ-CD-MOF crystals were obtained by raising the reaction system temperature appropriately and pre-adding the reaction solvent. In general, the preparation period was shortened from over 26 h to 6 h, while the crystals retained their porous and crystalline properties. The N_2 adsorption-desorption isotherms measured on activated γ-CD-MOFs (F1) defined a BET surface area of 495 $m^2 g^{-1}$. The crystalline phase and the functional groups of γ-CD-MOFs (F1) were identified by PXRD (Fig. S2) and FT-IR (Fig. S3), the profiles were consistent with those reported in the literature (Furukawa et al., 2012). SEM (Fig. S2) indicated clearly that γ-CD-MOF crystals are uniform cubic crystals with a size of approximately 7 μm. It is important to note that, by using the modified method with alternative values of t, T, C_{CD}, R, solvents and C_{CTAB}, γ-CD-MOF crystals with different sizes and shapes could be obtained.

3.1.1. Syntheses with different reactant concentrations

The size and shape of γ-CD-MOF crystals prepared under different concentrations have been investigated. On changing the total concentrations of γ-CD and KOH while keeping the molar ratio at 1:8 (C_{CD} of 25 mM for F1, 12.5 mM for F2 and 50 mM for F3), γ-CD-MOF crystals with identical crystallinity could be prepared as verified by PXRD (Fig. 1). The SEM images (Fig. 1) show that the size of γ-CD-MOF crystals increases with dilution of crystallization solution. With the increase of concentration of γ-CD from 12.5 mM (F2) to 25 mM (F1) and then to 50 mM (F3), the size of γ-CD-MOF crystals decreases from 7.1 ± 3.0 μm to 6.9 ± 1.2 μm and then to 4.3 ± 1.2 μm. Apparently, lower concentration of the crystallization solution results in larger cubic crystals of γ-CD-MOFs, a finding which is consistent with some conventional methods for (Brar et al., 2001) tuning the crystal size, and is most likely a result of the efficient suppression of the framework extension (Leff et al., 1995). We hypothesize that the control of the nucleation and crystal growth rates is the key factor in modifying the size of the γ-CD-MOF crystals, although higher reactant concentrations usually lead to increments in crystal growth rates in the case of other MOF materials (Diring et al., 2010; Gascon et al., 2008; Ramos-Fernandez et al., 2011).

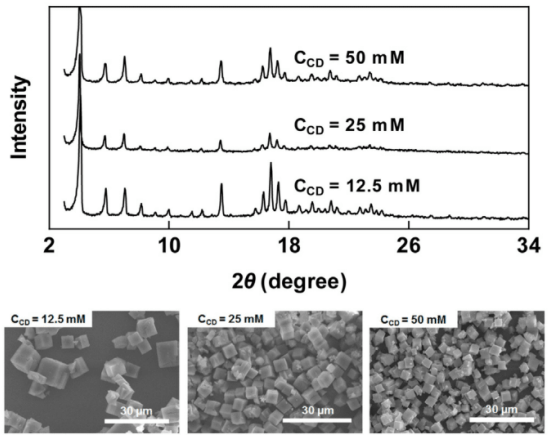

Fig. 1. PXRD crystallinity patterns and SEM morphology images of γ-CD-MOF crystals prepared with different concentrations of γ-CD: 12.5 mM (F2), 25 mM (F1) and 50 mM (F3). Higher concentrations of γ-CD showed no influence on the crystalline structure and resulted in a smaller size of γ-CD-MOFs.

3.1.2. Syntheses under different temperatures

The temperature had a distinct influence on the size and morphology of γ-CD-MOF crystals, whilst as shown in Fig. 2, the crystal structure of the γ-CD-MOFs did not change. With an increase of the temperatures from 40 °C (F4) to 50 °C (F1) and then to 60 °C (F5), the size of γ-CD-MOF crystals decreased from 10.5 ± 5.1 μm to 6.9 ± 1.2 μm and then to 5.3 ± 1.2 μm. It is clear that a higher temperature would promote the vapor diffusion of MeOH into the reactant solution, contributing to the rapid oversaturation of the precursors. Meanwhile, raising the temperature led to the γ-CD-MOF crystals being smaller and more uniform without affecting the crystallinity. These results suggested that by raising temperatures could be employed to prepare γ-CD-MOFs in a shorter period of time.

3.1.3. Syntheses with different periods of reaction time

Fig. 3 shows the PXRD patterns and SEM images of γ-CD-MOF crystals obtained at different time (6, 12 and 24 h). The results indicated that crystallinity varies with time. When the duration of the preparation was prolonged for 24 h, distinct crystalline structural changes at 16.7° in PXRD patterns were observed for sample F7, while for a long time heating resulted in distorting the crystal integrity of γ-CD-MOFs. From the morphologies revealed by the SEM images, the size of the γ-CD-MOFs gradually decreased from 6.9 ± 1.2 μm to 4.1 ± 1.1 μm when the crystallization time was increased from 6 to 24 h. Thus, longer time results in smaller γ-CD-MOF crystals. In the case of crystalline materials, smaller crystals are usually obtained when the nucleation rate is larger than the rate of crystal growth (Jhung et al., 2008; Lethbridge et al., 2005; Renzo, 1998). Our results suggested that the nuclei concentration of γ-CD-MOFs was sufficiently higher than the concentration required for rapid crystal growth and so led to the formation of small and homogeneous crystals.

3.1.4. Syntheses with different ratios of γ-CD to KOH

The γ-CD-MOFs are a prototypical mixed-ligand compound among MOFs, with the composition of potassium cations bridging by the hydroxyl groups of γ-CD. In this investigation, it was found that an increase of the molar proportion of KOH from 0.75 mol (F8) to 1 mol (F1) and then to 1.25 mol (F9) led to an increase in the size of γ-CD-MOFs from 5.3 ± 1.1 to 6.9 ± 1.2 μm and then to 8.1 ± 3.1 μm (Fig. 4). For the formation of CD-MOFs, the K^+ ions

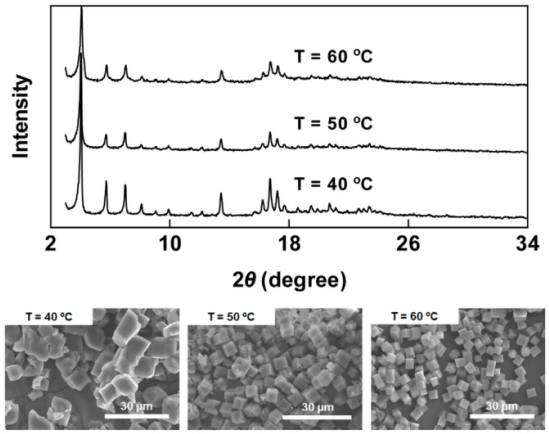

Fig. 2. PXRD crystallinity patterns and SEM morphology images of γ-CD-MOF crystals obtained at different temperatures: 40 (F4), 50 (F1) and 60 °C (F5). Higher temperatures showed no influence on the crystalline morphology and resulted in a smaller size of γ-CD-MOFs.

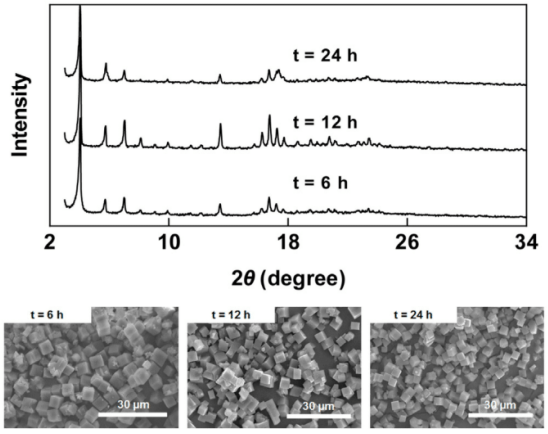

Fig. 3. PXRD crystallinity patterns and SEM morphology images of γ-CD-MOF crystals obtained after different reaction times of 6 h (F1), 12 h (F6) and 24 h (F7). The longer reaction time of 24 h showed the destruction of the crystalline structure of γ-CD-MOFs and resulted in a smaller size.

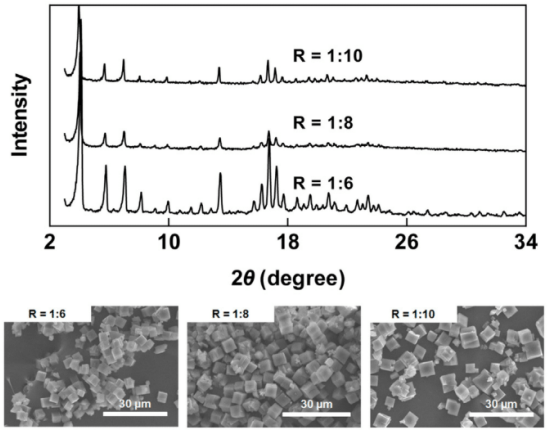

Fig. 4. PXRD crystallinity patterns and SEM morphology images of γ-CD-MOF crystals obtained with different ratios of γ-CD to KOH as 1:6 (F8), 1:8 (F1) and 1:10 (F9). Higher ratios of γ-CD to KOH showed no influence on the crystalline structure of γ-CD-MOFs and resulted in a smaller size.

were employed as the structure directing reagent, and at the same time, it was reported that KOH could produce sufficient basicity in aqueous solution to deprotonate the γ-CD hydroxyl group (Michida et al., 2015). As concluded by our results, increased concentration of K^+ and OH^- ions in the solution would facilitate the crystal growth rate in comparison to the nucleation rate and lead to larger crystals with higher polydispersity.

3.1.5. Syntheses with different solvents

The crystal structure (Fig. 5) of γ-CD-MOFs does not change when employing different solvents, while morphological changes are observed in SEM images. EtOH promoted the transformation of γ-CD and KOH solution into γ-CD-MOF crystals with the formation of hexagon-shaped and larger sized crystals. The cubic γ-CD-MOF crystals obtained from vapor diffusion of Me_2CO were much smaller in size. This observation is attributed to the faster vapor diffusion of Me_2CO because of its lowest boiling point, enabling the

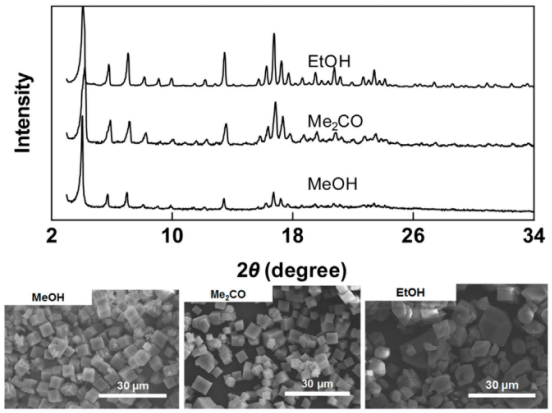

Fig. 5. PXRD crystallinity patterns and SEM morphology images of γ-CD-MOF crystals obtained with different solvents e.g., MeOH (F1), Me_2CO (F10) and EtOH (F11). Different solvents did not influence on the crystalline structure and the solvent with higher boiling point resulted in smaller size of γ-CD-MOF crystals.

formation of a large number of nuclei and hence rapid growth resulting in smaller crystals when compared with the other two solvents studied.

3.1.6. Syntheses with different amounts of the surfactant

CTAB is a cationic surfactant used as a capping agent for controlling the size and morphology of MOF crystals in aqueous systems. Increasing amounts of CTAB did not result (Fig. 6) in changes in the crystallinity of the γ-CD-MOF crystals as evidenced by PXRD. From the morphology shown by the SEM images, it is noteworthy that the average size of γ-CD-MOF crystals decrease from 8.0 ± 1.1 μm to 6.9 ± 1.2 μm and then to 4.1 ± 1.3 μm when the amount of CTAB is increased from 4 to 8 and then to 16 mg mL^{-1}, respectively. During the incubation with CTAB employed as a capping agent (Pan et al., 2011), the long hydrocarbon chains of CTAB can also play a crucial role in controlling the size of the γ-CD-MOF crystals. When CTAB is added to the crystallization medium, the CTAB molecules cover the surface of γ-CD-MOF crystals, and thus slow down the growth rate and reduce the final crystal size. Though CTAB is toxic, considering the good solubility of CTAB in ^{i}PrOH, ^{i}PrOH was used to wash and remove the residual CTAB thoroughly.

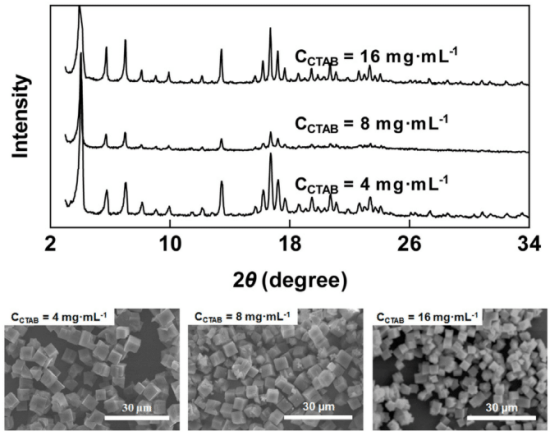

Fig. 6. PXRD crystallinity patterns and SEM morphology images of γ-CD-MOF crystals synthesized with different concentrations of CTAB as 4 mg mL^{-1} (F12), 8 mg mL^{-1} (F1) and 16 mg mL^{-1} (F13). Higher concentration of CTAB showed no influence on the crystalline structure and resulted in a smaller size of γ-CD-MOF crystals.

3.2. Crystalline stability of γ-CD-MOFs

3.2.1. Crystalline stability of γ-CD-MOFs at different temperatures

The crystalline stability of γ-CD-MOFs (F1) was investigated using SEM and PXRD techniques. Although the TGA profile of γ-CD-MOFs shows that the thermal decomposition of γ-CD-MOFs occurs at (Fig. S4) approximately 200 °C, the results do not establish the stability of γ-CD-MOFs under different conditions at elevated temperature.

Fig. 7 shows the PXRD diffractograms of γ-CD-MOFs after thermal stability test (compare Fig. S5). In Fig. 7a, although the characteristic and most intensive peaks of γ-CD-MOFs at 4.0° and 16.7° are still evident, major disturbances to the patterns at 5.7°, 7.0° and 16.7° were noted. Compared to the PXRD profiles of γ-CD-MOF crystals treated at 60, 80 and 100 °C for different periods of time, some minor disturbances of the profiles near 16.7° were identified, followed by those at 5.7° and 7.0°, which changed from two independent sharp peaks into four separate peaks. Therefore, it is concluded that the crystallinity of γ-CD-MOF crystals is susceptible to high temperature and decomposes on overheating. Nevertheless, γ-CD-MOFs can remain the cubic shape and appearance even at 100 °C after 24 h (Fig. S6).

3.2.2. Crystalline stability of γ-CD-MOFs in solvents

As evidenced by PXRD profiles (Fig. 7b), the γ-CD-MOF crystals are stable after soaking in DCM at 70 °C for 1 day. The crystalline stability exhibits a decreasing order for DCM, ^{i}PrOH, EtOH and Me_2CO. Major changes were noticed for crystalline stability in the case of MeOH and DMF solvents at 70 °C after 1 d, with marked changes in peak intensities at 16.7°. Thus, it can thus be inferred that the crystalline structure of γ-CD-MOF is more stable in DCM than in ^{i}PrOH, EtOH and Me_2CO. More substantial degradation was observed in MeOH and DMF. These results illustrate that the degradation in γ-CD-MOF crystals increases in parallel with solvent polarity. Based on the γ-CD content in the supernatant, it was demonstrated (Fig. S7) that the total release of γ-CD from γ-CD-MOF crystals in DMF is about 5% (70 °C, 1d). In addition, the morphology of γ-CD-MOFs is relatively stable even though the crystallinity of the crystals changes (Fig. S8) dramatically in some polar solvents.

3.2.3. Crystalline stability of γ-CD-MOFs at different humidities

From analysis of the PXRD profiles in Fig. 7c and d, it is clear that humidities play a crucial role in determining the crystalline stability of γ-CD-MOFs. Only minor changes were observed at 4.1°, 5.7° and 7.0° for the crystals treated at 75% RH for 10 d (Fig. 7c). Storage of γ-CD-MOFs at higher humidities of 92.5% RH, however, impacted the crystalline structure dramatically (Fig. 7d), and PXRD profiles indicated distorted crystal structure. For the γ-CD-MOF crystals stored at 92.5% RH for 1 d, the cubic crystals collapsed completely (Fig. S9). This observation can be explained by the fact that γ-CD-MOFs are principally composed of γ-CD and KOH, both of which are highly hydrophilic and are readily dissolved in water.

3.3. Adsorption of drugs to standard γ-CD-MOFs

The adsorption percentage of the 21 drugs to standard γ-CD-MOF crystals (F1) has been divided into three levels (seven drugs, including CAP, large than 5%, nine drugs 0.3% to 5%, and five drugs less than 0.3%) based on the adsorbed amount (Table S1). Considering the physiochemical properties of the seven drugs,

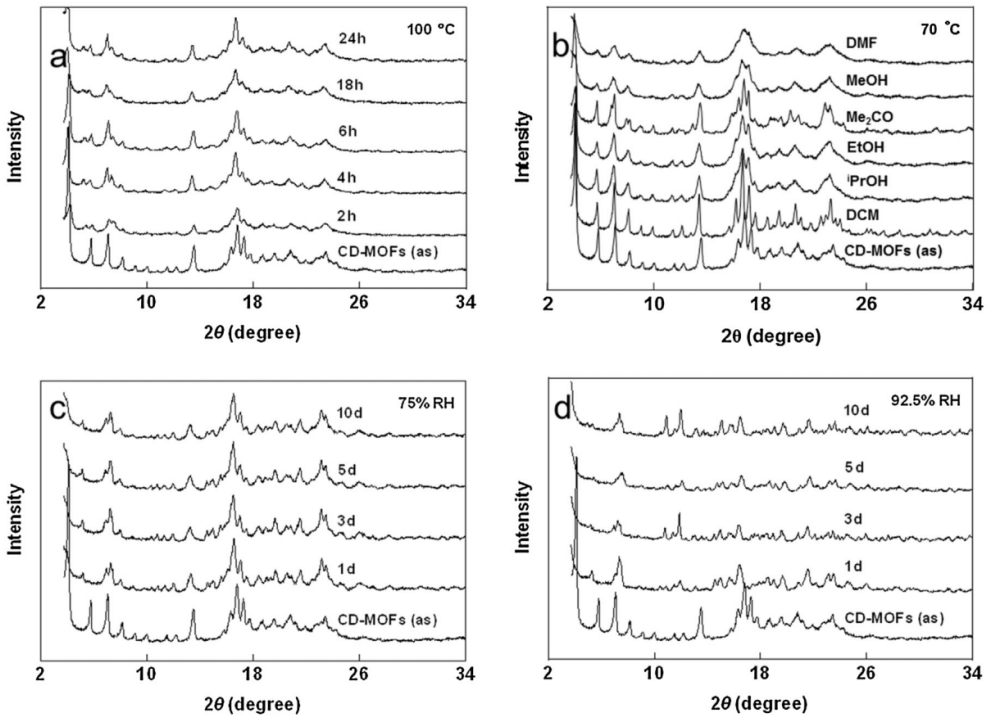

Fig. 7. PXRD crystallinity patterns of γ-CD-MOFs after different periods of time in comparison to the initial state (as: as-synthesized): (a) at 100 °C; (b) at different solvents after 1d; (c) 75% RH; (d) 92.5% RH.

apart from piroxicam, with one or more carboxyl function groups and a small pK_a value showed relatively high adsorption percentage, an observation which is believed to arise from the strong electrostatic interaction between the carboxyl groups in drug molecules and potassium ions in γ-CD-MOFs. Drugs with nitrogen or other heterocyclic rings showed relatively low adsorption percentage due to the steric hindrance of these rings for the interaction of drugs with γ-CD-MOFs.

An understanding of the γ-CD-MOFs adsorption behavior in organic solvent systems is helpful for the application of these porous materials. In our preliminary drug adsorption experiments, CAP exhibited the highest adsorption to γ-CD-MOFs compared with the other 20 drugs (Table S1). Considering the high stability of CAP in EtOH (Qu et al., 2006), we decided to investigate the γ-CD-MOFs adsorption capability to CAP in further detail. CAP was also selected for further study taking into consideration of its molecular size ($9.0 \times 5.7 \times 3.3$ Å), particularly the dimensions of the aperture windows (7.8 Å) and the internal pores (17 Å) of γ-CD-MOFs, both of which are sufficiently large to accommodate the CAP molecules. Additionally, the interaction of CAP and γ-CD-MOFs relies mainly on Van der Waals' forces when CAP is in the non-ionizing form, while the –COOH, –SH as well as =O groups of CAP can form hydrogen bonds with the hydroxyl group of γ-CD-MOFs.

The adsorption isotherms of γ-CD-MOFs for CAP were measured at three different concentrations (400, 1000 and 2000 mg L^{-1}) of CAP. The adsorption capacity of γ-CD-MOFs toward CAP was found to be related to the CAP solution concentration. A qualitative analysis of the adsorption curves (Fig. 8a) showed that the γ-CD-MOFs had a high efficiency towards CAP in EtOH solution, and the amount of adsorbed CAP on γ-CD-MOFs synthesized by vapor diffusion of MeOH (F1) and Me_2CO (F10) was recorded to be higher than that of EtOH (F11) under the experimental conditions investigated.

The CAP uptake rate and the contact time of the adsorption were described with adsorption kinetics at 25 °C at the initial concentration of 400 mg L^{-1}. As shown in Fig. 8c, the apparent adsorption equilibrium was usually established within 24 h. The pseudo-first-order model did not fit with our experimental data (Walker et al., 2011). However, the pseudo-second-order kinetic model provided the best correlation of the data (detailed methods could be found in S2) (Crini and Peindy, 2006; Qiu et al., 2015). This finding can be interpreted as chemisorption involving valency forces sharing or exchanging electrons between sorbent and sorbate. The coefficients for the linear plots of t/q_t against time for pseudo-second-order kinetics were greater than 0.99 for all systems (Fig. 8d). The adsorption behavior of CAP further illustrated the fact that some drugs could be chemisorbed by γ-CD-MOFs.

3.4. Adsorption of drugs to γ-CD-MOFs with damaged crystallinity

The adsorption of γ-CD-MOFs with damaged crystallinity (after testing stability in different solvents) was investigated. Samples of CAP in EtOH (Fig. 8b) showed that the crystals retained remarkably large adsorption capacities, although our previous PXRD studies of γ-CD-MOFs illustrated that the crystals were not stable under those extreme conditions. In addition, at lower concentrations of CAP towards some γ-CD-MOFs with damaged crystallinity (Figs. 8b and S10), some damaged γ-CD-MOFs (after immersing in MeOH and DCM at 70 °C for 24 h) exhibited a higher CAP adsorption behavior than standard γ-CD-MOFs. The pseudo-second-order kinetic model did not fit with the damaged γ-CD-MOFs (after soaking in ^{i}PrOH and DMF at 70 °C for 24 h, $R^2 < 0.9$,

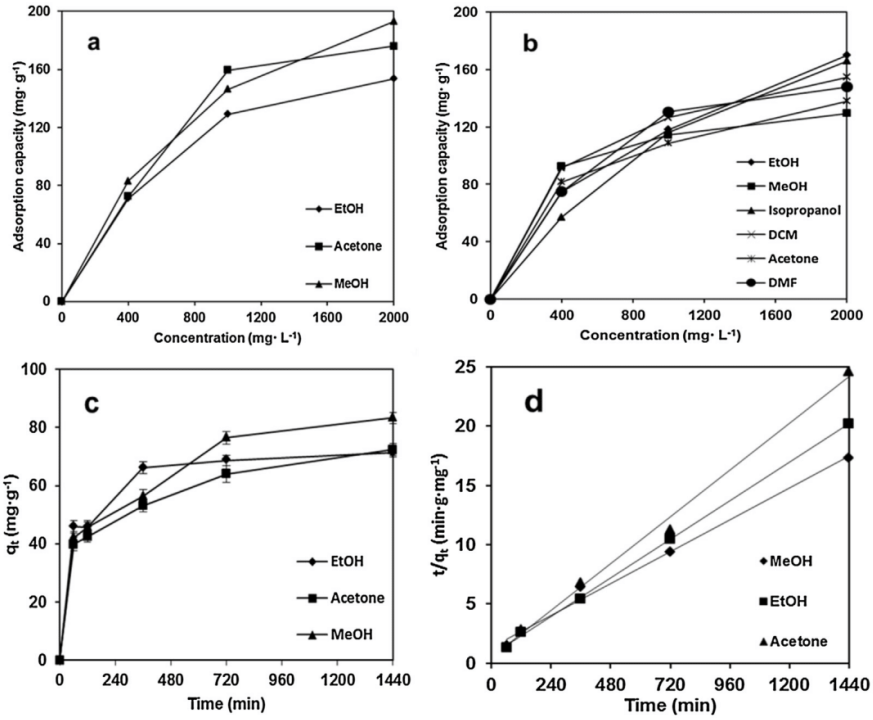

Fig. 8. The adsorption capacity of γ-CD-MOF crystals to CAP with different initial concentrations at 25 °C of (a) standard γ-CD-MOFs synthesized via vapor diffusion of MeOH (F1), Me_2CO (F10) and EtOH (F11); (b) γ-CD-MOFs with damaged crystallinity (after soaking in DCM, ^{i}PrOH, EtOH, Me_2CO, MeOH and DMF at 70 °C for 24 h); (c) Effects of contacted time on the adsorption of CAP (400 mg mL^{-1}) onto γ-CD-MOFs (n = 2); (d)The fitting results of the pseudo-second-order kinetics fit the experimental data well.

Fig. S11). To some extent, the above results illustrate the fact that the damaged γ-CD-MOFs would influence drug adsorption kinetics. Moreover, for CAP, adsorption onto the damaged γ-CD-MOFs was reduced compared to the standard γ-CD-MOF crystals at higher concentrations.

4. Conclusions

In this investigation, a fast solvent evaporation approach was developed to synthesize and tailor the γ-CD-MOFs to a controlled size, with the synthesis period shortened from that reported in the literature of over 26 to 6 h. The size of γ-CD-MOF crystals was adjusted by altering the reactant concentrations, reaction temperatures, reaction time, ratios of γ-CD to KOH and surfactant concentrations, without any marked changes in particle crystallinity and porosity. And the γ-CD-MOF crystals of hexagonal shape were obtained with the reaction solvent of EtOH. For the stability of standard γ-CD-MOFs, varying degrees of reduction in crystallinity or morphology were observed in γ-CD-MOF crystals at high temperature (100 °C), high humidity (92.5%) and with polar solvents (MeOH and DMF). More importantly, it was found that γ-CD was released and characteristic crystalline peaks in PXRD profiles disappeared when immersing the γ-CD-MOFs in polar solvent whilst the morphology remained unchanged. For drug adsorption, most of the molecules containing a carboxyl group showed relatively high adsorption to γ-CD-MOFs (>5%), while relative low adsorption (<5%) was found for drugs with nitrogen heterocyclic rings. From CAP adsorption experiment at higher concentration, γ-CD-MOFs showed an equilibrium CAP adsorption capacity of 19.3% (w/w), with a molar ratio between CAP and γ-CD as 1.6:1. Adsorption kinetics of CAP at lower concentration towards standard γ-CD-MOFs matched well with the pseudo-second-order model. Interestingly, some damaged γ-CD-MOFs being soaked in MeOH and DCM at 70 °C for 24 h exhibited higher CAP adsorption percentage than standard γ-CD-MOFs.

In summary, facile synthesis and size control approaches, together with crystalline stability information of γ-CD-MOF crystals are provided to support their application in drug delivery.

Acknowledgements

We are grateful for the financial support from National Science and Technology Major Project (2013ZX09402103) and National Natural Science Foundation of China (81373358). This research is also part of the Joint Center of Excellence in Integrated Nano-Systems (JCIN) at King Abdulaziz City for Science and Technology (KACST) and Northwestern University (NU). The authors would like to thank both KACST and NU for their continued support of this research.

Appendix A. Supplementary data

Supplementary data associated with this article can be found, in the online version, at http://dx.doi.org/10.1016/j.ijpharm.2016.09.029.

References

Brar, T., France, P., Smirniotis, P.G., 2001. Control of crystal size and distribution of zeolite A. Ind. Eng. Chem. Res. 40.
Chen, J., Li, K., Chen, L., Liu, R., Huang, X., Ye, D., Chen, J., Li, K., Liu, R., Huang, X., 2014. Conversion of fructose into 5-hydroxymethylfurfural catalyzed by recyclable

sulfonic acid-functionalized metal–organic frameworks. Green Chem. 16, 2490–2499.
Cheng, L., Gou, S., Xu, G., 2010. Three-dimensional hybrid organic-inorganic frameworks based on lanthanide(III) sulfate layers and organic pillars of 1,4-piperazinediacetic acid. J. Mol. Struct. 979, 214–220.
Chih-Min, W., Kwang-Hwa, L., 2009. Synthesis of novel organic-inorganic hybrid compounds: lanthanide phosphites incorporating a squarate ligand. Inorg. Chem. 48, 6335–6337.
Crini, G., Peindy, H., 2006. Adsorption of C.I Basic Blue 9 on cyclodextrin-based material containing carboxylic groups. Dyes Pigm. 70, 204–211.
Cychosz, K.A., Matzger, A.J., 2010. Water stability of microporous coordination polymers and the adsorption of pharmaceuticals from water. Langmuir ACS J. Surf. Colloids 26, 17198–17202.
Diring, S., Furukawa, S., Takashima, Y., Tsuruoka, T., Kitagawa, S., 2010. Controlled multiscale synthesis of porous coordination polymer in nano/micro regimes. Chem. Mater. 22, 4531–4538.
Forgan, R.S., Smaldone, R.A., Gassensmith, J.J., Hiroyasu, F., Cordes, D.B., Qiaowei, L., Wilmer, C.E., Botros, Y.Y., Snurr, R.Q., Slawin, A.M.Z., 2012. Nanoporous carbohydrate metal-organic frameworks. J. Am. Chem. Soc. 134, 406–417.
Furukawa, Y., Ishiwata, T., Sugikawa, K., Kokado, K., Sada, K., 2012. Nano- and microsized cubic gel particles from cyclodextrin metal–organic frameworks. Angew. Chem. Int. Ed. 51, 10566–10569.
Gascon, J., Aguado, S., Kapteijn, F., 2008. Manufacture of dense coatings of Cu-3(BTC)(2) (HKUST-1) on alpha-alumina. Microporous Mesoporous Mater. 113, 132–138.
Gassensmith, J.J., Hiroyasu, F., Smaldone, R.A., Forgan, R.S., Botros, Y.Y., Yaghi, O.M.J., Fraser, S., 2011. Strong and reversible binding of carbon dioxide in a green metal-organic framework. J. Am. Chem. Soc. 133, 15312–15315.
Ghose, S.K., Li, Y., Yakovenko, A., Dooryhee, E., Ehm, L., Ecker, L.E., Dippel, A.C., Halder, G.J., Strachan, D.M., Thallapally, P.K., 2015. Understanding the adsorption mechanism of Xe and Kr in a metal–organic framework from X-ray structural analysis and first-principles calculations. J. Phys. Chem. Lett. 1790–1794.
Holcroft, J.M., Hartlieb, K.J., Moghadam, P.Z., Bell, J.G., Barin, G., Ferris, D.P., Bloch, E. D., Algaradah, M.M., Nassar, M.S., Botros, Y.Y., Thomas, K.M., Long, J.R., Snurr, R. Q., Stoddart, J.F., 2015. Carbohydrate-mediated purification of petrochemicals. J. Am. Chem. Soc. 137, 5706–5719.
Horcajada, P., Gref, R., Baati, T., Allan, P.K., Maurin, G., Couvreur, P., Ferey, G., Morris, R.E., Serre, C., 2012. Metal-organic frameworks in biomedicine. Chem. Rev. 112, 1232–1268.
Ikezoe, Y., Washino, G., Uemura, T., Kitagawa, S., Matsui, H., 2012. Autonomous motors of a metal-organic framework powered by reorganization of self-assembled peptides at interfaces. Nat. Mater. 11, 1081–1085.
Jhung, S.H., Lee, J.H., Forster, P.M., Férey, G., Cheetham, A.K., Chang, J.S., 2006. Microwave synthesis of hybrid inorganic–organic porous materials: phase-selective and rapid crystallization. Chem. – Euro. J. 12, 7899–7905.
Jhung, S.H., Ji, H.L., Chang, J.S., 2008. Crystal size control of transition metal ion-incorporated aluminophosphate molecular sieves: effect of ramping rate in the syntheses. Microporous Mesoporous Mater. 112, 178–186.
Jiecheng, C., Ning, G., Chen, W., Wei, Z., Jian, L., Hui, W., Philipp, S., Bart Jan, R., Guangtao, L., 2014. Photonic metal-organic framework composite spheres: a new kind of optical material with self-reporting molecular recognition. Nanoscale 6, 11995–12001.
Joong, K.I., Abedin, K.N., Enamul, H., Hwa, J.S., 2011. Inside cover: chemical and thermal stability of isotypic metal–organic frameworks: effect of metal ions. Chem. Eur. J. 17, 6278 (23/2011. Chemistry).
Kılıç, A., Atalay-Oral, Ç., Sirkecioğlu, A., Tantekin-Ersolmaz, Ş.B., Ahunbay, M.G., 2015. Sod – ZMOF/Matrimid ®; mixed matrix membranes for CO2 separation. J. Membr. Sci. 489, 81–89.
Khan, N.A., Kang, I.J., 2011. Facile synthesis of nano-sized metal-organic frameworks, chromium-benzenedicarboxylate, MIL101. Chem. Eng. J. 166, 1152–1157.
Kumar, P., Kumar, P., Bharadwaj, L.M., Paul, A.K., Deep, A., 2014. Luminescent nanocrystal metal organic framework based biosensor for molecular recognition. Inorg. Chem. Commun. 43, 114–117.
Kumar, K.V., Charalambopoulou, G., Kainourgiakis, M., Stubos, A., Steriotis, T., 2015. Insights on the physical adsorption of hydrogen and methane in UiO series of MOFs using molecular simulations. Comput. Theor. Chem. 1061, 36–45.
Leff, D.V., Ohara, P.C., Heath, J.R., Gelbart, W.M., 1995. Thermodynamic control of gold nanocrystal size: experiment and theory. J. Phys. Chem. 99, 7036–7041.
Lethbridge, Z.A.D., Williams, J.J., Walton, R.I., Evans, K.E., Smith, C.W., 2005. Methods for the synthesis of large crystals of silicate zeolites. Microporous Mesoporous Mater. 79, 339–352.
Li, H., Eddaoudi, M., O'Keeffe, M., Yaghi, O.M., 1999. Design and synthesis of an exceptionally stable and highly porous metal-organic framework. Nat. Int. Weekly J. Sci. 402, 276–279.
Li, B., Zhang, Y., Ma, D., Li, L., Li, G., Li, G., Shi, Z., Feng, S., 2012. A strategy toward constructing a bifunctionalized MOF catalyst: post-synthetic modification of MOFs on organic ligands and coordinatively unsaturated metal sites. Chem. Commun. 48, 6151–6153.
Li, R.J., Li, M., Zhou, X.P., Ng, S.W., O'Keeffe, M., Li, D., 2014. ROD-8, a rod MOF with a pyrene-cored tetracarboxylate linker: framework disorder, derived nets and selective gas adsorption. CrystEngComm 16, 6291–6295.
Liao, W.M., Shi, H.T., Shi, X.H., Yin, Y.G., 2014. Pyrolytic cavitation, selective adsorption and molecular recognition of a porous Eu(III) MOF. Dalton Trans. 43, 15305–15307.
Manju, Roy, P.K., Ramanan, A., Rajagopal, C., 2014. Core?shell polysiloxane–MOF 5 microspheres as a stationary phase for gas–solid chromatographic separation. RSC Adv. 4, 17429–17433.
Michida, W., Ezaki, M., Sakuragi, M., Guan, G., Kusakabe, K., 2015. Crystal growth of cyclodextrin-based metal-organic framework with inclusion of ferulic acid. Cryst. Res. Technol. 50, 556–559.
Miller, S.R., Daniela, H., Tarek, B., Patricia, H., Jean-Marc, G., Christian, S., 2010. Biodegradable therapeutic MOFs for the delivery of bioactive molecules. Chem. Commun. 46, 4526–4528.
Pan, Y., Heryadi, D., Zhou, F., Zhao, L., Lestari, G., Su, H., Lai, Z., 2011. Tuning the crystal morphology and size of zeolitic imidazolate framework-8 in aqueous solution by surfactants. CrystEngComm 13, 6937–6940.
Qiu, M., Chen, C., Li, W., 2015. Rapid controllable synthesis of Al-MIL-96 and its adsorption of nitrogenous VOCs. Catal. Today 258, 132–138.
Qu, F., Zhu, G., Huang, S., Li, S., Sun, J., Zhang, D., Qiu, S., 2006. Controlled release of Captopril by regulating the pore size and morphology of ordered mesoporous silica. Microporous Mesoporous Mater. 92, 1–9.
Ramos-Fernandez, Enrique, V., Garcia-Domingos, Mariana, Juan-Alca?iz, Jana, Gascon, Jorge, Kapteijn, Freek, 2011. MOFs meet monoliths: hierarchical structuring metal organic framework catalysts. Appl. Catal. A Gen. 391, 261–267.
Renzo, F.D., 1998. Zeolites as tailor-made catalysts: control of the crystal size. Catal. Today 41, 37–40.
Smaldone, R.A., Forgan, R.S., Furukawa, H., Gassensmith, J.J., Slawin, A.M., Yaghi, O. M., Stoddart, J.F., 2010. Metal-organic frameworks from edible natural products. Angew. Chem. 49, 8630–8634.
Song, F., Lin, W., 2012. Chiral porous metal-organic frameworks with dual active sites for sequential asymmetric catalysis. Proc. R. Soc. A Math. Phys. Eng. Sci. 468, 2035–2052.
Stock, N., Biswas, S., 2012. Synthesis of metal-organic frameworks (MOFs): routes to various MOF topologies, morphologies, and composites. Chem. Rev. 112, 933–969.
Thomas-Gipson, J., Pérez-Aguirre, R., Beobide, G., Castillo, O., Luque, A., Pérez-Yáñez, S., Román, P., 2015. Unravelling the growth of supramolecular metal–organic frameworks based on metal-nucleobase entities. Crystal Growth Des. 15, 975–983.
Walker, M., Iyer, K., Heaven, S., Banks, C.J., 2011. Ammonia removal in anaerobic digestion by biogas stripping: an evaluation of process alternatives using a first order rate model based on experimental findings. Chem. Eng. J. 178, 138–145.
Wei, Y., Han, S., Walker, D.A., Fuller, P.E., Grzybowski, B.A., 2012. Nanoparticle core/shell architectures within MOF crystals synthesized by reaction diffusion. Angew. Chem. 51, 7435–7439.
Wen, L., Shi, W., Chen, X., Li, H., Cheng, P., 2012. A porous metal-organic framework based on triazoledicarboxylate ligands – synthesis, structure, and gas-sorption studies. Eur. J. Inorg. Chem. 2012, 3562–3568.
Yang, Y., Lin, R., Ge, L., Hou, L., Bernhardt, P., Rufford, T.E., Wang, S., Rudolph, V., Wang, Y., Zhu, Z., 2015. Synthesis and characterization of three amino-functionalized metal-organic frameworks based on 2-aminoterphthalic ligand. Dalton Trans. 44, 8190–8197.
Yun, W., Jin, Y., Ying-Ying, L., Jian-Fang, M., 2013. Controllable syntheses of porous metal-organic frameworks: encapsulation of Ln(III) cations for tunable luminescence and small drug molecules for efficient delivery. Chem. – Euro. J. 19, 14591–14599.

Supporting Information for

"Optimized synthesis and crystalline stability of γ-Cyclodextrin metal-organic frameworks for drug adsorptions**"**

Botao Liu[1,2,a], Haiyan Li[1,3,a], Xiaonan Xu[1], Xue Li[1,4], Nana Lv[1], Vikaramjeet Singh[1], J. Fraser Stoddart[3], Peter York[1], Xu Xu[2,*], Ruxandra Gref[4,*], Jiwen Zhang[1,2,*]

[1] Center for Drug Delivery System, Shanghai Institute of Materia Medica, Chinese Academy of Sciences, Shanghai 201203, China;

[2] School of Chemical and Environmental Engineering, Shanghai Institute of Technology, Shanghai 201418, China;

[3] Department of Chemistry and Department of Materials Science, Northwestern University, 2145 Sheridan Road, Evanston, Illinois 60208-3113, United States

[4] Institut de Sciences Moléculaires d'Orsay, Universite´ Paris-Sud, Université Paris-Saclay, UMR CNRS 8214, 91405 Orsay Cedex, France.

[a:] Who contributed equally to the manuscript

***Corresponding Author:**

Prof. Jiwen Zhang

Center for Drug Delivery Systems, Shanghai Institute of Materia Medica, Chinese Academy of Sciences, No. 501 of Haike Road, Shanghai 201203, China; Tel/Fax: +86-21-20231980; E-mail: jwzhang@simm.ac.cn.

Prof. Ruxandra Gref

Institut de Sciences Moléculaires d'Orsay, (UMR CNRS 8214), Universite´ Paris-Sud, Université Paris-Saclay, 91400 Orsay, France; Tel: +33 (1)69158234; E-mail: ruxandra.gref@u-psud.fr.

Prof. Xu Xu

Shanghai Institute of Technology, No. 100, Haiquan Road, Shanghai 201418, China; Tel: +86-21-60873372; E-mail: xuxu3426@sina.com.

S1. HPLC methods for determination of drugs

The analysis was carried out with an Agilent C18 column (4.6 mm×150 mm, 3.6 μm i.d.) and a flow rate of 1.0 mL·min^{-1} with different mobile phases depending upon the types of drugs. Namely, the captopril (CAP) was analyzed with injection volume of 10 μL, the column temperature was maintained at 40 °C and the mobile phase consisted of methanol, acetonitrile and 0.017 M sodium dihydrogen phosphate buffer (pH 3.2) (25:5:70, v/v). Silymarin and budesonide were determined with the mobile phase composed of acetonitrile and water (65:35, v/v) with the column temperature of 30 °C. The other drugs were detected with the column temperature of 25 °C, the injection volume of 20 μL and the mobile phase composed of 10% acetonitrile in 0.1% acetic acid aqueous solution, changing linearly over 10 min to 90% acetonitrile then maintained for 3 min, and then decreasing to 10% in 1 min and then maintained for 6 min. The detection wavelengths of the drugs and the drug adsorptions were listed in Table S1.

The percentage of drug adsorbed onto standard γ-CD-MOF crystals was measured by dissolving 5 mg of dried samples in a certain volume of water and analyzed by HPLC. The drug adsorption percentage (Y) was calculated according to the following equation.

$$\mathrm{Y}\,(\%) = \frac{\text{Amount of drug in γ-CD-MOFs}}{\text{Total amount of γ-CD-MOFs}} \times 100\% \qquad (1)$$

50 mg of γ-CD-MOFs (F1, F10, F11) were added into hermetically sealed conical flasks containing 25 mL of CAP ethanol solution (400, 1000, 2000 mg·L^{-1}), and shaken at 25 °C for 24 h. Meanwhile, γ-CD-MOF crystals with damaged crystallinity (pre-dispersed in 10 ml DCM, isopropanol, EtOH, acetone, MeOH and DMF at 70 °C for 24 h, then adsorbed onto CAP in ethanol solution) were also processed in the same way. The CAP value of the solution was determined by the

above HPLC method. The adsorption capacity (q) of γ-CD-MOFs towards CAP was calculated as follows:

$$q_t = \frac{V(C_0 - C_t)}{W} \quad (2)$$

where q_t ($\mu g \cdot mg^{-1}$) is the adsorption capacity at contact time t, V is the volume of CAP solution (mL), C_0 is the initial concentration of CAP ($\mu g \cdot mL^{-1}$), C_t is the concentration of CAP at contact time t ($\mu g \cdot mL^{-1}$), and W is the weight of CD-MOFs (mg).

Table S1. Summary of chromatographic detection wavelengths of drugs and drug adsorptions determined by HPLC

NO	Drug	Detection wavelength(nm)	Adsorption percentage (±SD%, n=2)
1	Captopril	215	12.59±0.11
2	Flurbiprofen	247	12.10±0.11
3	Salicylic acid	230	9.83±1.07
4	Piroxicam[a]	350	8.44±0.20
5	Fenbufen	281	7.97±0.16
6	Ketoprofen[b]	260	7.40±0.03
7	Pseudolaric Acid B[b]	252	5.32±0.09
8	Prednisolone	246	4.54±0.21
9	Silymarin	276	4.53±0.11
10	Indapamide	240	4.27±0.21
11	Tolbutamide[b]	228	3.92±0.27
12	Theophylline	270	3.49±0.04
13	Meloxicam[c]	353	3.22±0.00
14	Nifedipine	235	1.00±0.01
15	Budesonide	240	0.38±0.24
16	Paracetamol	257	0.30±0.03
17	Fluconazole	260	0.17±0.00
18	Ethionamide[d]	291	0.04±0.01
19	Metronidazole	320	0.02±0.02
20	Diazepam	240	0.02±0.00
21	Caffeine[e]	273	0.01±0.00

Note: a represented the loading solvent as acetone; b represented the loading solvent as methanol; c represented the loading solvent as chloroform; d represented the loading solvent as ethanol (2 mL) and methanol (1 mL); e represented the loading solvent as ethanol (2 mL) and chloroform (1 mL); the other loadings used ethanol.

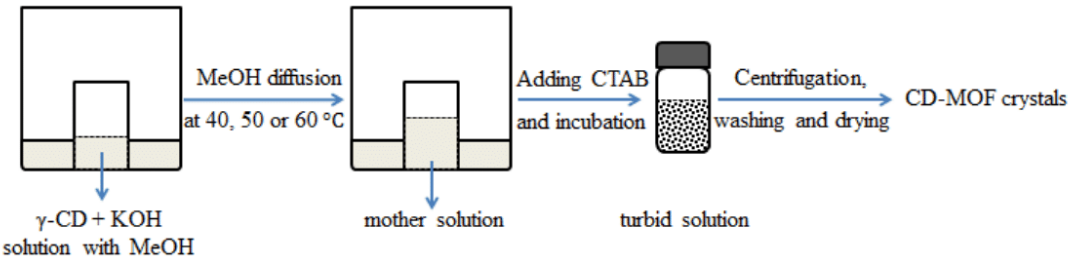

Figure S1. Schematic presentation for the synthesis of micron sized γ-CD-MOF crystals

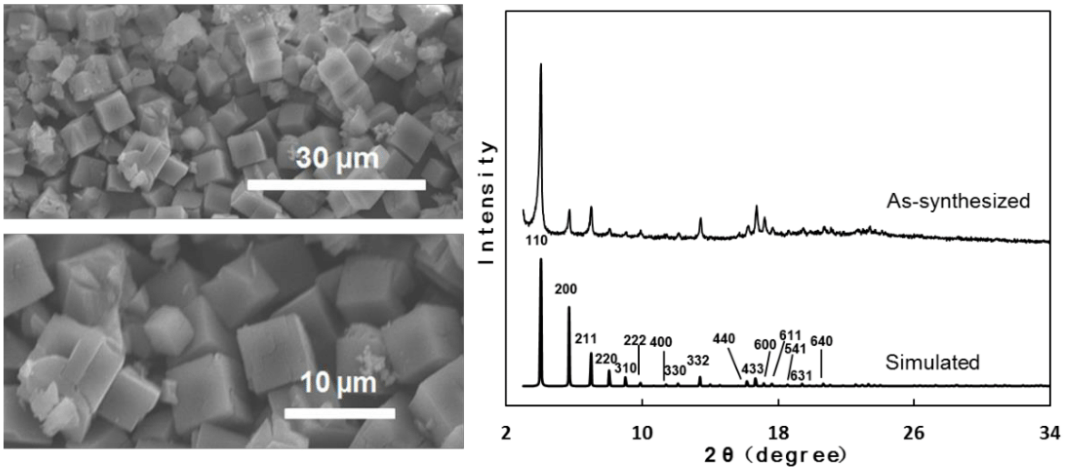

Figure S2. SEM images and XRPD pattern of γ-CD-MOFs.

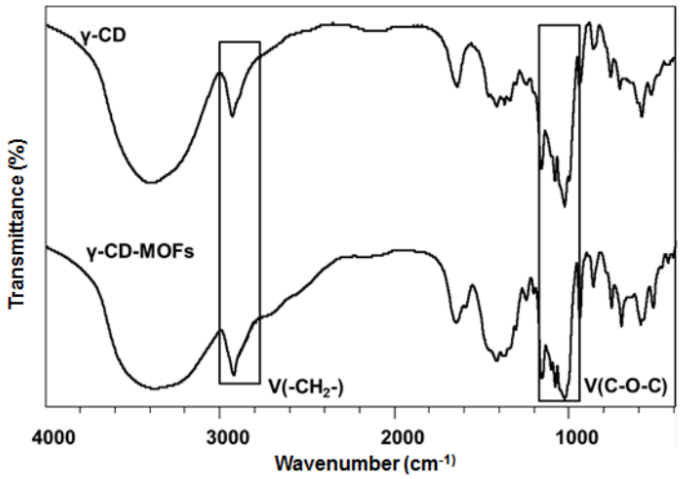

Figure S3. FT-IR patterns of γ-CD and γ-CD-MOFs.

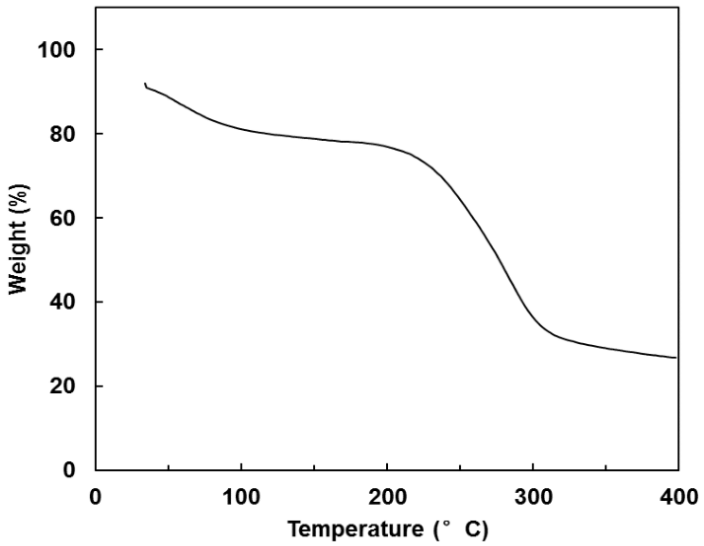

Figure S4. Thermogravimetric analysis of γ-CD-MOFs

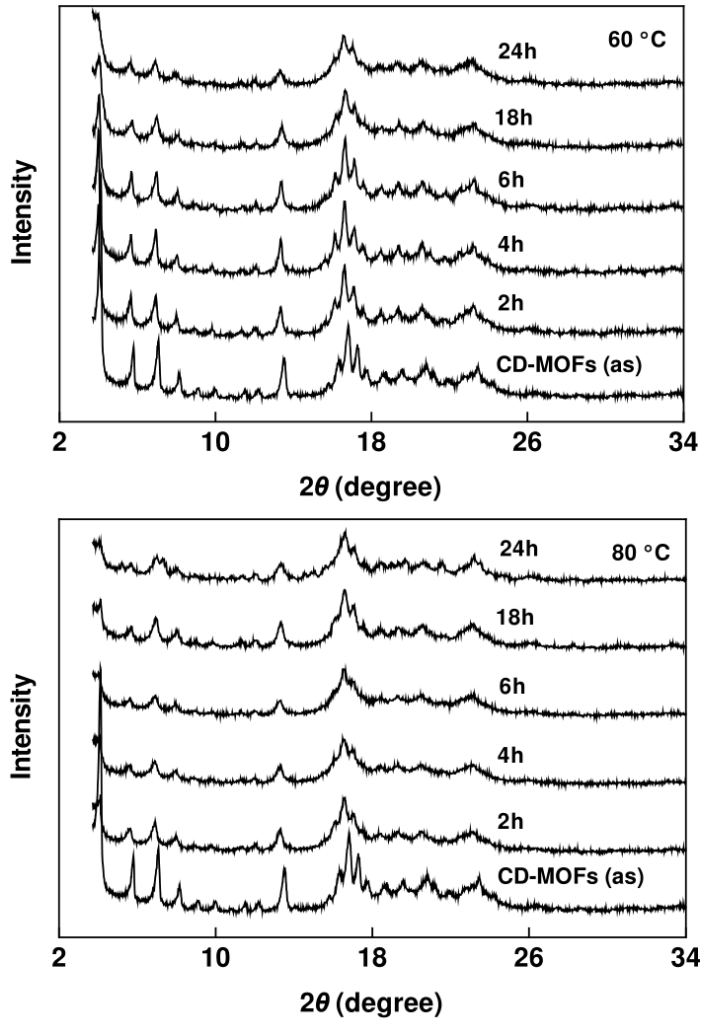

Figure S5. PXRD patterns of γ-CD-MOFs (as: as-synthesized) at 60, 80 °C after different time

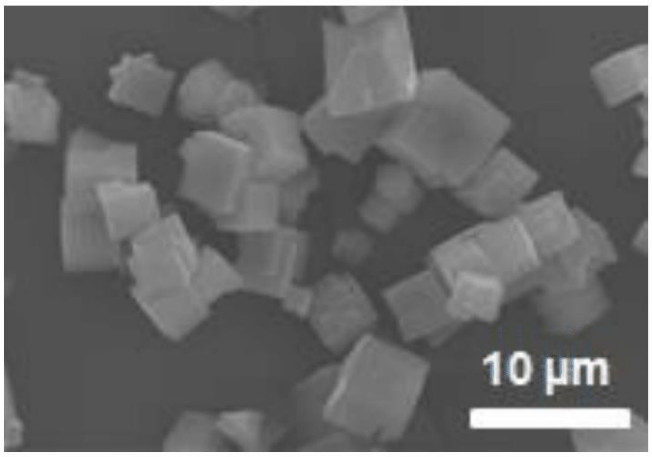

Figure S6. SEM image of γ-CD-MOFs at 100 °C after 24 h

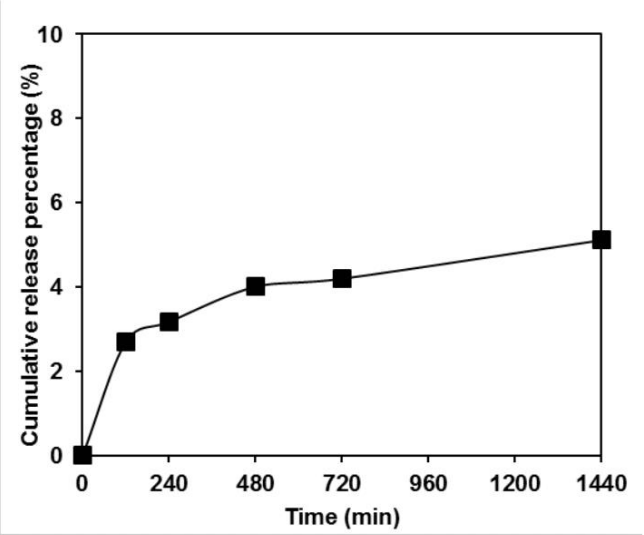

Figure S7. The release profiles of γ-CD from γ-CD-MOFs at DMF (70 °C)

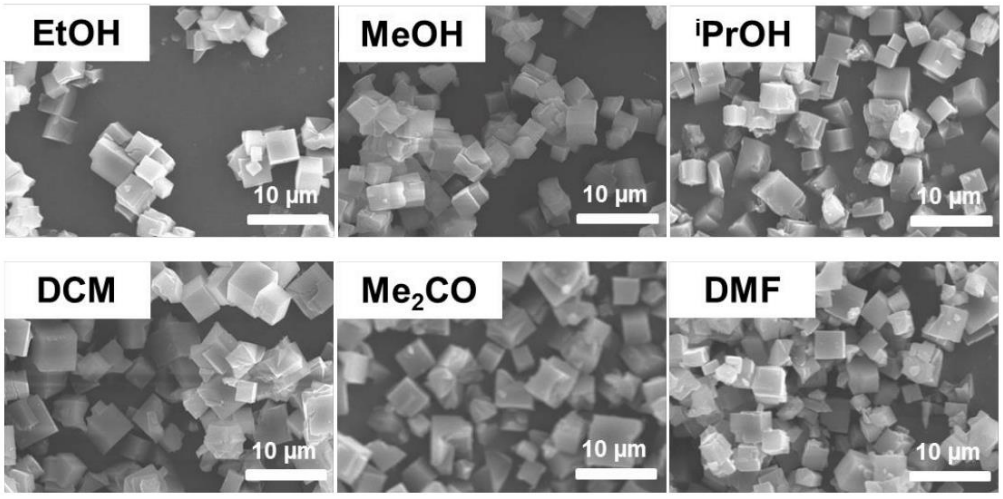

Figure S8. SEM image of γ-CD-MOFs at 100 °C after 24 h

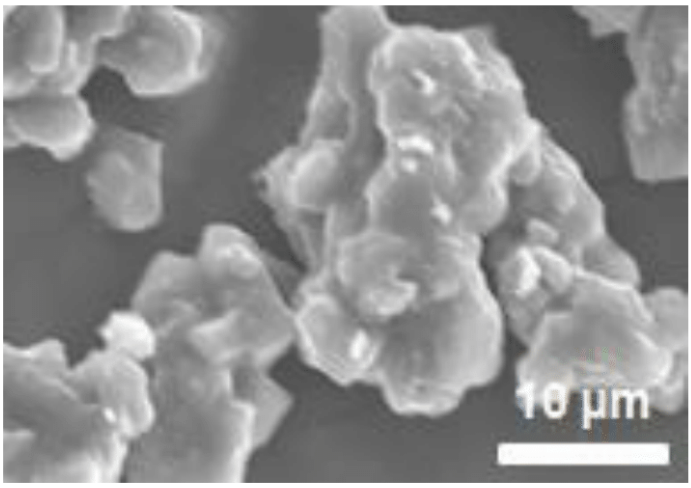

Figure S9. SEM image of γ-CD-MOFs at 92.5% RH after 1 d

S2. Adsorption kinetics

The Lagergren pseudo-first-order rate expression is one of the most widely used sorption rate equations for the sorption of a solute from a liquid solution. It may be represented as:

$$\frac{d_q}{d_t} = k_1(q_e - q_t) \quad (3)$$

$$\ln(q_e - q_t) = \ln q_e - k_1 t \quad (4)$$

where q_t is the amount of CAP sorbed at time t (mg· g^{-1}), q_e is the amount of CAP sorbed at equilibrium (mg· g^{-1}) and k_1 is the pseudo-first-order rate constant (min^{-1}). Equation (4) is derived from equation (3) by integrating for the boundary conditions t = 0 to t = t and q_t =0 to $q_t = q_e$.

The Ho-Mckay pseudo-second-order rate expression is (Qiu et al., 2015):

$$\frac{dq_t}{dt} = k_2(q_e - q_t)^2 \quad (5)$$

$$\frac{t}{q_t} = \frac{1}{k_2 q_e^{\,2}} + \frac{1}{q_e} t \quad (6)$$

where k_2 is the pseudo-second-order rate constant (g mg^{-1} min^{-1}). Equation (6) is derive from equation (5) by integrating for the boundary conditions t = 0 to t = t and q_t = 0 to $q_t = q_t$.

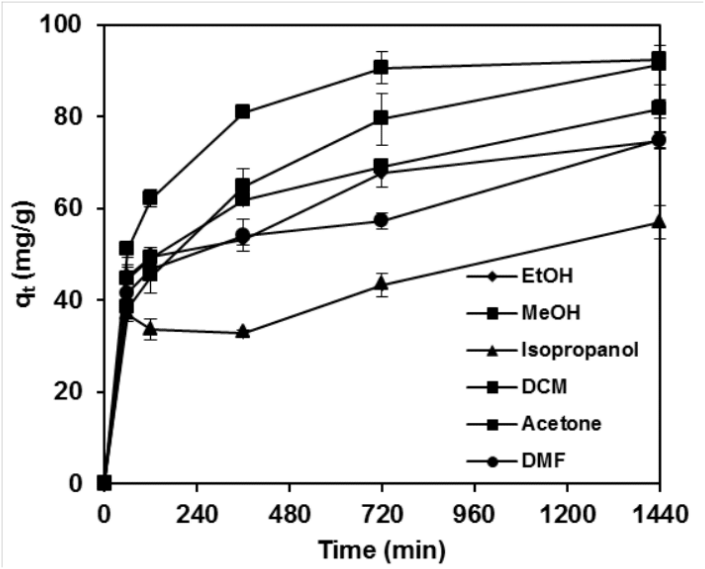

Figure S10. Effects of contacted time on the adsorption of CAP (400 $mg \cdot mL^{-1}$) onto γ-CD-MOFs with damaged crystallinity **(n=2)**

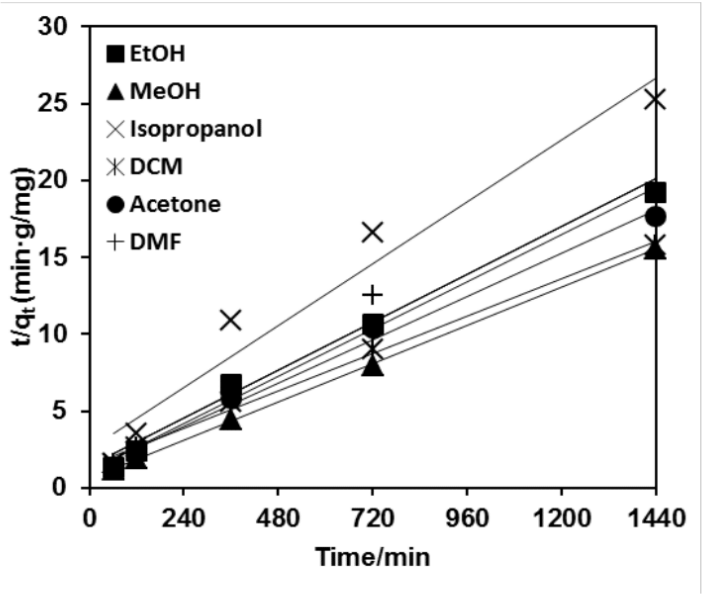

Figure S11. The fitting of pseudo-second-order kinetics of adsorptions for CAP onto γ-CD-MOFs with damaged crystallinity

Subchapter 3.2

Cyclodextrin-based metal-organic frameworks particles as efficient carriers for lansoprazole: study of morphology and chemical composition of individual particles

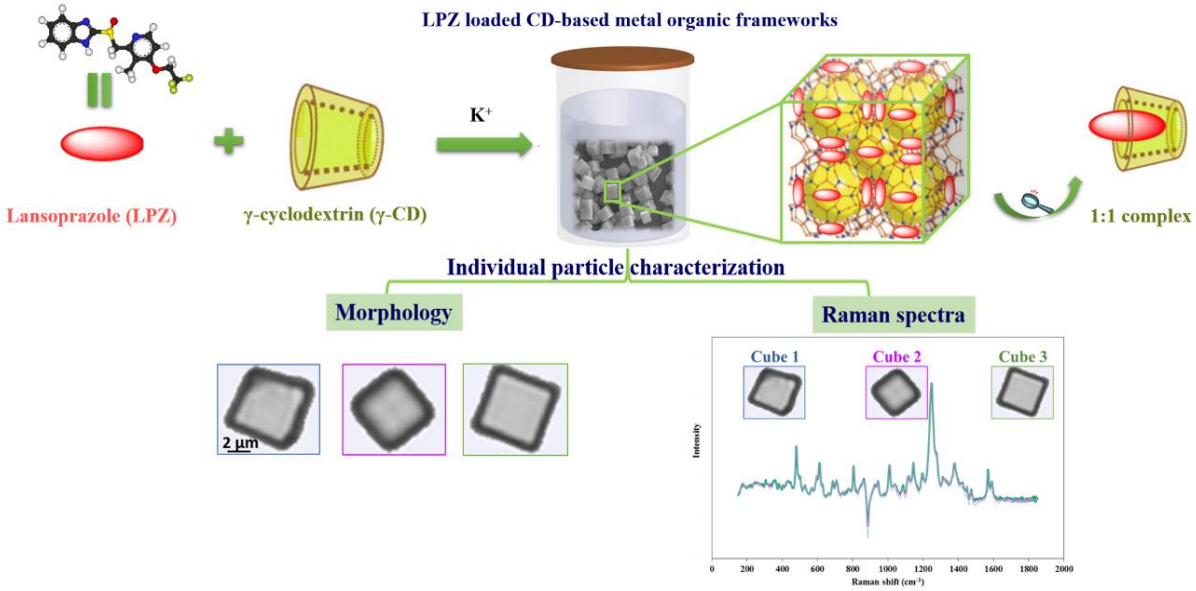

General Objectives and Author Contributions

In this subchapter, CD-MOFs around 6 μm with monodispersed size distribution were used as drug carrier for Lansoprazole (LPZ). The molecular dimensions of LPZ is about 4 × 17 Å, which fits to the dimensions of γ-CD cavity (7.8 Å) and the internal spherical cavities (17 Å) of CD-MOF.

In addition to drug absorption by impregnation shown in subchapter 3.1, a new approach was used in this subchapter for drug encapsulation, namely, co-crystallization. By impregnation approach, the obtained payloads were not as high as expected, at best around 12.6% (wt) in the case of captopril, possibly because the small pore windows of the CD-MOFs limit the penetration of drugs. Therefore, co-crystallization was used for LPZ, where the drug was added during particle synthesis. Remarkably, LPZ payloads reached 23.2±2.1% (wt) which corresponds to a molar ratio of 1:1 between LPZ and γ-CD.

To well characterize the LPZ loaded CD-MOFs, the study of morphology and chemical composition of individual particles was performed with Raman microscopy. It was demonstrated that there were no significant differences on Raman spectra of individual particles, indicating that each individual particle had identical chemical composition. Molecular modelling was performed for deeper insight into the interaction between the LPZ and CD-MOFs. Moreover, it was demonstrated that even after two years storage, the incorporated drug inside the CD-MOFs maintained its spectroscopic characteristics. This study lay the foundations for further application of CD-MOFs as LPZ carriers for drug delivery.

G Model
IJP 16704 No. of Pages 9

ARTICLE IN PRESS

International Journal of Pharmaceutics xxx (2017) xxx–xxx

Contents lists available at ScienceDirect

International Journal of Pharmaceutics

journal homepage: www.elsevier.com/locate/ijpharm

Cyclodextrin-based metal-organic frameworks particles as efficient carriers for lansoprazole: Study of morphology and chemical composition of individual particles

Xue Li[a,b], Tao Guo[b], Laurent Lachmanski[c], Francesco Manoli[d], Mario Menendez-Miranda[a], Ilse Manet[d], Zhen Guo[b], Li Wu[b], Jiwen Zhang[b,*], Ruxandra Gref[a,**]

[a] Institut des Sciences Moléculaires d'Orsay, UMR CNRS 8214, Paris-Sud University, Paris Saclay, 91400 Orsay, France
[b] Center for Drug Delivery System, Shanghai Institute of Materia Medica, Chinese Academy of Sciences, Shanghai 201203, China
[c] Malvern Instruments, 30 rue Jean Rostand, Orsay, 91405, France
[d] Istituto per la Sintesi Organica e la Fotoreattività, ISOF, CNR, via P. Gobetti 101, 40129 Bologna, Italy

ARTICLE INFO

Article history:
Received 31 March 2017
Received in revised form 22 May 2017
Accepted 23 May 2017
Available online xxx

Keywords:
Metal-organic frameworks
CD-MOF
γ-cyclodextrin
Raman spectroscopy
Nanoparticle
Individual particle characterization

ABSTRACT

Cyclodextrin-based metal-organic frameworks (CD-MOFs) represent an environment-friendly and biocompatible class of MOFs drawing increasing attention in drug delivery. Lansoprazole (LPZ) is a proton-pump inhibitor used to reduce the production of acid in the stomach and recently identified as an antitubercular prodrug. Herein, LPZ loaded CD-MOFs were successfully synthesized upon the assembly with γ-CD in the presence of K^+ ions using an optimized co-crystallization method. They were characterized in terms of morphology, size and crystallinity, showing almost perfect cubic morphologies with monodispersed size distributions. The crystalline particles, loaded or not with LPZ, have mean diameters of around 6 μm. The payloads reached 23.2 ± 2.1% (wt) which corresponds to a molar ratio of 1:1 between LPZ and γ-CD. It was demonstrated that even after two years storage, the incorporated drug inside the CD-MOFs maintained its spectroscopic characteristics. Molecular modelling provided a deeper insight into the interaction between the LPZ and CD-MOFs. Raman spectra of individual particles were recorded, confirming the formation of inclusion complexes within the tridimensional CD-MOF structures. Of note, it was found that each individual particle had the same chemical composition. The LPZ-loaded particles had remarkable homogeneity in terms of both drug loading and size. These results pave the way towards the use of CD-MOFs for drug delivery purposes.

1. Introduction

Metal Organic Frameworks (MOFs) have recently emerged as crystalline porous materials of interest for biomedical applications, with potential applications in drug delivery and imaging. Their high porosity, large surface areas, and versatility in terms of composition and functionalities make the MOFs particularly appealing for the incorporation of high drug payloads (Della Rocca et al., 2011; Horcajada et al., 2012; Li and Huo, 2015). Many efforts have been carried out to synthesize biocompatible MOFs using endogenous linkers or pharmaceutical acceptable excipients (McKinlay et al., 2010; Sontz et al., 2015; Su et al., 2015).

In particular, γ-cyclodextrin (γ-CD), a naturally available oligosaccharide enzymatically produced from starch, was used as a ligand to synthesize environment-friendly and biocompatible MOFs (Li et al., 2007). Advantageously, γ-CDs form inclusion complexes with a variety of drugs (Challa et al., 2005; Davis and Brewster, 2004). The γ-CD based metal-organic frameworks (CD-MOFs) were synthesized from γ-CD and K^+ ions employing a vapor diffusion method (Smaldone et al., 2010; Forgan et al., 2012; Furukawa et al., 2012;). It is widely recognized that size and polydispersity are crucial parameters in the design of drug delivery systems. In the originally reported synthesis (Smaldone et al., 2010), the size of CD-MOF crystals was around 200–400 μm. It was

* Corresponding authors at: Center for Drug Delivery Systems, Shanghai Institute of Materia Medica, Chinese Academy of Sciences, No. 501 of Haike Road, Shanghai 201203, China.
** Corresponding author at: Institut Sciences Moléculaires Sciences d'Orsay, (UMR CNRS 8214), Université Paris-Sud, Université Paris-Saclay, 91400 Orsay, France.
E-mail addresses: jwzhang@simm.ac.cn (J. Zhang), ruxandra.gref@u-psud.fr (R. Gref).

http://dx.doi.org/10.1016/j.ijpharm.2017.05.056
0378-5173/

then discovered that the addition of cetyltrimethyl ammonium bromide (CTAB) in the preparation enabled the formation of smaller crystals (1–10 μm). Eventually, nanocrystals (200–300 nm) could be obtained by the addition of both CTAB and methanol during the synthesis procedure (Furukawa et al., 2012).

CD-MOFs with controlled sizes have shown their usefulness to incorporate molecules of interest (Michida et al., 2015; Moussa et al., 2016; Liu et al., 2016; Smaldone et al., 2010; Liu et al., 2017), including anti-inflammatory drugs (e.g., furbiprofen, fenbufen, ketoprofen and piroxicam), angiotensin converting enzyme inhibitors (e.g., captopril), food additives (e.g., curcumin, and sucralose), dyes (e.g., 4-phenylazophenol and rodamine B), and various pharmaceutical ingredients (e.g., salicylic acid, ferulic acid, and pseudolaric acid B). Drugs were loaded by impregnation in CD-MOFs (Moussa et al., 2016; Liu et al., 2016; Smaldone et al., 2010), but the obtained payloads were at best around 12.6% (wt) in the case of captopril (Liu et al., 2016), possibly because the small pore windows of the CD-MOFs limits drug penetration. The co-crystallization approach, where the drug was added during particle synthesis, enabled reaching higher payloads of 18.5% (wt) and 12.7% (wt) in the case of rhodamine B and ferulic acid, respectively (Smaldone et al., 2010).

Our aim here was to design CD-MOFs containing high payloads of lansoprazole (LPZ), a proton-pump inhibitor used to reduce the production of acid in the stomach and recently identified as an antitubercular prodrug targeting cytochrome bc1 (Rybniker et al., 2015). The administration of this drug is challenging because of its instability and strong tendency to crystallize. CD-MOFs were propose as carriers able to avoid drug degradation and crystallization over long-term storage. Crystalline LPZ-loaded CD-MOF with homogeneous sizes of around 6 μm were successfully synthesized *via* co-crystallization, showing cubic morphologies. The sizes are compatible with an oral or pulmonary administration as dry powder. LPZ payloads determined by both elemental analysis and HPLC, reached 23.2% (wt). To the best of our knowledge, these are the highest loadings reported so far with CD-MOFs.

Characterization studies on drug-loaded particles are currently performed on batches, but not on individual particles. By this way, no information can be drawn on the homogeneity of the particles in terms of drug incorporation. Indeed, each particle is unique in size, morphology and composition. For biomedical applications it is of outmost importance to gain insights on the quality of preparations, by analyzing individual particles to determine their size, morphology, crystallinity and chemical composition. To address this goal, Raman microscopy, which takes the advantages of both Raman spectroscopy and optical microscopy, was used here as a versatile powerful tool to record the morphologies and Raman spectra of individual MOF crystals.

2. Experimental

2.1. Materials and reagents

The chemical compounds, γ-CD, potassium hydroxide (KOH), cetyltrimethyl ammonium bromide (CTAB), isopropanol, trimethylamine, phosphoric acid, ethanol and methanol were purchased from Sinopharm Chemical Reagent Co. Ltd (France). Lansoprazole (LPZ) was provided by Zhuhai Rundu Co. Ltd (China). All chemicals were of analytical grade. Pure water used in all experiments was filtered (18.4 MΩ cm) by a Milli-Q system (Millipore, Milford, MA, USA).

2.2. Synthesis of CD-MOFs

CD-MOF crystals were synthesized by a modified methanol diffusion method as previously reported (Liu et al., 2016). The crystals were prepared by reacting γ-CD (0.125 mM) with 200 mM KOH in aqueous solution. The solution was then filtered through a 0.45 μm membrane into a glass vial followed by methanol diffusion at room temperature for several days until first crystals formed. CD-MOF obtained in this stage were named CD-MOF-1. To obtain monodispersed CD-MOF crystals, the supernatant was transferred into another glass tube with the addition of CTAB (8 mg mL^{-1}), which could trigger the rapid precipitation of CD-MOF crystals and then the suspension was incubated at room temperature for 3 h. The precipitate was harvested, washed thrice with isopropanol and finally dried at 50 °C overnight under vacuum to collect the CD-MOF crystals of about 5–10 μm, namely CD-MOF-2.

2.3. Synthesis of LPZ loaded CD-MOFs

LPZ-loaded CD-MOF crystals were synthesized in a similar way as empty CD-MOF. Briefly, the crystals were prepared by mixing LPZ (81.3 mM), γ-CD (0.125 mM) and KOH (200 mM) in 5.0 mL aqueous solution. The solution was filtered through a 0.45 μm organic filter membrane into a glass tube followed by methanol vapor diffusion for 24 h. The synthesized LPZ-loaded CD-MOF crystals were harvested by filtering through a 1.0 μm membrane and then washed with ethanol three times to remove the free drugs on the surface of the particles. After that, the drug loaded particles were dried at 50 °C under vacuum overnight. The LPZ loaded CD-MOF particles obtained in this stage were named LPZ/CD-MOF-1.

The supernatant was transferred into a new tube with the addition of CTAB (8 mg/mL) and incubated at room temperature for 3 h. The formed LPZ loaded CD-MOF crystals, namely LPZ/CD-MOF-2, were washed thrice with ethanol and dried at 50 °C overnight under vacuum.

The CD-MOFs loaded or not with LPZ were stored at room temperature in closed vials up to two years.

2.4. Characterization of CD-MOF crystals with or without LPZ

Morphological characterization of CD-MOF crystals with or without LPZ was conducted by SEM (S-3400N, Hitachi) and Raman microscopy (Morphologi G3-ID, Malvern®, Orsay). For SEM investigations, the particles were immobilized with an adhesive tape on a metal stub and then coated with gold. For Raman microscopy, the particles were spread on a slide and optical images of more than 2500 individual particles were captured automatically. Statistical analysis of sizes and morphologies was carried out using Morphologi software.

Crystallinity of the samples was characterized by X-ray powder diffraction (XRPD) analysis. Diffraction patterns of the samples were detected on an advance diffractometer (Bruker D8, Bruker, Germany). The detection was performed at ambient temperature, with tube current of 40 mA. Monochromatized CuKα radiation was used to irradiate the samples. The diffraction data was collected at a 2θ angle range of 3–40° with the stepwise scan mode of 8°/min on a diffractometer (X/Pert Pro 3040/60, PANalytical, Holland).

Chemical composition of individual CD-MOF crystals with or without LPZ were characterized by Raman microscopy. Raman spectra were obtained from 100 to 1900 cm^{-1}. As control, Raman spectrum of LPZ powder was also performed.

Drug payload is defined as the weight percentage of drug in the drug-loaded CD-MOF and was calculated using Eq. (1):

$$Payload\ (\%) = \frac{Encapsulated\ Drug\ (mg)}{Drug\ loaded\ CD-MOF\ (mg)} \times 100 \quad (1)$$

Elemental analysis allowed obtaining the drug payload of CD-MOF particles, which was further confirmed by HPLC-UV-vis method.

To analyze the amounts of the drugs by HPLC, 6.0 mg of the samples were dissolved in water (3 mL) and filtered using a 0.22 μm membrane. The analysis was carried out by HPLC (Agilent 1290, USA) using a Phenomenex C18 column (4.6 mm × 150 mm, 5 μm) with a flow rate of 1.0 mL min^{-1} and an injection volume of 20 μL. LPZ was detected at 284 nm with the column temperature of 40 °C. The mobile phase was composed of methanol, water, triethylamine and phosphoric acid (640:360:5:1.5, pH was adjusted to 7.3 with phosphoric acid).

2.5. Molecular simulation

Molecular simulation of LPZ loaded CD-MOF was carried on to gain insights into the interaction between LPZ and CD-MOFs. The crystal structure of empty CD-MOF was extracted from the single crystal structure of MOF-1 in literature (Forgan et al., 2012).

In the docking model, an expanded non-periodic structure was used, in which the OH^- ion was replaced by H_2O and the K^+ ion was deleted since it doesn't affect the rigid docking results. The structure of LPZ molecule was built using the Materials Visualizer module in Materials Studio (MS, Accelrys Inc.) 7.0. The Forcite module in MS was employed to perform minimization and molecular dynamics (MD) simulation. The docking program AutoDock Vina 1.1.2 was used for automated molecular docking calculation (Trott and Olson, 2010).

In order to have a deep insight of the interaction between LPZ and γ-CD in different forms, docking protocol was separately executed for LPZ and γ-CD in four models:

1) one LPZ molecule and dual-γ-CD unit (D-γ-CD) which was extracted from MOF model, namely 1:2 (LPZ: D-γ-CD) complex; 2) two LPZ molecules and D-γ-CD from CD-MOF model, namely 2:2 (LPZ: D-γ-CD) complex; 3) two LPZ molecules and two γ-CD model, namely 2:2 (LPZ: γ-CD) complex; and 4) one LPZ molecule and a single γ-CD model, namely 1:1 (LPZ: γ-CD) complex. The docking results with relatively low energy were used for the energy optimization and MD simulation. In MD protocols, C and O in CD-MOF model were fixed and the COMPASS II force field was adopted. NVT ensemble and Berendsen temperature control methods were employed for a total period of 50 ps. All the models were performed in vacuum. The non-bond cutoff distance of 18.5 Å, spline width of 1.0 Å, and buffer width of 0.5 Å were applied respectively. For minimization, an algorithm was employed to converge the total energy of the system to less than 2.0×10^{-5} kcal mol^{-1}, the residual force to less than 0.001 kcal mol^{-1} $Å^{-1}$, the displacement of atoms to less than 1×10^{-5} Å. In the auto dock protocol, a Lamarckian Genetic Algorithm (LGA) in combination with a grid-based energy evaluation method was used for pre-calculating grid maps according to the interatomic potentials of all atom types presenting in the host and guest molecules, including the Lennard-Jones potentials for Van der Waals interactions and Coulomb potentials for electrostatic interactions. A grid map with dimensions of 35 Å × 35 Å × 35 Å and a grid spacing of 0.375 Å, was placed to cover CD-MOF for the first LPZ modelling. In order to perform the modelling with two LPZ molecules (the case of 2:2 (LPZ: D-γ-CD) complex and 2:2 (LPZ: γ-CD) complex), a second grid map of 21 Å × 21 Å × 21 Å, with a grid spacing of 0.375 Å, was placed to cover the D-γ-CD and CD-MOF structure. Thanks to AutoDockTools, the atomic partial charges were calculated by the Gasteiger-Marsili method. The parameters used for global search were an initial population of 50 individuals, with a maximal energy evaluations number of 1,500,000 and a maximal number generations of 50,000 as an end criterion. Other docking parameters were set as default. The final optimized model was used for presentation.

2.6. Spectroscopic study

Ultraviolet absorption spectra were recorded on Perkin-Elmer Lambda 950 spectrophotometer using an integrating sphere. 1 cm

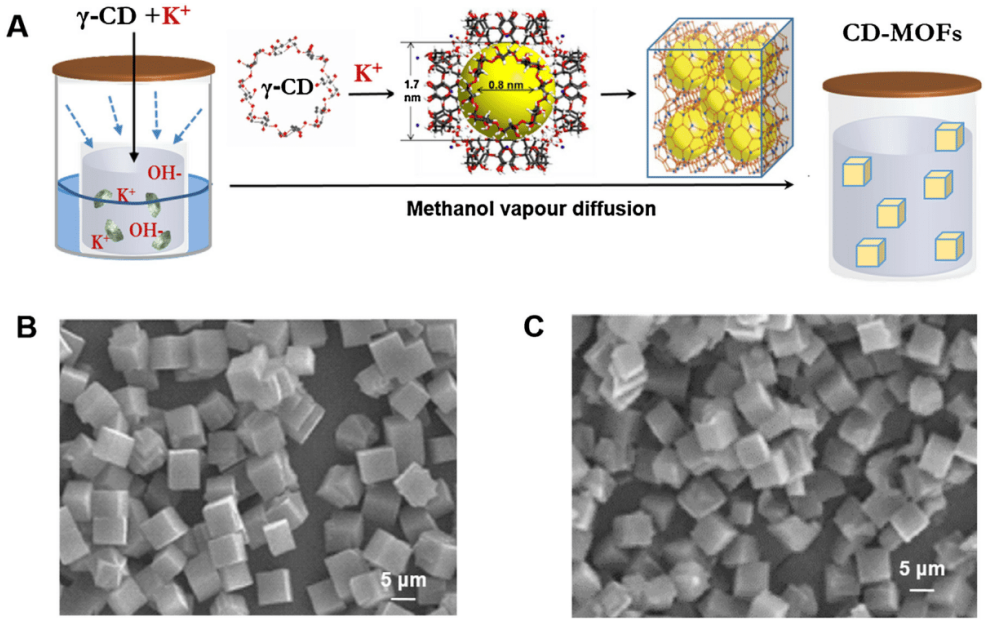

Fig. 1. Schematic representation of CD-MOF synthesis and structure (A). SEM micrographs of CD-MOF-2 (B) and LPZ/CD-MOF-2 (C).

cuvettes were used and water or alcohol solutions were used a reference. Fluorescence spectra were measured on an Edinburgh FLSP920 spectrofluorometer with excitation at 280 nm registering spectra with 1 nm steps and 0.5 or 1 s dwell time. Slits were kept narrow to 2 or 4 nm band width in excitation and emission. Right angle detection was used. All the fluorescence measurements were carried out at 295 K in 1 cm quartz cuvettes. Steady-state fluorescence spectra were registered in air-equilibrated solutions. The measurements were performed on freshly prepared solutions.

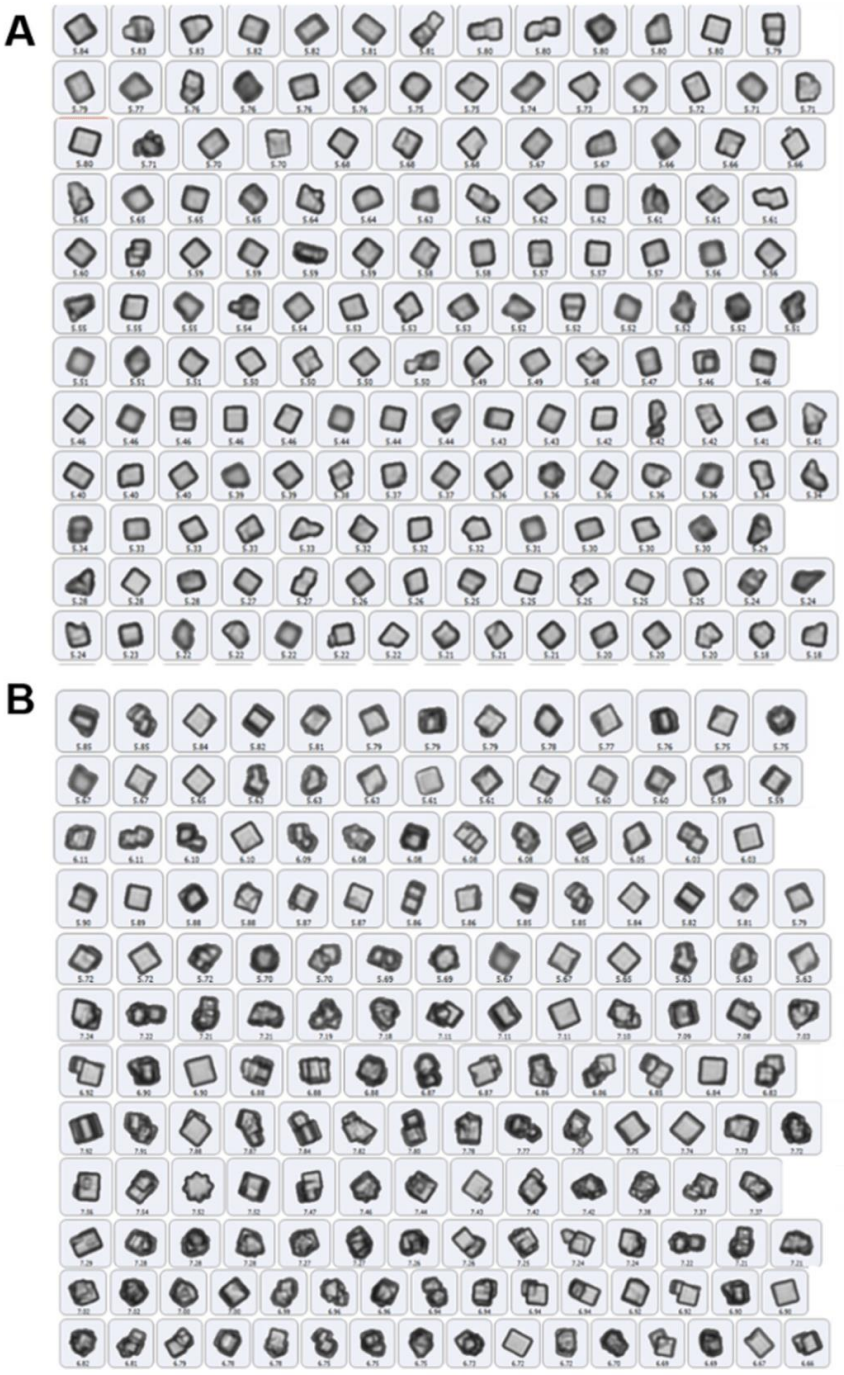

Fig. 2. Typical images of CD-MOF-2 (A) and LPZ/CD-MOF-2 (B) with an LPZ payload of 23% (wt) obtained with a Raman microscope by analyzing more than 2500 particles.

Fluorescence lifetimes were measured in air-equilibrated solutions with a time correlated single photon counting system (IBH Consultants Ltd.). A nanosecond LED source of 278 nm was used for excitation and the emission was collected at right angle at 320 nm (bandwidth 8 nm). The software package for the analysis of the emission decays was provided by IBH Consultants Ltd. Fluorescence intensity decay profiles I(t) were fitted using a monoexponential function and deconvolution of the instrumental response function. Fitting yields the lifetime τ_i and pre-exponential factor a_i of the emitting species were calculated:

$$I(t) = \sum_i a_i \times \exp(-t/\tau_i) \quad (2)$$

3. Results and discussions

3.1. Synthesis and morphological characterization of LPZ loaded CD-MOFs

CD-MOF crystals were successfully obtained by adapting a vapor diffusion method (Smaldone et al., 2010). As shown in Fig. 1A, the spontaneous coordination of alkali metal cations and γ-CD generates $(\gamma\text{-CD})_6$ units which further assemble, by regular repetition, into a body-centered cubic packing architecture with mesoporous pores (Fig. 1A, yellow) having a diameter of 17 Å delimited by the γ-CDs cavities of 7.8 Å in diameter.

The synthesized CD-MOFs are cubic crystals (Fig. 1B) in agreement with previously published data (Liu et al., 2016; Smaldone et al., 2010; Smith et al., 2015). The addition of CTAB during the synthesis produced CD-MOF cubes (namely, CD-MOF-2) with homogeneous sizes of around 6 μm (Fig. 1B). On the contrary, the CD-MOF-1 synthesized in the absence of CTAB had a broad size distribution, ranging from 1 to 200 μm (Fig.S1A). Remarkably, LPZ-loaded CD-MOFs (LPZ/CD-MOF-2) synthesized with CTAB presented both the same size (~6 μm) and cubic morphology as their non-loaded analogues (Fig. 1C).

To gain a deep understanding on the structural patterns of the synthesized CD-MOFs, a morphological characterization of individual particles was performed by Raman microscopy. More than 2500 individual empty particles (CD-MOF-2) and drug loaded ones (LPZ/CD-MOF-2) were observed.

The morphology of the particles obtained by Raman microscopy (Fig. 2A and B) was in agreement with that observed by SEM (Fig. 1B and C). Regular cubic structures were observed in all cases. Moreover, from the statistical analysis of all the particles observed, it was determined that the average size of CD-MOF-2 cubes was 6.5 ± 1.8 μm (Fig. 2C). Similar sizes (6.7 ± 2.3 μm) were obtained in the case of LPZ/CD-MOF-2 cubes (Fig. 2C). These data confirm the previous SEM studies, showing that LPZ incorporation in the CD-MOFs did not significantly affect their morphology.

Quantification of S and N content in the LPZ/CD-MOF-1 and LPZ/CD-MOF-2 crystals by elemental analysis enabled determining their payload which reached 21.4 ± 2.3% (wt) and 23.2 ± 2.1% (wt), respectively. The payloads of 20.8 wt% correspond to a 1:1 molar ratio between the incorporated LPZ molecules and the CDs in CD-MOFs. These results clearly show the excellent affinities of LPZ for the CD-MOFs. Of interest, the presence of CTAB during the synthesis of the particles did not affect their LPZ loadings. To the best of our knowledge, the obtained loadings are the highest reported so far with CD-MOFs.

Complementary HPLC analysis were performed, enabling determining LPZ payloads in CD-MOFs of 22.3 ± 1.9% (wt) which are in good agreement with the results of elemental analysis.

The crystallinity of the particles was investigated by XRPD (Fig. 3B). The diffraction patterns of CD-MOFs were in good agreement with previously reported data (Smaldone et al., 2010) and there was no significant difference in the drug loaded particles (LPZ/CD-MOF-2) and empty particles (CD-MOF-2) (Fig. 3B). The peaks corresponding to the crystalline LPZ were not observed in the LPZ/CD-MOFs showing that the drug was incorporated in amorphous state. It was previously shown that incorporation of drugs with high tendency to crystallize is very challenging as the drugs might form crystals difficult to be separated from the drug-loaded particles (Layre et al., 2005; Nikolakakis et al., 2000).

The study was completed with a spectroscopic approach to investigate the stability of the incorporated LPZ. Indeed, it was reported that LPZ rapidly degrades in water or in the presence of moisture (Della Greca et al., 2006). The LPZ/CD-MOF-2 particles stored up to two years were dissolved in large volumes of ethanol or water and absorption and fluorescence spectra were recorded and compared to the ones of free LPZ. CD-MOF did not emit at all in the studied regions. The extracted drug had similar spectra as the free drug (Fig. 4) except for a small red shift of 3 nm in the MOFs (Fig. 4A). On the contrary, solutions of LPZ in water protected from light degraded after 48 h storage at room temperature (Fig. 4A) as already reported (Shin et al., 2004).

The fluorescence lifetimes in ethanol, for excitation at 278 nm, were 3.88 ns for free LPZ and 3.87 ns for the drug extracted from the LPZ/CD-MOF-2 particles. The identical spectra and lifetimes tend to indicate that the drug was not degraded upon incorporation and storage in CD-MOFs. However, further studies would be needed to support this hypothesis.

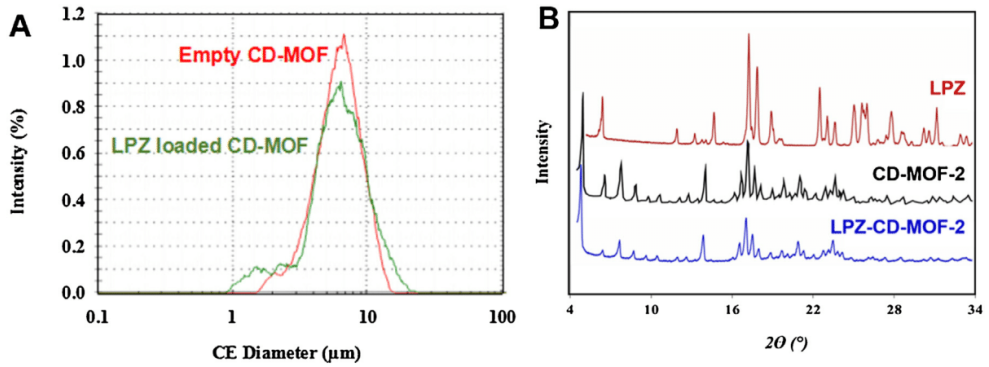

Fig. 3. Size distributions (A) and crystallinity (B) of empty CD-MOF, and LPZ/CD-MOF with 23% (wt) drug loading. Size distributions were obtained after statistical analysis of 2500 particles by Raman microscopy.

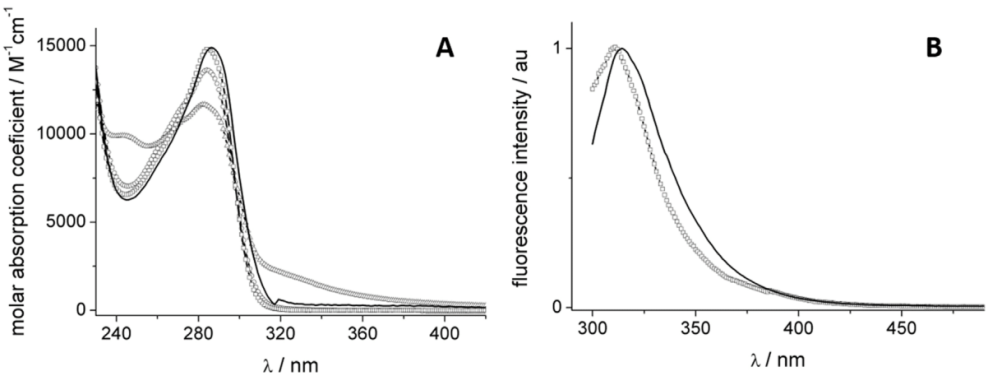

Fig. 4. A. Absorption spectra of LPZ in EtOH (squares) and LPZ/CD-MOFs in EtOH (black line) and water, fresh solution (circles) and after 48 h (triangles); B. fluorescence spectra of LPZ (squares) and LPZ/CD-MOFs (black line) in EtOH, λ_{exc} = 270 nm.

3.2. Molecular simulation

Previous data showed a high interaction between LPZ and CD-MOFs and the loadings correspond to a molar ratio of 1:1 between the drug and the CDs in CD-MOFs. For a deeper insight into the interaction between LPZ and CD-MOFs, molecular simulations were performed with a molar ratio between LPZ and γ-CD of 1:1. The crystal structure of CD-MOF was simulated using the method previously reported (Forgan et al., 2012). In the crystal structure of CD-MOF (Fig. 1A), K^+ ions coordinated with single α-1,4-linked D-gluco-pyranosyl residues in γ-CD and formed $(\gamma\text{-CD})_6$ units which constituted the sides of the cubic chamber, where the primary faces of the unit pointed inwards and the secondary faces outwards. All the γ-CD in this structure faced with another γ-CD which is from its adjacent $(\gamma\text{-CD})_6$ units, forming a dual γ-CD channel (D-γ-CD). The simulation showed that the hydrophilic large CD-MOF pores (Fig. 1A, yellow) were not suitable to host the LPZ molecules, which preferred to insert in the γ-CD cavities of the CD-MOFs (Fig. 5) (for further details see SI Section I.2).

The interaction between LPZ and the D-γ-CD unit in CD-MOF was further investigated by extracting the D-γ-CD unit structure from that of CD-MOF (Forgan et al., 2012). Since the γ-CD in CD-MOF was coordinated with K+ ions, the D-γ-CD unit was more compacted inside CD-MOF crystals than in solution (Fig. 6A). When one LPZ molecule was loaded in this compacted as D-γ-CD unit, molecular simulations showed that the drug molecule located in the channel formed between the two γ-CDs interacting with both cavities (Fig. 6A) and the calculated binding energy was −24.09 kcal mol-1. When two LPZ molecules were inserted in the same compacted D-γ-CD unit (corresponding to the molar ratio of 2:2 between γ-CD and LPZ), it was found that each drug molecule located in one γ-CD cavity (Fig. 6B).

The binding energy in this case was −71.40 kcal mol-1. It is interesting to point out that this binding energy of 2:2 (LPZ: D-γ-CD) complexes was more than twice higher than the energy for of 1:2 (LPZ: D-γ-CD) complexes. This suggests that the 2:2 structure is more stable than the 1:2 one structure.

The single LPZ molecule inside the D-γ-CD unit was bended, with the benzo imidazole and pyridine moieties interacting with the CDs. Similar interactions took place when molecular simulations were performed with two LPZ molecules interacting with two γ-CDs (Fig. 6C). In all studies studied cases, LPZ interacted with the γ-CD cavities and adopted a bended conformation.

3.3. Raman spectra of individual CD-MOF crystals

Raman microscopy is a versatile technique combining both the advantages of Raman spectroscopy and microscopy. It enables investigating thousands of individual particles to gain insights on their morphology and composition. Typical Raman spectra of CD-MOF crystals containing or not LPZ were recorded and compared to the spectra of LPZ and CD (Fig. 7A).

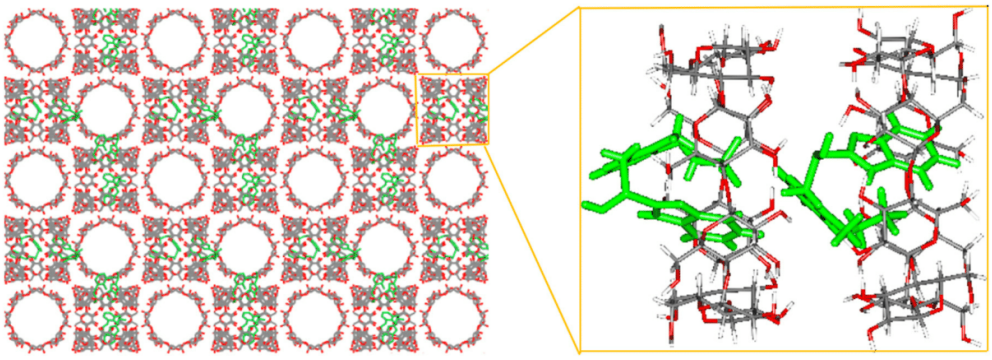

Fig. 5. Molecular model of LPZ loaded CD-MOF at the proportion of γ-CD and LPZ as 1:1 after docking and optimization.

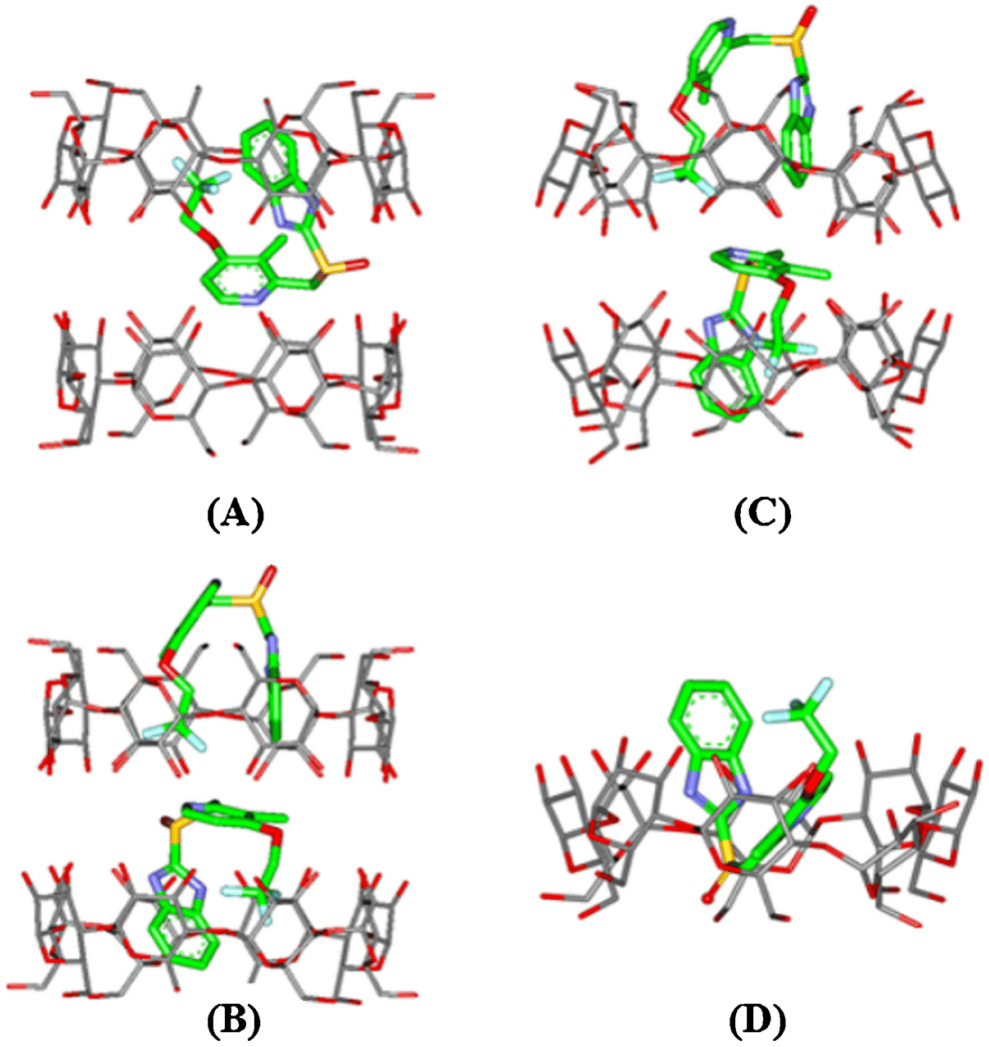

Fig. 6. Final configuration after optimization. (A):1:2 (LPZ: D-γ-CD) complex; (B):2:2 (LPZ: D-γ-CD) complex; (C): 2:2 (LPZ: γ-CD) complex (D):1:1 (LPZ: γ-CD) complex with other atoms deleted.

The Raman spectrum of CD-MOF crystals is very similar to the γ-CD one, presenting a main peak at 480 cm^{-1} corresponding to skeletal vibrations of α-1,4 glyosidic bonds. The peaks corresponding to the CDs were well detected in the CD-MOFs loaded with LPZ, together with the peaks corresponding to the LPZ. This is another evidence of the effective drug entrapment. Moreover, it was observed that some of the LPZ peaks were shifted upon incorporation in the CD-MOFs suggesting that interactions took place in the studied system (Fig. 7A), There were no significant shifts in the 1200 cm^{-1} region (peaks highlighted in blue in Fig. 7A). However, all the LPZ peaks in the region of 1600 to 1400 cm^{-1} corresponding to C—C cycle ring stretching (benzo imidazole and pyridine moieties) were shifted. This was also the case with the LPZ C—N stretching bands from 1328 to1266 cm^{-1}. These peaks were shifted very probably because of the interactions taking place between CD and LPZ. This assumption was further confirmed by the decrease in intensity of the specific ring stretches of the pyridine moiety under 1200 cm^{-1}, including the band at 600 cm^{-1} (in plane ring mode) and the peak at 1000 cm^{-1} (symmetric ring breathing shifting and broadening). In a nutshell, the Raman investigations confirmed the effective LPZ incorporation in CD-MOFs and suggested an interaction between γ-CD and LPZ, more specifically between the CDs and the benzo imidazole and pyridine moieties of LPZ. These experimental findings corroborate well the simulation experiments which showed that upon the spontaneous formation of inclusion complexes between LPZ and CDs, the drug molecules were bended interacting with the CD cavities mainly through their benzo imidazole and pyridine moieties.

In addition to the confirmation of the interactions between the drug and its carrier, it was of particular interest to investigate the composition of individual particles. Fig. 7B presents typical Raman spectra of several randomly chosen individual LPZ/CD-MOF-2 particles. Remarkably, the spectra perfectly superimposed, confirming the high homogeneity in terms of drug loading of the

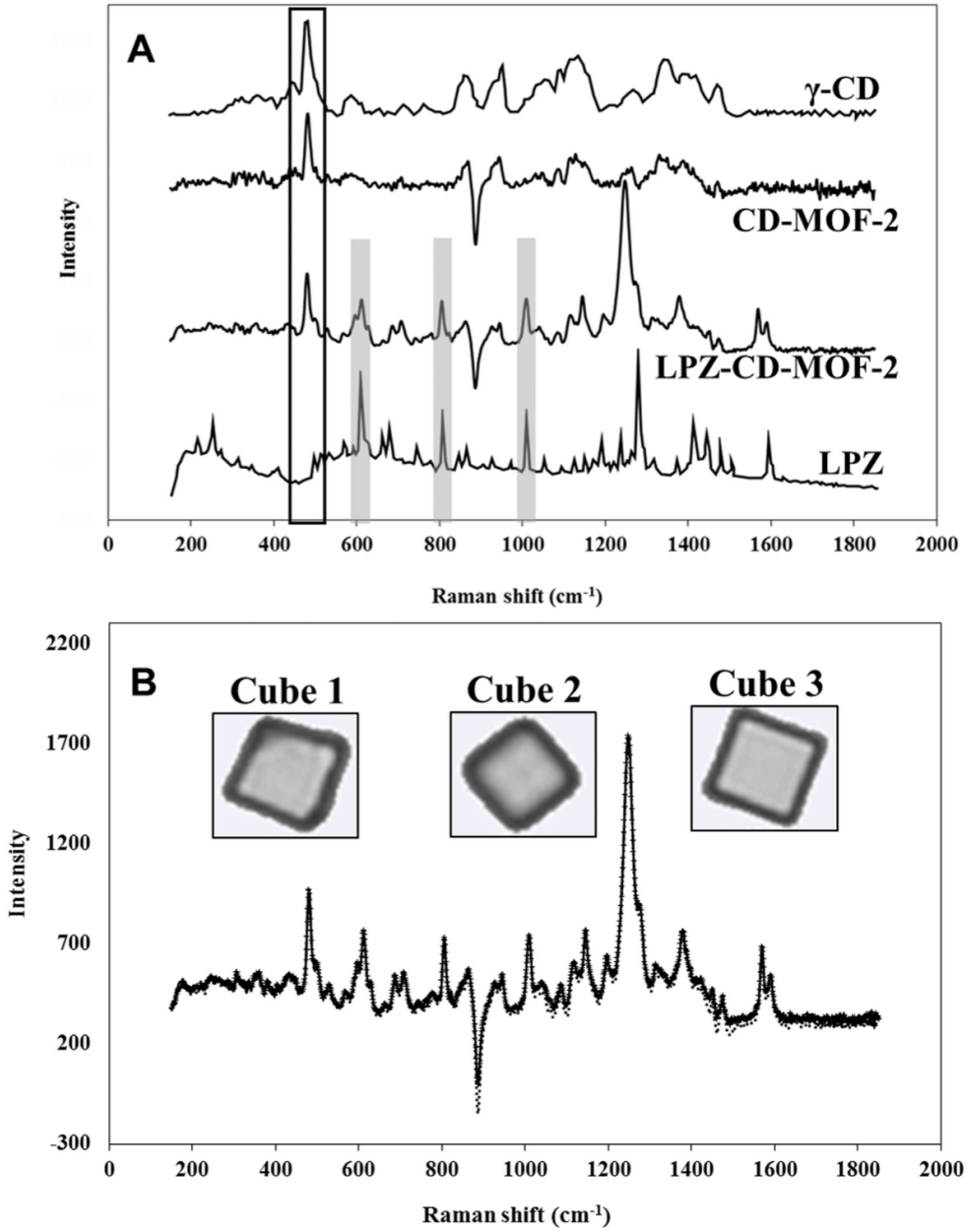

Fig. 7. A. Raman spectra of γ-CD, empty CD-MOF, LPZ loaded CD-MOF, LPZ powder; B. Raman spectra of three different individual LPZ loaded CD-MOF cubes: cube 1 (dotted line); cube 2 (black line); cube 3 (crosses).

synthesized LPZ/CD-MOF-2 particles through the co-crystallization method.

It is worth pointing out that currently, investigations of drug loading are carried on using batches of particles, but not on individual ones. For example, chromatographic, spectroscopic and elemental analysis methods are quantitative and precise, but they provide average information on the global drug payloads. Herein, the Raman spectra on individual particles gave new insights of the CD-MOF composition.

4. Conclusion

LPZ-loaded CD-MOFs were successfully synthesized, obtaining cubic crystals with an uniform size of around 6 μm. Drug payloads as high as 23.2 wt% were obtained and results indicated that each CD in the CD-MOFs was able to host one drug molecule. Structural and chemical characterizations of individual particles were performed by Raman microscopy. Remarkably, each particle had the same composition corresponding to a molar ratio LPZ: γ-CD of

1:1. This study paves the way for the applications of CD-MOFs as LPZ carriers for drug delivery.

Acknowledgements

We are grateful for the financial support from the ANR-14-CE08-00177 project, the FP7-PEOPLE-ITN-2013 "Cyclon Hit" project (N° 608407) and from Natural Science Foundation of China (81430087). This work was supported by a public grant overseen by the French National Research Agency (ANR) as part of the "Investissements d'Avenir" program (Labex NanoSaclay, reference: ANR-10-LABX-0035). X. Li acknowledges support from China scholarship council (CSC, N° 201408330166). We acknowledge Dr. Haiyan Li, Dr. Samir Safi, Pr. Ines Ramos, and Pr. Nicola Woodroofe for helpful discussions.

Appendix A. Supplementary data

Supplementary data associated with this article can be found, in the online version, at http://dx.doi.org/10.1016/j.ijpharm.2017.05.056.

References

Challa, R., Ahuja, A., Ali, J., Khar, R.K., 2005. Cyclodextrins in drug delivery: an updated review. AAPS PharmSciTech. 6, 329–357.
Davis, M.E., Brewster, M.E., 2004. Cyclodextrin-based pharmaceutics: past, present and future. Nat. Rev. Drug Discov. 3, 1023–1035.
Della Greca, M., Iesce, M.R., Previtera, L., Rubino, M., Temussi, F., Brigante, M., 2006. Degradation of lansoprazole and omeprazole in the aquatic environment. Chemosphere 63, 1087–1093.
Della Rocca, J., Liu, D., Lin, W., 2011. Nanoscale metal-organic frameworks for biomedical imaging and drug delivery. Acc. Chem. Res. 44, 957–968.
Forgan, R.S., Smaldone, R.A., Gassensmith, J.J., Furukawa, H., Cordes, D.B., Li, Q., Wilmer, C.E., Botros, Y.Y., Snurr, R.Q., Slawin, A.M.Z., Stoddart, J.F., 2012. Nanoporous carbohydrate metal–organic frameworks. J. Am. Chem. Soc. 134, 406–417.
Furukawa, Y., Ishiwata, T., Sugikawa, K., Kokado, K., Sada, K., 2012. Nano- and microsized cubic gel particles from cyclodextrin metal-organic frameworks. Angew. Chem. Int. Ed. 51, 10566–10569.
Horcajada, P., Gref, R., Baati, T., Allan, P.K., Maurin, G., Couvreur, P., Férey, G., Morris, R., Serre, C., 2012. Metal organic frameworks in biomedicine. Chem. Rev. 112, 1232–1268.
Layre, A.M., Gref, R., Richard, J., Requier, D., Chacun, H., Appel, M., Domb, A.J., Couvreur, P., 2005. Nanoencapsulation of a crystalline drug. Int. J. Pharm. 298, 323–327.
Li, S., Huo, F., 2015. Metal–organic framework composites: from fundamentals to applications. Nanoscale 7, 7482–7501.
Li, Z., Wang, M., Wang, F., Gu, Z., Du, G., Wu, J., Chen, J., 2007. γ-Cyclodextrin: a review on enzymatic production and applications. Appl. Microbiol. Biotechnol. 77, 245–255.
Liu, B., Li, H., Xu, X., Li, X., Lv, N., Singh, V., Stoddart, J.F., York, P., Xu, X., Gref, R., Zhang, J., 2016. Optimized synthesis and crystalline stability of γ-cyclodextrin metal-organic frameworks for drug adsorption. Int. J. Pharm. 514, 212–219.
Liu, B., He, Y., L, Han, Singh, V., Xu, X., Guo, T., Meng, F., Xu, X., York, P., Liu, Z., Zhang, J., 2017. Microwave-assisted rapid synthesis of γ γ-cyclodextrin metal–organic frameworks for size control and efficient drug loading. Cryst. Growth Des 17, 1654–1660. doi:http://dx.doi.org/10.1021/acs.cgd.6b01658.
McKinlay, A.C., Morris, R.E., Horcajada, P., Férey, G., Gref, R., Couvreur, P., Serre, C., 2010. BioMOFs: metal-organic frameworks for biological and medical applications. Angew. Chemie Int. Ed. 49, 6260–6266.
Michida, W., Ezaki, M., Sakuragi, M., Guan, G., Kusakabe, K., 2015. Crystal growth of cyclodextrin-based metal-organic framework with inclusion of ferulic acid. Cryst. Res. Technol. 50, 556–559.
Moussa, Z., Hmadeh, M., Abiad, M.G., Dib, O.H., Patra, D., 2016. Encapsulation of curcumin in cyclodextrin-metal organic frameworks: dissociation of loaded CD-MOFs enhances stability of curcumin. Food Chem. 212, 485–494.
Nikolakakis, I., Kachrimanis, K., Malamataris, S., 2000. Relations between crystallisation conditions and micromeritic properties of ibuprofen. Int. J. Pharm. 201, 79–88.
Rybniker, J., Vocat, A., Sala, C., Busso, P., Pojer, F., Benjak, A., Cole, S.T., 2015. Lansoprazole is an antituberculous prodrug targeting cytochrome bc1. Nat. Commun. 6, 7659.
Shin, J.M., Cho, Y.M., Sachs, G., 2004. Chemistry of Covalent Inhibition of the Gastric (H. , pp. 7800–7811.
Smaldone, R.A., Forgan, R.S., Furukawa, H., Gassensmith, J.J., Slawin, A.M.Z., Yaghi, O. M., Stoddart, J.F., 2010. Metalorganic frameworks from edible natural products. Angew. Chemie Int. Ed. 49, 8630–8634.
Smith, M.K., Angle, S.R., Northrop, B.H., 2015. Preparation and analysis of cyclodextrin-based metal-organic frameworks: laboratory experiments adaptable for high school through advanced undergraduate students. J. Chem. Educ. 92, 368–372.
Sontz, P.A., Bailey, J.B., Ahn, S., Tezcan, F.A., 2015. A metal organic framework with spherical protein nodes: rational chemical design of 3D protein crystals. J. Am. Chem. Soc. 137, 11598–11601.
Su, H., Sun, F., Jia, J., He, H., Wang, A., Zhu, G., 2015. A highly porous medical metal? organic framework constructed from bioactive curcumin. Chem. Commun. 51, 5774–5777.
Trott, O., Olson, A., 2010. NIH public access. J. Comput. Chem. 31, 455–461.

Supporting Information for

Cyclodextrin-based metal-organic frameworks particles as efficient carriers for lansoprazole: study of morphology and chemical composition of individual particles

Xue Li[1,2], Tao Guo[2], Laurent Lachmanski[3], Francesco Manoli[4], Mario Menéndez[1], Ilse Manet[4], Zhen Guo[2], Li Wu[2], Jiwen Zhang[2#], Ruxandra Gref[1#]

[1] Institut des Sciences Moléculaires d'Orsay, UMR CNRS 8214, Paris-Sud University, Paris Saclay, 91400 Orsay, France

[2] Center for Drug Delivery System, Shanghai Institute of Materia Medica, Chinese Academy of Sciences, Shanghai 201203, China

[3] Malvern Instruments, 30 rue Jean Rostand, Orsay, 91405, France

[4] Istituto per la Sintesi Organica e la Fotoreattività, ISOF, CNR, via P. Gobetti 101, 40129 Bologna, Italy.

Corresponding Author:

Prof. Ruxandra Gref

Institut Sciences Moléculaires Sciences d'Orsay, (UMR CNRS 8214), Université Paris-Sud, Université Paris-Saclay, 91400 Orsay, France; Tel: +33 (1)69158234; E-mail: ruxandra.gref@u-psud.fr.

Prof. Jiwen Zhang

Center for Drug Delivery Systems, Shanghai Institute of Materia Medica, Chinese Academy of Sciences, No. 501 of Haike Road, Shanghai 201203, China; Tel/Fax: +86-21-20231980; E-mail: jwzhang@simm.ac.cn.

S1. Images of CD-MOF-1 and LPZ-CD-MOF-1

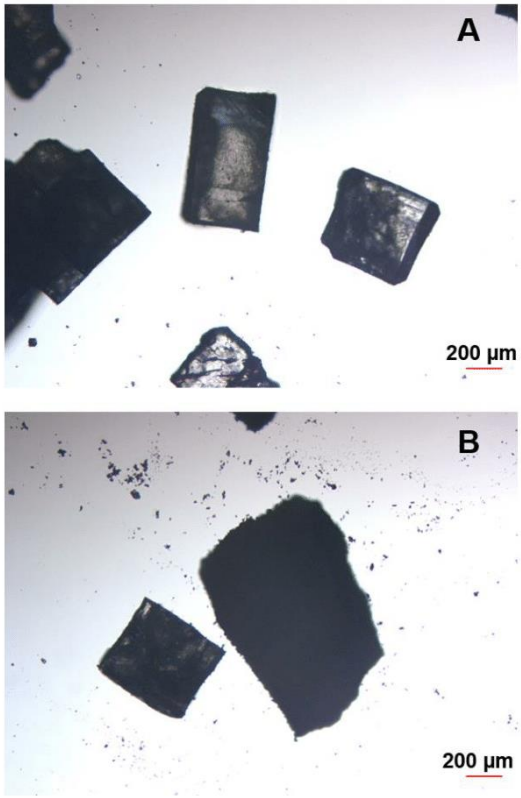

Fig. S1. Images of CD-MOF-1 (A) and LPZ-CD-MOF-1 (B)

S2. Molecular Simulation

CD-MOF are porous crystalline materials represented by the formula $K_2(C_{48}H_{80}O_{40})(OH)_2$, composed of γ-CD, K^+ and OH^- ions giving rise to electrostatic interactions. The crystal structure of CD-MOF was extracted from the single crystal structure of MOF-1 as reported (Forgan et al., 2012). The crystal cell parameters are a=b=c=31.006 Å, α=β=γ=90.00° (Fig.S2)

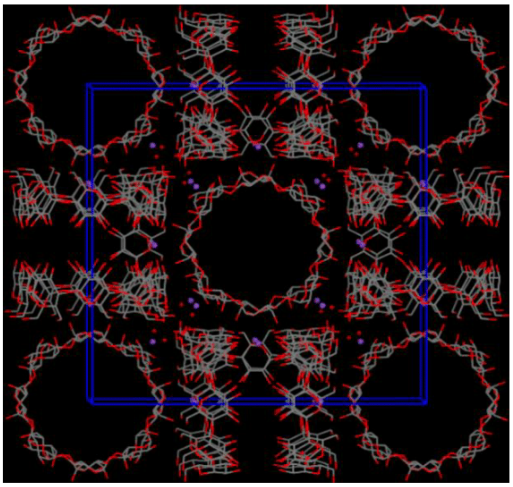

Fig. S2. Crystal structure of CD-MOF. Gray: Carbon; Red: Oxygen; Purple: Kalium; Hydrogen atoms were deleted.

The modelling is performed with the molar ratio between LPZ and γ-CD of 1:1. To reach this ratio, 2 LPZ molecules were needed for a D-γ-CD unit. The modelling was performed in two steps by adding 2 LPZ molecules in CD-MOF one by one. LPZ could access the structures through 7.8 Å windows, and interacted with the D-γ-CD units inside CD-MOF structure. When the first LPZ was loaded (before optimization) the docking free energy was about -7.7 kcal/mol, and the second was about -5.5 kcal·mol^{-1}. The hydrophilic chamber of CD-MOF was not suitable for LPZ molecule to stay due to the low docking free energy (only about -5.1 kcal/mol). Therefore, the two LPZ molecules preferred to huddle up in the cavities of the D-γ-CD unit in CD-MOF, and every γ-CD contains one LPZ molecule. (Shin et al., 2004)

Reference

Forgan, R.S., Smaldone, R.A., Gassensmith, J.J., Furukawa, H., Cordes, D.B., Li, Q., Wilmer, C.E., Botros, Y.Y., Snurr, R.Q., Slawin, A.M.Z., Stoddart, J.F., 2012. Nanoporous Carbohydrate Metal–Organic Frameworks. J. Am. Chem. Soc. 134, 406–417.

Subchapter 3.3

Composite CD-MOF nanocrystals-containing microspheres for sustained drug delivery

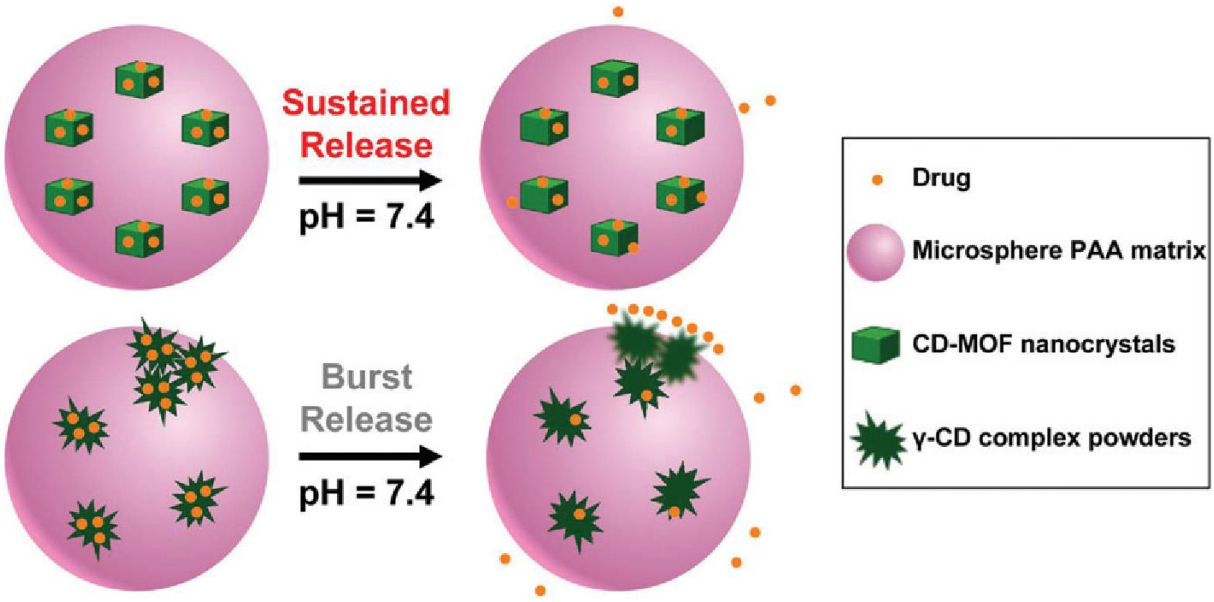

General Objectives and Author Contributions

CD-MOFs have shown their high drug loading capacity up to 23% (wt) in subchapter 3.2, however, their applications in the biomedical field are severely hampered by their physical frailness and their high solubility in aqueous media. Therefore, surface modification is needed in order to improve the stability of CD-MOFs in aqueous media and also to control the drug release. Herein, CD-MOFs were embedded in a biocompatible polyacrylic acid (PAA) polymer matrices by a solid in oil-in-oil (s/o/o) emulsifying solvent evaporation method. Briefly, several steps were included:

1) Nano-scaled CD-MOFs were firstly synthesized to obtain a good dispersion inside PAA matrices.

2) Drugs of interest, Ibuprofen (IBU) and Lansoprazole (LPZ), were loaded in CD-MOFs by co-crystallisation.

3) Morphology, size distribution, and crystallinity of CD-MOFs, loaded or not with drugs were well characterized.

4) CD-MOF nanocrystals-containing microspheres, namely drug-CD-MOF/PAA composite microspheres, were prepared by a solid in oil-in-oil emulsifying solvent evaporation method. As controls, microspheres containing only drug, or drug-CD complex were prepared in parallel.

5) Morphology, size, and drug release of the prepared microspheres were investigated.

6) The cellular toxicities of CD-MOF nanocrystals, blank PAA microspheres, pure IBU, IBU-CD-MOF nanocrystals and the IBU-CD-MOF/PAA composite microspheres were evaluated in J774 macrophages using MTT assay.

As a result, the composite microspheres exhibit not only spherical shapes and sustained drug release over a prolonged period of time, but they also demonstrate reduced cell toxicity.

This work has been performed in collaboration with Dr. J. Zhang in Shanghai Institute of Materia Medica (China) and Dr. J. F. Stoddart in Northwestern University (USA). X. Li conducted the experiments with LPZ. N. Lv focused on IBU related experiments, and Dr. H. Li contributed to data analysis and manuscript writing.

Nanoscale

PAPER

View Article Online
View Journal

Cite this: DOI: 10.1039/c6nr07593b

Composite CD-MOF nanocrystals-containing microspheres for sustained drug delivery†

Haiyan Li,‡[a,b] Nana Lv,‡[a,c] Xue Li,‡[a,d] Botao Liu,[a,e] Jing Feng,[a] Xiaohong Ren,[a] Tao Guo,[a] Dawei Chen,[c] J. Fraser Stoddart,*[b] Ruxandra Gref*[d] and Jiwen Zhang*[a,e]

Metal–organic frameworks (MOFs), which are typically embedded in polymer matrices as composites, are emerging as a new class of carriers for sustained drug delivery. Most of the MOFs and the polymers used so far in these composites, however, are not pharmaceutically acceptable. In the investigation reported herein, composites of γ-cyclodextrin (γ-CD)-based MOFs (CD-MOFs) and polyacrylic acid (PAA) were prepared by a solid in oil-in-oil (s/o/o) emulsifying solvent evaporation method. A modified hydrothermal protocol has been established which produces efficiently at 50 °C in 6 h micron (5–10 μm) and nanometer (500–700 nm) diameter CD-MOF particles of uniform size with smooth surfaces and powder X-ray diffraction patterns that are identical with those reported in the literature. Ibuprofen (IBU) and Lansoprazole (LPZ), both insoluble in water and lacking in stability, were entrapped with high drug loading in nanometer-sized CD-MOFs by co-crystallisation (that is more effective than impregnation) without causing MOF crystal degradation during the loading process. On account of the good dispersion of drug-loaded CD-MOF nanocrystals inside polyacrylic acid (PAA) matrices and the homogeneous distribution of the drug molecules within these crystals, the composite microspheres exhibit not only spherical shapes and sustained drug release over a prolonged period of time, but they also demonstrate reduced cell toxicity. The cumulative release rate for IBU (and LPZ) follows the trend: IBU-γ-CD complex microspheres (*ca.* 80% in 2 h) > IBU microspheres > IBU-CD-MOF/PAA composite microspheres (*ca.* 50% in 24 h). Importantly, no burst release of IBU (and LPZ) was observed from the CD-MOF/PAA composite microspheres, suggesting an even distribution of the drug as well as strong drug carrier interactions inside the CD-MOF. In summary, these composite microspheres, composed of CD-MOF nanocrystals embedded in a biocompatible polymer (PAA) matrix, constitute an efficient and pharmaceutically acceptable MOF-based carrier for sustained drug release.

Received 26th September 2016,
Accepted 12th April 2017

DOI: 10.1039/c6nr07593b

rsc.li/nanoscale

Introduction

In addition to ensuring prolonged drug concentrations above therapeutically active levels, achieving sustained release is an important prerequisite[1] for efficient micro- and nanoparticulate drug carriers employed to improve drug efficacy and safety. In an attempt to avoid initial rapid and uncontrolled drug release, strategies based on organic polymers[2] or inorganic porous materials[3] have been advanced. While organic–inorganic hybrid materials have also received some attention,[4] metal–organic frameworks (MOFs) composed of metal clusters and organic linkers are an emerging new class of porous materials.[5] On account of their large surface areas, together with our ability to tune their porous structures for improved drug interactions and high drug loadings, MOFs are well suited to serve as efficient carriers for drug delivery.[6] In recent years, there has been a growing interest in encapsulating drugs in MOFs. See Table S1.† Although the anti-inflammatory

[a]*Center for Drug Delivery System, Shanghai Institute of Materia Medica, Chinese Academy of Sciences, 501 Haike Road, Shanghai 201203, China. E-mail: jwzhang@simm.ac.cn*
[b]*Department of Chemistry, Northwestern University, 2145 Sheridan Road, Evanston, IL 60208, USA. E-mail: stoddart@northwestern.edu*
[c]*School of Pharmacy, Shenyang Pharmaceutical University, 103 Wenhua Road, Shenyang 110016, China*
[d]*Institut des Sciences Moléculaires d'Orsay (ISMO), UMR CNRS 8214, Université Paris Sud, Université Paris-Saclay, Orsay 91400, France. E-mail: ruxandra.gref@u-psud.fr*
[e]*School of Chemical and Environmental Engineering, Shanghai Institute of Technology, 500 Haiquan Road, Shanghai 201418, China*
†Electronic supplementary information (ESI) available. See DOI: 10.1039/c6nr07593b
‡These authors contributed equally to this work.

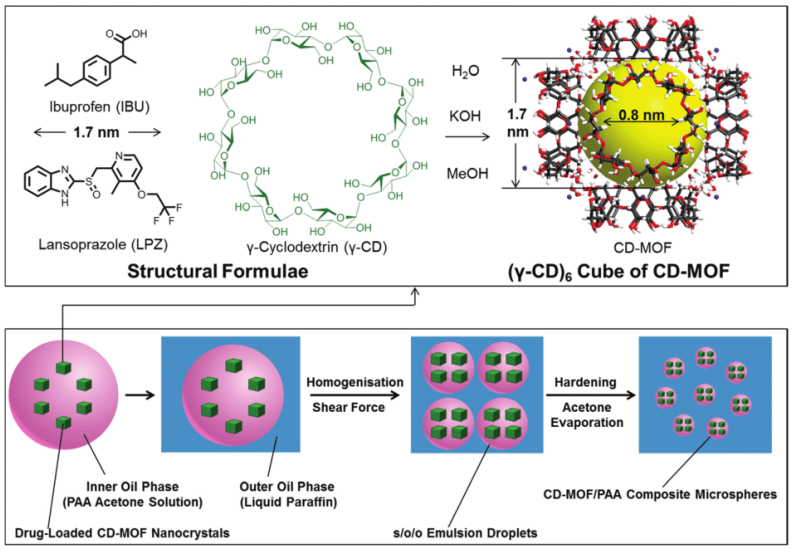

Fig. 1 Schematic representation (bottom) of the procedure for preparing the CD-MOF/PAA composite microspheres. The box (top) shows the structural formulae for Ibuprofen (IBU), Lansoprazole (LPZ) and γ-cyclodextrin (γ-CD). CD-MOF is represented by the $(\gamma\text{-CD})_6$ cube which illustrates the spherical cavity (diam 1.7 nm) and γ-CD orifices (diam 0.8 nm) that define channels running orthogonally throughout the CD-MOF crystals.

drug Ibuprofen[7] (IBU) has been the most investigated to date, antiviral[8] (*e.g.*, Azidothymidine-triphosphate and Edofovir), anti-cancer (*e.g.*, Busulfan,[9] Doxorubicin,[10] 5-Fluorouracil,[11] and a Cisplatin[12] prodrug), and cationic antiarrythmic (*e.g.*, Procainamide) drugs[13] have also attracted considerable attention of late.

Biocompatible materials are required for the application of porous solids to drug delivery. MOFs based on transition metals, such as Co/Ni/Cr/Gd *etc*. and/or non-pharmaceutical grade organic linkers which are considered to be toxic, are not acceptable for healthcare applications.[6] It follows that some efforts have been made to synthesise biocompatible MOFs with endogenous linkers and employing pharmaceutically acceptable excipients.[14] In particular, γ-cyclodextrin (γ-CD), a cyclic oligosaccharide, which can be produced[15] microbiologically from starch on the kilogram scale, has been employed[15d] together with Group IA (K/Rb/Cs) metal salts to synthesise the environmentally friendly cyclodextrin metal–organic frameworks we call CD-MOFs. They are all body-centred cubic extended structures containing large spherical pores of 17 Å in diameter with apertures of 7.8 Å across. CD-MOF crystals are defined by a porous, body-centred cubic array of $(\gamma\text{-CD})_6$ cubic units, which are linked by coordination of the secondary face hydroxyl groups on alternating D-glucopyranosyl residues to one of the alkali metal cations. Following activation (removal of aqueous methanol), these materials are permanently porous with surface areas of up to 1200 $m^2\ g^{-1}$ and are capable[16] of storing gases ($N_2/H_2/CO_2/CH_4$) as well as small molecules such as Rhodamine B and 4-phenylazophenol within their porous frameworks. The robust crystallinity and high porosity of the CD-MOF prepared using RbOH and γ-CD renders it a good candidate for MOF-based sensors[17] and memristors.[18] This CD-MOF has also been employed as a template for the synthesis of silver and gold nanoparticles[19] starting from $AgNO_3$ and $HAuCl_4$, respectively, as precursors. Recently, CD-MOFs have been used to address some of the most challenging separations and purifications surrounding petroleum feedstocks,[20] showing separation factors and resolutions superior to those reported for other MOF-based materials.

Applications of CD-MOFs in the biomedical field, however, are severely hampered by their physical frailness and their high solubility in aqueous media, such that they cannot maintain their extended frameworks intact prior to reaching the target tissues or organs. In this investigation, CD-MOF vesicles with monodisperse submicron sizes have been produced as pharmaceutically acceptable composite microspheres, which are composed (Fig. 1) of CD-MOFs and polyacrylic acid (PAA), obtained by a solid in oil-in-oil (s/o/o) emulsifying solvent evaporation technique. These composite microspheres have been demonstrated to encapsulate two drugs-namely, Ibuprofen (IBU) and Lansoprazole (LPZ) – (i) by impregnation and (ii) by co-crystallisation protocols and shown to exhibit sustained *in vitro* drug release. The composite microspheres, which were co-crystallised in the presence of IBU, exhibit improved cytocompatibility.

Results and discussion

Synthesis and characterisation of CD-MOFs

The preparation of crystalline, homogeneous, monodispersed and stable MOFs is of utmost importance[21] for their

applications in drug delivery systems. Amongst the various synthetic routes – such as hydrothermal/solvothermal,[22] mechanochemical,[23] microwave-assisted,[24] ultrasonic[25] *etc.* – reported in the literature, it is generally recognised[22] that the hydrothermal/solvothermal method is one of the best for controlling particle size while also obtaining high yields. In the originally reported[15] synthesis, CD-MOF crystals of around 200–400 microns in diameter were prepared by reacting γ-CD with 8 equiv. of KOH in aqueous solution, followed by vapour diffusion of MeOH into the solution at ambient temperature during one week. Subsequently, a modified procedure has been reported[26] to produce CD-MOF crystals with micron and nanometer sizes that involves incubating γ-CD and 8 equiv. of KOH in H_2O under MeOH vapor for about 24 h. Addition of cetyl trimethylammonium bromide (CTAB) to the supernatant leads[26] to the preparation of CD-MOF crystals with smaller diameters (1–10 μm). It was also found[26] that addition of both CTAB and MeOH were required in order to obtain crystals in the micron to submicron region (200–300 nm). Thus, for the synthesis of CD-MOFs smaller than 40 μm, long incubation times (26–32 h) are needed, and several steps are required. More importantly, these procedures always lead to the production of polydisperse CD-MOF crystals which are difficult to separate and not so suitable for drug loading applications. The size distribution of MOF crystals is a key parameter – since it dictates the chemical and physical properties (packing, external surface features, rheology, reactivity, *etc.*) of the particles – in establishing well-defined, reproducible, and stable drug delivery formulations.

In the present investigation, a modified hydrothermal method was developed in order to shorten the reaction time for the preparation of CD-MOF crystals with narrow size distributions, both in the micron and nanometer regimes. The influences of the incubation parameters – *e.g.*, reactant concentrations, molar ratios of γ-CD to KOH, the nature of the solvents, the amounts of CTAB, temperature and time – on the size and crystallinity of the CD-MOF crystals went in tandem with PXRD and SEM characterisations. In the final analysis, a hydrothermal route with an incubation temperature of 50 °C and pre-addition of MeOH to the aqueous solution of γ-CD and KOH was developed that led to the production of micron- and nanometer-sized CD-MOF crystals within 6 h. In this manner, high yields (80% for CD-MOF microcrystals and 90% for CD-MOF nanocrystals) were obtained. The size distributions of CD-MOF nanocrystals were characterised employing both SEM and DLS techniques. As indicated by the SEM images (Fig. 2a and b), micron (5–10 μm) and nanometer (500–700 nm) CD-MOF crystals were produced. In situ measurements of the CD-MOF nanocrystals by optical fiber dynamic light scattering also revealed a mean diameter of 650 nm with a very narrow size distribution and a polydispersity index of 0.22 (Fig. S3†). These crystals displayed cubic morphologies with smooth surfaces and uniform size distributions. The PXRD patterns (Fig. 2c) confirmed the crystalline morphologies of CD-MOF, and, consistent with those reported[15,26] in the literature, the microcrystals display a little larger intensity and smaller peak broadening than their counterpart nanocrystals. The N_2 adsorption-desorption isotherms (Fig. S8†) revealed that the Brunauer–Emmett–Teller (BET) surface areas for the activated CD-MOF microcrystals and nanocrystals were 786 and 668 $m^2\ g^{-1}$, respectively.

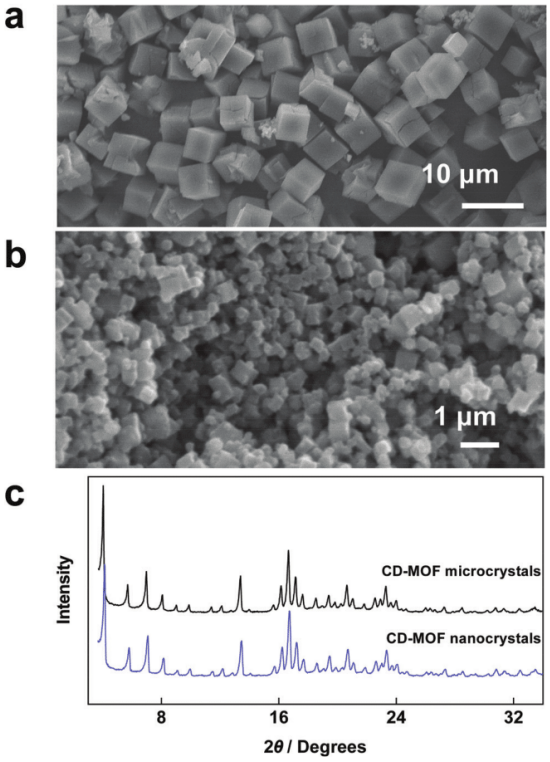

Fig. 2 SEM Images. (a) Micron-sized CD-MOF crystals. (b) Nanometer-sized CD-MOF crystals. (c) PXRD patterns of activated CD-MOF microcrystals and CD-MOF nanocrystals.

Encapsulation of drugs into CD-MOF crystals

The use of porous MOFs has been reported,[8a,27] not only in the encapsulation of unprecedented capacities of the analgesic and anti-inflammatory drug Ibuprofen – from 0.2 to 1.4 g per g of MOF – and its progressive release over 2 to 21 days depending on the solid. The encapsulation of IBU and LPZ – with molecular dimensions of about 5 × 10 and 4 × 17 Å, respectively – inside CD-MOFs was carried out using both an impregnation approach[7] and a co-crystallisation method.[15a] These particular drugs were selected for investigation, taking into consideration their molecular structures in relation particularly to the dimensions of the cylindrical channel apertures (diameter 7.8 Å) between the $(\gamma\text{-CD})_6$ cubes and the internal spherical cavities (diameter 17 Å) of the $(\gamma\text{-CD})_6$ cubes, suggesting that they might stand a chance of accommodating drug molecules with average diameters of 8 Å or less. In addition, the carboxyl group present in IBU should be prone to

forming hydrogen bonds with the γ-CD linkers, as well as strong electrostatic interactions with the K^+ cations, favouring its loading inside the CD-MOF architecture. The solvents used in the impregnation approach were assessed by loading IBU or LPZ into micron-sized CD-MOF crystals and those solvents with higher drug loading were employed to incorporate drugs into nanometer-sized CD-MOF crystals. After activation[7,15a] of the CD-MOF microcrystals to remove residual organic solvents and H_2O, IBU or LPZ was loaded (Fig. 3) by impregnation in a range of solvents, including EtOH, MeOH, Me_2CO, CH_2Cl_2 and DMF. A systematic study revealed that the maximum IBU loadings were achieved after three days of incubation, whereas only 20 h was needed in the case of LPZ. The best impregnation results (about 12% w/w) for IBU, which were obtained with CD-MOF microcrystals in EtOH, MeOH and CH_2Cl_2, corresponded to a molar ratio of CD-MOFs to IBU of 1 : 1. In the case of LPZ, a maximum drug loading (DL) of 9.4% (w/w) was achieved by soaking the CD-MOF microcrystals in EtOH, resulting in a molar ratio of CD-MOF to LPZ of 2.7. The lowest loadings (about 6% w/w) were recorded in Me_2CO for IBU, and DMF for LPZ (about 0.4% w/w). Next, EtOH was employed to encapsulate IBU and LPZ into CD-MOF nanocrystals by using the impregnation approach (Table S2†). In the case of both IBU and LPZ loadings, by impregnation, however, the crystallinity of the CD-MOF is impaired (Fig. 4a and b) as a consequence of the progressive degradation of the extended structures in the solvents employed to load the drugs (Fig. S2†).

A convenient co-crystallisation method was also developed to encapsulate the drugs directly during the particle synthesis (Table S2, Fig. S4†) by taking advantage of the relatively mild reaction conditions[15a] for preparing CD-MOFs, at a temperature which can maintain the integrity of the drug molecules during the loading process. The PXRD traces shown in Fig. 4 reveal that IBU/LPZ loading by co-crystallisation does not influence the crystallinity of the CD-MOF nanocrystals. IBU and LPZ are crystalline drugs with characteristic PXRD peaks quite different from those of CD-MOF: these peaks are not present (Fig. 4a) in IBU/LPZ-loaded CD-MOF nanocrystals, indicating

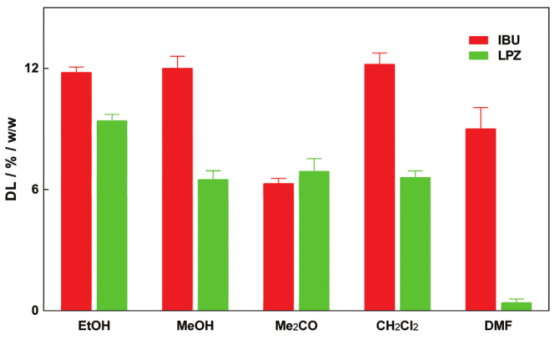

Fig. 3 Drug loading percentages (%, w/w) of IBU and LPZ in CD-MOF microcrystals with a range of impregnation solvents. Drug loading values are based on repeating experiments on three batches of crystals.

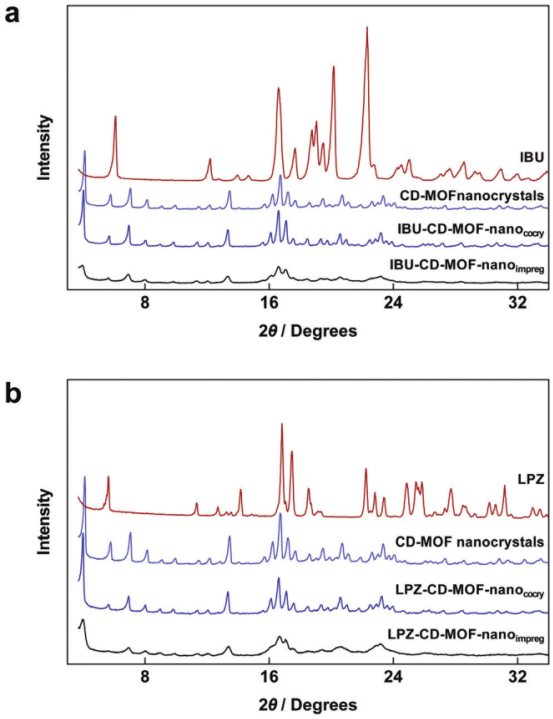

Fig. 4 PXRD Images of drug-loaded CD-MOF nanocrystals. (a) IBU. (b) LPZ. IBU/LPZ-CD-MOF-$nano_{cocry}$ and CD-MOF-$nano_{impreg}$ indicate the drug-loaded CD-MOF nanocrystals prepared by co-crystallisation and impregnation. The drug loading values are 12.7% for IBU-CD-MOF-$nano_{cocry}$, 13.0% for IBU-CD-MOF-$nano_{impreg}$, 4.5% for LPZ-CD-MOF-$nano_{cocry}$ and 1.6% for LPZ-CD-MOF-$nano_{impreg}$.

the IBU/LPZ is entrapped in a molecular state. In the IR spectrum of IBU/LPZ-loaded CD-MOF nanocrystals (Fig. S6†), the characteristic vibrational band of drug (the carboxylic group in IBU at 1722 cm^{-1} and the aromatic ring in LPZ at 1580 cm^{-1}) disappear. In the TGA curves (Fig. S7†), the decomposition temperature of IBU-loaded CD-MOF nanocrystals increases significantly to 200 °C, compared with that of the individual components (IBU at 150 °C and CD-MOF at 175 °C), indicating IBU has been incorporated into the CD-MOF pores and experiences a relatively strong interaction with the framework. Additionally, the BET surface area of the CD-MOF nanocrystals decreases dramatically after drug incorporation (Fig. S8†), indicating that the drug fills completely and/or blocks the pores of the material leaving little to no accessible pore volume for nitrogen.[7a] All of these results confirm the incorporation of drug molecules into CD-MOF pores, which is in agreement with the recently reported[27b] grand canonical Monte Carlo (GCMC) simulations of IBU adsorption inside several different MOFs including CD-MOF. In these simulations, strong electrostatic interactions were identified between IBU and CD-MOFs on account of the existence of charge-compensating OH^- anions present in CD-MOFs which enhance the adsorbate–

adsorbent interactions and induce the adsorption of IBU at lower fugacities than in other MOFs with smaller pores. IBU molecules were shown to locate themselves in the cylindrical channels of diameters 7.8 Å between the $(\gamma\text{-CD})_6$ cubes, followed by saturation of the spherical cavities with diameters of 17 Å inside CD-MOF. In these confined regions, complex electrostatic interactions occur between the IBU carbonyl oxygen atoms and the alkali metal cations in the CD-MOFs in addition to hydrophobic interactions with surfaces of the CD cavities. In a nutshell, these considerations support the encapsulation of IBU in a molecular state in confined microdomains inside CD-MOFs. Similar results have been observed[15a] for other organic molecules, such as Rhodamine B and 4-phenylazophenol trapped inside CD-MOFs. In particular, simulations suggest that the high energy for IBU adsorption in CD-MOFs is potentially beneficial when it comes ultimately controlling the release of IBU.

In summary, the co-crystallisation method appears to be the more convenient and efficient way to load drugs into CD-MOFs, while still preserving their framework's crystallinity and allowing for significantly higher DL values in the case of LPZ (Table S2†). The co-crystallisation method was therefore chosen in preference to the impregnation approach for all subsequent preparations of microspheres from CD-MOF nanocrystals. These materials exhibit equivalent or higher DL values (12.7% for IBU and 4.5% for LPZ) than those (13.0% for IBU and 1.6% for LPZ) obtained by the impregnation approach.

Preparation and characterisation of CD-MOF/PAA composite microspheres

Given the instability of MOF crystals in aqueous media and even in hydroxylic solvents, their incorporation into larger biocompatible microspheres presents itself as an attractive strategy to circumvent these inconveniences.[28] An s/o/o emulsifying solvent evaporation technique[29] has been employed to prepare CD-MOF/PAA composite microspheres. Since the size of the solid dispersed in the internal phase when preparing microspheres needs to be as small as possible, drug-loaded nanometer-sized CD-MOFs (diameter 500–700 nm, Fig. S5†), obtained by the co-crystallisation method were selected in order to prepare PAA composite microspheres (Fig. 1). For controls, microspheres were also prepared from (i) only PAA (blank PAA microspheres), (ii) only the drug itself (drug microspheres) and (iii) the drug-γ-CD complex (drug-γ-CD microspheres) by incorporating equivalent amounts of the drugs or drug-γ-CD complexes in the preparation of the microspheres. An extensive optimisation procedure has been carried out in order to select parameters that favour the production of spherical microspheres with narrow size distributions, while preserving the integrity of the drugs during the preparation procedures. It was discovered, however, that the PAA copolymer bearing carboxyl groups degrades LPZ. Thus, a modified PAA copolymer (Eudragit RS100) without carboxyl groups was used to prepare microspheres containing LPZ. Electron microscopy images (Fig. 5) of the optimised formulations show that the size of the microspheres containing IBU is within a range of 20–50 μm, whereas the size of microspheres containing LPZ is around 50–100 μm. It is worth pointing out that the composite microspheres have much better sphericities than those prepared using the pure drug or drug-γ-CD complexes. This observation can be attributed to a more efficient dispersion of the IBU/LPZ-CD-MOF nanocrystals in the microspheres. In the case of the CD-MOF/PAA composite microspheres, the drug-loaded CD-MOFs are crystals with uniform nanometer sizes and can be well dispersed in the internal Me_2CO when preparing microspheres, hence providing a good chance to be blended into PAA polymer matrices so as to result in the uniform dispersion of drugs in microspheres. On the contrary, the size of the drug-γ-CD complexes was larger and not as uniform when compared with that of the drug-loaded CD-MOF nanocrystals, even after sieving. Particle aggregation in the viscous internal oil phase (PAA Me_2CO solutions) occurred during microsphere preparation with drug-γ-CD complexes. In summary, nanometer-sized CD-MOF crystals disperse well in Me_2CO droplets, leading to their uniform distribution in the microspheres after coacervation of the oil droplets.

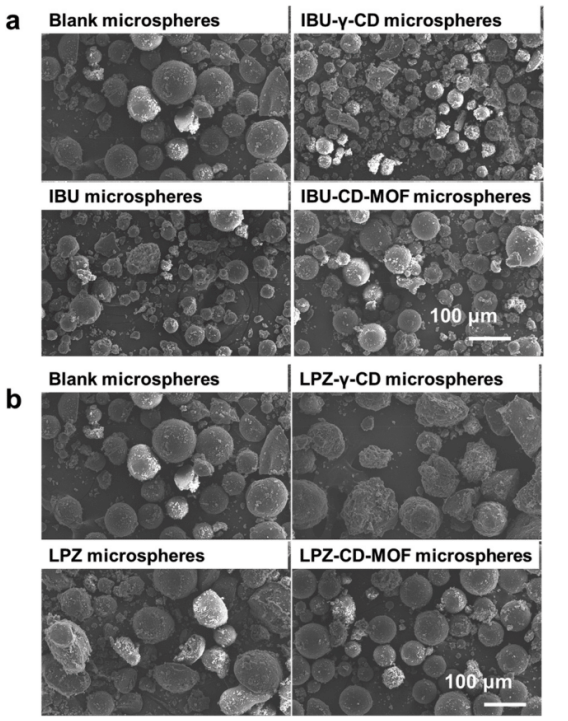

Fig. 5 SEM Images of blank microspheres and microspheres prepared using the drug alone (IBU/LPZ microspheres), the drug-γ-CD complex (IBU/LPZ-γ-CD microspheres) and drug-loaded CD-MOF nanocrystals (IBU/LPZ-CD-MOF microspheres). (a) IBU series, (b) LPZ series. The scale bars for all of the images are the same.

Sustained drug release

Achieving sustained drug release is an important requirement[1] for drug formulations. Burst release is considered[1] to be one of the main drawbacks hampering important applications of the drug-loaded carriers in the fields of viral infection and anti-cancer treatments.[6,8] *In vitro* cumulative drug release profiles of IBU- and LPZ-loaded CD-MOF/PAA microspheres were examined (Fig. 6) under simulated physiological conditions. Microspheres containing the IBU-γ-CD and LPZ-γ-CD complexes both showed (Fig. 6a and b, respectively) a very fast burst and uncontrolled release – *i.e.*, 70% in 30 min and 80% in 2 h for the microspheres prepared from both the IBU-γ-CD and LPZ-γ-CD complexes. Also, the cumulative release percentages of IBU/LPZ-γ-CD microspheres are higher than 100%, which might be a consequence of the uneven distribution of drugs in the IBU/LPZ-γ-CD microspheres with poor sphericities (Fig. 5). In fact, better sustained drug release was achieved (Fig. 6a and b) with free drug entrapment! By far the best results were obtained (Fig. 6a and b), however, when the drug-loaded CD-MOF nanocrystals were incorporated into PAA composite microspheres (about 60% in 24 h). IBU is released slowly over 48 h, whereas LPZ enables a sustained release also during 48 h with an almost linear profile. This observation no doubt reflects (i) the excellent dispersion of nanometer-sized drug-CD-MOFs in the internal Me_2CO when preparing microspheres and finally their uniform encapsulation in PAA microspheres as well as (ii) the homogeneous distribution of drug molecules within CD-MOF nanocrystals, resulting from the co-crystallisation-loading process.

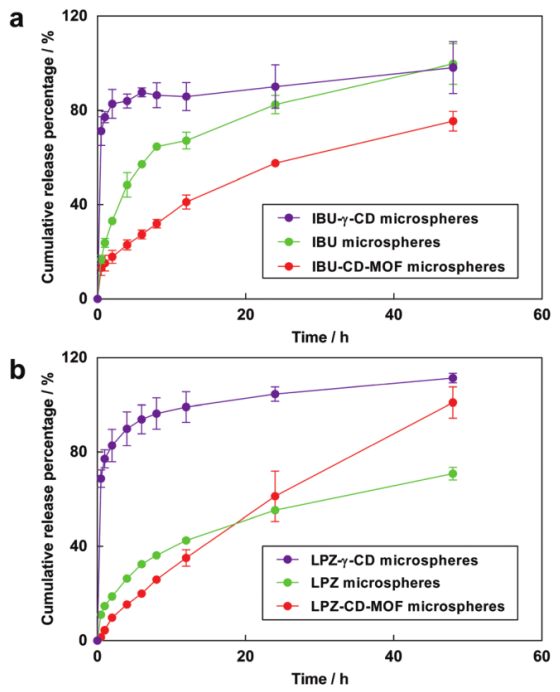

Fig. 6 The release profiles for the drug-loaded CD-MOF/PAA composite microspheres (IBU/LPZ-CD-MOF microspheres), the drug-γ-CD complex microspheres (IBU/LPZ-γ-CD microspheres) and microspheres containing the pure drug (IBU/LPZ microspheres) within 48 h. The release percentage values are based on repeating experiments on three batches of microspheres. The release medium for (a) IBU was PBS with a pH of 7.4 and that for (b) LPZ was a carbonate buffer solution with a pH of 9.7 on account of the instability of LPZ at pH 7.4.

In addition, the slow release of the drugs from CD-MOF/PAA composite microspheres also suggests that most of the drugs remain in the CD-MOF nanocrystals during their incorporation into the microspheres: it follows that the small size of the cavities and pores in the microporous CD-MOF restricts the diffusion of the drugs incorporated within them into the outer oil phase during the microsphere preparation process. Taking into account the bio-adhesive properties of PAA and its excellent biocompatibility, the composite microspheres appear to be promising for biomedical applications and, in particular, oral drug delivery.

We have made a comparison between our work and another CD-MOF-based composite,[30] in which hydrophobic C_{60} was incorporated into the CD-MOF crystals and the resulting hybrid materials have been exploited for drug delivery applications. A drug loaded CD-MOF/C_{60} composite was formed by trapping the anticancer drug doxorubicin (DOX) within CD-MOFs, followed by C_{60} incorporation. By comparison, 78.5% of the drug (DOX) is released from the composite within 6 h, *i.e.*, much faster than that for the composite microspheres (<30% of the drug (IBU/LPZ) released within 6 h), demonstrating the significant sustained release advantageous of the composite microspheres in our study.

In view of the higher drug-loading of CD-MOF nanocrystals prepared by co-crystallisation (Table S2†), together with the maintenance of the original crystallinity of CD-MOF nanocrystals and the shorter time needed for loading (6 h) in comparison with the impregnation method, drug-loaded CD-MOF nanocrystals resulting from co-crystallisation were used to prepare microspheres in this study. In future research, the release behaviour of microspheres prepared from CD-MOFs impregnated with drug molecules will be investigated in order to elucidate the effect of the crystallinity of the CD-MOFs on drug releasing ability and, we suspect, illustrate the advantage of CD-MOFs prepared by co-crystallisation.

Cytotoxicity

The cellular toxicities of CD-MOF nanocrystals, blank PAA microspheres, pure IBU, IBU-CD-MOF nanocrystals and the IBU-CD-MOF/PAA composite microspheres were evaluated by determining the cell viability values (Fig. 7) using an MTT assay.[31] For the CD-MOF nanocrystals, the cell viability decreases with the concentration of CD-MOF nanocrystals. At relatively high concentrations (up to 1.4 mg mL^{-1}), the cell viability was still high, >75%. Similar to pure IBU, high cell viability (>90%) was observed at relatively high IBU concentrations (up to 0.2 mg mL^{-1}). Some of the cell viability values for IBU group (Fig. 7) are higher than 100%, which might be a result

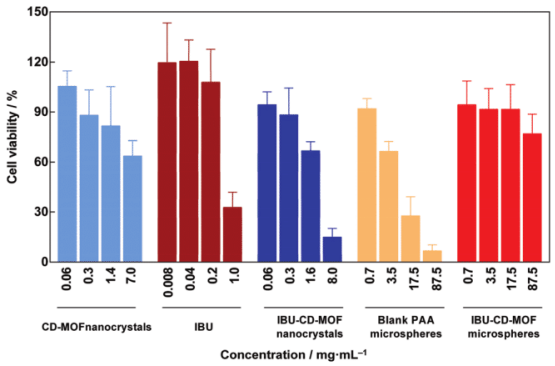

Fig. 7 Cytotoxicity of CD-MOF nanocrystals, blank PAA microspheres, IBU, IBU-CD-MOF nanocrystals and IBU-CD-MOF/PAA composite microspheres (IBU-CD-MOF microspheres) in a J774 macrophage cell line at various concentrations. The concentrations for IBU-CD-MOF nanocrystals and IBU-CD-MOF microspheres were selected according to the IBU loading values (see Tables S2 and S4†), corresponding to IBU concentrations of 0.008, 0.04, 0.2 and 1.0 mg mL^{-1}, equivalent to that for pure IBU. The cell viability values are based on repeating experiments on five batches of cells.

of the fact that IBU can promote the growth of some normal cells.[32] The IBU-loaded CD-MOF nanocrystals were found to be more toxic towards J774 macrophages[31] compared with CD-MOF nanocrystals and pure IBU: the cell viability value was 67% at the concentration of 1.6 mg mL^{-1}, corresponding to a CD-MOF nanocrystal concentration of 1.4 mg mL^{-1} and an IBU concentration of 0.2 mg mL^{-1}. The toxicity of IBU-CD-MOF/PAA composite microspheres, however, was reduced dramatically when including IBU-CD-MOF nanocrystals into composite microspheres. Even for samples at high concentrations of 17.5 mg mL^{-1}, corresponding to a CD-MOF nanocrystal concentration of 1.4 mg mL^{-1} and IBU concentration of 0.2 mg mL^{-1}, the cell viability was ~90%. For the blank PAA microspheres, the cell viability was <30% at a concentration of 17.5 mg mL^{-1}. This finding suggests that IBU-CD-MOF/PAA composite microspheres have a better cytocompatibility than either of the two individual components. In summary, the results (Fig. 7) confirm that the composite of CD-MOF nanocrystals in PAA microspheres improves the cytocompatibility of each separate component, allowing them to be used as safe carriers for sustained drug delivery.

A limitation of the s/o/o technique is that the drug loading of the CD-MOF/PAA microspheres is relatively low (about 1%, w/w) and would be better employed to deliver drugs requiring lower doses (<10 mg), such as anti-tumor drugs. Although the system should be as simple as possible for drug delivery, the low water resistance of CD-MOF, however, limits its application. CD-MOF dissolves in water rapidly: consequently, the drugs are released extremely fast, limiting our ability to measure their prolonged release.[30] In order to improve the water resistance of CD-MOF materials, composite microspheres containing CD-MOF nanocrystals have been investigated. They exhibit not only sustained drug release over a prolonged period of time, but also demonstrate reduced cell toxicity, compared with the microspheres containing pure drug and the drug-γ-CD complex. The one-pot polymer coatings on the surface of CD-MOF nanocrystals, based on a molecular anchoring strategy, will be the subject of further investigations in order to simplify the synthesis procedure and improve the drug loading of the microspheres.

Conclusions

A modified hydrothermal method has been established that produces CD-MOF particles of well-defined sizes. The insoluble and not so stable drugs, Ibuprofen and Lansoprazole, can be trapped inside CD-MOFs by a co-crystallisation method that is more effective than an impregnation approach and leads to increased drug loadings as well as no reduction in CD-MOF crystal degradation during the loading process. Incorporation of CD-MOF nanocrystals inside composite PAA microspheres, not only allows drug release to be controlled over a prolonged period of time, but it also brings about a reduction in the cell toxicity of CD-MOF-based drug carriers. The CD-MOF/PAA composite microspheres have spherical shapes on account of the good dispersion of the CD-MOF nanocrystals that can be achieved inside the PAA matrices. Our findings constitute a rare example of MOF nanoparticles embedded into a biocompatible polymer matrix. These composite microspheres incorporating CD-MOF nanocrystals could find useful applications in the biomedical field.

Author contributions

J. Fraser Stoddart, Ruxandra Gref and Jiwen Zhang conceived and designed the experiments; Haiyan Li, Nana Lv and Xue Li conducted the experiments, analyzed data and wrote the manuscript; Botao Liu and Jing Feng contributed to the drug release tests; Xiaohong Ren carried out the cell tests; Tao Guo and Dawei Chen contributed to the solid characterizations.

Acknowledgements

We are grateful for the financial support from the Natural Science Foundation of China (81373358, 81430087 and 81573392). Xue Li acknowledges the support from China Scholarship Council (CSC, 201408330166). Prof. Ruxandra Gref acknowledges the support from the Marie Curie FP7-PEOPLE-ITN-2013 "Cyclon Hit" grant (608407) and the French National Agency of Research (ANR-14-CE08-0017, Anti-TB-nano). This research is part of the Joint Center of Excellence in Integrated Nano-Systems (JCIN) at King Abdulaziz City for Science and Technology (KACST) and Northwestern University (NU). The authors would like to thank both KACST and NU for their continued support of this research.

Notes and references

1 (*a*) P. Agarwal and I. D. Rupenthal, *Drug Discovery Today*, 2013, **18**, 337–349; (*b*) V. D. Prajapati, G. K. Jani and J. R. Kapadia, *Expert Opin. Drug Delivery*, 2015, **12**, 1283–1299; (*c*) S. De Robertis, M. C. Bonferoni, L. Elviri, G. Sandri, C. Caramella and R. Bettini, *Expert Opin. Drug Delivery*, 2015, **12**, 441–453; (*d*) J. V. Andhariya and D. J. Burgess, *Expert Opin. Drug Delivery*, 2016, **13**, 593–608; (*e*) I. E. Lee, A. Hashidzume and A. Harada, *Macromol. Rapid Commun.*, 2015, **36**, 2055–2059.

2 (*a*) P. Dandekar, R. Jain, M. Keil, B. Loretz, L. Muijs, M. Schneider, D. Auerbach, G. Jung, C. M. Lehr and G. Wenz, *J. Controlled Release*, 2012, **164**, 387–393; (*b*) Y. Yu, C. K. Chen, W. C. Law, J. Mok, J. Zou, P. N. Prasad and C. Cheng, *Mol. Pharm.*, 2013, **10**, 867–874; (*c*) E. Mohammadifar, A. N. Kharat and M. Adeli, *J. Mater. Chem. B*, 2015, **3**, 3896–3921; (*d*) H. P. Merkle, *Eur. J. Pharm. Biopharm.*, 2015, **97**, 293–303; (*e*) D. Shetty, J. K. Khedkar, K. M. Park and K. Kim, *Chem. Soc. Rev.*, 2015, **44**, 8747–8761; (*f*) M. Dangol, H. Yang, C. G. Li, S. F. Lahiji, S. Kim, Y. Ma and H. Jung, *J. Controlled Release*, 2016, **223**, 118–125; (*g*) I. Matai and P. Gopinath, *ACS Biomater. Sci. Eng.*, 2016, **2**, 213–223.

3 (*a*) S. J. Son, X. Bai and S. B. Lee, *Drug Discovery Today*, 2007, **12**, 650–656; (*b*) E. Gultepe, D. Nagesha, S. Sridhar and M. Amiji, *Adv. Drug Delivery Rev.*, 2010, **62**, 305–315; (*c*) Z. Li, J. C. Barnes, A. Bosoy, J. F. Stoddart and J. I. Zink, *Chem. Soc. Rev.*, 2012, **41**, 2590–2605; (*d*) Y. Wang, Q. F. Zhao, N. Han, L. Bai, J. Li, J. Liu, E. X. Che, L. Hu, Q. Zhang, T. Y. Jiang and S. L. Wang, *Nanomedicine*, 2015, **11**, 313–327.

4 (*a*) S. Begu, A. Aubert-Pouessel, R. Polexe, E. Leitmanova, D. A. Lerner, J. M. Devoisselle and D. Tichit, *Chem. Mater.*, 2009, **21**, 2679–2687; (*b*) L. Contessotto, E. Ghedini, F. Pinna, M. Signoretto, G. Cerrato and V. Crocellà, *Chemistry*, 2009, **15**, 12043–12049; (*c*) M. Catauro, D. Verardi, D. Melisi, F. Belotti and P. Mustarelli, *J. Appl. Biomater. Biomech.*, 2010, **8**, 42–51; (*d*) D. Liu, B. Herranz-Blanco, E. Mäkilä, L. R. Arriaga, S. Mirza, D. A. Weitz, N. Sandler, J. Salonen, J. Hirvonen and H. A. Santos, *ACS Appl. Mater. Interfaces*, 2013, **5**, 12127–12134; (*e*) L. Z. Sun, Y. Z. Wang, T. Y. Jiang, X. Zheng, J. H. Zhang, J. Sun, C. H. Sun and S. L. Wang, *ACS Appl. Mater. Interfaces*, 2013, **5**, 103–113; (*f*) J. G. Heck, J. Napp, S. Simonato, J. Möllmer, M. Lange, H. M. Reichardt, R. Staudt, F. Alves and C. Feldmann, *J. Am. Chem. Soc.*, 2015, **137**, 7329–7336.

5 (*a*) H. K. Chae, D. Y. Siberio-Pérez, J. Kim, Y. Go, M. Eddaoudi, A. J. Matzger, M. O'Keeffe and O. M. Yaghi, *Nature*, 2004, **427**, 523–527; (*b*) O. M. Yaghi, *Nat. Mater.*, 2007, **6**, 92–93; (*c*) L. E. Kreno, K. Leong, O. K. Farha, M. Allendorf, R. P. Van Duyne and J. T. Hupp, *Chem. Rev.*, 2012, **112**, 1105–1125; (*d*) A. Bétard and R. A. Fischer, *Chem. Rev.*, 2012, **112**, 1055–1083; (*e*) T. R. Cook, Y. R. Zheng and P. J. Stang, *Chem. Rev.*, 2013, **113**, 734–777; (*f*) D. Y. Du, J. S. Qin, S. L. Li, Z. M. Su and Y. Q. Lan, *Chem. Soc. Rev.*, 2014, **43**, 4615–4632; (*g*) Y. J. Cui, B. Li, H. J. He, W. Zhou, B. L. Chen and G. D. Qian, *Acc. Chem. Res.*, 2016, **49**, 483–493.

6 (*a*) J. Della Rocca, D. Liu and W. Lin, *Acc. Chem. Res.*, 2011, **44**, 957–968; (*b*) P. Horcajada, R. Gref, T. Baati, P. K. Allan, G. Maurin, P. Couvreur, G. Férey, R. E. Morris and C. Serre, *Chem. Rev.*, 2012, **112**, 1232–1268; (*c*) C. Y. Sun, C. Qin, X. L. Wang and Z. M. Su, *Expert Opin. Drug Delivery*, 2013, **10**, 89–101; (*d*) J. Zhuang, C. H. Kuo, L. Y. Chou, D. Y. Liu, E. Weerapana and C. K. Tsung, *ACS Nano*, 2014, **8**, 2812–2819; (*e*) S. Z. Li and F. W. Huo, *Nanoscale*, 2015, **7**, 7482–7501; (*f*) W. Cai, C.-C. Chu, G. Liu and Y.-X. J. Wáng, *Small*, 2015, **11**, 4806–4822; (*g*) H. Q. Zheng, Y. N. Zhang, L. F. Liu, W. Wan, P. Guo, A. M. Nyström and X. D. Zou, *J. Am. Chem. Soc.*, 2016, **138**, 962–968.

7 (*a*) P. Horcajada, C. Serre, M. Vallet-Regí, M. Sebban, F. Taulelle and G. Férey, *Angew. Chem., Int. Ed.*, 2006, **45**, 5974–5978; (*b*) R. Babarao and J. Jiang, *J. Phys. Chem. C*, 2009, **113**, 18287–18291; (*c*) F. Ke, Y. P. Yuan, L. G. Qiu, Y. H. Shen, A. J. Xie, J. F. Zhu, X. Y. Tian and L. D. Zhang, *J. Mater. Chem.*, 2011, **21**, 3843–3848; (*d*) M. O. Rodrigues, M. V. de Paula, K. A. Wanderley, I. B. Vasconcelos Jr. Alves and T. A. Soares, *Int. J. Quantum Chem.*, 2012, **112**, 3346–3355; (*e*) Q. Hu, J. C. Yu, M. Liu, A. P. Liu, Z. S. Dou and Y. Yang, *J. Med. Chem.*, 2014, **57**, 5679–5685.

8 (*a*) P. Horcajada, C. Serre, G. Maurin, N. A. Ramsahye, F. Balas, M. Vallet-Regí, M. Sebban, F. Taulelle and G. Férey, *J. Am. Chem. Soc.*, 2008, **130**, 6774–6780; (*b*) V. Agostoni, T. Chalati, P. Horcajada, H. Willaime, R. Anand, N. Semiramoth, T. Baati, S. Hall, G. Maurin, H. Chacun, K. Bouchemal, C. Martineau, F. Taulelle, P. Couvreur, C. Rogez-Kreuz, P. Clayette, S. Monti, C. Serre and R. Gref, *Adv. Healthcare Mater.*, 2013, **2**, 1630–1637; (*c*) V. Agostoni, R. Anand, S. Monti, S. Hall, G. Maurin, P. Horcajada, C. Serre, K. Bouchemal and R. Gref, *J. Mater. Chem. B*, 2013, **1**, 4231–4242; (*d*) R. Anand, F. Borghi, F. Manoli, I. Manet, V. Agostoni, P. Reschiglian, R. Gref and S. Monti, *J. Phys. Chem. B*, 2014, **118**, 8532–8539; (*e*) V. Rodriguez-Ruiz, A. Maksimenko, R. Anand, S. Monti, V. Agostoni, P. Couvreur, M. Lampropoulou, K. Yannakopoulou and R. Gref, *J. Drug Targeting*, 2015, **23**, 759–767.

9 T. Chalati, P. Horcajada, P. Couvreur, C. Serre, M. Ben Yahia, G. Maurin and R. Gref, *Nanomedicine*, 2011, **6**, 1683–1695.

10 T. Kundu, S. Mitra, P. Patra, A. Goswami, D. Díaz and R. Banerjee, *Chem. – Eur. J.*, 2014, **20**, 10514–10518.

11 (*a*) C. Y. Sun, C. Qin, C. G. Wang, Z. M. Su, S. Wang, X. L. Wang, G. S. Yang, K. Z. Shao, Y. Q. Lan and E. B. Wang, *Adv. Mater.*, 2011, **23**, 5629–5632; (*b*) H. N. Wang, X. Meng, G. S. Yang, X. L. Wang, K. Z. Shao, Z. M. Su and C. G. Wang, *Chem. Commun.*, 2011, **47**, 7128–7130; (*c*) J. S. Qin, Y. Q. Lan, D. Y. Du, W. L. Li, J. P. Zhang, S. L. Li, Z. M. Su, X. L. Wang, Q. Xu, K. Z. Shao and Y. Q. Lan, *Chem. Sci.*, 2012, **3**, 2114–2118; (*d*) F. R. Lucena, L. C. de Araújo, M. D. Rodrigues, T. G. da

Silva, V. R. Pereira, G. C. Militão, D. A. Fontes, P. J. Rolim-Neto, F. F. da Silva and S. C. Nascimento, *Biomed. Pharmacother.*, 2013, **67**, 707–713.

12 (*a*) K. M. Taylor-Pashow, J. Della Rocca, Z. Xie, S. Tran and W. Lin, *J. Am. Chem. Soc.*, 2009, **131**, 14261–14263; (*b*) R. C. Huxford, J. Della Rocca and W. Lin, *Curr. Opin. Chem. Biol.*, 2010, **14**, 262–268; (*c*) C. B. He, K. D. Lu, D. M. Liu and W. B. Lin, *J. Am. Chem. Soc.*, 2014, **136**, 5181–5184.

13 (*a*) J. An, S. J. Geib and N. L. Rosi, *J. Am. Chem. Soc.*, 2009, **131**, 8376–8377; (*b*) R. Ananthoji, J. F. Eubank, F. Nouar, H. Mouttaki, M. Eddaoudi and J. P. Harmon, *J. Mater. Chem.*, 2011, **21**, 9587–9594.

14 (*a*) C. Serre, F. Millange, S. Surblé and G. Férey, *Angew. Chem., Int. Ed.*, 2004, **43**, 6285–6289; (*b*) C. Serre, S. Surblé, C. Mellot-Draznieks, Y. Filinchuk and G. Férey, *Dalton Trans.*, 2008, **40**, 5462–5464; (*c*) S. Keskin and S. Kızılel, *Ind. Eng. Chem. Res.*, 2011, **50**, 1799–1812; (*d*) I. Imaz, M. Rubio-Martínez, J. An, I. Solé-Font, N. L. Rosi and D. Maspoch, *Chem. Commun.*, 2011, **47**, 7287–7302; (*e*) D. Cunha, M. Ben Yahia, S. Hall, S. R. Miller, H. Chevreau, E. Elkaïm, G. Maurin, P. Horcajada and C. Serre, *Chem. Mater.*, 2013, **25**, 2767–2776; (*f*) T. Baati, L. Njim, F. Neffati, A. Kerkeni, M. Bouttemi, R. Gref, M. F. Najjar, A. Zakhama, P. Couvreur and C. Serre, *Chem. Sci.*, 2013, **4**, 1597–1607.

15 (*a*) R. A. Smaldone, R. S. Forgan, H. Furukawa, J. J. Gassensmith, A. M. Slawin, O. M. Yaghi and J. F. Stoddart, *Angew. Chem., Int. Ed.*, 2010, **49**, 8630–8634; (*b*) R. S. Forgan, R. A. Smaldone, J. J. Gassensmith, H. Furukawa, D. B. Cordes, Q. Li, C. E. Wilmer, Y. Y. Botros, R. Q. Snurr, A. M. Slawin and J. F. Stoddart, *J. Am. Chem. Soc.*, 2012, **134**, 406–417; (*c*) Z. Liu and J. F. Stoddart, *Pure Appl. Chem.*, 2014, **86**, 1323–1334; (*d*) Z. Liu, S. T. Schneebeli and J. F. Stoddart, *Chimia*, 2014, **68**, 315–320; (*e*) M. K. Smith, S. R. Angle and B. H. Northrop, *J. Chem. Educ.*, 2015, **92**, 368–372.

16 (*a*) J. J. Gassensmith, H. Furukawa, R. A. Smaldone, R. S. Forgan, Y. Y. Botros, O. M. Yaghi and J. F. Stoddart, *J. Am. Chem. Soc.*, 2011, **133**, 15312–15315; (*b*) D. Wu, J. J. Gassensmith, D. Gouvêa, S. Ushakov, J. F. Stoddart and A. Navrotsky, *J. Am. Chem. Soc.*, 2013, **135**, 6790–6793.

17 (*a*) S. B. Han, Y. H. Wei, C. Valente, R. S. Forgan, J. J. Gassensmith, R. A. Smaldone, H. Nakanishi, A. Coskun, J. F. Stoddart and B. A. Grzybowski, *Angew. Chem., Int. Ed.*, 2011, **50**, 276–279; (*b*) J. J. Gassensmith, J. Y. Kim, J. M. Holcroft, O. K. Farha, J. F. Stoddart, J. T. Hupp and N. C. Jeong, *J. Am. Chem. Soc.*, 2014, **136**, 8277–8282.

18 S. M. Yoon, S. C. Warren and B. A. Grzybowski, *Angew. Chem., Int. Ed.*, 2014, **53**, 4437–4441.

19 Y. H. Wei, S. B. Han, D. A. Walker, P. E. Fuller and B. A. Grzybowski, *Angew. Chem., Int. Ed.*, 2012, **51**, 7435–7439.

20 (*a*) J. M. Holcroft, K. J. Hartlieb, P. Z. Moghadam, J. G. Bell, G. Barin, D. P. Ferris, E. D. Bloch, M. M. Algaradah, M. S. Nassar, Y. Y. Botros, K. M. Thomas, J. R. Long, R. Q. Snurr and J. F. Stoddart, *J. Am. Chem. Soc.*, 2015, **137**, 5706–5719; (*b*) K. J. Hartlieb, J. M. Holcroft, P. Z. Moghadam, N. A. Vermeulen, M. M. Algaradah, M. S. Nassar, Y. Y. Botros, R. Q. Snurr and J. F. Stoddart, *J. Am. Chem. Soc.*, 2016, **138**, 2292–2301.

21 (*a*) W. K. Wan, L. Yang and D. T. Padavan, *Nanomedicine*, 2007, **2**, 483–509; (*b*) N. Daum, C. Tscheka, A. Neumeyer and M. Schneider, *Wiley Interdiscip. Rev.: Nanomed. Nanobiotechnol.*, 2012, **4**, 52–65; (*c*) M. Björnmalm, Y. Yan and F. Caruso, *J. Controlled Release*, 2014, **190**, 139–149; (*d*) N. P. Mortensen, P. Durham and A. J. Hickey, *J. Microencapsulation*, 2014, **31**, 785–795; (*e*) A. Sen Gupta, *Wiley Interdiscip. Rev.: Nanomed. Nanobiotechnol.*, 2016, **8**, 255–270.

22 (*a*) S. S. Chui, S. M. Lo, J. P. Charmant, A. G. Orpen and I. D. Williams, *Science*, 1999, **283**, 1148–1150; (*b*) Y. Q. Tian, C. X. Cai, Y. Ji, X. Z. You, S. M. Peng and G. H. Lee, *Angew. Chem., Int. Ed.*, 2002, **41**, 1384–1386; (*c*) M. Latroche, S. Surblé, C. Serre, C. Mellot-Draznieks, P. L. Llewellyn, J.-H. Lee, J.-S. Chang, S. H. Jhung and G. Férey, *Angew. Chem., Int. Ed.*, 2006, **45**, 8227–8231; (*d*) S. S. Kaye, A. Dailly, O. M. Yaghi and J. R. Long, *J. Am. Chem. Soc.*, 2007, **129**, 14176–14177; (*e*) Z. Wang and S. M. Cohen, *Chem. Soc. Rev.*, 2009, **38**, 1315–1329.

23 (*a*) A. Pichon, A. Lazuen-Garay and S. L. James, *CrystEngComm*, 2006, **8**, 211–214; (*b*) T. Friscic, *J. Mater. Chem.*, 2010, **20**, 7599–7605; (*c*) T. Friscić, D. G. Reid, I. Halasz, R. S. Stein, R. E. Dinnebier and M. J. Duer, *Angew. Chem., Int. Ed.*, 2010, **49**, 712–715; (*d*) M. Klimakow, P. Klobes, A. F. Thüunemann, K. Rademann and F. Emmerling, *Chem. Mater.*, 2010, **22**, 5216–5221.

24 (*a*) Z. Ni and R. I. Masel, *J. Am. Chem. Soc.*, 2006, **128**, 12394–12395; (*b*) K. M. Taylor-Pashow, J. Della Rocca, Z. Xie, S. Tran and W. Lin, *J. Am. Chem. Soc.*, 2009, **131**, 14261–14263; (*c*) P. Horcajada, T. Chalati, C. Serre, B. Gillet, C. Sebrie, T. Baati, J. F. Eubank, D. Heurtaux, P. Clayette, C. Kreuz, J. S. Chang, Y. K. Hwang, V. Marsaud, P. N. Bories, L. Cynober, S. Gil, G. Férey, P. Couvreur and R. Gref, *Nat. Mater.*, 2010, **9**, 172–178; (*d*) A. Centrone, Y. Yang, S. Speakman, L. Bromberg, G. C. Rutledge and T. A. Hatton, *J. Am. Chem. Soc.*, 2010, **132**, 15687–15691.

25 (*a*) W. J. Son, J. Kim, J. Kim and W. S. Ahn, *Chem. Commun.*, 2008, **47**, 6336–6338; (*b*) L. G. Qiu, Z. Q. Li, Y. Wu, W. Wang, T. Xu and X. Jiang, *Chem. Commun.*, 2008, **31**, 3642–3644; (*c*) D. W. Jung, D. A. Yang, J. Kim and W. S. Ahn, *Dalton Trans.*, 2010, **39**, 2883–2887; (*d*) J. Kim, S. T. Yang, S. B. Choi, J. Sim, J. Kim and W. S. Ahn, *J. Mater. Chem.*, 2011, **21**, 3070–3076.

26 Y. Furukawa, T. Ishiwata, K. Sugikawa, K. Kokado and K. Sada, *Angew. Chem., Int. Ed.*, 2012, **51**, 10566–10569.

27 (*a*) P. Horcajada, C. Serre, M. Vallet-Regí, M. Sebban, F. Taulelle and G. Férey, *Angew. Chem., Int. Ed.*, 2006, **118**, 6120–6124; (*b*) M. C. Bernini, D. Fairen-Jimenez, M. Pasinetti, A. J. Ramirez-Pastor and R. Q. Snurr, *J. Mater. Chem. B*, 2014, **2**, 766–774; (*c*) M. Paul and P. Dastidar,

Chemistry, 2016, **22**, 988–998; (*d*) J. L. Liu, Y. Fu, X. B. Fu, Y. X. Li, D. K. Liang, Y. Song, C. Y. Pan, G. P. Yu and X. X. Xiao, *RSC Adv.*, 2016, **6**, 20834–20842.

28 (*a*) S. Basu, M. Maes, A. Cano-Odena, L. Alaerts, D. E. De Vos and I. F. J. Vankelecom, *J. Membr. Sci.*, 2009, **344**, 190–198; (*b*) R. Adams, C. Carson, J. Ward, R. Tannenbaum and W. Koros, *Microporous Mesoporous Mater.*, 2010, **131**, 13–20; (*c*) M. J. C. Ordonez, K. J. Balkus, J. P. Ferraris and I. H. Musselman, *J. Membr. Sci.*, 2010, **361**, 28–37; (*d*) K. Diaz, L. Garrido, M. Lopez-Gonzalez, L. F. del Castillo and E. Riande, *Macromolecules*, 2010, **43**, 316–325; (*e*) R. Ostermann, J. Cravillon, C. Weidmann, M. Wiebcke and B. M. Smarsly, *Chem. Commun.*, 2011, **47**, 442–444; (*f*) T. Ben, C. J. Lu, C. Y. Pei, S. X. Xu and S. L. Qiu, *Chem. – Eur. J.*, 2012, **18**, 10250–10253; (*g*) T. Ishiwata, Y. Furukawa, K. Sugikawa, K. Kokado and K. Sada, *J. Am. Chem. Soc.*, 2013, **135**, 5427–5432; (*h*) S. Nagata, K. Kokado and K. Sada, *Chem. Commun.*, 2015, **51**, 8614.

29 (*a*) M. Kawata, M. Nakamura, S. Goto and T. Aoyama, *Chem. Pharm. Bull.*, 1986, **34**, 2618–2623; (*b*) K. G. Carrasquillo, A. M. Stanley, J. C. Aponte-Carro, P. De Jésus, H. R. Costantino, C. J. Bosques and K. Griebenow, *J. Controlled Release*, 2001, **76**, 199–390; (*c*) Y. D. Han, H. Y. Tian, P. He, X. S. Chen and X. B. Jing, *Int. J. Pharm.*, 2009, **378**, 159–166; (*d*) M. Jelvehgari, J. Barar, H. Valizadeh, S. Shadrou and A. Nokhodchi, *Pharm. Dev. Technol.*, 2011, **16**, 637–644.

30 H. Li, M. R. Hill, R. Huang, C. Doblin, S. Lim, A. J. Hill, R. Babarao and P. Falcaro, *Chem. Commun.*, 2016, **52**, 5973–5976.

31 (*a*) T. J. Mosmann, *Immunol. Methods*, 1983, **65**, 55–63; (*b*) J. Carmichael, W. G. DeGraff, A. F. Gazdar, J. D. Minna and J. B. Mitchell, *Cancer Res.*, 1987, **47**, 936–942; (*c*) M. V. Berridge, P. M. Herst and A. S. Tan, *Biotechnol. Annu. Rev.*, 2005, **11**, 127–152; (*d*) C. Tamames-Tabar, D. Cunha, E. Imbuluzqueta, F. Ragon, C. Serre, M. J. Blanco-Prieto and P. Horcajada, *J. Mater. Chem. B*, 2014, **2**, 262–271.

32 S. Schnell, A. Kawano, C. Porte, L. E. Lee and N. C. Bols, *Environ. Toxicol.*, 2009, **24**, 157–165.

Electronic Supplementary Material (ESI) for Nanoscale.

Composite CD-MOF nanocrystals-containing microspheres for sustained drug delivery

Haiyan Li[†‡], Nana Lv[†§‡], Xue Li[†×‡], Botao Liu[†¶], Jing Feng[†], Xiaohong Ren[†], Tao Guo[†], Dawei Chen[§], J. Fraser Stoddart[ǂ*], Ruxandra Gref [×*], Jiwen Zhang[†¶*]

[†] *Center for Drug Delivery System, Shanghai Institute of Materia Medica, Chinese Academy of Sciences, 501 Haike Road, Shanghai 201203, China*

[ǂ] *Department of Chemistry, Northwestern University, 2145 Sheridan Road, Evanston, IL 60208, USA*

[§] *School of Pharmacy, Shenyang Pharmaceutical University, 103 Wenhua Road, Shenyang 110016, China*

[×] *Institut des Sciences Moléculaires d'Orsay (ISMO), UMR CNRS 8214, Université Paris Sud,Université Paris-Saclay,Orsay 91400, France*

[¶] *School of Chemical and Environmental Engineering, Shanghai Institute of Technology, 500 Haiquan Road, Shanghai 201418, Chinar*

*E-mail: jwzhang@simm.ac.cn; ruxandra.gref@u-psud.fr; stoddart@northwestern.edu

---

Supporting Information

Table of Contents

1. Materials / General Methods / Instrumentation

γ-Cyclodextrin (γ-CD) was purchased from MaxDragon Biochem Ltd (China), ibuprofen (IBU) was obtained from Melonepharma Co Ltd and lansoprazole (LPZ) was provided by Zhuhai Rundu Co Ltd (China). Polyacrylic acid polymer (Eudragit RS 100) was provided by Evonik (Rohm Pharma GMBH, Darmstadt, Germany). Aluminum tristearate was purchased from Alfa Aesar (China). RPMI-1640 Medium was purchased from Corning Incorporated (Corning, NY, USA). Penicillin, streptomycin, acetic acid, polysorbate 80 (Tween 80) and dimethyl sulphoxide (Me_2SO) were obtained from Sigma-Aldrich (St Louis, MO, USA). Methanol (MeOH), potassium hydroxide (KOH), cetyl trimethyl ammonium bromide (CTAB), isopropanol ($^{i}PrOH$), ethanol (EtOH), acetone (Me_2CO), dichloromethane (CH_2Cl_2), acetic acid (HOAc) and other reagents of analytical grade were all purchased from Sinopharm Chemical Reagent Co Ltd (Shanghai, China) and used without further purification. Water was purified by Milli-Q system (Millipore). Morphological and size characterization of samples was conducted using a scanning electron microscope (S3400, Hitachi). The specimens were immobilised on a metal stub with double-sided adhesive tape and coated with gold, then observed under definite magnification. The size distributions of CD-MOF nanocrystals were also characterised by *in situ* measurements using Vasco Flex (Cordouan-tech, France) equipped with an in situ head, which is a flexible nanoparticle size analyser based on optical fiber dynamic light scattering. The crystallinity of the samples was characterized by powder X-ray diffractometric (PXRD) analysis. Diffraction patterns were detected with a Bruker D8 Advance diffractometer (Bruker, USA) of the locked coupled scan type. Samples were irradiated with monochromatised CuKα radiation and analysed over a 2θ angle range 3–40°. The PXRD pattern was collected with the tube voltage of 40 kV, and tube current of 40 mA and a scan speed of 0.1 s per step. Fourier-Transform Infrared

spectroscopy (FT-IR) spectra of samples were obtained using an FT-IR spectrometer (Nicolet Continuum XL, Thermo Fisher Scientific, USA). Briefly, the sample and KBr were mixed well in a ratio of 1:10, followed by compression to form a disk. 128 scans were carried out in wavenumber range 400–4000 cm^{-1} at a resolution of 4 cm^{-1}. Thermogravimetric analyses (TGA) were performed using a TGA/SDTA851 thermal analysis system (Mettler Toledo, Switzerland) at a heating rate of 10 °C·min^{-1} under an atmosphere of nitrogen. ^{1}H Nuclear magnetic resonance (^{1}H NMR) spectra were recorded at ambient temperature on a Bruker Avance 500 spectrometer, with a working frequency of 500 MHz for ^{1}H nuclei. A N_2 adsorption-desorption isotherm was measured using a liquid N_2 bath (−196 °C) and a porosimeter (TriStar 3000 V6.05 A, Micromeritics, USA). In order to remove interstitial solvents before measurement, the CD-MOF samples were activated by immersing them in CH_2Cl_2 for three days, dried under vacuum at 50 °C for 12 h and then at 50 °C for 6 h for outgassing. The drug loaded samples were dried under vacuum at 50 °C for 12 h and then at 50 °C for 6 h for outgassing without activation.

2. Synthetic Protocols

2.1 Preparation of Micron and Nanometer-Sized CD-MOFs

CD-MOFs were synthesised by solvent evaporation by employing an adaption of a published procedure.[S1] Compared with the published procedure at room temperature, higher temperature (50 °C) of MeOH diffusion was employed in this investigation. Noticeably, it was found that pre-addition of MeOH to the aqueous solution of γ-CD and KOH can shorten the synthesis time and improve the efficiency. Micron-sized CD-MOFs were prepared from a mixture of γ-CD (162 mg, 0.125 mmol) with 8 molar equiv of KOH (56 mg, 1 mmol) in H_2O (5 mL). The aqueous solution was filtered through a 0.45 μm filter membrane into a glass tube, and MeOH (0.5 mL) was added, followed by vapour diffusion of MeOH into the aqueous solution at 50 °C. After 6 h,

the supernatant was transferred into another glass tube with addition of CTAB (8 mg·mL^{-1}). After thoroughly dissolving CTAB, the aqueous solution was incubated overnight at room temperature. The precipitate was then harvested and washed with ^{i}PrOH three times, and dried (37 °C) overnight to produce CD-MOFs ca. 5–10 μm cubes (CD-MOF microcrystals). The synthetic procedure to produce nanometer-sized CD-MOFs (CD-MOF nanocrystals) was identical to that employed in the preparation of CD-MOF microcrystals, except that MeOH with the same volume of supernatant was added before CTAB was dissolved.

The stability of CD-MOF microcrystals was investigated by suspending CD-MOF microcrystals (500 mg) in different solvents (10 mL) at 70 °C, including EtOH, MeOH, Me_2CO, CH_2Cl_2, DMF and ^{i}PrOH. After 1 day, the crystallinity of CD-MOF crystals was characterised by PXRD. In addition, the release profile of CD molecules from CD-MOF microcrystals incubated in DMF was also measured. CD-MOF microcrystals (500 mg) were suspended in DMF (10 mL) at 70 °C. An aliquot (0.5 mL) of supernatant was subjected to analytical HPLC in order to quantify the released organic linker, γ-CD. The concentration of the released γ-CD in the supernatant was determined using the HPLC (Agilent 1290, USA) equipped with an evaporative light-scattering detector (ELSD). The analysis was carried out with the Diamonsil C18 column (4.6 mm×150 mm, 5 μm i.d.), under a flow rate of 1.0 mL·min^{-1} and an injection volume of 20 μL. The column temperature was kept at 25 °C. The mobile phase was composed of MeCN and H_2O (60:40). The ELSD detection was carried out with the drift tube temperature of 70 °C, the nebulizer gas pressure of 3.0 bar, and the photomultiplier of 1.0. The retention time for γ-CD occurred at about 2.5 min.

2.2 Encapsulation of Drugs in CD-MOFs

IBU and LPZ were used as model drugs. IBU- and LPZ-loaded CD-MOFs were prepared by

both impregnation and co-crystallisation techniques.

Impregnation Method. Impregnation was performed by soaking the dried CD-MOF powders in ethanolic solutions of the drugs. CD-MOFs (100 mg) soaked in an EtOH solution of IBU (40 mg·mL^{-1}, 2.5 mL) and CD-MOFs (200 mg) soaked in an EtOH solution of LPZ (14 mg·mL^{-1}, 3.6 mL) were incubated at 37 °C with a shaking speed of 100 rpm for an appropriate period of time. The drug-loaded CD-MOFs were collected by centrifugation and washed with the same incubation solvent three times (3×14 mL) until no drug molecules could be detected in the washing solution, ensuring any surface adsorbed free drug molecules were completely removed. After that, the sample was dried under vacuum overnight at 37 °C. In order to investigate the effect of solvents on drug loading, five solvents were selected as the incubation solvents namely EtOH, DMF, Me_2O, MeOH, and CH_2Cl_2. The drug concentrations were the same as those described above.

Co-crystallisation Method. The preparation of drug-loaded CD-MOFs by means of co-crystallisation was similar to that employed in the synthesis of CD-MOF nanocrystals, except that LPZ (30 mg·mL^{-1}) was added to the γ-CD-KOH solution initially, while IBU was dissolved in MeOH (20 mg·mL^{-1}) before CTAB was added. The effect of the drug concentration (20/30/40 mg·mL^{-1} for IBU and 10/20/30 mg·mL^{-1} for LPZ) on the drug loading was investigated.

2.3 Fabrication of CD-MOF/PAA Composite Microspheres

The CD-MOF/PAA composite microspheres were prepared by the solid in oil-in-oil (s/o/o) emulsifying solvent evaporation technique. Briefly, drug-loaded CD-MOF nanocrystals (50 mg) were uniformly dispersed in PAA Me_2CO solution (150 mg·mL^{-1}, 3 mL). A dispersion agent, aluminum tristearate (120 mg) was added to this solution and dispersed by sonication. The PAA solution containing aluminum tristearate and CD-MOF nanocrystals was poured into liquid

paraffin (20 mL) previously cooled at 10 °C. Then, the mixture was emulsified by Ultra-Turrax (IKA®, Germany) with a speed of 10,000 rpm for 5 min at 10 °C. The emulsion was heated to 35 °C gradually (heating rate of 1 °C·min^{-1}) and maintained at 35 °C for 3 h under stirring at 500 rpm to remove Me_2CO. The microspheres were collected by centrifugation, washed two times with n-hexane (25 mL each time) and dried under vacuum overnight.

For comparison, blank microspheres, IBU/LPZ microspheres and IBU/LPZ-γ-CD microspheres were also synthesised according to the emulsifying solvent evaporation procedure described above. The blank microspheres were prepared from PAA polymer. IBU/LPZ microspheres are obtained from drug raw materials and IBU/LPZ-γ-CD microspheres were synthesised from drug-γ-CD complexes (sieved with 200-mesh sieve). The drug-γ-CD complex was synthesised as follows. γ-CD (770 mg) was dissolved in the $NaHCO_3$-NaOH-buffered solution, $NaHCO_3$ (90 mg) was dissolved in H_2O (30 mL) and the pH was adjusted to 11 with 0.1 M NaOH solution while the temperature was maintained as 40 °C. The drug (220 mg for LPZ and 122 mg for IBU) was dissolved in EtOH (15 mL) so as to result in a molar ratio of drug to γ-CD of 1:1. The drug solution was added to γ-CD solution drop-by-drop while stirring for 2 h. EtOH in the resulting clear solution was removed by rotary evaporation at 45 °C for 40 min and the remaining liquid was dried under N_2 purging. The resulting residue was dried under vacuum at 35 °C overnight. The drug loadings of IBU-γ-CD and LPZ-γ-CD complexes were 11.2±0.44 and 19.6±0.31%, respectively.

In order to verify the presence of drug-loaded CD-MOF crystals in the microspheres, they were dissolved and CD-MOF crystals were isolated as follows. The microspheres (100 mg) were placed in a 10-mL Eppendorf tube and EtOH (8 mL) was added under sonication (10 min) to dissolve the PAA polymer. The suspension was centrifuged (12,000 rpm, 5min) and precipitates, which were composed of CD-MOF and aluminum tristearate crystals with different densities,

were isolated. They were further separated after being dispersed in CH_2Cl_2 (8 mL) and centrifuged (12,000 rpm, 5 min), resulting in CD-MOF crystals in the precipitate and aluminum stearate floating in the upper layer. The CD-MOF crystals in the precipitate were harvested and dried for observation by SEM.

Drug loading (DL) is defined as the percent of drug measured in the drug-loaded CD-MOF or CD-MOF/PAA microsphere samples and was calculated according to the following equation:

$$\mathrm{DL}\,(\%) = \frac{\text{Amount of drug in CD-MOFs or microspheres}}{\text{Total amount of drug-loaded CD-MOFs or microspheres}} \times 100 \qquad \text{(S1)}$$

The DL values of encapsulated drugs in CD-MOFs were measured by dissolving the sample (10 mg) in H_2O (6 mL). The amounts of the drugs were analysed by HPLC (Agilent 1290, USA). For CD-MOF/PAA composite microspheres, the drug loading was determined by dissolving the microspheres (5 mg) in 67% MeOH (v/v, 3 mL) under sonication for 10 min and analysing the solution by HPLC, equipped with a diode array detector. The analysis was carried out using a Phenomenex C18 column (4.6 mm×150 mm, 5 μm) with a flow rate of 1.0 $mL \cdot min^{-1}$ and an injection volume of 20 μL. IBU was detected at 263 nm and the column temperature was set at 35 °C. The mobile phase was composed of NaOAc buffer solution and MeCN (40:60, v/v). The NaOAc buffer solution was obtained by dissolving NaOAc (6.13 g) in pure H_2O (750 mL) and adjusting the pH to 2.5 with glacial HOAc. For LPZ, the detection wavelength was set at 284 nm. The mobile phase was composed of MeOH, H_2O, TEA and H_3PO_4 (640:360:5:1.5, pH was adjusted to 7.3 with H_3PO_4). The column temperature was maintained at 40 °C.

2.4 In vitro Release of Drugs from Microspheres

Microspheres equivalent to 1 mg of IBU or LPZ were suspended in the release medium (50 mL) containing polysorbate 80 (0.02%, w/v) and the suspension was maintained at 37 °C with a stirring rate of 100 rpm. The release medium for IBU was PBS with pH 7.4, and that for LPZ

was a carbonate buffer solution with pH 9.7 because of the instability of LPZ at pH of 7.4. These release mediums were prepared according to Chinese Pharmacopeia 2010. Samples (1.0 mL) were withdrawn at regular time intervals (0.5, 1, 2, 4, 6, 8, 12, 24 and 48 h) and the same volume of fresh medium was added. The concentration of the drug in each sample was determined by the HPLC and the release percentage was calculated. Experiments were performed in triplicate.

2.5 Cytotoxicity Assays

The cytotoxicity of CD-MOF and CD-MOF/PAA composite microspheres was evaluated on J774 macrophage cells using the MTT (3-(4,5-dimethylthiazol-2-yl)-2,5-diphenyltetrazolium bromide) method. J774A.1 Cells (mouse macrophages, ATCC® TIB-67™) were grown in RMPI 1640 medium supplemented with 10% (v/v) fetal bovine serum (Gibco, USA), penicillin (100 $U \cdot mL^{-1}$) and streptomycin (100 $\mu g \cdot mL^{-1}$). Cells were maintained in a humidified incubator with 95% air and 5% CO_2 at 37 °C and seeded into 96-well microtiter plates at a density of 2000 $cells \cdot well^{-1}$. After incubating overnight, samples (20 μL) at concentrations equivalent to the IBU concentrations, ranging from 0.008 to 1.0 $mg \cdot mL^{-1}$ (with a five-fold dilution gradient) were added to the medium and incubated for 24 h. Then, MTT (15 μL, 5 $mg \cdot mL^{-1}$) was added to the cell culture medium and incubated for 4 h. Subsequently, the medium was replaced by Me_2SO (150 μL) to dissolve the insoluble crystals of formazan formed by living cells. The absorbance at 490 nm was read using a microplate reader (Multiskan GO, Thermo Fisher). Non-treated cells were used as a control and the cell viability (%) was calculated using Eq. S2. Results were expressed as mean ± standard deviation.

$$\text{Cell viability}\,(\%) = \frac{A_{490,\,\text{sample}}}{A_{490,\,\text{control}}} \times 100 \qquad \text{(S2)}$$

3. Data on Drug Encapsulation in MOF Particles[S2–S34]

Table S1 Overview of Drug Encapsulation in Metal-Organic Frameworks Particles

MOF	Metal Ion	Organic Linker	Inner Pore Size (Å)	Drug	Loading Method	Drug Loading (%, w/w)	Ref
MIL-100 (Cr)	Cr	BTC	25–29	Ibuprofen	Impregnation	25.9	S2
MIL-101 (Cr)	Cr	BDC	29–34	Ibuprofen	Impregnation	58	S2
MIL-53 (Cr) and MIL-53 (Fe)	Cr, Fe	BDC	8.6	Ibuprofen	Impregnation	20	S3
Bio-MOF-1	Zn	BPDC	5.2	Procainamide HCl	Cation exchange	18	S4
MIL-101 (Fe)	Fe	BDC	29–34	Ethoxysuccinato-cisplatin prodrug	Postsynthetic modification	12.8	S2, S5
MIL-101 (Cr)	Cr	BDC	29–34	Ibuprofen	Computational prediction	52.6	S2, S6
UMCM-1	Zn	BDC and H_3BTB	24–32	Ibuprofen	Computational prediction	57.6	S6
BioMIL-1	Fe	Nicotinic acid	–	Nicotinic acid	Active molecules as	71.5	S7
M-CPO-27	Co and Ni	2,5-Dihydroxyterephthalic acid	11–12	NO	Active molecules as	17.4	S8
NCP-1	Tb	Disuccinatocisplatin	–	Disuccinatocisplatin	Active molecules as	75	S9
$Ag_3(1)$	Ag	3-Phosphonobenzoic acid	–	Silver ions	Active molecules as	64.4	S10
$[(CH_3)_2NH_2]_2$ $[Zn(TATAT)_{2/3}]$	Zn	5,5',5"-(1,3,5-Triazine-2,4,6-triyl)tris (azanediyl)triisophthalate	14.3–31.3	5-FU	Impregnation	33.3	S11
HKUST-1	Cu	BTC	6–12	Nimesulide	Impregnation	16.7	S12

MOF	Metal Ion	Organic Linker	Inner Pore Size (Å)	Drug	Loading Method	Drug Loading (%, w/w)	Ref
MIL-100 (Cr)	Cr	BTC	25–29	Peptides	Incubation	9–15	S13
MIL-101 (Cr)	Cr	BDC	29–34	Peptides	Incubation	20–39	S13
MIL-53 (Al)	Al	BDC	8.6	Peptides	Incubation	19–35	S13
MIL-100 (Fe)	Fe	BTC	25–29	Busulfan	Impregnation	26±3	S14
MIL-53 (Fe)	Fe	BDC	8.6	Busulfan	Impregnation	10±2	S14
MIL-88A (Fe)	Fe	Fumaric acid	6	Busulfan	Impregnation	8±1	S14
MIL-89 (Fe)	Fe	Muconic acid	11	Busulfan	Impregnation	14±2	S14
MOP-15	Cu	5-NH_2-*m*-Benzenedicarboxylate	16	5-FU	Impregnation	23.76	S15
Rho-ZMOF	In	4,5-Imidazoledicarboxylic acid	18.2	Procainamide HCl	Impregnation	9.9	S16
MIL-88B (Fe)	Fe	Terephthalate organic linkers bearing different functional groups	8	Caffeine	Impregnation	9.8–22.8	S17
$[Zn(BDC)(H_2O)_2]_n$	Zn	BDC	7	Ibuprofen	Impregnation	44.5	S18
IFMC-1	Zn	4,5-Di(1H-tetrazol-5-yl)-2H-1,2,3-triazole	11.6	5-FU	Impregnation	30.48	S19
Cu-BTC	Cu	BTC	9	5-FU	Impregnation	45.0	S20
CPO-27-Ni	Ni	2,5-Dihydroxyterephthalic acid	11–12	NO	Impregnation	15.3	S21
MIL-100 (Fe)	Fe	BTC	25–29	Caffeine	Impregnation	49.5±1.9	S22

MOF	Metal Ion	Organic Linker	Inner Pore Size (Å)	Drug	Loading Method	Drug Loading (%, w/w)	Ref
MIL-53 (Fe)	Fe	BDC	8.6	Caffeine	Impregnation	29.2±1.5	S22
UiO-66 (Zr)	Zr	BDC	8–11	Caffeine	Impregnation	22.4±3.4	S22
MIL-101 (Cr)	Cr	BDC	29–34	Naproxen	Incubation	–	S23
MOF-74-Fe (II)	Fe	2,5-Dioxido-1,4-benzenedicarboxylate	10.8	Ibuprofen	Ion exchange and salt	15.5	S24
UiO-66 (Zr)	Zr	BDC	8–11	Caffeine and Ibuprofen	Impregnation	20.4 and 20.7	S22, S25
Gd-pDBI	Gd	1,4-Bis(5-carboxy-1H-benzimidazole-2-yl)benzene	12–19	Doxorubicin	Sonication and stirring	12	S26
UiO-NMOFs	Zr	Aminotriphenyldicarboxylic acid	–	Cisplatin prodrug; Pooled SiRNAs	Post-synthetic encapsulation;	12.3±1.2; 81.6±0.6	S27
MIL-100 (Fe)	Fe	BTC	25–29	Topotecan	Impregnation	33	S28
CD-MOF-2	Rb	γ-CD	17	Rhodamine B	Co-crystallization	–	S29
MIL-100 (Al)	Al	BTC	25–29	Pd nanoparticles	Chemical wetting	10	S30
MIL-100 (Fe)	Fe	BTC	25–29	Azidothymidine-triphosphate	Impregnation	36.0	S31
MIL-100 (Fe)	Fe	BTC	25–29	Phosphorylated Azidothymidine	Impregnation	24.4±0.9	S32
MIL-100 (Fe)	Fe	BTC	25–29	Doxorubicin	Impregnation	30.7±0.8	S33
MIL-100 (Fe)	Fe	BTC	25–29	Phosphated gemcitabin	Impregnation	9.0	S34
CD-MOF-1	K	γ-CD	17	Ibuprofen Lansoprazole	Cocrystallsiation	12.7 4.5	This study

BTC: 1,3,5-Benzene tricarboxylic acid; BDC: 1,4-Benzenedicarboxylic acid; BPDC: Adenine and biphenyldicarboxylate; H_3BTB: 1,3,5-Tris(4-carboxyphenyl)benzene

4. Residual of CTAB, Stability and Size Distribution of CD-MOFs

As described in the Section 2.1 on the "Preparation of Micron and Nanometer-Sized CD-MOFs", the freshly obtained CD-MOF microcrystals and nanocrystals were washed with ^{i}PrOH three times, and dried (37 °C) overnight for further use. The ^{1}H NMR spectrum (**Fig. S1**) shows that there is no CTAB trapped in the CD-MOF nanocrystal after washing the CD-MOF nanocrystals with ^{i}PrOH three times. In addition, MeOH (δ = 3.34 ppm) was completely removed after the CD-MOF nanocrystals had been dried (37 °C) overnight.

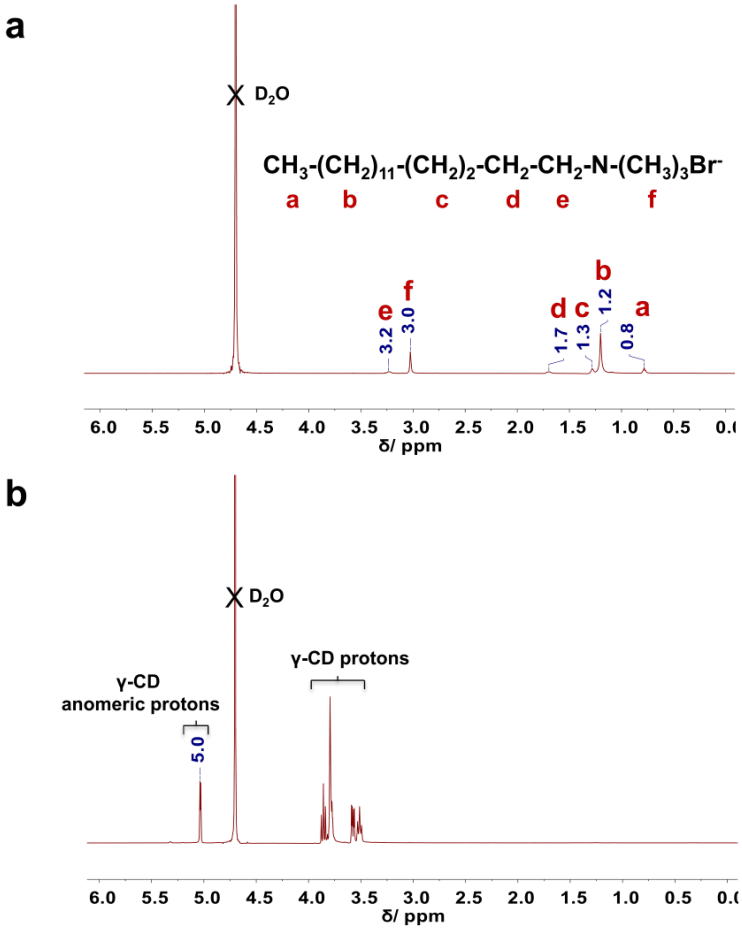

Fig. S1 ^{1}H NMR spectrum (500 MHz) in D_2O of a) CTAB (5 mg·mL^{-1}) and b) redissolved CD-MOF nanocrystals prepared from potassium hydroxide and γ-CD (10 mg·mL^{-1}), referenced to the H_2O peak (δ = 4.79 ppm).

The crystallinity of CD-MOFs decreases (**Fig. S2**) after one day of incubation with DMF, MeOH, Me_2CO and EtOH at 70 °C. In the case of DMF and MeOH, the intensity for all of the peaks decreased significantly and peaks at 16.7° disappeared, indicating the instability of CD-MOF microcrystals in DMF and MeOH. This observation might be a result of the relatively higher solubility of γ-CD in these two solvents. **Fig. S2** also illustrates the CD release profile for the CD-MOF microcrystals incubated in DMF at 70 °C for three days. It should be noted that about 4% of the total amount of the organic linker in the CD-MOF microcrystals was released after one day of incubation and 6% after three days of incubation.

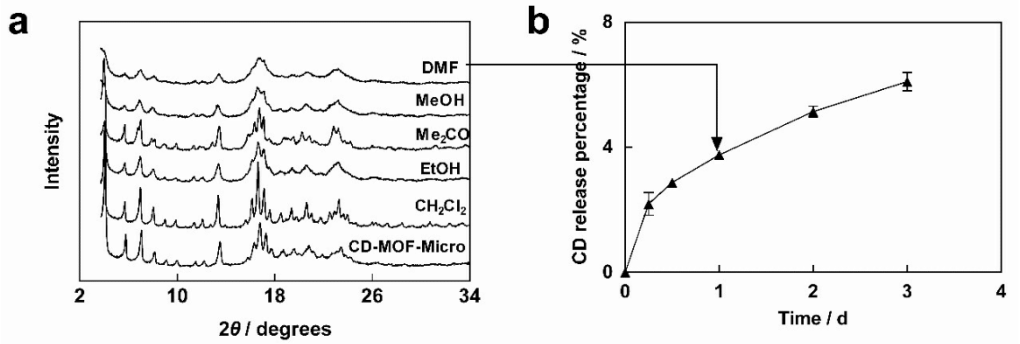

Fig. S2 a) PXRD Pattern of CD-MOF microcrystals incubated in different solvents at 70 °C for one day. b) The CD release profile for the incubation in DMF at 70 °C for three days. Error bars are based on repeating experiments on three batches of crystals.

The crystal size distributions of CD-MOF nanocrystals were characterised employing both SEM and DLS techniques. The SEM images (**Fig. 2b**) show the CD-MOF nanocrystals with diameters of 500–700 nm. The DLS result (**Fig. S3**) also reveals a mean diameter of 650 nm, with a polydispersity index of 0.22.

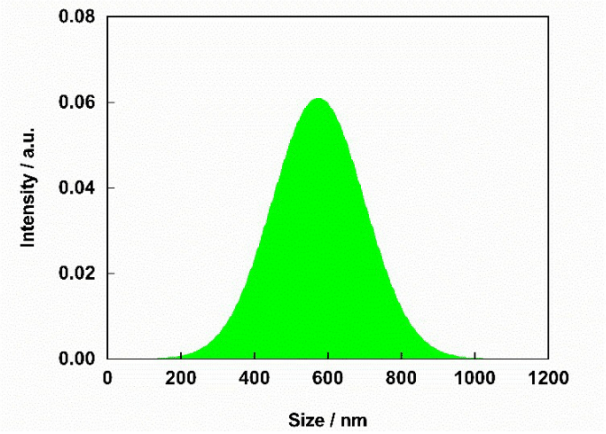

Fig. S3 Intensity particle size distribution of CD-MOF nanocrystals

5. Characterisation of Drug-Loaded CD-MOF Nanocrystals

The amount of drug-loaded into CD-MOFs of micron and nanometer sizes by impregnation and co-crystallisation methods are listed in **Table S2**. It is evident that IBU loading into CD-MOF microcrystals decreased from 12.0 to 6.6% compared with that obtained by the impregnation method. The LPZ loading in CD-MOF microcrystals however, increased from 9.4 to 16.6%, when the impregnation method was replaced by the co-crystallisation technique. In the case of the CD-MOF nanocrystals used to prepare microspheres, drug loading by the co-crystallisation was equivalent to or higher than that by the impregnation method.

Table S2 Drug loading by the impregnation (in EtOH) and the co-crystallisation method for micron and nanometer-sized CD-MOFs

Drug	CD-MOFs	DL (%, w/w) [c]	
		Impregnation	Co-crystallization
IBU	Micro[a]	12.0±0.7	6.6±0.4
	Nano[b]	13.0±0.2	12.7±0.6
LPZ	Micro[a]	9.4±0.3	16.6±0.4
	Nano[b]	1.6±0.1	4.5±0.3

[a] Micro indicates CD-MOF microcrystals with the size of 5–10 μm; [b] Nano indicates CD-MOF nanocrystals with the size of 500–700 nm; [c] DL values are based on repeating experiments on three batches of crystals.

Combined with HPLC analysis, ^{1}H NMR spectroscopy was also employed to estimate the amount of the drug within the CD-MOF nanocrystals prepared by co-crystallisation (**Fig. S4**). When the integral for the anomeric protons (δ ~ 5 ppm) of the γ-CD units is set to 8, representing one γ-CD torus, the aromatic proton signals of IBU (δ ~ 7 ppm) have a combined integral of 4.66 (**Fig. S4a**, four aromatic protons in each IBU molecule). This integral represents a molar ratio of 4:4.66 between γ-CD and IBU, corresponding to the IBU loading percentage of 14.6% (w/w) in IBU-loaded CD-MOF nanocrystals, a result which is similar with that of 12.6% (w/w) measured by HPLC. For LPZ (**Fig. S4b**), when integrating anomeric protons (δ ~ 5 ppm) of the γ-CD units and the pyridine-proton signal of LPZ (δ ~ 8 ppm), a molar ratio of 1:0.18 between γ-CD and LPZ is obtained, corresponding to the LPZ loading percentage of 4.5% (w/w) in LPZ-loaded CD-MOF nanocrystals, which is similar to that of 4.5% (w/w) measured by HPLC.

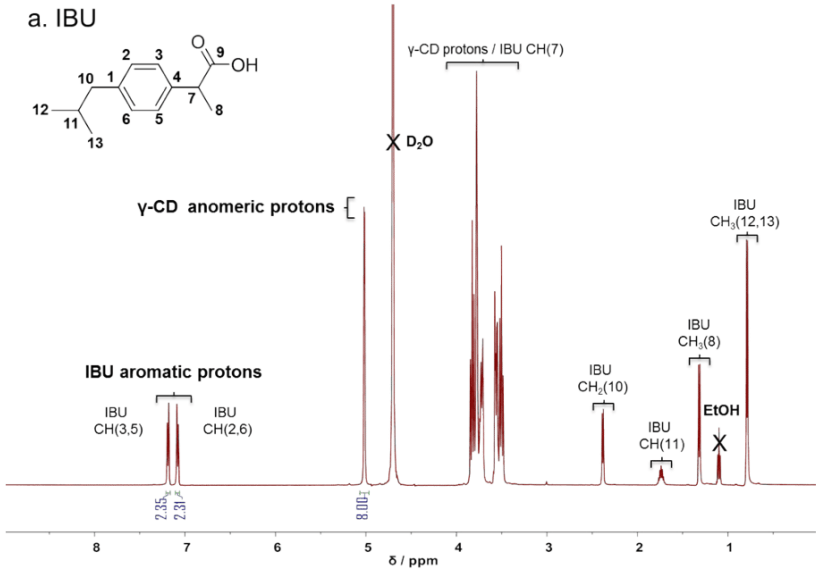

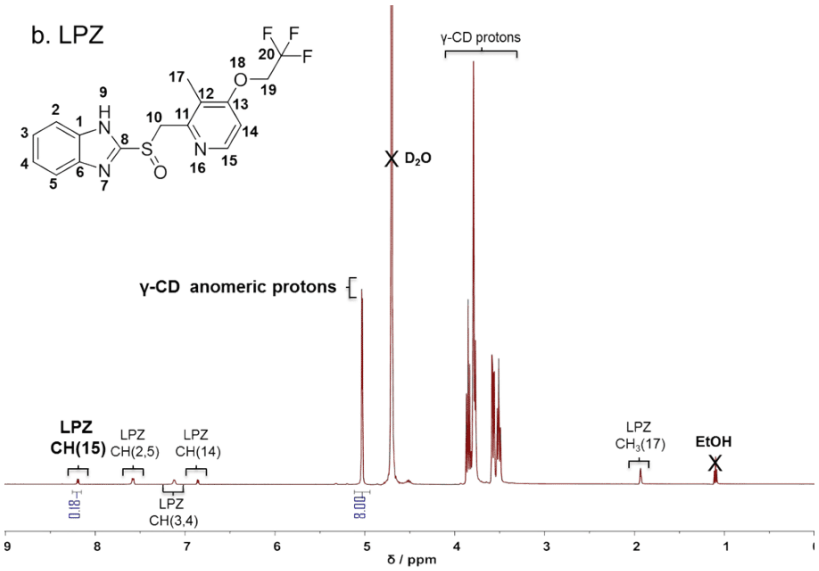

Fig. S4 ^{1}H NMR spectrum (500 MHz) in D_2O of drug-loaded CD-MOF nanocrystals prepared by co-crystallisation (10 mg·mL^{-1}). a) IBU and b) LPZ.

From the SEM images (**Fig. S5**) of the drug-loaded CD-MOFs, it can be concluded that the size of the drug-loaded CD-MOF nanoparticles is about 500–700 nm. The crystallinity of the drug-loaded CD-MOFs, produced by the co-crystallisation technique, was retained as shown by the identical PXRD features mentioned in the main text. In the case of IBU/LPZ loading by impregnation, however the crystallinity of the CD-MOFs was altered as a consequence of the progressive degradation of the MOFs in the solvents.

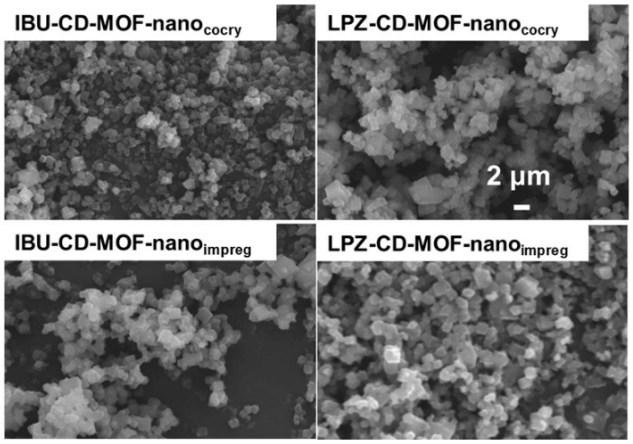

Fig. S5 SEM images of drug-loaded CD-MOF nanocrystals prepared by co-crystallisation and impregnation techniques.

Fig. S6 displays the IR spectra of the drug-loaded CD-MOFs. The characteristic vibrational band of the carboxylic group (ν(C=O)) in IBU, located at 1722 cm^{-1}, cannot be identified in the IBU-loaded CD-MOF nanocrystals. The ν(C=O) band is present, however, in a physical mixture with equivalent composition at 1722 cm^{-1}, indicating that the IR spectrum of IBU-loaded CD-MOF nanocrystals is different from that of the corresponding physical mixture. For LPZ, the characteristic vibrational band for the aromatic ring located at 1580 cm^{-1} also disappeared in the LPZ-loaded CD-MOF nanocrystals. In a physical mixture with an equivalent composition (LPZ loading of 4.5%), the characteristic vibrational band of the aromatic ring in LPZ at 1580 cm^{-1} was not detected as a consequence of the relative low loading of the drug (< 5%).

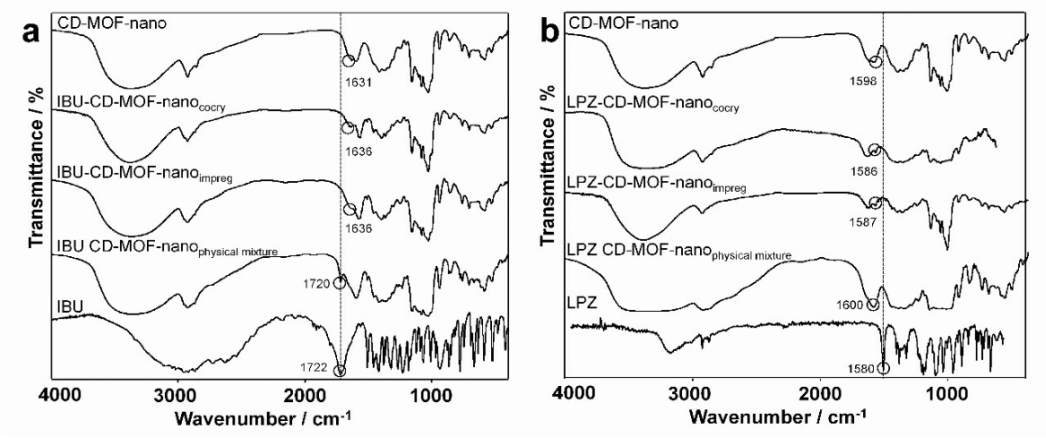

Fig. S6 IR Spectra of drug-loaded CD-MOF nanocrystals prepared by the co-crystallisation and impregnation techniques. a) IBU. b) LPZ.

TGA analysis was also used to confirm the incorporation of IBU into CD-MOF framework together with IR analysis (**Fig. S7**). After solvent loss below 100 ºC, the decomposition temperature is approximately 150 ºC for pure IBU and 175 ºC for CD-MOF. For the physical mixture of IBU and CD-MOF (87:13, w/w), the weight loss of about 14% (w/w) is found at 150–275 ºC, which can be identified as the IBU content. For IBU-loaded CD-MOF nanocrystals, however, weight loss does not appear until 200 ºC.

For LPZ, decomposition is observed at approximately 170 ºC, and the weight loss curve of LPZ-loaded CD-MOF nanocrystals almost overlaps with that of pure CD-MOF nanocrystals, an observation which is most likely a result of the relatively low drug loading percentage (4.5%).

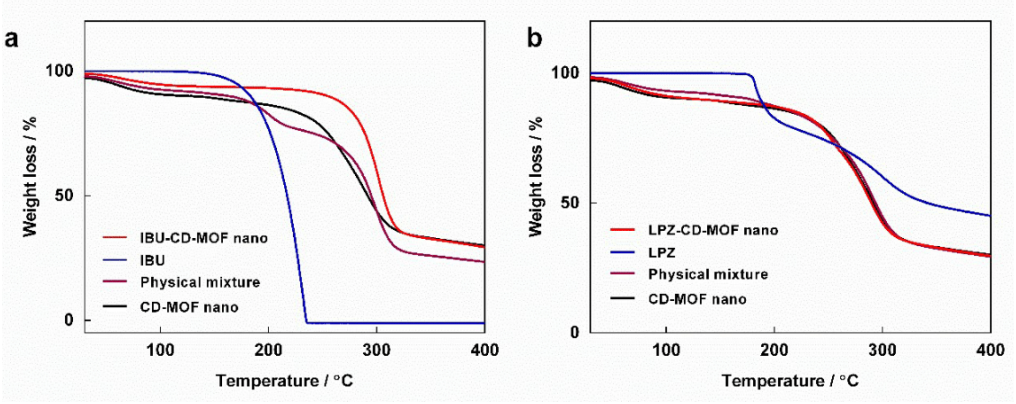

Fig. S7 TGA traces of drug-loaded CD-MOF nanocrystals prepared by the co-crystallisation. a) IBU. b) LPZ.

The BET surface area of CD-MOF materials was determined by N_2 adsorption using BET method. **Fig. S8** shows the nitrogen isotherms for CD-MOF microcrystals, CD-MOF nanocrystals and the drug-containing samples. The isotherms for CD-MOF crystals show the characteristic of the microporosities with a steep N_2 uptake in the low-pressure regions (P/P_0<0.05). The BET surface areas are 1002, 786, 668, 96 and 158 $m^2 \cdot g^{-1}$ for CD-MOF (100-micron meter), CD-MOF microcrystals, CD-MOF nanocrystals, IBU-loaded and LPZ-loaded CD-MOF nanocrystals, respectively (**Table S3**). The surface areas of CD-MOF micron and nanocrystals are decreased compared with that of the CD-MOF (100-micron meter). This observation might be as a result of the size reduction[S35], and the trace amount of CTAB residue in the sample, which is under the detection limit of ^{1}H NMR spectroscopy and might block partially the pores of CD-MOF. After drug incorporation, the BET surface area of the CD-MOF nanocrystals decreases dramatically,

indicating the drug fills completely and/or blocks the pores of the material leaving little to no accessible pore volume for nitrogen.[S2]

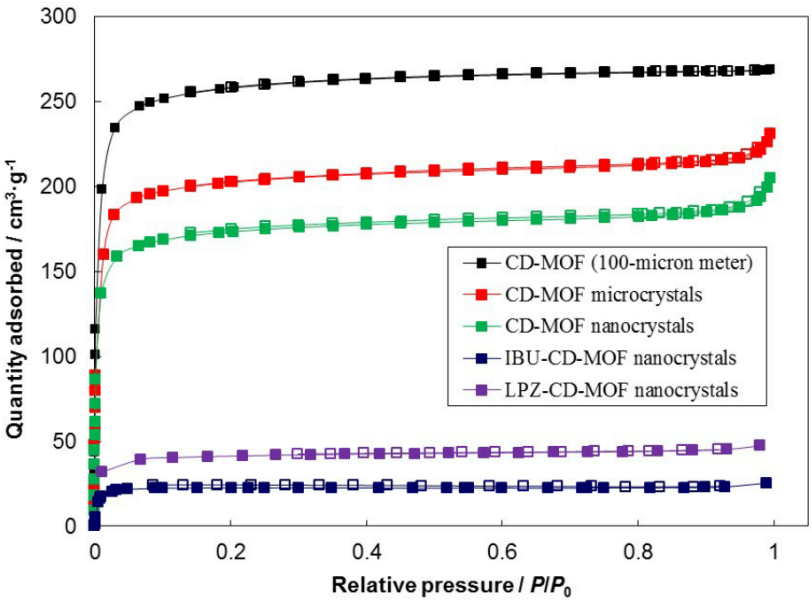

Fig. S8 N_2 Adsorption-desorption isotherms measured at 77 K for activated samples of CD-MOF microcrystals, CD-MOF nanocrystals and drug-loaded CD-MOF nanocrystals prepared by co-crystallisation. Filled and open symbols represent adsorption and desorption curves, respectively.

Table S3 The surface area of CD-MOFs and drug-loaded CD-MOF nanocrystals

	Surface area ($m^2 \cdot g^{-1}$)		
	S_{BET}	S_{micro}	$S_{external}$
CD-MOF (100-micron meter)	1002	950	52
CD-MOF microcrystals	786	754	32
CD-MOF nanocrystals	668	625	43
IBU-CD-MOF nanocrystals	96	88	8
LPZ-CD-MOF nanocrystals	158	133	24

S_{BET}: BET surface area; S_{micro}: micropore surface area; $S_{external}$: external surface area; The micropore surface area and the external surface area are calculated by the *t*-plot method.

6. Characterisation and Drug Release of the Composite Microspheres

In order to verify the presence of the drug-loaded CD-MOF crystals in the microspheres, samples were treated with EtOH and CH_2Cl_2 so as to remove and separate PAA and aluminum tristearate crystals from the CD-MOFs. The SEM images (**Fig. S9**) of the

retrieved CD-MOFs verify the intact morphology of the drug-loaded CD-MOFs crystals in the microspheres.

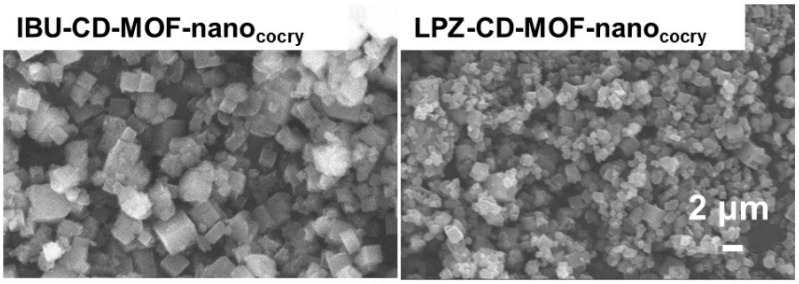

Fig. S9 SEM Images of the drug-loaded CD-MOF nanocrystals encapsulated in PAA composite microspheres after dissolving the microspheres with EtOH and removal of aluminum stearate.

For the drug loading of microspheres shown in **Table S4**, most of the values were consistent with the theoretical values, except for the microspheres prepared by IBU raw materials. The measured DL values were relatively higher than the theoretically calculated ones, an observation which might result from the adhesion of PAA on the side of the beaker and loss of PAA during microsphere preparation.

Table S4 Drug loading of microspheres prepared by drug raw material, drug-γ-CD complex and drug-loaded CD-MOF nanocrystals

Drug	DL (%, w/w) [a]		
	Drug microspheres	Drug-γ-CD microspheres	Drug-loaded CD-MOF microspheres
IBU	2.63±0.01 (8.06)	0.82±0.00 (0.90)	1.18±0.02 (1.02)
LPZ	9.85±0.21 (8.06)	1.52±0.03 (1.58)	0.59±0.00 (0.36)

a Values are based on repeating experiments on three batches of crystals and values in the parentheses represent the theoretical drug loading percentages. The components for all of the microspheres are drug or drug-γ-CD complex or drug-loaded CD-MOF (8.06%, w/w), PAA (72.58%, w/w) and aluminum tristearate (19.35%, w/w).

In the FT-IR spectrum (**Fig. S10**) of blank PAA microspheres , the sharp peaks at 2800–3000, 1600–1800 and 800–900 cm^{-1} can be assigned to the characteristic stretching

vibrations of C–H, C=O and C–O bonds in PAA. Compared with blank microspheres, the changes in these three characteristic peaks are observed in LPZ-CD-MOF/PAA composite microspheres and also in the LPZ and LPZ-CD microspheres. Especially in the case of the LPZ-CD-MOF/PAA composite microspheres, these peaks disappear or are broadened, indicating the strong interactions between the two components – namely, CD-MOFs and PAA – in the composite microspheres. In the case of the microspheres loaded with IBU, there is no significant change in the main characteristic peaks compared with those of the blank microspheres.

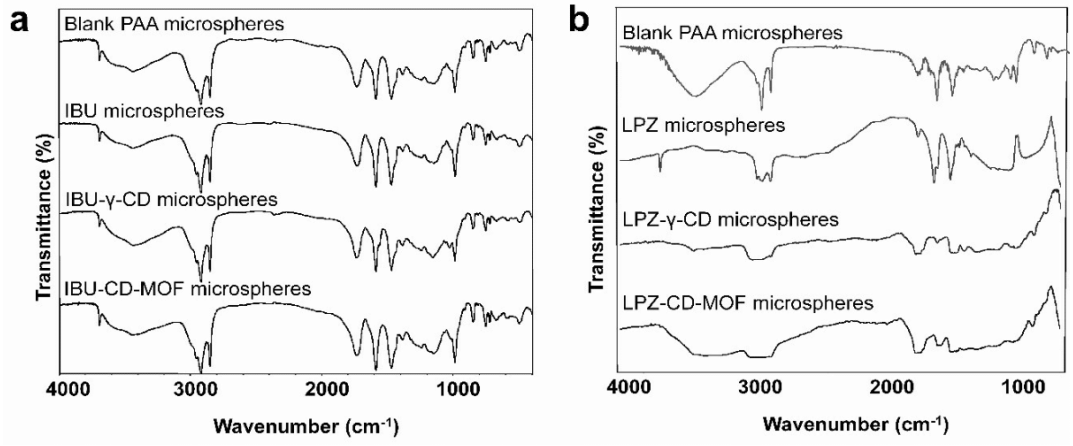

Fig. S10 IR Spectra of blank PAA microspheres, drug microspheres, drug-γ-CD microspheres and drug-loaded CD-MOF microspheres. a) IBU. b) LPZ.

Fig. S11 shows the release profiles of microspheres within the first 6 h, exhibiting the drug release behaviour in the initial stages. Microspheres containing drug-γ-CD complexes showed a very fast "burst" and uncontrolled release, i.e., 70% in 30 min, 80% in 2 h for both of the microspheres prepared from IBU and LPZ-γ-CD complexes. When drug-loaded CD-MOF nanocrystals were incorporated into the composite microspheres, steady and slow drug release was achieved, with release percentages being not more than

20% at 6 h: no burst release was observed.

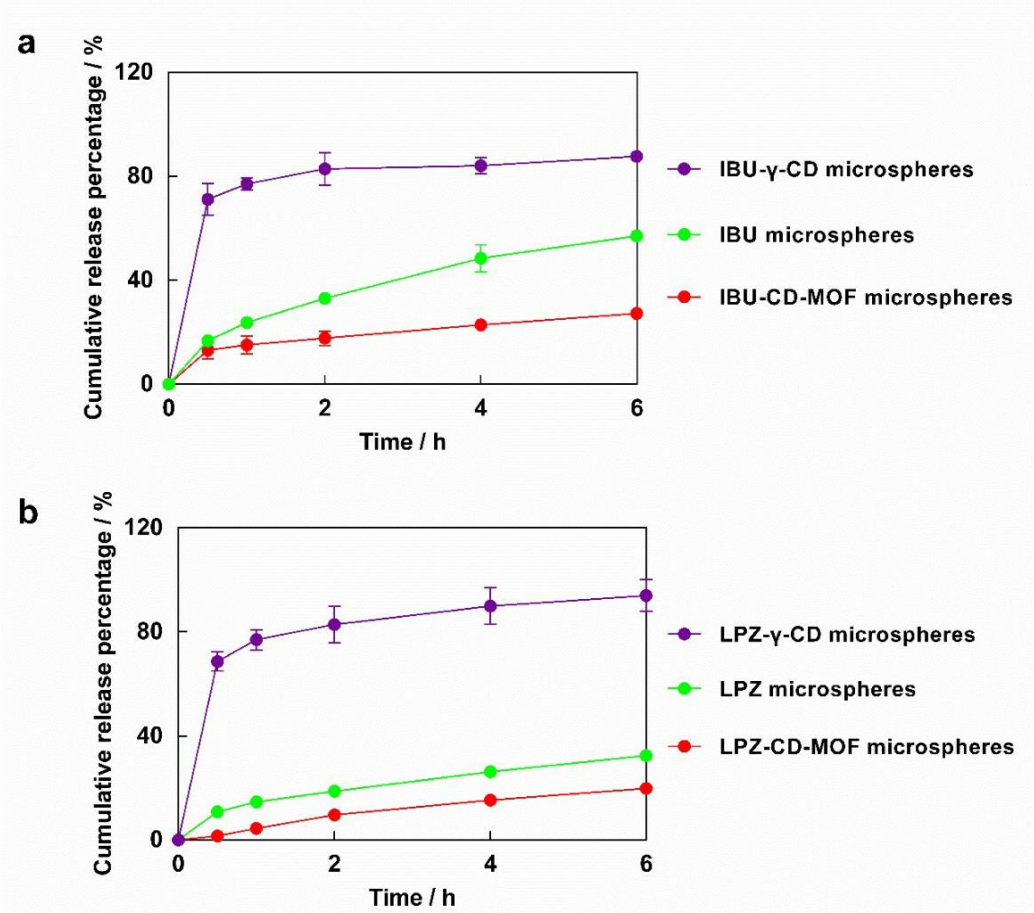

Fig. S11 The release profiles drug microspheres, drug-γ-CD microspheres and drug-CD-MOF microspheres. a) IBU. b) LPZ. Error bars are based on repeating experiments on three batches of microspheres.

7. References

S1 R. A. Smaldone, R. S. Forgan, H. Furukawa, J. J. Gassensmith, A. M. Slawin, O. M. Yaghi and J. F. Stoddart, *Angew. Chem. Int. Ed.*, 2010, **49**, 8630-8634. (b) Y. Furukawa, T. Ishiwata, K. Sugikawa, K. Kokado and K. Sada, *Angew. Chem. Int. Ed.*, 2012, **51**, 10566-10569.

S2 (a) P. Horcajada, C. Serre, M. Vallet-Regí, M. Sebban, F. Taulelle and G. Férey, *Angew. Chem. Int. Ed.*, 2006, **45**, 5974-5978. (b) N. Lv, T. Guo, B. T. Liu, C. F. Wang, V. Singh, X. N. Xu, X. Li, D. W. Chen, R. Gref and J. W. Zhang, *Pharm. Res.*, 2016, Epub ahead of print.

S3 P. Horcajada. C. Serre, G. Maurin, N. A. Ramsahye, F. Balas, M. Vallet-Regí, M. Sebban, F. Taulelle and G. Férey, *J. Am. Chem. Soc.*, 2008, **130**, 6774-6780.

S4 (a) J. An, S. J. Geib and N. L. Rosi, *J. Am. Chem. Soc.*, 2009, **131**, 8376-8377. (b) J. An and N. L. Rosi, *J. Am. Chem. Soc.*, 2010, **132**, 5578-5579.
S5 K. M. Taylor-Pashow, Rocca. J. Della, Z. Xie, S. Tran and W. Lin, *J. Am. Chem. Soc.*, 2009, **131**, 14261-14263.
S6 (a) K. Koh, A. G. Wong-Foy and A. J. Matzger, *Angew. Chem. Int. Ed.*, 2008, **47**, 677-680. (b) R. Babarao and J. Jiang, *J. Phys. Chem. C*, 2009, **113**, 18287-18291.
S7 S. R. Miller, D. Heurtaux, T. Baati, P. Horcajada, J. M. Grenèche and C. Serre, *Chem. Commun.*, 2010, **46**, 4526-4528.
S8 N. J. Hinks, A. C. Mckinlay, B. Xiao, P. S. Wheatley and R. E. Morris, *Micropor. Mesopor. Mat.*, 2010, **129**, 330-334.
S9 R. C. Huxford, Rocca. J. Della and W. Lin, *Curr. Opin. Chem. Biol.*, 2010, **14**, 262-268.
S10 M. Berchel, T. L. Gall, C. Denis, S. L. Hir, F. Quentel, C. Elléouet, T. Montier, J-M. Rueff, J-Y. Salaün, J-P. Haelters, G. B. Hix, P. Lehn and P-A. Jaffrès, *New J. Chem.*, 2011, **35**, 1000-1003.
S11 C. Y. Sun, C. Qin, C. G. Wang, Z. M. Su, S. Wang, X. L. Wang, G. S. Yang, K. Z. Shao, Y. Q. Lan and E. B. Wang, *Adv. Mater.*, 2011, **23**, 5629-5632.
S12 F. Ke, Y. P. Yuan, L. G. Qiu, Y. H. Shen, A. J. Xie, J. F. Zhu, X. Y. Tian and L. D. Zhang, *J. Mater. Chem.*, 2011, **21**, 3843-3848.
S13 Z. Y. Gu, Y. J. Chen, J. Q. Jiang and X. P. Yan, *Chem. Commun.*, 2011, **47**, 4787-4789.
S14 (a) P. Horcajada, T. Chalati, C. Serre, B. Gillet, C. Sebrie, T. Baati, J. F. Eubank, D. Heurtaux, P. Clayette, C. Kreuz, J. S. Chang, Y. K. Hwang, V. Marsaud, P. N. Bories, L. Cynober, S. Gil, G. Férey, P. Couvreur and R. Gref, *Nat. Mater.*, 2010, **9**, 172-178. (b) T. Chalati, P. Horcajada, P. Couvreur, C. Serre, M. Ben Yahia, G. Maurin and R. Gref, *Nanomedicine (Lond)*, 2011, **6**, 1683-1695.S15 H.N. Wang, X. Meng, G. S. Yang, X. L. Wang, K. Z. Shao, Z. M. Su and C. G. Wang, *Chem. Commun.*, 2011, **47**, 7128-7130.
S16 R. Ananthoji, J. F. Eubank, F. Nouar, H. Mouttaki, M. Eddaoudi and J. P. Harmon, *J. Mater. Chem.*, 2011, **21**, 9587-9594.
S17 C. Gaudin, D. Cunha, E. Ivanoff, P. Horcajadab, G. Chevéc, A. Yasric, O. Logetc, C. Serreb and G. Maurina, *Micropor. Mesopor. Mat.*, 2012, **157**, 124-130.
S18 (a) M. Eddaoudi, H.L. Li and O. M. Yaghi, *J. Am. Chem. Soc.*, 2000, **122**, 1391-1397. (b) M. O. Rodrigues, M. V. de Paula, K. A. Wanderley, I. B. Vasconcelos, Jr. Alves and T. A. Soares, *Int. J. Quantum. Chem.*, 2012, **112**, 3346-3355.
S19 J. S. Qin, Y. Q. Lan, D. Y. Du, W. L. Li, J. P. Zhang, S. L. Li, Z. M. Su, X. L. Wang, Q. Xu, K. Z. Shao and Y. Q. Lan, *Chem. Sci.*, 2012, **3**, 2114-2118.
S20 (a) A. Vishnyakov, P. I. Ravikovitch, A. V. Neimark, M. Bulow, Q. M. Wang, *Nano Letters*, 2003, **6**, 713-718. (b) F.R. Lucena, L.C. de Araújo, M. D. Rodrigues, T. G. da Silva, V. R. Pereira, G. C. Militão, D. A. Fontes, P. J. Rolim-Neto, F. F. da Silva

and S. C. Nascimento, *Biomed. Pharmacother.*, 2013, **67**, 707-713.
S21 (a) S. Rojas, P. S. Wheatley, E. Quartapelle-Procopio, B. Gilc, B. Marszalekc, R. E. Morris and E. Barea , *CrystEngComm.*, 2013, **15**, 9364-9367. (b) D. Cattaneo, S.J. Warrender, M.J. Duncan, C.J. Kelsall, M.K. Doherty, P.D. Whitfield, I. L. Megson, R. E. Morris, *RSC Adv.*, 2016, **6**, 14059-14067.S22 D. Cunha, M. Ben Yahia, S. Hall, S. R. Miller, H. Chevreau, E. Elkaïm, G. Maurin, P. Horcajada and C. Serre, *Chem. Mater.*, 2013, **25**, 2767-2776.
S23 Y. L. Hu, C. Y. Song, J. Liao, Z. L. Huang and G. K. Li, *J. Chromatogr. A*, 2013, **1294**, 17-24.
S24 Q. Hu, J. C. Yu, M. Liu, A. P. Liu, Z. S. Dou and Y. Yang, *J. Med. Chem.*, 2014, **57**, 5679-5685.
S25 S. Devautour-Vinot, S. Diaby, D. D. Cunha, C. Serre, P. Horcajada and G. Maurin, *J. Phys. Chem. C*, 2014, **118**, 1983-1989.
S26 T. Kundu, S. Mitra, P. Patra, A. Goswami, D. Díaz and R. Banerjee, *Chem. – Eur. J.*, 2014, **20**, 10514-10518.
S27 C. B. He, K. D. Lu, D. M. Liu and W. B. Lin, *J. Am. Chem. Soc.*, 2014, **136**, 5181-5184.
S28 M. R. di Nunzio, V. Agostoni, B. Cohen, R. Gref and A. A. Douhal, *J. Med. Chem.*, 2014, **57**, 411-420.
S29 M. Tsotsalas, J. Liu, B. Tettmann, S. Grosjean, A. Shahnas, Z. Wang, C. Azucena, M. Addicoat, T. Heine, J. Lahann, J. Overhage, S. Bräse, H. Gliemann and C. Wöll, *J. Am. Chem. Soc.*, 2014, **136**, 8-11.
S30 C. Zlotea, R. Campesi, F. Cuevas, E. Leroy, P. Dibandjo, C. Volkringer, T. Loiseau, G. Férey and M. Latroche, *J. Am. Chem. Soc.*, 2010, **132**, 2991-2997.
S31 V. Agostoni, T. Chalati, P. Horcajada, H. Willaime, R. Anand, N. Semiramoth, T. Baati, S. Hall, G. Maurin, H. Chacun, K. Bouchemal, C. Martineau, F. Taulelle, P. Couvreur, C. Rogez-Kreuz, P. Clayette, S. Monti, C. Serre and R. Gref, *Adv. Healthc. Mater.*, 2013, **2**, 1630-1637.
S32 V. Agostoni, R. Anand, S. Monti, S. Hall, G. Maurin, P. Horcajada, C. Serre, K. Bouchemal and R. Gref, *J. Mater. Chem.* B, 2013, **1**, 4231-4242.
S33 R. Anand, F. Borghi, F. Manoli, I. Manet, V. Agostoni, P. Reschiglian, R. Gref and S. Monti, *J. Phys. Chem.* B, 2014, **118**, 8532-8539.
S34 V. Rodriguez-Ruiz, A. Maksimenko, R. Anand, S. Monti, V. Agostoni, P. Couvreur, M. Lampropoulou, K. Yannakopoulou and R. Gref, *J. Drug Target.*, 2015, **23**, 759-767.
S35 A. Pardakhty, M. Ranjbar, *Nanomed. J.*, 2016, **3**: 248-252.

Chapter 4

Particles based on Iron-trimesate MOFs and their biomedical applications

Subchapter 4.1

New insights into the degradation mechanism of metal-organic frameworks drug carriers

Accepted by Scientific Report

General Objectives and Author Contributions

"Cage" porous particles based on MOFs have emerged as a new class of ordered porous materials for drug delivery. Iron trimesate MOFs: MIL-100 (Fe) are considered among the most efficient materials because of their biodegradability, biocompatibility, and unprecedented drug loading capability. Among all the investigated molecules, MIL-100 (Fe) interacted most efficiently with phosphated ones which could be efficiently soaked from their aqueous solutions. However, MIL-100 (Fe) rapidly degraded in phosphate buffers. It is important to understand the complex interactions taking place between MIL-100 (Fe) and different phosphated molecules. Therefore, in this subchapter, we developed a method based on Raman microscopy to track the morphology and chemical composition of individual particles.

Briefly, the degradation of nanoMOFs and microMOFs were firstly studied in phosphate buffer saline (PBS). In particular, the degradation behavior of individual particles in PBS was tracked by Raman microscopy. Of upmost interest, it was possible to detect modifications of the chemical composition on different regions on the same particle during degradation. A formation of an erosion front during MOF degradation was clearly observed with obvious modification on Raman spectra.

To understand if the phosphated molecules would lead to degradation, Gemcitabine-monophosphate (Gem-MP) and β-CD-phosphates (CD-P) were chosen as model molecules. Gem-MP is a small molecule could be penetrated within the porous MOF structures, in contrast, CD-P is larger than the cage of MOF and could stay only on the surface of the particles as coating material. In both cases, phosphated drugs/coating materials did not contribute to particle degradation.

All the authors have contributed in this work. X. Li contributed to experiments on the nanoMOFs synthesis, characterization, surface coating, and drug loading, and wrote the main manuscript.

New insights into the degradation mechanism of metal-organic frameworks drug carriers

X. Li[1], L. Lachmanski[2], S. Safi[2], S. Sene[3], C. Serre[3], J.M. Grenèche[4], J. Zhang[5], R. Gref[1*]

[1] *Institut des Sciences Moléculaires d'Orsay, UMR 8214 CNRS, Université Paris-Sud, Université Paris-Saclay, Orsay, 91405, France*

[2] *Malvern Instruments, 30 rue Jean Rostand, Orsay, 91405, France*

[3] *Institut de Matériaux Poreux de Paris, FRE 2000 CNRS ENS-ESPCI, PSL Research University, Paris, 75005, France*

[4] *Institut des Molécules et des Matériaux du Mans (IMMM) - UMR 6283 CNRS, Le Mans, 72085 France*

[5] *Shanghai Institute of Materia Medica, Chinese Academy of Sciences, Shanghai, 201203, China*

*Corresponding author: E-mail address: ruxandra.gref@u-psud.fr

Abstract

A versatile method based on Raman microscopy was developed to follow the degradation of iron carboxylate Metal Organic Framework (MOF) nano- or micro-particles in simulated body fluid (phosphate buffer). The analysis of both the morphology and chemical composition of individual particles, including observation at different regions on the same particle, evidenced the formation of a sharp erosion front during particle degradation. Interestingly, this front separated an intact non eroded crystalline core from an amorphous shell made of an inorganic network. According to Mössbauer spectrometry investigations, the shell consists essentially of iron phosphates. Noteworthy, neither drug loading nor surface modification affected the integrity of the tridimensional MOF network. These findings could be of interest in the further development of next generations of MOF drug carriers.

Introduction

Metal-organic frameworks (MOFs) are a recent class of ordered porous materials formed by the coordination of metal clusters and organic ligands. Due to their versatile chemistry, high pore volumes and large surface areas, MOFs attracted growing interest in various areas, including gas storage[1,2], catalysis[3-5], separation science[6], sensing[7,8], ionic conduction[9] and more recently, biomedicine[10-13]. Lately, biodegradable micro- or meso-porous iron polycarboxylate MOFs were employed as drug carriers[10,11,14-18]. More particularly, iron trimesate MIL-100 and iron terephthalate MIL-101 (MIL stands for Materials of Institute Lavoisier) were considered among the most efficient materials to load drugs because of their large pore sizes (24-29 and 27-34 Å for MIL-100 and MIL-101, respectively)[19]. As an example, ibuprofen payloads reached up to 35 wt% and 140 wt% for MIL-100 and MIL-101, respectively[11]. However, nano-scaled MOFs (nanoMOFs) made of biocompatible MIL-101(Fe) suffer from a very fast degradation in phosphate buffer saline (PBS) hampering their applications for controlled drug delivery[20]. In contrast, MIL-100(Fe) nanoMOFs degraded in a more progressive manner compatible with biomedical applications and were well tolerated *in vivo*[21]. A variety of drugs have been successfully incorporated into MIL-100(Fe) nanoMOFs, including antiviral drugs (cidofovir[10], azidothimidine triphosphate (AZT-TP) and azidothimidine monophosphate (AZT-MP))[15,22], anticancer drugs (busulfan[16], topotecan[18], doxorubicin[23] and gemcitabine-monophosphate (Gem-MP)[24]), biological gases (nitric oxide)[25], caffeine[26], aspirin[27] and metallodrugs[28].

The highest loading efficiencies were reported in the case of phosphated drugs, including AZT-TP, AZT-MP and Gem-MP[15,22,24]. MIL-100 were able to soak the drugs within minutes from their aqueous solution, reaching elevated drug loadings (around 30, 25 and 36 wt% for Gem-MP, AZT-TP and AZT-MP, respectively) and encapsulation efficiencies higher than 98%. It was demonstrated that coordination of the drug's phosphate groups on the iron(III) Lewis acid sites in MIL-100 nanoMOFs played a main role, leading to an efficient encapsulation[22,24]. Indeed, the same drugs without phosphate groups were poorly incorporated[22].

Phosphate molecules are essential components in every living organism. When non-controlled, strong interactions between phosphates and MOFs can lead to a fast degradation and thus to "burst" drug release. Therefore, it is of outmost importance in the development of MOFs drug carriers to gain deep understanding on their degradation in the presence of phosphates. It was shown that MIL-100(Fe) particles exhibit good colloidal stability and biodegradability in a

series of simulated physiological fluids[29] and the degradation of nanoMOF has been studied in different cell culture medium as reported[29]. There was around 10wt% of trimesate released in Dulbecco's Modified Eagle's medium (DMEM), but only around 5% released in Minimum Essential Medium Eagle (MEM). Trimesate release was dependent on the composition of the cell culture medium, especially on its content in phosphates. Intravenously administered nanoMOFs in rats were rapidly sequestered by the liver and spleen, then further biodegraded and directly eliminated in urine or feces[30]. The trimesate linkers were progressively eliminated in urine[21]. All these studies have shown the biodegradability of nanoMOFs for potential biomedical applications, but their degradation mechanism is not fully understood yet. . Recently, Bezverkhyy *et al.*[32] demonstrated that MIL-100(Fe) nanoMOFs maintained their crystalline structures while heated in water at 100 °C for 48 h, but partially degraded. On the contrary, at neutral pH the particles degraded within one hour yielding poorly crystallized iron oxide (ferrihydrite). These experiments were however conducted in media without phosphate groups, not mimicking the biological conditions. In other studies, it was shown that the MIL-100(Fe) nanoMOFs progressively disintegrated in PBS because of the strong interactions between phosphates and iron and that this degradation was well correlated to drug release[15,18,23].

One can also tailor the MOF particle size according to the targeted application and route of administration even leading to micron-sized MOF (microMOF) particles[33]. NanoMOFs had been reported to exhibit a narrower particle size distributions than microMOFs but were more prone to faster degradation because of larger surface areas[33]. However, no study dealt yet with the influence of the MOF particle size on the degradation mechanism. Moreover, the investigations on MIL-100(Fe) MOF degradation were conducted so far using batches of particles, but never on individual particles. In addition it has not been assessed yet at the particle level if drug loading or surface modification impacts the stability of the nanoMOF. It is therefore of main interest to study the degradation of individual MOFs.

To address this goal we have used here Raman microscopy to monitor *in situ* the degradation in phosphate-containing media of individual MIL-100(Fe) MOF particles of different sizes. This versatile method combines the advantages of both Raman spectroscopy and optical microscopy. The utility of Raman microscopy as a rapid, label-free, and non-destructive method was proven in many applications where chemical analysis and imaging are simultaneously required. This technique allows to qualitatively or quantitatively characterize the chemical composition and structure of a sample. In the pharmaceutical field, Raman microscopy is used mainly to characterize the distribution of molecules of interest in tablets, to determine the

crystallinity of the materials, to investigate purity and chemical composition of complex devices.

In this study, MOF batches were analyzed in terms of particle size distribution and shape. Raman spectra of individual particles were recorded, enabling to assess the homogeneity of the MOF population in terms of chemical composition and morphology. Of note, the degradation of each particle in PBS was monitored up to 8 days, enabling to detect eroded and intact zones in the same particle. Finally, we showed that the integrity of the MIL-100(Fe) MOFs was maintained after drug loading and surface modification.

Results and discussion

Synthesis and characterization of nanoMOFs. Nano-scaled MIL-100(Fe) particles were successfully prepared as reported by a solvent-free and fluoride-free "green" hydrothermal microwave assisted method using as reactants iron chloride and trimesic acid[34]. As schematized in Fig.1A, the spontaneous coordination of Fe(III) trimers and trimesic acid generates hybrid supertetrahedra which further assemble into a zeotypic architecture consisting of: i) small mesoporous cages (Ø =25 Å), delimited by pentagonal openings (5.6 Å) and ii) large mesoporous cages (Ø =29 Å) accessible through both pentagonal and larger hexagonal windows (8.6 Å)[11]. The nanoMOFs' Powder X-Ray Diffraction (PXRD) patterns and nitrogen porosimetry BET surface areas (S_{BET} = 1690 ± 50 m^2/g) are in agreement with previously published data[15,19].

As illustrated in Fig.1B, the nanoMOFs appear as small crystals with a faceted morphology and rhombic structures. The Transmission Electron Microscopy (TEM) analysis of more than 8000 nanoMOFs particles allowed estimating their average diameter of 187 ± 55 nm and a mean circularity of around 0.89 (Fig, 1C) in agreement with the sharp-edged shapes observed by TEM (Fig 1B). The mean diameter of the nanoMOFs measured by Differential Light Scattering (DLS, number values) is 216 ± 21 nm with a polydispersity index (PdI) of 0.131.

In a complementary approach, the size of individual nanoMOFs was determined by nanoparticle tracking analysis (NTA), a method which combines an optical microscope and a laser illumination unit[35]. The mean diameter of each particle was calculated from its trajectory in Brownian motion, using the Stokes–Einstein equation. The obtained mean diameter of 196 ± 59 nm (Fig.1D) was in agreement with those obtained by both DLS and TEM studies. These findings support the fact that the nanoMOFs have a relatively narrow particle size distribution.

Synthesis and characterization of MIL-100(Fe) microMOFs

MicroMOFs were synthesized by a similar method as nanoMOFs, but with longer reaction times to allow the crystals to grow larger. The microMOFs displayed a crystalline structure according to PXRD patterns and nitrogen porosimetry BET surfaces of around 1700 ± 60 m^2/g. More than 2000 individual particles were observed by Raman microscopy. Typically, the microMOFs appeared as crystals with irregular shapes (Fig. 1E). Statistical analysis showed that microMOFs possess a mean circularity (0.84) slightly lower than the nanoMOFs (Fig. 1F). MicroMOF samples contained: i) a main population with an average diameter of around 3 µm and ii) a smaller population of much larger particles of size around 60 µm (Fig. 1G). Contrary to nanoMOFs which had a narrow size distribution, microMOFs possess thus a bimodal size distribution, possibly because of the difficulty to control crystal nucleation and growth, a process dependent on many experimental parameters. These findings highlight the importance to perform individual particle analysis to gain insights into the degradation of MIL-100(Fe) particles of different sizes.

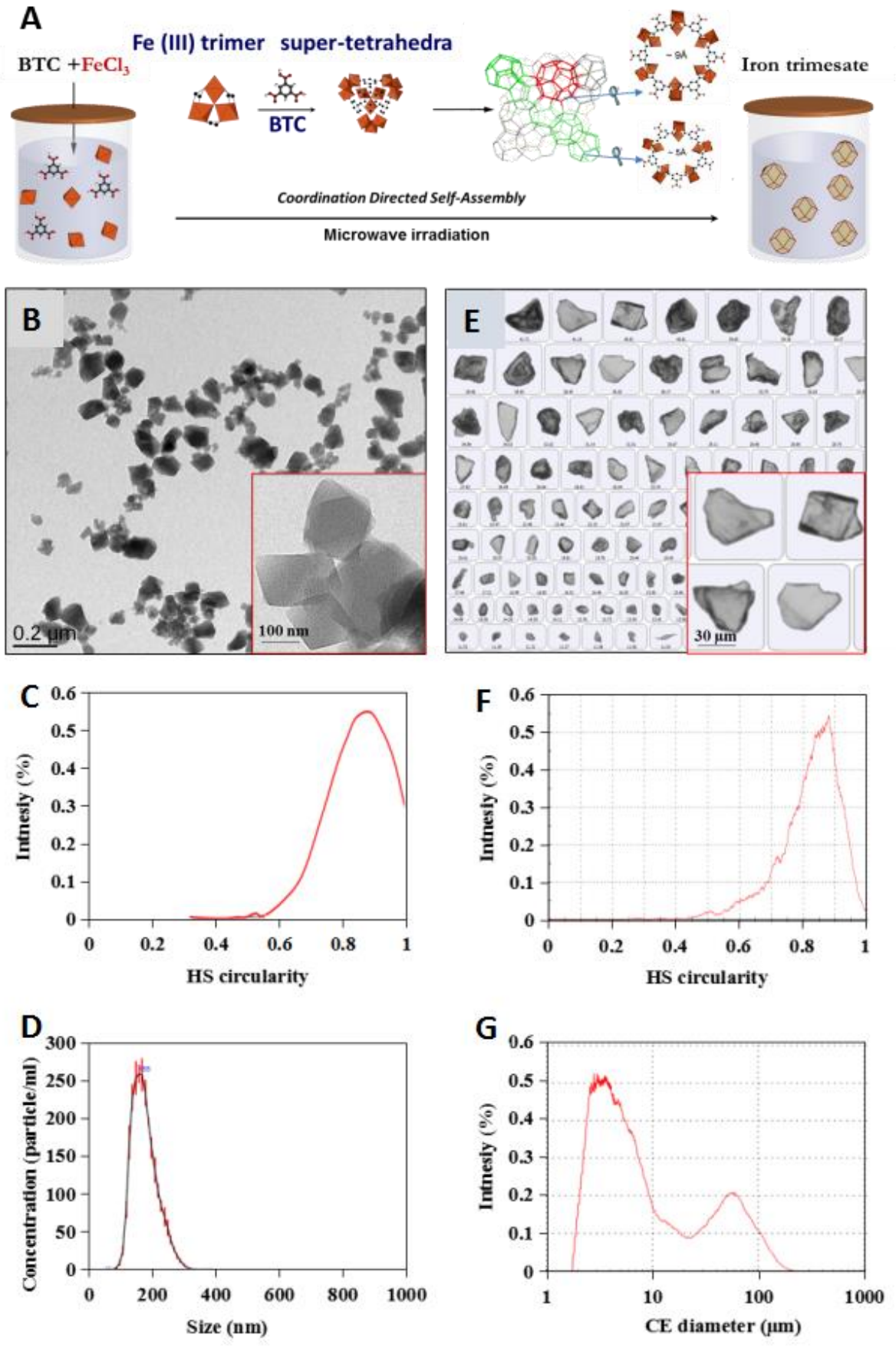
A
BTC +FeCl3
Fe (III) trimer
super-tetrahedra
BTC
Iron trimesate
Coordination Directed Self-Assembly
Microwave irradiation
B
0.2 μm
100 nm
E
30 μm
C
Intnesty (%)
HS circularity
F
Intnesty (%)
HS circularity
D
Concentration (particle/ml)
Size (nm)
G
Intnesty (%)
CE diameter (μm)

Fig.1. Schematic representation of the "green" hydrothermal synthesis of MOFs (A) and their morphological characterization, including TEM images of nanoMOFs (B) and optical images of microMOFs (E); circularity for nanoMOFs (C) and microMOFs (F) calculated from more than 8000 particles for nanoMOFs and 2000 particles for microMOFs, respectively, as well as size distributions for nanoMOFs (D) and microMOFs (G). Iron polyhedra, oxygen, carbon atoms are in orange, red and black, respectively.

Degradation of nanoMOFs

To study the effect of phosphates on nanoMOF degradation, the crystalline particles were incubated in PBS with different phosphate concentrations and in water, as a control. NanoMOFs incubated in PBS (1.19 mM) at 37°C experienced a rapid degradation, releasing large amounts (34 ± 3 wt %) of their constituting ligand, trimesate, after only 6 h. These data are in agreement with previously reported studies, where 29.9 ± 2.1 wt% trimesate was released under similar conditions [28]. Comparable amounts of ligands (31 ± 3 wt %) were released but after two days of incubation in PBS when diluted ten times (0.12 mM)(for details see SI section). In both cases, the concentration of nanoMOFs was 0.5 mg/mL, corresponding to 0.1 mM Fe. This highlights the influence of the concentration of phosphates on the degradation mechanism: the higher the concentration of phosphates, the faster the degradation of nanoMOFs in PBS.

In contrast, nanoMOFs released negligible amounts (less than 2 wt %) of their trimesate constituting ligand within two days incubation in pure water at 37°C, in agreement with previous investigations [15,22], where less than 1 wt% trimesate was released after incubation for three days. This is in agreement with the nanoMOFs' diameter that remained practically unchanged over two days incubation in water (224 ± 25 nm).

Note that nanoMOFs lost their crystallinity in PBS within only 4 h, whereas they maintained an intact crystallinity in water, as indicated by PXRD results (Fig. S1).

These observations were well corroborated by TEM investigations, evidencing the nanoMOF morphological aspects before (Fig. 2A) and after (Fig. 2B) degradation in PBS. Noteworthy, degradation in PBS leads to a progressive rounding (Fig. 2B) of the nanoMOF sharp initial edges (Fig. 2A), in agreement with a progressive disorganization of the crystalline 3D structure. Interestingly, DLS measurements showed that despite the degradation, the nanoMOFs maintained practically the same mean diameter (Fig. 2C), with a moderate decrease in size from 221 ± 24 nm to 187 ± 22 nm after two days incubation in PBS, despite the fact more than 30 % of their constitutive ligand has left the particles, as shown above.

In a nutshell, it confirms that these iron carboxylate based nanoMOFs are remarkably stable in water, but degrade in PBS with a progressive departure of the constitutive organic linkers associated with an amorphization. However, it is remarkable that despite their dramatic morphological and structural changes in PBS, nanoMOFs maintain practically unchanged diameters over two days. Based on these findings, it was interesting to further investigate the degradation of larger particles (microMOFs) in PBS.

Degradation of MIL-100(Fe) microMOFs

As shown in Fig.2D, MIL-100(Fe) microMOFs are red-orange crystals with irregular shapes. The red color is attributed to Fe^{3+} species in the $[Fe_3O(OH)(H_2O)_2]^{6+}$ clusters linked by carboxylate anions[27]. Contrary to nanoMOFs, microMOFs degrade very slowly and therefore concentrated PBS (11.9 mM) was used to accelerate the process. After 8 days of incubation in this medium, the particles changed color (Fig. 2E). However, surprisingly, the size of the particles monitored by Raman microscopy remained unchanged (less than 0.5 % variation in all dimensions) (Fig. 2F) as it was previously shown in the case of nanoMOFs. Grey regions (arrows in Fig. 2E) were clearly observed, whereas the core of the particles maintained its initial red color.

In a nutshell, MOF particles degraded with the formation of a grey shell delimiting a red-colored core. Raman microscopy was further used to study the composition of these different regions in the same particle.

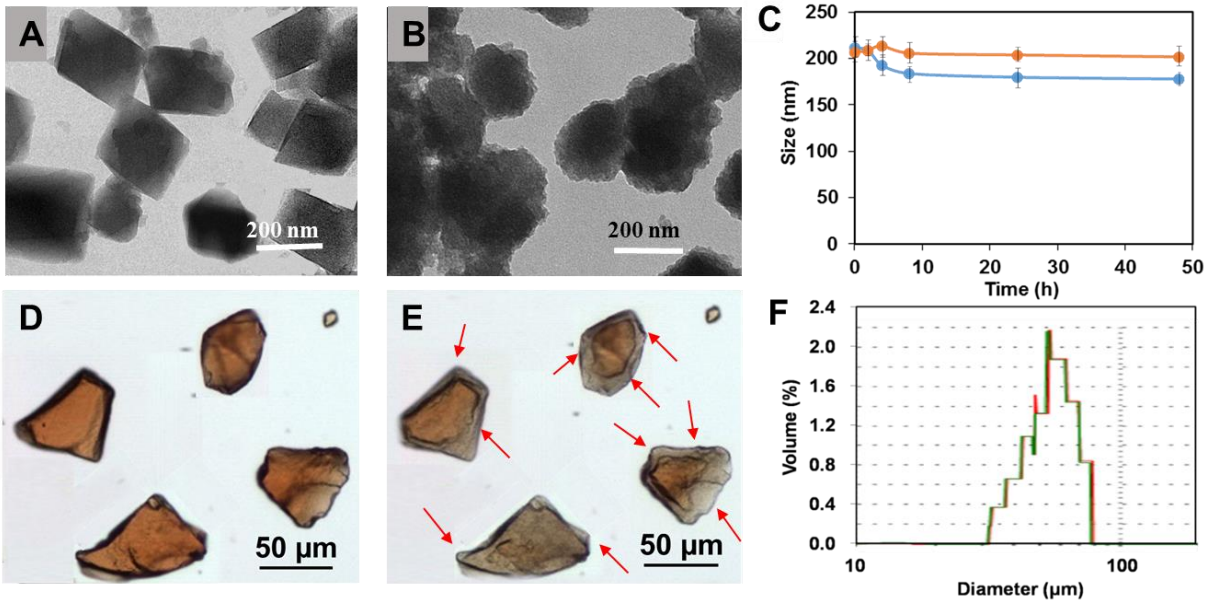

Fig.2 Morphology of MIL-100(Fe) nano-and microMOFs and size variations after incubation in water or PBS. TEM images of nanoMOFs before (A) and after (B) degradation in PBS (1.19 mM) for 6 hours. Size variation (C) of nanoMOFs (100 µg/mL) in MilliQ water (orange) and PBS (0.12 mM, blue) for 2 days. Images of microMOFs observed by Raman-microscopy before (D) and after (E) degradation in PBS (11.9 mM) for 8 days; size distribution (F) of microMOFs before (green) and after (red) degradation.

Individual MIL-100(Fe) particle degradation

Typical Raman spectra of microMOFs show the specific MIL-100(Fe) peaks in the 100-1900 cm^{-1} region (Fig. 3). The peak A at 210 cm^{-1} is attributed to the ordered crystalline iron-based structure, whereas the B bands from 450 cm^{-1} to 600 cm^{-1} are related to lattice vibrations and network binding modes. The principal peaks in Fig. 3 correspond to the fingerprints of the trimesate linker, the aromatic ring peaks at 800 cm^{-1} (peak C) and 1000 cm^{-1} (peak D). The E peaks around 1200 cm^{-1} can be assigned to the C–O–Fe stretching of Fe-trimesate, whereas F bands ranging from 1400 cm^{-1} to 1600 cm^{-1} are related to the H–O–H bonding vibrations, which indicate that the Fe-trimesate network contains coordinated water.

Figure 3 presents a typical image of a microMOF particle before (left) and after 8 days degradation in PBS (right). The morphology was dramatically changed with the appearance of a sharp transition delimiting a red-colored core (region I) from a grey shell (region II). Of note, Raman microscopy enabled monitoring Raman spectra in both I and II regions. The spectrum of region I consisted of peaks very similar to those characteristic of non-degraded MOFs, with the exception of peak D which was broadened at its base. On the contrary, in region II, all peaks disappeared and only a large peak D could be detected. The disappearance of band A indicates an amorphous phase formation. Peaks B shifted to lower wavelengths, become much broader, and less resolved, suggesting a change in coordination environment. The disappearance of the well resolved peaks C could be interpreted as a proof of trimesate release. The band D which was broadened but did not disappear could be ascribed to symmetric and asymmetric stretching vibrations of Fe–O–P bonds, strongly indicating the formation of phosphate complexes by coordination with phosphate ions [32]. This is also in agreement with the disappearance of peak F in the eroded region II, indicating that coordinated water faded away.

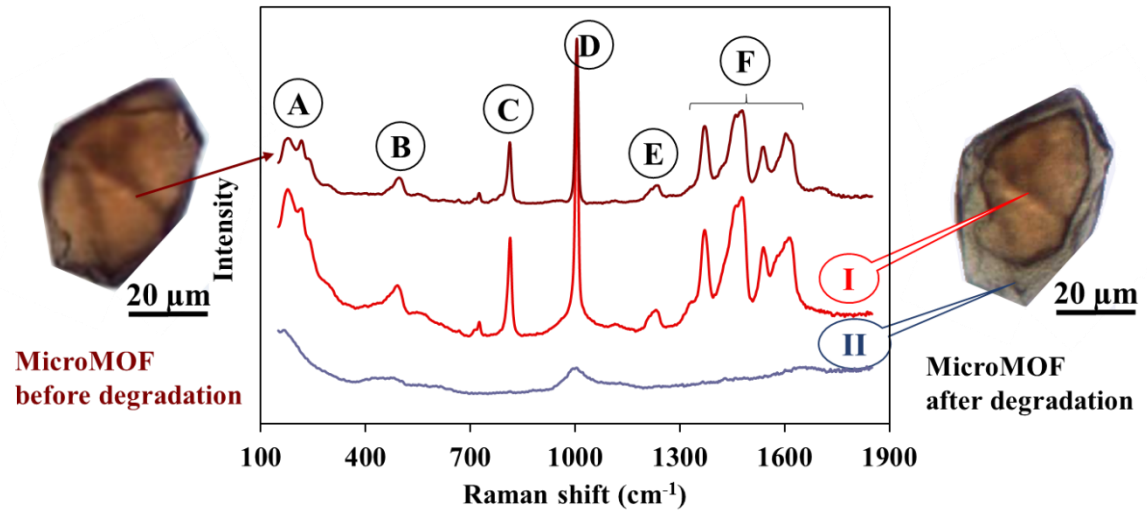

Fig.3 Raman spectra of a single microMOFs particle of around 50 microns before (brown) and after (red and blue) degradation for 8 days in PBS (11.9 mM). Raman spectra were recorded on the same particle, both in the red core (region I) and in the degraded grey shell (region II).

In conclusion, Raman spectra gave useful insights regarding MOF degradation in PBS, suggesting that the most probable degradation mechanism is the competitive replacement of trimesate by phosphate ions in PBS solution. Advantageously, Raman microscopy enabled obtaining spectra in different regions on the same particle. To gain further insights on the degradation mechanism, single particles were tracked over their degradation in PBS during 8 days.

Automated imaging was used to gain a deeper understanding of the kinetics of the degradation process of each selected particle, since it can provide a direct measurement of the size, shape, color, surface area, and circularity of each particle. Images were captured every half an hour during 8 days to track the degradation process. Selected images illustrate the typical morphologies of one single particle during degradation (Fig. 4). Although shells (eroded zones) with a grey color were clearly formed and progressively penetrated into the particles, no significant variation in size could be detected.

Additionally, the variation of mean intensity and surface area was also investigated. Mean intensity is a precise parameter to evaluate the color of a particle, based on the amount of light reflected by a particle. The darker the particle, the less is the reflected light, resulting in lower intensities. Figure 4 shows a sharp increase in the intensity of a MOF particle in the first 6 hours, indicating a rapid color change, which was too subtle to be observed by the naked eye.

This fast phase was followed by a slower increase in mean intensity, accompanied by no detectable surface area variation (Fig. 4, progressive phase).

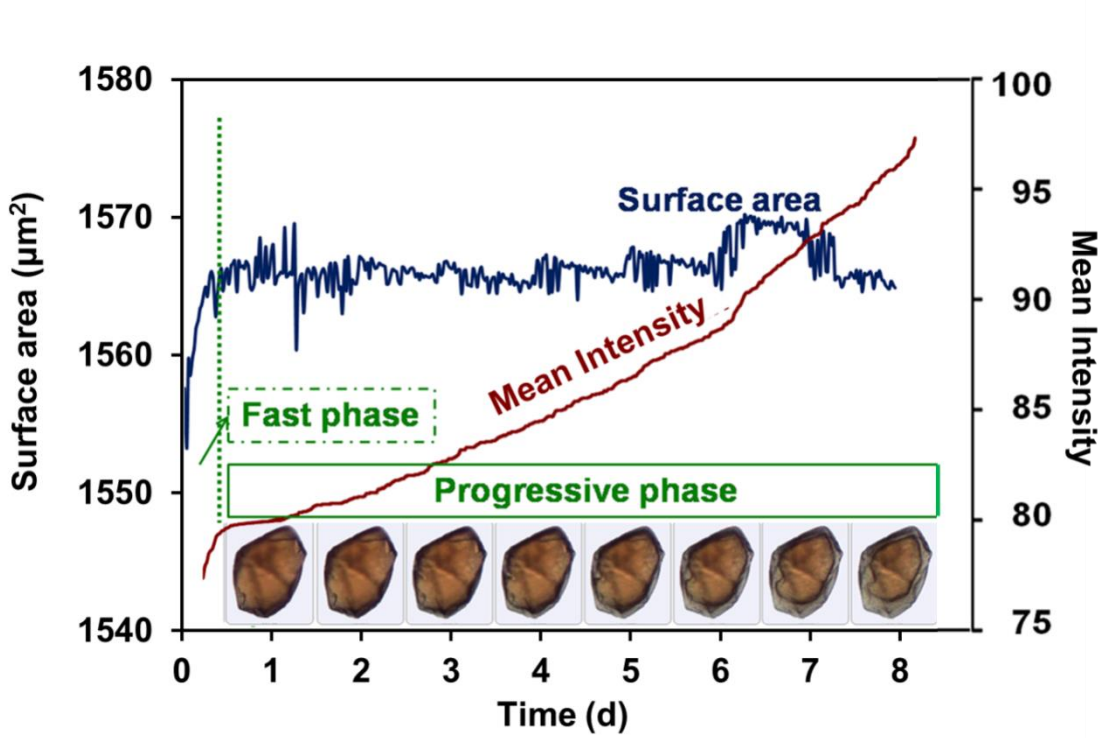

Fig.4 Kinetic study of the degradation of a microMOFs (size around 50 µm in length) in PBS (11.9 mM) at room temperature. Particle surface area and mean intensity were recorded each 30 min up to 8 days. A fast degradation phase was observed in the first 6 hours with a rapid increase in mean intensity. A second phase occurred in the following 8 days with the formation of an eroded zone with a clear color change (progressive phase).

It can be speculated that in the first hours after incubation, a fast coordination reaction occurred between phosphates in the incubation medium and accessible iron sites at the MOF surface. This phase was followed by a slower diffusion of phosphates in the eroded region. The advancement of the degradation front was presumably limited by the diffusion of the reacting species (phosphates) from the media into the MOFs and by the diffusion of released trimesate out of the matrix.

Mössbauer spectrometry

^{57}Fe Mössbauer spectrometry was applied to MIL-100(Fe) particles to probe several chemical features of interest, such as the Fe oxidation state, the type of Fe species, the possible presence of Fe-containing phases different from of MIL-100(Fe) and any Fe oxide resulting from degradation. Mössbauer spectra were recorded at 300 and 77K with different velocities and

only typical Mössbauer ones are illustrated in Fig. 5. The hyperfine structures result essentially from the presence of quadrupolar components. The refined values of the isomer shift indicate unambiguously the presence of only high supersaturation (HS) Fe^{3+} species whatever the sample (nano-and microMOFs) and their degradation state. It could be concluded that no Fe reduction phenomenon occurred in PBS.

At 300K, the hyperfine structures of the nano-and microMOF samples after degradation was modified (Fig. 5). Before degradation, the spectrum was well described by means of 3 quadrupolar components (Fig. 5), in agreement with the crystallographic MIL-100(Fe) structure, while after degradation, quadrupolar doublets with broadened lines were observed. The best physical description requires a discrete distribution of quadrupolar doublets suggesting a structure close to that of a typical amorphous structure. The Mössbauer spectra recorded at 77K are similar to those obtained at 300K at low velocity scale and their corresponding hyperfine structures confirm previous conclusions (Fig.S2). A deep analysis of the 12 mm/s spectra at 77K allows a small magnetic component (estimated at about 2% in at Fe) to be observed, as displayed on the insets of Fig.S2, where relative transmission scale has been strongly extended. It corresponds clearly to hematite in the case of the degraded microMOFs while it could be attributed to poorly crystallized hematite (including traces of ultra-fine grains of goethite). Taking into account the presence of phosphates in the media surrounding the microMOF, it is plausible that a highly disordered FeP based skeleton phase was formed, corroborating our previous hypothesis.

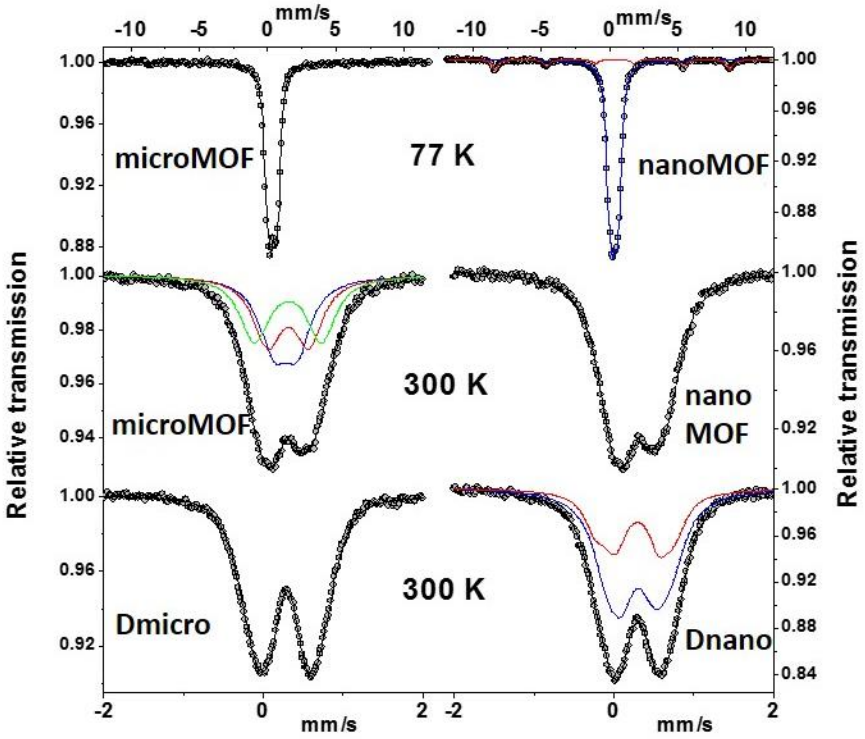

Fig. 5. Mössbauer spectra of nano-and microMOF obtained at 77 K and at 300K. Spectra of degraded nanoMOF (Dnano) and microMOF (Dmicro) obtained at 300K.

Energy dispersive X-ray analysis (EDX) was performed in order to obtain the Fe/P ratios of the intact MOFs, half degraded microMOFs, and totally degraded microMOFs. The results showed that there is a significant reduction of Fe/P ratios from 1000 (intact MOFs) to 7.6 (half degraded microMOFs) and 0.9 (totally degraded microMOFs), confirming that P was coordinated inside the porous MOF structures.

To demonstrate the progressive coordination of phosphates during the degradation process, Infra-Red (IR) spectroscopy was performed out on micro-MOFs at different degradation times (see Fig. S3). In addition to the decrease in intensity of the carboxylate stretching bands at ca. 1390 and 1580 cm^{-1}, one could observe the progressive increase of intensity of the phosphate bands centered at 1050 cm^{-1}. Although one cannot exclude that amorphous Fe oxide is also formed during the degradation process, this confirms the progressive incorporation of phosphates throughout of the particles when dispersed into PBS. The broadness of the phosphate bands is also in agreement with the amorphous character of the degradation product.

MOF stability during drug loading

Gem-MP has been successfully loaded in MIL-100(Fe) MOFs, following the previous methodology, which acted as efficient “nanosponges”, soaking the drugs from their aqueous

solutions to reach within minutes unprecedented amounts (up to 30 wt%) of drug with loading efficiencies higher than 98%[24]. This is due to the coordination of the phosphate group of the drug on the Fe metal sites. In this study, the results from Gem-MP quantification by HPLC showed a high payload of 25 wt%. It is therefore important to investigate if drug loading induces a degradation of the MOF structure as it was the case when the MOFs were incubated in the presence of phosphates in PBS.

The drug loaded particles were studied by Raman microscopy. Gem-MP did not present characteristic Raman peaks in the studied region, facilitating the studies. Fig. 6 does not reveal any significant differences in the MIL-100(Fe) microMOFs Raman spectra before and after drug loading. These studies are in agreement with HPLC investigations, showing less than 2% of loss of the constitutive trimesate. Of note, the microMOFs maintained their crystalline structure after Gem-MP loading[24]. In a nutshell, the MOF 3D structure was maintained after drug loading with no impact of the drug on the MOF long-range or local structure.

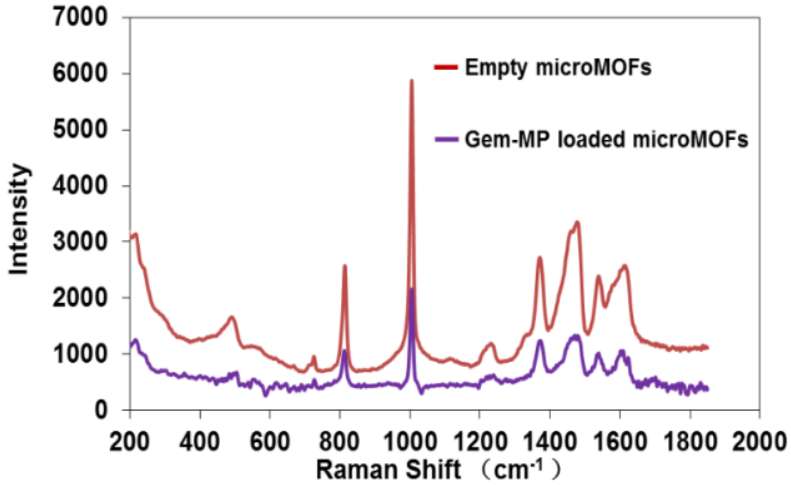

Fig.6 Effect of loading of Gem-MP in MIL-100(Fe) on the Raman spectra of the particles. MOFs particles before (red) and after (purple) Gem-MP loading.

Previously we showed that MOFs immersed in PBS degraded with kinetics dependent upon the phosphates concentration. When Gem-MP was loaded in MOFs at the maximum payload of 30 wt%, the equivalent amount of phosphates was 0.038 mM, whereas the molar ratio P/Fe was only 0.38, which could explain why MOFs did not degrade during drug entrapment.

MOF stability during coating

Cyclodextrins (CDs) bearing several phosphate anchoring groups (CD-P) were successfully used to functionalize the surface of MOF particles[33]. Taking advantage of the fact that the size of CD-P is larger than the MIL-100(Fe) windows (Fig. 7) the coating could be achieved by a

simple way consisting in incubating the MOFs with CD-P in water. This "green" method allowed the formation of CD-P shells within minutes and the coating was stable, even in biological media[33], due to the cooperative coordination between phosphates on CD-P and Fe sites at the MOF's surface.

In this study, CD-P coatings were produced on microMOFs following the previous protocol[33]. As reported in the previous work[33], elemental analysis was used to evaluate the coating efficacy of grafting CD-P, showing that around 17 wt% of CD-P was associated to the MOFs. The particles, before and after coating, were studied by Raman microscopy. Of note, CD-P did not present any specific peak in the observed region. It was found that after coating, the particles maintained same morphology, color and Raman spectra, indicating that CD-P surface modification did not induce particle degradation. Similarly as in the case of drug loading, the P/Fe ratio in CD-P coated microMOFs was lower than 1 (only 0.6), which could explain why the microMOFs did not degrade after coating. The good stability of the particles after CD coating offer thus promising possibilities to load drugs of interest and graft ligands for targeting purposes.

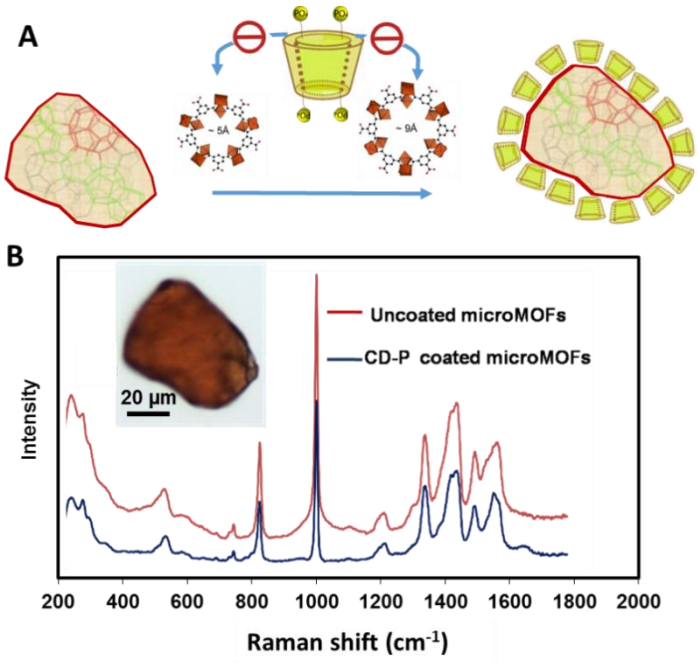

Fig.7 Raman spectra of individual MIL-100(Fe) MOF particles, coated or not with P-CD. Schematic representation of the coating procedure (A) and experimental results (B) for MOF particles before and after CD-P coating.

Conclusion

Whatever their size, MIL-100(Fe) MOFs degrade in PBS losing their constitutive trimesate

linkers and eventually became amorphous with a clear impact of the phosphate concentration and the particle size: the higher the phosphate concentration and the lower the particle the faster the degradation of the MOF particles. Interestingly, nano-and microMOFs both kept their initial sizes during degradation but transformed into inorganic edifices. Raman microscopy enabled gaining insights on the degradation mechanism and showed that intact cores were separated from the eroded regions by clearly visible erosion fronts. Iron phosphates were identified by Mössbauer spectrometry (and IR spectroscopy) as main components in the eroded regions. In contrast, neither drug entrapment and nor particle coating did affect the integrity of the tridimensional MOF network due to the more diluted conditions. These findings are of interest in the development of stable drug-loaded MOF particles. Further studies will be focused on the degradation of other engineered MOF materials of interest in biomedicine.

Materials and Methods

Chemicals. Iron (III) chloride hexahydrate (98%, Alfa Aesar, Schiltigheim, France), 1,3,5-benzenetricarboxylic acid (BTC, 95%, Sigma-Aldrich, Saint-Quentin-Fallavier, France) and absolute ethanol (99%, Carlo Erba, Val-de-Reuil, France) were used for MOF synthesis. PBS (11.9 mM, pH 7.4 ± 0.1) was purchased from Life Technology Co., Ltd. (Saint Aubin, France). It contains 11.9 mM phosphates, 137 mM NaCl and 2.7 mM KCl. Gem-MP ($CH_{12}F_2N_3OP$) was purchased from Toronto Research Chemicals, Canada. Phosphated β-cyclodextrin sodium salt (CD-P, Cyclolab, CY-2017.1, molecular formula: $C_{42}H_{70}O_{47}P_4Na_4$) was used for coating. Milli-Q water was obtained from a Millipore apparatus equipped with a 0.22µm filter. Reagents and solvents were used without further purification.

Nano-and micro-MOFs synthesis. MIL-100(Fe) iron trimesate nanoMOFs were synthesized by adapting a previously described method[1]. Briefly, nanoMOFs were obtained by microwave-assisted hydrothermal synthesis from a mixture of iron chloride (8.97 mmol) and BTC (4.02 mmol) in 20 mL of deionized water. The mixture was heated for 6 min at 130°C under stirring. The power applied was 800 Watts (Mars-5, CEM, US) with a power maximum output 1,600 ± 240 Watts and frequency at full power 2,450 mHz. The resulting nanoMOFs, recovered by centrifugation, were washed with absolute ethanol 6 times to remove the residual non reacted organic acid. A last centrifugation at 5500 ×g was performed during 1 min in absolute ethanol to sediment the largest particles and recover the supernatants as a suspension of monodisperse nanoparticles. Nanoparticles were stored wet in ethanol until final use.

To prepare microMOFs, a reaction mixture composed of 2.7 g iron (III) chloride hexahydrate

(10.00 mmol) and 2.1 g trimesic acid (10.00 mmol) in 50 mL of water, was placed in a large Teflon bomb under magnetic stirring for 15 minutes. The Teflon reactor was encased in a metal bomb with controlled pressure, before being placed in an autoclave with a 1 hour heating ramp to 130 °C, and held at this temperature for 72 hours. The product was then cooled before being filtered and was then washed by heating under reflux, first in 700 mL of ethanol at 75 °C for 2 hours and finally in 700 mL of water at 90 °C for 2 hours. The product was then collected by filtration under vacuum and stored as powder after being dried in air.

MOFs characterization. The crystallinity and purity of MIL-100(Fe) particles were assessed by PXRD patterns which were collected in a conventional high resolution (θ-2θ) D5000 Bruker diffractometer (λ_{Cu} $K\alpha$, $K\alpha_2$) from 1º to 20º (2θ) using a step size of 0.02º and 4° per step in continuous mode. The morphologies of microMOFs were investigated by Raman microscopy (Malvern® Morphologi G3-ID). Briefly, optical images of more than 2000 particles were captured and statistical analysis of size and circularity were carried out.

Dynamic light scattering (DLS) and Nanoparticle tracking analysis (NTA) were performed by a Zetasizer (Malvern® Nano-ZS90) and Nanosight (Malvern® LM10), to characterize the size distribution of nanoMOFs. Zeta potential of nanoMOFs was characterized by a Zetasizer (Malvern® Nano-ZS90). Nanosight analysis is a combination of a conventional optical microscope and a laser to illuminate the nanoparticles introduced into the visualizing unit with a 1.0 mL syringe system. Individual particles could be visualized as point-scatter moving under Brownian motion. Measurements were performed for 5 times over a period of 60 s at 25°C. The particle size and concentration were analyzed using the NTA software. Transmission electron microscopy (TEM) images for nanoMOFs were collected using a JEOL® JEM-2200FS microscope. The circularity of nanoMOFs was obtained from TEM images and analyzed by Origin 9.0 software.

Statistical analysis of MIL-100(Fe) degradation. The size distribution and morphology of MOFs after degradation in PBS were characterized. Briefly, Raman microscopy was applied for microMOFs to investigate their size and circularity before and after incubation in PBS (11.9 mM) for 8 days. TEM was used for nanoMOFs to observe the morphological variation after incubation in PBS (1.19 mM) for 6 hours. DLS was used to characterize the mean diameter variation during degradation of nanoMOFs in PBS with different concentrations (11.9 mM, 1.19 mM and 0.12 mM).

HPLC determination of the Gem-MP loading and trimesate release. The detection of Gem-MP and trimesate was carried out in HPLC (Agilent 1100, USA) connected to a Phenomenex C18 column (4.6 × 250 mm, 5 µm) at a flow rate of 1.0 mL/min. For the analysis of Gem-MP, a mobile phase consisting of 84% buffer (0.2M TEAA):16% MeOH was used. It was detected at 254 nm with an injection volume of 20 µl. Analysis of trimesate was performed with a mobile phase containing 90% buffer (5.75 g/L of $NH_4H_2PO_4$): 10% Acetonitrile (5 mM TBAP). The injection volume was 5 µl and the detection wavelength was set at 220 nm.

Individual analysis of MIL-100(Fe) degradation. Individual particles were observed by Raman microscopy and Raman spectra were obtained for degraded and non-degraded particles. Microparticles were kept in PBS (11.9 mM) for 8 days under the monitor of Raman microscopy. Images were captured every 30 min to track the degradation process using automated imaging. Surface areas and intensity mean were extracted from the software and kinetic analysis was carried out in function of surface areas and intensity mean. Raman spectra were recorded at the laser wavelength of 785 nm. The laser spot was 3 µm in diameter with power output as 15 mW.

Transmission ^{57}Fe Mössbauer spectrometry was performed using a conventional electromagnetic transducer with a constant acceleration and a ^{57}Co/Rh γ-ray source. Mössbauer spectra were recorded at 300 K and 77 K using a bath cryostat on samples which consist in a powdered layer containing about 5 mg of Fe/cm^2. The hyperfine structure was modeled by a least-square fitting procedure involving quadrupolar doublets and/or Zeeman sextets composed of lorentzian lines using unpublished program 'MOSFIT'. The isomer shift values (IS) are referred to that of α-Fe at 300 K, used as a standard to calibrate the spectrometer.

EDX analysis. The chemical compositions of the samples were determined by EDX performed on a FEI Magellan 400 Scanning Electron Microscope. Three samples were analyzed: i) intact MOFs; ii) half degraded microMOFs; iii) totally degraded microMOFs. Twelve spectra were obtained for each sample and the content of P, Fe, and Cl was calculated by getting the average of the 12 spectra. Finally, Fe/P ratios were calculated for each sample.

PXRD analysis. PXRD patterns were collected in reflection mode using a PANalytical Empyrean Series 2 diffractometer with an average wavelength of 1.541 Å Cu Kα (45 kV and 40 mA). Measurements were performed at room temperature between 3° and 100° in 2θ, using a step size of 0.026° step, and a counting time per step of 200 s.

Investigation of drug loaded MIL-100(Fe). Gem-MP was loaded in microMOFs by adapting a previously described method [24]. Briefly, MOFs in ethanol were re-dispersed in water under

gentle magnetic stirring overnight. Then Gem-MP loaded MOFs were prepared by soaking for one week microMOFs in Gem-MP aqueous solution (0.5 mg/mL) using a weight ratio 1:2 (Gem-MP: microMOFs) to reach maximal loadings of 30 wt%. Afterwards, Raman spectra of Gem-MP loaded MOFs were obtained by Raman microscopy.

Investigation of CD-P coated MIL-100(Fe). MIL-100(Fe) MOFs were coated with CD-P as previously described[33]. Briefly, MOFs were suspended in a CD-P aqueous solution under gentle stirring at room temperature for 24 hours. The initial MOFs/CD-P weight ratio was 1:0.5, and the final MOFs concentration was 4 mg/mL. The coated MOFs were recovered by centrifugation (5000 g for 5 min) and were washed with deionized water in order to remove the excess CD-P which was not associated to the MOFs surface. Finally, Raman spectra and images of CD-P coated MOFs were recorded by Raman microscopy.

References

1. Pal, T.K. *et al*. Significant Gas Adsorption and Catalytic Performance by a Robust Cu(II) -MOF Derived through Single-Crystal to Single-Crystal Transmetalation of a Thermally Less-Stable Zn(II) -MOF. *Chemistry*. **21**, 19064-19070 (2015).
2. Dinca, M. & Long, J. R. Hydrogen storage in microporous metal-organic frameworks with exposed metal sites. *Angew. Chem., Int. Ed.* **47**, 6766–6779 (2008).
3. Lee, J., *et al*. Metal-organic framework materials as catalysts. *Chem. Soc. Rev.* **38**, 1450–1459 (2009).
4. Ma, L. Q., Abney, C., & Lin, W. B. Enantioselective catalysis with homochiral metal-organic frameworks. *Chem. Soc. Rev.* **38**, 1248–1256 (2009).
5. Ma, L. Q., Falkowski, J. M., Abney, C., & Lin, W. B. A series of isoreticular chiralmetal-organic frameworks as a tunable platform for asymmetric catalysis. *Nat. Chem.* **2**, 838–846 (2010).
6. Wang, X. *et al*. An Anion Metal-Organic Framework with Lewis Basic Sites-Rich toward Charge-Exclusive Cationic Dyes Separation and Size-Selective Catalytic Reaction. *Inorg Chem.* **55**, 2641-26419 (2016).
7. Kang, Y., Zheng, X.J., & Jin, L.P. A microscale multi-functional metal-organic framework as a fluorescence chemosensor for Fe(III), Al(III) and 2-hydroxy-1-naphthaldehyde. *J Colloid Interf. Sci.* **5**, 1-6 (2016).

8. Karmakar, A., Kumar, N., Samanta, P., Desai, A.V., & Ghosh, S.K. A Post-Synthetically Modified MOF for Selective and Sensitive Aqueous-Phase Detection of Highly Toxic Cyanide Ions. *Chemistry*. **22**, 864-868 (2016).
9. Horike, S., Umeyama, D. & Kitagawa. S. Ion conductivity and transport by porous coordination polymers and metal-organic frameworks. *Acc. Chem. Res.,* **46**, 2376–2384 (2013).
10. Horcajada, P. *et al*. Porous metal–organic-framework nanoscale carriers as a potential platform for drug delivery and imaging. *Nat. Mater.* **9**, 172–178 (2010).
11. Horcajada, P. *et al*. Metal-organic frameworks as efficient materials for drug delivery. *Angew. Chem. Int. Ed.* **45**, 5974–5978 (2006).
12. Huxford, R. C., Della Rocca, J. & Lin, W. Metal–organic frameworks as potential drug carriers. *Curr. Opin. Chem. Biol.* **14**, 262–268 (2010).
13. Horcajada, P. *et al*. Metal-organic frameworks in biomedicine. *Chem. Rev.* **112**, 1232–1268 (2012).
14. Baati, T. *et al*. In depth analysis of the in vivo toxicity of nanoparticles of porous iron(III) metal–organic frameworks. *Chem. Sci.* **4**, 1597-1607 (2013).
15. Agostoni, V. *et al*. Towards an Improved anti-HIV Activity of NRTI via Metal-Organic Frameworks Nanoparticles. *Adv. Healthcare Mater.* **2**, 1630-1637 (2013).
16. Chalati, T. *et al*. Porous metal organic framework nanoparticles to address the challenges related to busulfan encapsulation. *Nanomedicine* **6**, 1683-1695 (2011).
17. Horcajada, P. *et al*. Flexible porous metal-organic frameworks for a controlled drug delivery. *J. Am. Chem. Soc.* **130**, 6774-6780 (2008).
18. di Nunzio, M. R., Agostoni, V., Cohen, B., Gref, R., & Douhal, A. A "ship in a bottle" strategy to load a hydrophilic anticancer drug in porous metal organic framework nanoparticles: efficient encapsulation, matrix stabilization and photodelivery, *J. Med. Chem.* **57**, 411-420 (2014).
19. Ferey, G, *et al*. A chromium terephthalate-based solid with unusually large pore volumes and surface area. *Science.* **309**, 2040–2042 (2005).
20. Kathryn, M. L. *et al*, Post-Synthetic Modifications of Iron-Carboxylate Nanoscale Metal-Organic Frameworks for Imaging and Drug Delivery. *J. Am. Chem. Soc.*, **131**, 14261-14263 (2009).
21. Simon-Yarza,T. *et al.* In vivo behavior of MIL-100 nanoparticles at early times after intravenous administration. *Int J Pharm.* **511**, 1042-7 (2016).

22. Agostoni, V. *et al*. Impact of phosphorylation on the encapsulation of nucleoside analogues within porous iron (III) metal-organic framework MIL-100(Fe) nanoparticles. *J. Materials Chemistry B.* **1**, 4231-4242 (2013).
23. Anand, R. et al. Host-guest interactions in Fe (III)-trimesate MOF nanoparticles loaded with doxorubicin. *J. Phys. Chem. B.* **118**, 8532-8539 (2014).
24. Rodriguez-Ruiz, V. et al. Efficient ‘‘green’’ encapsulation of a highly hydrophilic anticancer drug in metal–organic framework nanoparticles. *J. Drug Target,* **23**, 759-767 (2015).
25. Bartha, B., Mendtb, M., Pöppl, A., & Hartmann, M. Adsorption of nitric oxide in metal-organic frameworks: Low temperature IR and EPR spectroscopic evaluation of the role of open metal sites. *Micropor. Mesopor.Mat.* **216,** 97-110 (2015).
26. Cunha, D. et al. Rationale of drug Encapsulation and release from biocompatible porous Metal–Organic Frameworks. *Chem. Mater.* **25**, 2767–2776 (2013).
27. Singco, B. et al. Approaches to drug delivery: Confinement of aspirin in MIL-100(Fe) and aspirin in the de novo synthesis of metal–organic frameworks. *Micropor. Mesopor. Mat,* **223**, 254–260 (2016).
28. Rojas, S., Carmona, F.J., Maldonado, C.R., Barea, E. & Navarro, J.A.R. RAPTA-C incorporation and controlled delivery from MIL-100(Fe) nanoparticles, *New J. Chem.*, **40**, 5690 -5694 (2016).
29. Bellido E *et al*. Understanding the Colloidal Stability of the Mesoporous MIL-100(Fe) Nanoparticles in Physiological Media. *Langmuir **30***, 5911-5920 (2014).
30. Grall, R. et al. In vitro biocompatibility of mesoporous metal (III; Fe, Al, Cr) trimesate MOF nanocarriers. *J. Mater. Chem. B* **3,** 8279–8292 (2015).
31. Baati, T. et al. In depth analysis of the in vivo toxicity of nanoparticles of porous iron(III) metal–organic frameworks. *Chem. Sci.* **4**, 1597-1607 (2013).
32. Bezverkhyy, I., Weber, G. & Bellat, J.P. Degradation of fluoride-free MIL-100(Fe) and MIL-53(Fe) in water: Effect of temperature and pH. *Micropor. Mesopor.Mat.* **219**, 117-124 (2016).
33. Agostoni, V. *et al*. A ‘‘green’’ strategy to construct non-covalent, stable and bioactive coatings on porous MOF nanoparticles. *Sci. Rep*. **7925**, 1-7 (2015).
34. Agostoni, V. et al. ‘Green’ fluorine-free mesoporous iron (III) trimesate nanoparticles for drug delivery. *Green Materials* **1**, 209-217 (2013).

35. Tong, M, Brown, O.S., Stone, P.R., Cree, L.M., & Chamley, L.W. Flow speed alters the apparent size and concentration of particles measured using NanoSight nanoparticle tracking analysis. *Placenta* **38**, 29-32 (2016).

Acknowledgments

We acknowledge support from the European Marie Curie network CycloN Hit (N° 608407) and from the French National Research Agency (ANR) ANR-14-CE08-0017. This work was supported by ANR as part of the "Investissements d'Avenir" program (Labex NanoSaclay, reference: ANR-10-LABX-0035). X. Li acknowledges support from China scholarship council (N° 201408330166). Prof. J. Zhang is grateful for the support from the National Natural Science Foundation of China (N°81430087). We thank Katie Buxton for help with the synthesis of microMOFs. We are grateful to Drs. Sergio Marco and Sylvain Trepout (Curie Institute, Orsay, France) for help with TEM and statistical studies. We acknowledge Dr. Farid Nouar for his help with EDX experiment.

Author contributions

R.G. and X.L. wrote the main manuscript. R.G. designed the experiments. X.L. contributed to the nanoMOFs synthesis, characterization, surface coating and drug loading. J.M.G. performed and analyzed the Mössbauer experiments. S.S. performed the EDX and PXRD experiments. J.Z., C.S. and J.M.G. contributed to the scientific discussions. S.S., L.L. and X.L. performed the Raman microscopy experiments. All authors reviewed the manuscript.

Additional Information

Supplementary information accompanies this paper at..

Competing financial interests: The authors declare no competing financial interests.

Supplementary Information

New insights into the degradation mechanism of metal-organic frameworks drug carriers

X. Li[1], L. Lachmanski[2], S. Safi[2], S. Sene[3], C. Serre[3], J.M. Greneche[4], J. Zhang[5], R. Gref[1*]

[1] *Institut des Sciences Moléculaires d'Orsay, UMR 8214 CNRS, Université Paris-Sud, Université Paris-Saclay, Orsay, 91405, France*

[2] *Malvern Instruments, 30 rue Jean Rostand, Orsay, 91405, France*

[3] *Institut de Matériaux Poreux de Paris, FRE 2000 CNRS ENS-ESPCI, PSL Research University, Paris, 75005, France*

[4] *Institut des Molécules et des Matériaux du Mans (IMMM) - UMR 6283 CNRS, Le Mans, 72085 France*

[5] *Shanghai Institute of Materia Medica, Chinese Academy of Sciences, Shanghai, 201203, China*

*Corresponding author: E-mail address: ruxandra.gref@u-psud.fr

Supplementary Methods

Trimesate release from nanoMOFs in PBS. NanoMOFs were incubated in PBS (11.9 mM, 1.19 mM and 0.12 mM) at 37°C. The samples were centifugated and the amount of trimesate in the supernatant was assessed by HPLC. Analysis of trimesate was performed with a mobile phase containing 90% buffer (5.75 g/L of $NH_4H_2PO_4$): 10% Acetonitrile (5 mM TBAP). The injection volume was 5 µl and the detection wavelength was set at 220 nm. As controls, MOFs were incubated in water instead of PBS under the same conditions and trimesate release was monitored.

PXRD analysis. The crystallinity and purity of MIL-100 (Fe) nanoMOFs before and after degradation were assessed by PXRD. PXRD patterns were collected using a high resolution (θ-2θ) D5000 Bruker diffractometer (λ_{Cu} $K\alpha$, $K\alpha_2$) from 1º to 90º (2θ) using a step size of 0.02º and 4° per step in continuous mode. Four samples were used for the analysis: i) intact nanoMOFs; ii) totally degraded nanoMOFs after incubation in PBS (11.9 mM) for 4 h; iii) half-degraded microMOFs after incubation in PBS (11.9 mM) for 3 days, and iv) totally degraded microMOFs after incubation in PBS (11.9 mM) for 1 month.

Fourier transform infrared spectroscopy (FTIR) analysis. 100 mg of microMOFs were

incubated in 50 mL of PBS (11.9 mM) at 37 °C with stirring speed at 100 rpm. The samples were collected by centrifugation after incubation for 1 h, 2 h, 4 h, 6 h, 12 h, 24 h, 3 d, 5 d, and 7 d. The samples were dried at 100°C overnight. IR spectra were recorded in KBr disk on a Nicolet 205 FTIR.

Supplementary Results

NanoMOFs degraded quickly in concentrated PBS (11.9 mM), with their crystallinity lost (Fig. S1) and 32 ± 3.0 wt % of trimesate released after 4 hours incubation (Table S1). When PBS was diluted to 1.19 mM, it took 6 hours to get totally degraded, releasing 34 ± 2.6 wt % of trimesate. NanoMOF can also be degraded even in extremely diluted PBS (0.12 mM), releasing 31 ± 2.8 wt % after two days incubation. Whereas, there was no degradation observed in water after 2 days incubation, with less than 2 wt % of their trimesate released and the crystallinity well preserved.

Table S1. Trimesate release of nanoMOF in PBS (11.9 mM, 1.19 mM, and 0.12 mM) and in water during incubation at 37°C.

PBS concentration (mM)	Incubation time (h)	Trimesate release (wt%)
11.9	4	32 ± 3.0
1.19	6	34 ± 2.6
0.12	48	31 ± 2.8
0 (water)	48	$\leq$ 2 ± 0.2

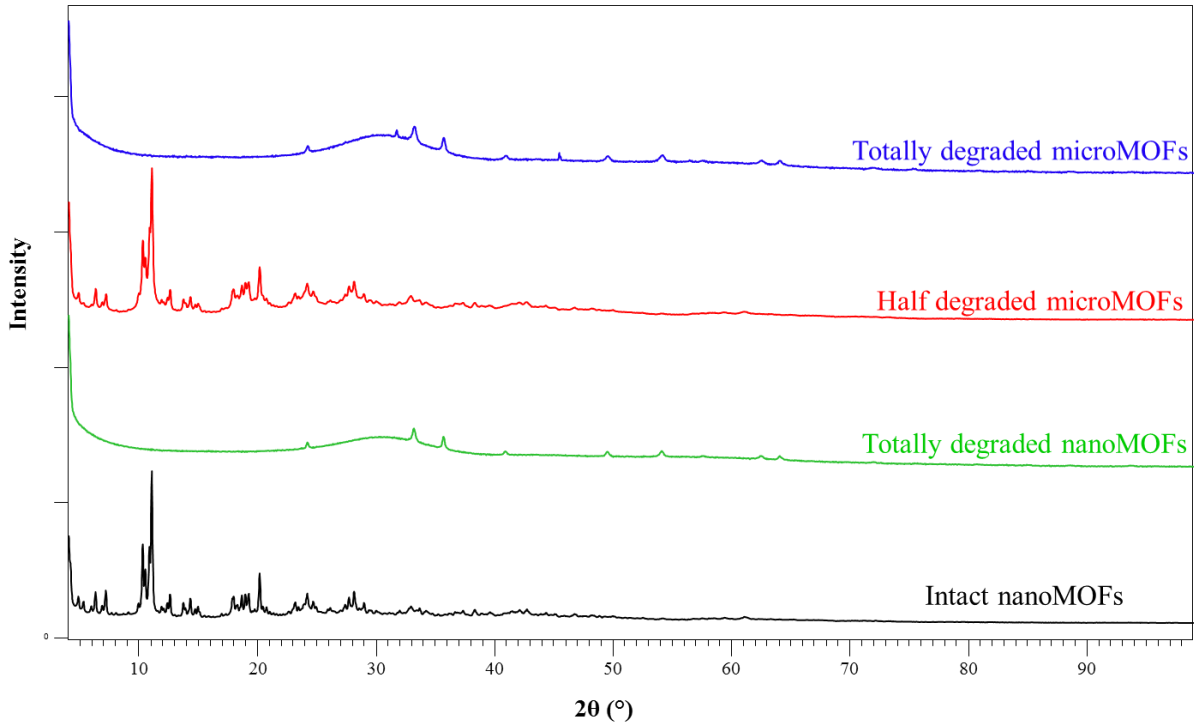

Fig. S1. PXRD pattern of intact nanoMOFs (black), totally degraded nanoMOFs (green), half-degraded microMOFs (red), and totally degraded microMOFs (blue).

The Mössbauer spectra at 77K of degraded nanoMOF and microMOF are illustrated in Fig. S2. Experiments were performed at 2 and 12 mm/s. The low velocity scale spectra are similar to those obtained at 300K and their corresponding hyperfine structures confirm previous conclusions. A deep analysis of the 12 mm/s spectra at 77K allows a small magnetic component (estimated at about 2% in at Fe) to be observed, as displayed on the insets of Fig.S2, where relative transmission scale has been strongly extended. It corresponds clearly to hematite in the case of the degraded microMOFs while it could be attributed to poorly crystallized hematite (including traces of ultra-fine grains of goethite).

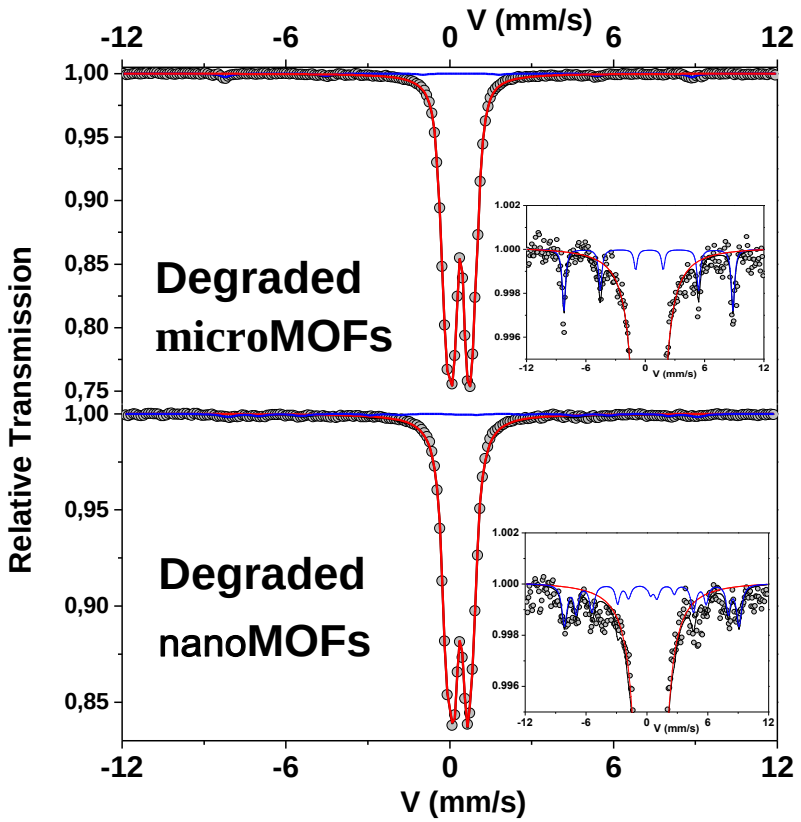

Fig. S2 Mössbauer spectra at 77K of degraded nanoMOF and microMOF

Energy dispersive X-ray analysis (EDX) was performed in order to obtain the Fe/P ratios of the intact MOFs, half degraded microMOFs, and totally degraded microMOFs. The results showed that there is significant reduce of Fe/P ratios from 1000 (intact MOFs) to 7.6 (half degraded microMOFs) and 0.9 (totally degraded microMOFs), confirming that P was coordinated inside the amorphous matrices of MOF structure during the degradation process.

Table S2. Fe/P ratios of the intact MOFs, half degraded microMOFs, and totally degraded microMOFs.

Type of MOFs	Fe (%)	P	Fe/P
intact	92.55 ± 1.43	0.09 ± 0.41	~ 1000
Half-degraded	74.94 ± 3.10	9.89 ± 3.64	~ 7.6
Totally degraded	42.60 ± 11.98	44.57 ± 13.26	~ 0.9

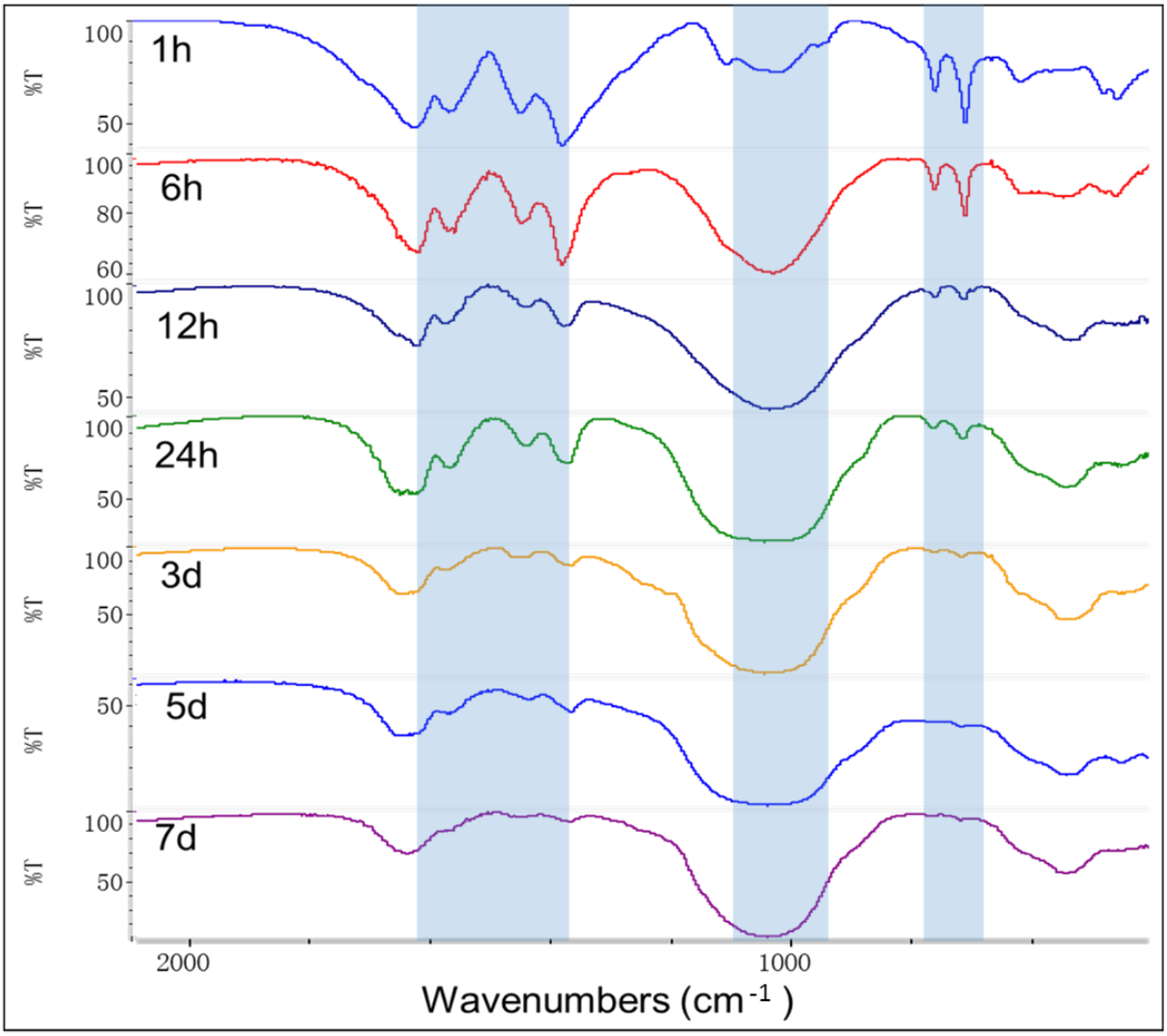

Fig. S3 FTIR spectra of microMOFs during their degradation in PBS

Subchapter 4.2

Two drugs in two different mesoporous cages inside the same nanoparticle: design and applications

In preparation

General Objectives and Author Contributions

Because of their high pore volumes and surface areas, MIL-100 (Fe) was shown to load a series of drugs, such as antibiotics and anticancer drugs, which are able to efficiently penetrate within the porous MOF structures. However, to the best of our knowledge, there is no report on synergic drugs co-encapsulation in MOF particles yet. Combinatorial drug therapies emerge among the most promising strategies to treat complex pathologies such as cancer and severe infections. Herein, Amoxicillin (AMOX) and Potassium Clavulanate (CL), the typical synergic antibiotics, were chosen for drug co-encapsulation in MIL-100 (Fe).

As described before, MIL-100 (Fe) contains two types of cages: small cages (24 Å) with pentagonal (5.6 Å) window and large cages (29 Å) with hexagonal windows (8.6 Å). The dimension of AMOX (12×9×4 Å) allows it penetrate only within the large cages. CL, with a significant smaller dimension (8×5×4 Å) than AMOX, is expected to travel through both the large and small cages. Interestingly, AMOX has larger affinity than CL, making it occupy the large cages and CL in the small cages.

Briefly, this study included four parts:

1) AMOX or CL was encapsulated as single component by by a simple "green" methods, where the as-synthesized nanoMOFs were impregnated the in aqueous drug solutions. The encapsulated AMOX and CL loadings plateaued at 13 and 27 wt%, respectively.

2) Co-encapsulation of AMOX and CL was achieved by impregnating the as-synthesized nanoMOFs in aqueous drug combination solutions. High payloads for both drugs were obtained: 13 wt% for AMOX and 22 wt% for CL, which is quite similar to the individual drug loadings.

3) Molecular simulations showed that each drug located in a separate compartment within the interconnected 3D structure of nanoMOFs.

4) I*n vitro* study on infected macrophages indicated that the drug loaded nanoMOFs were efficiently internalized in the cells, and surprisingly, could co-localize with the bacteria and act synergistically with the entrapped drugs to kill intracellular bacteria.

All the authors have contributed in this work. X. Li performed the experiments on the nanoMOFs synthesis, characterization and drug loading, and also contributed to the analysis of the data and writing of the main manuscript.

Two drugs in two different mesoporous cages inside the same nanoparticle: design and applications

Authors

N. Semiramoth[1,&], X. Li[2,&], G. Maurin[3], J. Josse[4], V. Tafani[4], F. Laurent[4], G. Salzano[2], D. Foulkes[1], N. Ghermani[1], S. Hal[3], M. Moya-Nilges[5], P. Couvreur[1], L. Majlessi[6], M.F. Bernet-Camard[7], J. Zhang[8], R. Gref[2*].

Affiliations

[1] Institut Galien, Université Paris-Sud, UMR CNRS 8612, 92290 Chatenay Malabry, France.

[2] Institut de Sciences Moléculaires, UMR CNRS 8214, Université Paris-Sud, Université Paris-Saclay, 91405 Orsay Cedex, France.

[3]Institut Charles Gerhardt, Université Montpellier, UMR 5253 UM CNRS ENSCM, 34095 Montpellier Cedex 5, France.

[4] Centre International de Recherche en Infectiologie (CIRI), INSERM U1111, Hospices Civils de Lyon, Hôpital de la Croix-Rousse, 69004 Lyon, France.

[5]Imagopole, Ultrastructural Microscopy Platform, Institut Pasteur, 75724 Paris Cedex 15, France.

[6]Unit for Integrated Mycobacterial Pathogenomics, Institut Pasteur, 75015 Paris, France

[7]EA4043-Ecosystème Microbien Digestif et Santé, Université Paris-Sud, 92296 Châtenay-Malabry.

[8]Center for Drug Delivery Systems, Shanghai Institute of Materia Medica, Chinese Academy of Sciences, Shanghai 201203, China.

[&]Equally contributing first authors

Correspondence and requests for materials: Dr Ruxandra Gref

ruxandra.gref@u-psud.fr

Abstract

Combinatorial drug therapies emerge among the most promising strategies to treat complex pathologies such as cancer and severe infections. Metal-organic frameworks nanoparticles (nanoMOFs) were used here to address the challenging aspects related to the co-incorporation of a drug combination. Amoxicillin (AMOX) and potassium clavulanate (CL), a typical example of drugs used in tandem, were efficiently co-incorporated with payloads up to 36 wt%. Each drug adopted a different penetration pathway to eventually locate in a separate compartment within the porous interconnected frameworks. Molecular simulations predicted drug loadings and locations and corroborated well the experimental findings. Furthermore, nanoMOFs were efficiently internalized in macrophages infected with *S. aureus*, were found in high amounts nearby the pathogen and contributed together with the entrapped drugs to eradicate it. These results pave the way towards the design of engineered nanocarriers in which both the loaded drugs and their carrier play a role in fighting intracellular infections.

The treatment of complex pathologies such as cancer and severe viral or bacterial infections involves taking into consideration multiple molecular and genomic pathways. In this context, combinatorial drug therapies are considered among the most effective strategies [1-4] and a recent trend is to co-incorporate synergic drugs in nanoparticles (NPs) able to target them to the diseased sites. Indeed, nanotechnology revolutionizes drug delivery by achieving: i) drug targeting; ii) transcytosis of drugs across biological barriers; iii) delivery of drugs to intracellular targets and iv) visualization of sites of drug delivery (theranostics).

The treatment of intracellular infections is particularly challenging, requiring the drugs to bypass cellular membranes to reach their target, the pathogens located in intracellular niches. Unfortunately, many drugs poorly penetrate inside cells, necessitating to increase the administered doses with might lead to side effects and drug resistance. Ideally, drugs could be loaded in NPs, which would act as "Trojan horses" to co-localize with the pathogens and release their drug cargo. Amoxicillin (AMOX) and potassium clavulanate (CL) are typical examples of drugs used in tandem to treat a variety of bacterial infections, mainly rhinosinusitis, ear infections, pharyngolaryngitis, tonsillitis, bronchitis and urinary tract infections[5]. However, these polar drugs are poorly permeable across the cell membranes and lack efficacy in intracellular infections.[6-8]

There are still few examples of NPs with different compartments engineered for drug co-incorporation. Anisotropic Janus NPs [9-12], nanocapsules[13] and polymersomes[14,15] are composed of several macroscopic compartments, each one being adapted to accommodate a specific drug. Nevertheless, the preparation methods of anisotropic NPs are relatively complex and require the use of organic solvents and surfactants. Another example is porous NPs in which drug combinations were physically adsorbed[16,17]. However, as a general trend, when drugs were co-encapsulated, they impeded each other leading to dramatically reduced loadings. For example, the loading of gemcitabine monophosphate in NPs made of coordination polymers was drastically reduced from 57 ± 2 wt% to 12 ± 2 wt% when oxaliplatin was co-encapsulated[18].

NanoMOFs based on porous iron (III) trimesate were used here to address the challenge of co-incorporating drugs with high loadings. NanoMOFs have emerged as a new class of versatile, biodegradable and non-toxic drug nanocarriers [19-21]. Because of their high pore volumes and surface areas, nanoMOFs were shown to load unprecedented amounts (within the 20-150 wt % range) of a series of drugs able to efficiently penetrate within the porous MOF structures [19,20,22-25].

Here we show that AMOX and CL can be efficiently co-incorporated in nanoMOFs following a solvent-free "green" procedure. Each drug was located in a specific compartment inside the porous nanoMOF structure, following a distinct incorporation mechanism. Remarkably, molecular simulations predicted the location of each drug as well as the maximal loadings, in good agreement with the experimental results. Advantageously, a high number of cell-internalized nanoMOFs were found to co-localize with bacteria and to degrade within hours. Contrary to free drugs, drug-loaded nanoMOFs efficiently reduced the intracellular bacterial loads, *in vitro* in a model of macrophages infected with *Staphylococcus aureus* (*S. aureus*).

Results and discussion

NanoMOFs synthesis and drug incorporation

NanoMOFs made of non-toxic mesoporous iron (III) trimesate MIL-100(Fe) (MIL standing for Material from Institute Lavoisier) are of particular interest for drug encapsulation. MIL-100(Fe) nanoMOFs are built up from iron (III) octahedra trimers and trimesate linkers (1,3,5-benzene tricarboxylate) that self-assemble to build a porous architecture delimiting two types of compartments: large (29 Å) and small (24 Å) mesoporous cages (Fig.1). The two types of cages are accessible for drug adsorption inside the crystalline MOF structure through microporous pentagonal (~5 Å) and hexagonal windows (~9 Å) [26].

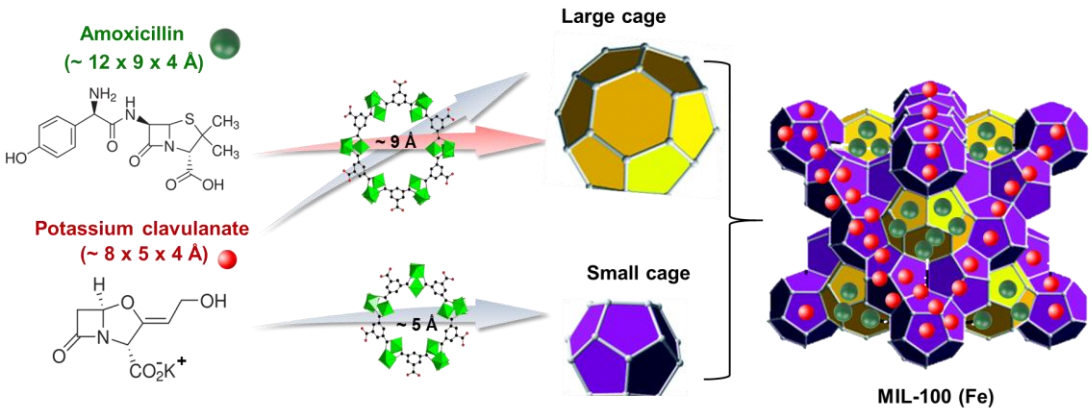

Figure 1. Schematic representation of drug incorporation in nanoMOFs. AMOX, bulkier than CL, can only cross the large hexagonal windows, whereas CL can penetrate through both pentagonal and hexagonal windows. Therefore, AMOX and CL are prone to locate in large or in large and small cages, respectively

MIL-100(Fe) nanoMOFs with mean diameters of 273 ± 23 nm and BET surface areas of 1490 ± 100 $m^2.g^{-1}$ were successfully prepared by a solvent-free "green" hydrothermal method. They displayed a crystallized structure in agreement with previously reported data[22,27] and a facetted morphology (Fig. 2a).

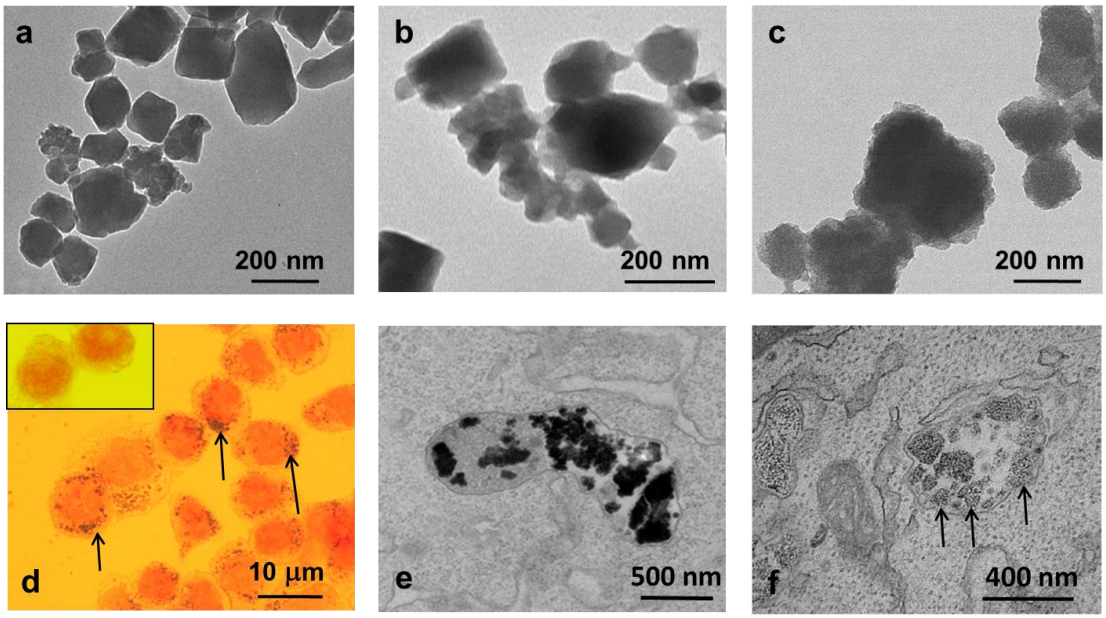

Figure 2. Microscopic investigation of nanoMOFs before and after their internalisation in J774 macrophages. TEM images of nanoMOFs: empty (a), loaded with AMOX and CL (b) and after 4 h degradation in PBS (c). J774 cells before (d, insert) and after (d, black arrows) nanoMOF uptake (optical microscopy). TEM images of cellular compartments containing nanoMOFs after 1 h (e) and 6 h (f) incubation with cells.

In a first step, AMOX and CL were encapsulated as single components by impregnating the as-synthesized nanoMOFs in aqueous solutions of each drug. The molecular dimensions of AMOX (12×9×4 Å) (Fig. 1) are very similar to the ones of azidothimidine-triphosphate (AZT-TP) which was previously shown to exclusively access the large cages of MIL-100(Fe) through the hexagonal windows [26]. Given its dimensions, AMOX is expected to cross only the large hexagonal MOF windows to access the large cages. In contrast, CL, with significant smaller dimensions (8×5×4 Å) than AMOX (Fig. 1), is able to cross both the pentagonal and the hexagonal windows of the interconnected 3D structure allowing the occupancy of both small and large mesoporous cages.

In drug loading experiments, nanoMOFs suspensions were incubated with aqueous drug solutions with increasing concentrations to estimate the maximal loadings for each drug (Fig. 3a). At weight ratios nanoMOF: drug of 32:1, the encapsulation efficiencies (EE) were higher

than 98%, showing that the drugs were efficiently soaked by the MOF "nanosponges" from their aqueous solutions (for EE calculations see methods I.3). This clearly shows the excellent affinity of nanoMOFs for the studied antibiotics and is in line with recent findings showing that MOFs can be used to remove trace antibiotics as pollutants in wastewater.

Maximal AMOX and CL loadings were 13 and 27 wt%, respectively. Even at these maximal loadings, the morphology and crystalline structure of the nanoMOFs were unaffected, as revealed by: i) identical powder X-ray diffraction patterns before and after encapsulation (Fig. S1) and ii) similar shape and facetted morphologies of the pristine and the drug-loaded nanoMOFs (Fig. 2b).

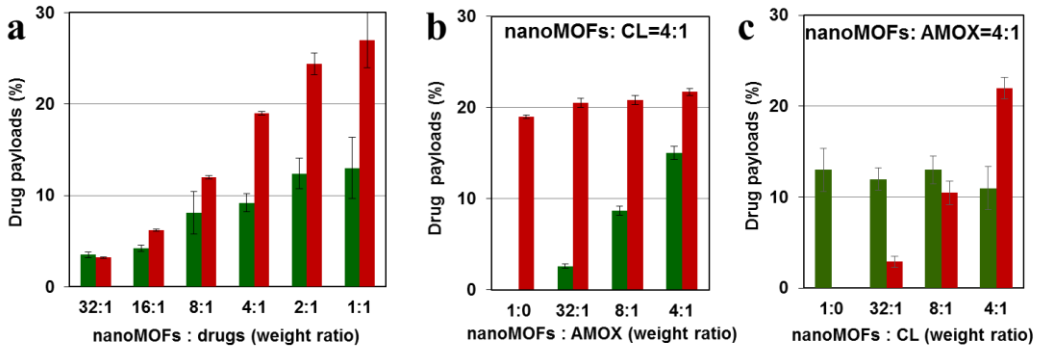

Figure 3. (Co)-incorporation of drugs as a function of the NanoMOF: drug ratio used in the preparation procedure (green: AMOX; red: CL). (a) Incorporation of individual drugs; (b, c) Co-incorporation of AMOX and CL

The nanoMOFs loaded with maximal amounts of AMOX (13 wt%) had similar mean diameters (284 ± 18 nm) as the unloaded ones (273 ± 23 nm). However, an aggregation was observed with CL-loaded nanoMOFs at their maximal loading (27 wt%). In this case, the mean diameters reached 457±46 nm after CL incorporation. Possibly, a fraction of CL located in the nanoMOF top layers induced a bridging effect, leading to their aggregation.

The proof that the drugs were mainly located inside the nanoMOF cages and not at the external surface came from BET experiments. After encapsulation of maximal amounts of AMOX and CL, BET surfaces decreased from 1490 $m^2.g^{-1}$ to 994 and 643 $m^2.g^{-1}$ for AMOX and CL at maximal loadings, respectively. These findings are consistent with an efficient pore filling by the encapsulated molecules, without altering their tridimensional crystalline structure, as previously reported with other drugs [10,22,23].

Molecular simulations of drug incorporation

Molecular simulations were performed to gain further understanding on the possible location of AMOX and CL and their interactions with the host MOF matrices. Grand Canonical Monte Carlo (GCMC) simulations were conducted first to predict the optimal uptake for both drugs as single components in MIL-100(Fe), taking into account the NP available porous volume (for details see methods I.4).

The simulated AMOX uptake in the nanoMOFs of 15.5 wt% was in good agreement with the experimental data (13 wt%). This is in good agreement with the experimental N_2 adsorption data which showed that the BET surface area evolved from 1490 $m^2.g^{-1}$ (empty nanoMOF) to 994 $m^2.g^{-1}$ (nanoMOF loaded with AMOX at their maximal capacity). These data support the assumption that AMOX was exclusively incorporated in the large cages of MIL-100(Fe) since the volume ratio between large cages and small cages is 1:2.

Contrary to AMOX (12×9×4 Å), CL, with significant smaller dimensions (8×5×4 Å) (Fig. 1), is expected to penetrate through the entire MOF 3D structure, allowing the occupancy of both small and large mesoporous cages. Indeed, this assumption was confirmed experimentally by a drastic reduction of the BET surface after CL incorporation (643 $m^2.g^{-1}$), as compared to AMOX-loaded nanoMOFs (994 $m^2.g^{-1}$) and empty ones (1490 $m^2.g^{-1}$). Moreover, the simulated CL uptake of 30.6 wt% was in good agreement with the experimental loading of 27 wt%. Altogether, these data unambiguously demonstrate that when adsorbed as a single component, CL accommodates in both types of MIL-100(Fe) cages.

Co-incorporation of AMOX and CL

Furthermore, AMOX and CL were co-incorporated in the nanoMOFs by the same "green" strategy used for single drugs and consisting in incubating the nanoMOFs with aqueous solutions of both drugs. Extensive studies were carried on, by varying the molar ratio AMOX: CL in an attempt to gain insights on the competition between the two drugs for the nanoMOF cages. Fig. 3b shows that when AMOX was loaded at 13 wt%, i.e. the maximal nanoMOF capacity previously determined for this drug, it was still possible to load additional 22 wt% CL in the MOFs. More precisely, Fig. 3b shows that whatever the AMOX content in the nanoMOFs (from 2 to 13 wt%), the amount of CL which could additionally be loaded was practically constant (20 ± 2 wt%). This overrules the possibility that AMOX impedes CL incorporation in the nanoMOFs. Moreover, the AMOX loadings were unaffected by CL loading (13 ± 0.9%, 13 ± 0.8% for AMOX with or without CL). In conclusion, AMOX and CL could be simultaneously

loaded without impeding each other. The combinational payload reached at maximum 35 wt%, including 22 wt% of CL and 13 wt% of AMOX.

As in the case of single drugs, co-incorporation of AMOX and CL did not alter the nanoMOF crystalline structure (identical X-ray diffraction patterns, Fig. S1) nor their morphology (Fig. 2b). Interestingly, after co-incorporation of both drugs at their maximal loadings (13 wt% and 22 wt% for AMOX and CL, respectively) there was less than 10% variation of the mean diameters (273 ± 23 nm and 298 ± 9 nm, before and after drug loading, respectively). The nanoMOFs loaded with both drugs were stable upon storage and in cell culture media.

As previously, GCMC simulations were performed to gain insights into the possible locations of co-incorporated AMOX and CL. A careful analysis of the GCMC runs evidenced that each drugs followed a distinct pore filling mechanism. The AMOX molecules were almost exclusively incorporated in the large cages with an uptake of 15.5 wt%, identical to the one simulated above in the case of AMOX adsorption as single component. In contrast, CL was able to accommodate both small and large cages. Interestingly, almost all the entire fraction of the encapsulated CL molecules occupied the small cages with less than 5% CL located in the large cages near the windows. The simulated CL uptake in these compartments was 20 wt%, in excellent agreement with the experimental results (22 wt%). In conclusion, GCMC simulations were a powerful tool to predict the competitive adsorption of AMOX and CL in MIL-100(Fe) nanoMOFs.

Furthermore, the density probability plot reported in Fig. 4 clearly showed that the drugs were characterized by totally different distributions inside the MOF. The two distinct preferential adsorption regions (AMOX, green and CL, red) suggest independent incorporation mechanisms.

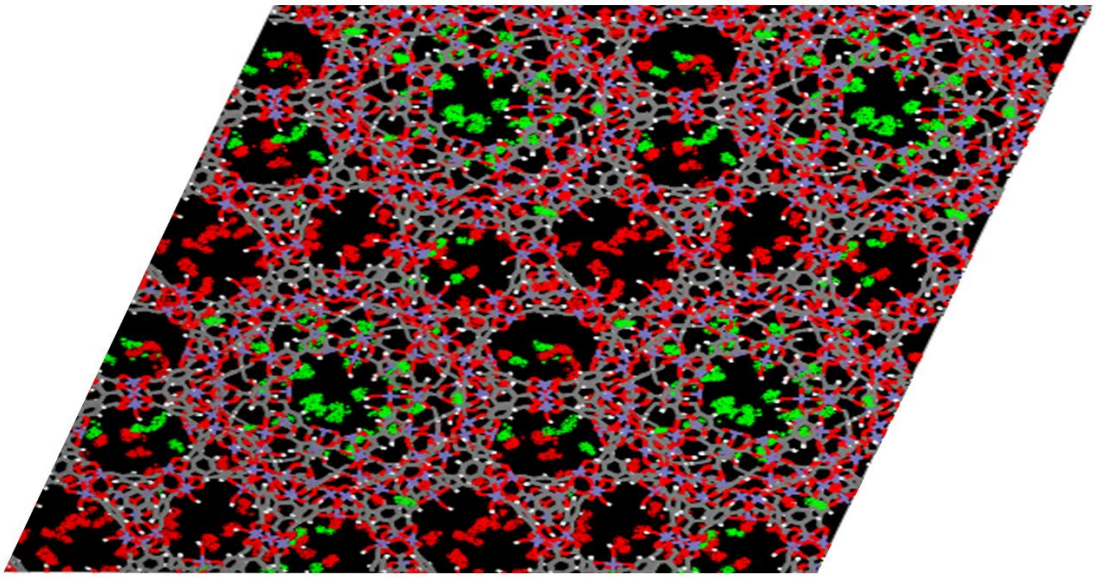

Figure 4. Density probability plots for AMOX (green) and CL (red) in the cages of MIL-100(Fe). Data were extracted from the GCMC simulations conducted for the co-encapsulation of the two drugs (uptakes of 15.5 wt% and 20 wt% for AMOX and CL, respectively).

The preferential arrangements of AMOX and CL in the large and small cages, respectively, were determined by Monte Carlo simulations (see methods I.4). Figure 5a shows that in the large cage, AMOX adapted its conformation to establish relatively strong interactions with the cage walls, displaying several interacting pairs characterized by distances below 3.0 Å. More precisely, the carbonyl and the hydroxyl functions of AMOX interacted with the Fe metal sites and the carbonyl groups of the MIL-100(Fe) framework, respectively. As illustrated in Fig.5b, CL showed similar interactions as AMOX with the small cage walls, although this molecule contains a lower number of active sites as compared to AMOX. The calculated interacting distances were significantly longer, suggesting a weaker host/drug interaction. These results were confirmed by simulated adsorption enthalpies, which were in the rage of -224 kJ/mol and -150 kJ/mol for AMOX and CL, respectively. In a nutshell, simulation studies clearly demonstrated that AMOX has a stronger affinity than CL for the MIL-100(Fe) framework. This supports the previous experimental findings, which showed that once incorporated in the large cages, AMOX couldn't be displaced by CL, a drug with lower affinity than AMOX for the nanoMOFs.

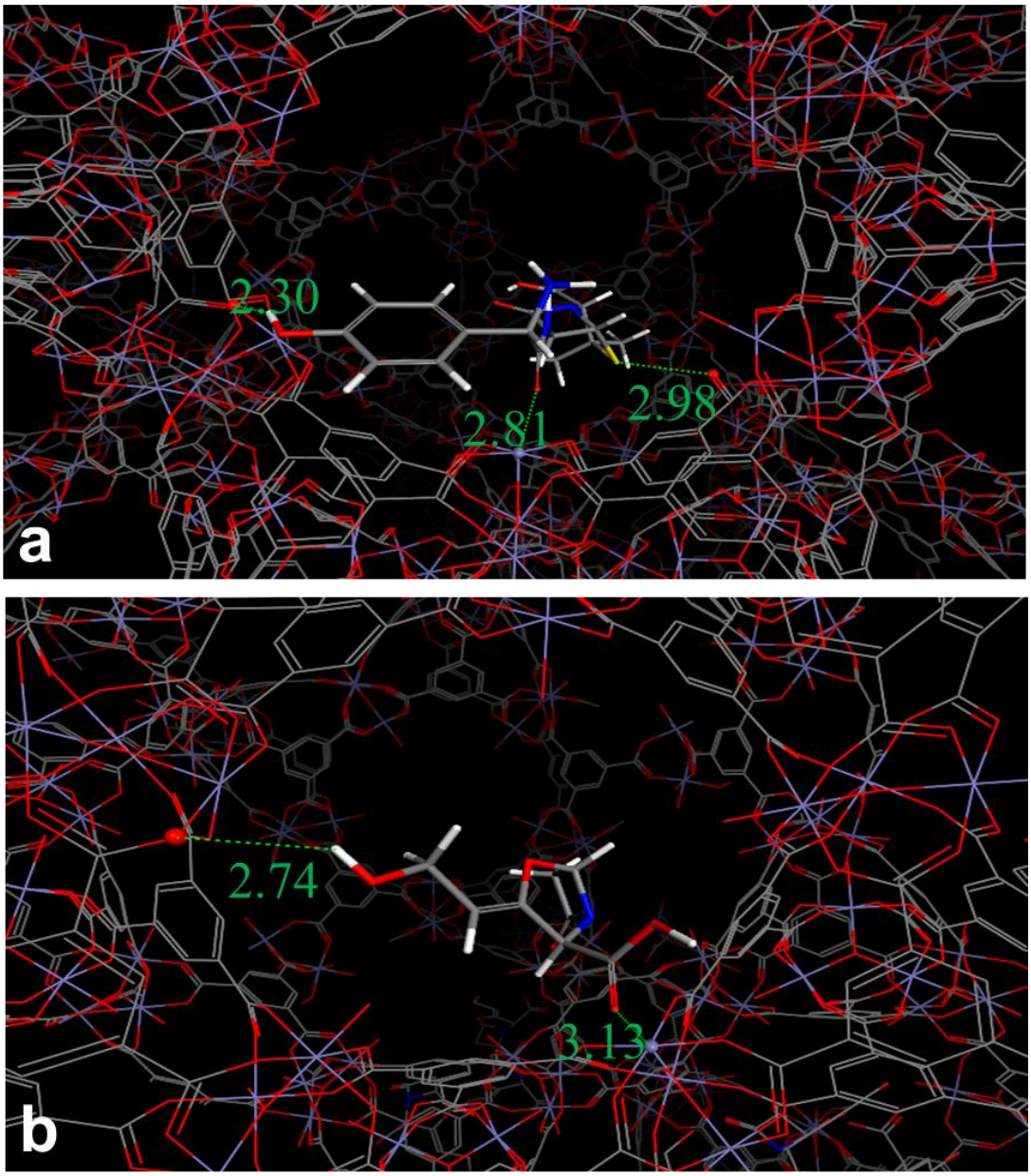

Figure 5. Preferential geometries of AMOX (a) and CL (b) in the large and the small mesoporous cages of MIL-100(Fe), respectively. Calculations were issued from Monte Carlo simulations performed with one drug molecule per cage. For clarity reasons, the hydrogen atoms of the framework are not represented. The characteristic drug/MOF interacting distances are reported in Å.

Given the capacity of MIL-100(Fe) nanoMOFs to incorporate high amounts of both AMOX and CL (total loading 35 wt%), these nanocarriers were further studied *in vitro* on infected cells to test their antibacterial properties.

Uptake of nanoMOFs by macrophages and effects on intracellular *S. aureus*

S. aureus possesses several virulence mechanisms to accommodate a diversity of niches. On one side, *S. aureus* can be the production of toxins that favor cell lysis and tissue destruction in acute infections. On the other side, it can invade and survive in host cells such as epithelial cells, osteoblasts, neutrophils or macrophages and be responsible for chronic infections. Indeed, several main antibiotics such as β-lactams and aminoglycosides lack of efficacy to eradicate intracellular pathogens [26,28,29], as they can poorly bypass cell membranes and/or are rapidly cleared off by efflux pumps (Fig. 6a). Contrary to free drugs, nanoMOFs are able to efficiently penetrate inside infected macrophages and to release their drug cargo near pathogens could be powerful alternatives to treat intracellular infections [26,30,31]. The ability of nanoMOFs loaded with AMOX and CL to address this important goal was tested here. Firstly, the cytotoxicity of nanoMOFs at various concentration was tested (data not shown). The nanoMOFs were found to be non-cytotoxic in J774 macrophages at concentrations up to 50 µg/mL. Indeed, after 24 h of contact with nanoMOFs, cell viability was higher than 90%. The internalization of nanoMOFs by macrophages was studies at concentration of 25 µg/mL.

Efficient internalization of nanoMOFs is crucial to eliminate intracellular pathogens. The presence of nanoMOFs was first confirmed by optical microscopy investigations (Fig. 2d). It was found that nanoMOFs were efficiently taken up by J774 cells, mainly by phagocytosis and in a lesser extent by a clathrin-dependent pathway (Fig. S2). In agreement with these findings, a large number of nanoMOFs were found in endosomal or/and phagolysosomal compartments of non-infected cells (Fig. 2e). After 6 h incubation, the nanoMOFs degraded inside these compartments, showing a blurry transparent structure (Fig. 2f) similar to the previous one reported in *in vitro* degradation studies in PBS[32].

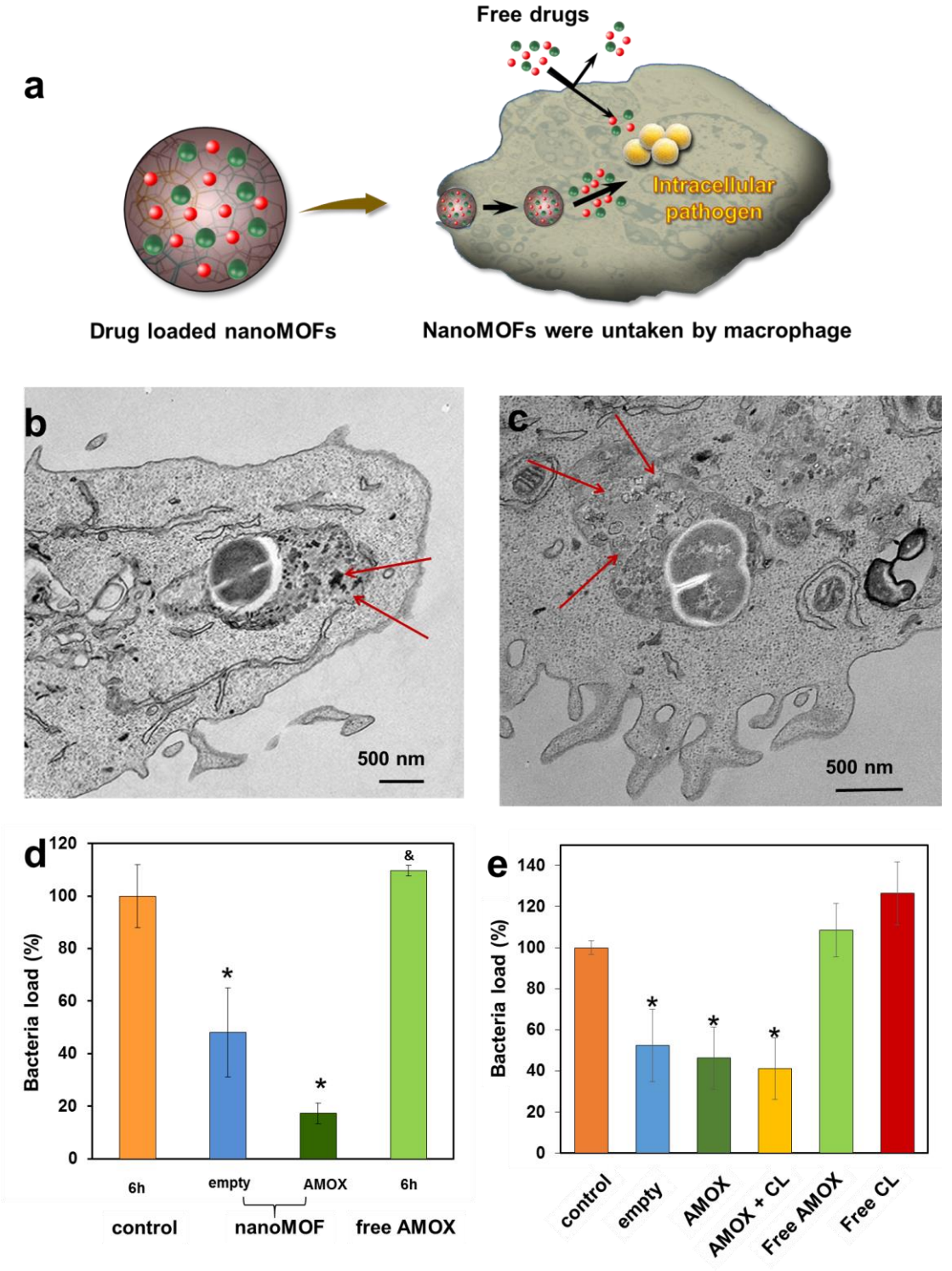

Figure 6. The internalization of drug loaded nanoMOFs in infected macrophages and their antibacterial effects. Schematic representation (a); TEM images of J774 macrophages showing nanoMOFs co-localized with *S. aureus* after 1 h incubation (b, red arrows) and partially degraded after 6 h (c, red arrows); Antibacterial effects of free AMOX, empty and drug-loaded nanoMOFs on *S. aureus* (ATCC55585) (d) and of AMOX and CL on a clinical

penicillin-resistant *S. aureus* (e).

Finally, we investigated the effect of nanoMOFs on intracellular *S. aureus* in *in vitro* cell infection models using J774 murine macrophages. Cells were first pre-incubated with nanoMOFs, loaded or not with drugs, during 2 h. Then, cells were washed and infected with *S. aureus* for 2 h. At the end of the infection time, extracellular bacteria were eliminated and cells were incubated with gentamicin for 1 h or 6 h. This experimental protocol allowed us to focus on killing of intracellular staphylococci by internalized nanoMOFs without dealing with what happens in the extracellular environment. First, we evaluated the effect of empty nanoMOFs and AMOX-loaded nanoMOFs on penicillin-susceptible *S. aureus* ATCC 55585. As we observed on TEM images, several nanoMOFs were found to co-localize with intracellular *S. aureus* in the phagosomes of infected cells, even after 1h post incubation (Fig. 6b). After 6 h incubation, intracellular nanoMOFs structure became blurred indicating their degradation as it was observed in non-infected cells (Fig. 2f, Fig. 6b). Quantification of intracellular staphylococci reported a decrease of 80% after 6h incubation with AMOX-loaded nanoMOFs. As expected, free AMOX known to poorly penetrate inside the cells[33,34] had no effect on intracellular bacteria. Interestingly, a decrease of intracellular bacteria number was also reported with empty nanoMOFs (Fig. 6d). The bactericidal effect of this cell-internalized free nanoMOFs was reported proportional both to the amount of nanoMOFs initially in contact with the cells and the incubation time (Fig.S3). A significant bactericidal effect of empty nanoMOFs was observed when the amount of nanoMOFs initially in contact with the cells was higher than 12.5 µg/mL and after 6 h of incubation.

To confirm our results and test the co-encapsulation biologic activities, we evaluated the intracellular efficacy of nanoMOFs loaded with AMOX and CL on a clinical penicillin-resistant *S. aureus*. We still observed a decrease of the number of intracellular staphylococci with empty nanoMOFs, but this effect was not significantly enhanced by the incorporation of AMOX or of AMOX and CL (Fig. 6e). Experiments with longer incubation times (up to 24 h) gave similar results. The antibacterial effect of empty nanoMOFs on intracellular bacteria overwhelmed that of the incorporated drugs. Of note, nanoMOFs had no direct effect on *S. aureus* (MIC > 250 µg/mL). Further studies will be needed to decipher the bactericidal effect of nanoMOFs which could be related to reactive oxygen species (ROS) production [35,36], without toxic effects of the J774 macrophages.

Conclusion

Here we showed for the first time that two drugs can be efficiently incorporated in MOFs, each one being preferentially adsorbed in the large or small mesoporous cages. The drugs followed individual incorporation mechanisms without impeding each other, resulting in total loadings as high as 35 wt%. Molecular modelling corroborated well the experimental findings and predicted the preferential location of each molecule. It was discovered that, nanoMOFs were prone to co-localize with intracellular pathogens and had an intrinsic bactericidal action, contributing, together with the incorporated drugs, to reduce the bacterial loads. These results pave the way towards the design of engineered NPs in which each component (drugs and nanocarrier) plays a role in fighting intracellular infections.

Methods

Methods, including statements of data availability and any associated accession codes and references, are available.

References

1. Peer, D., Karp, J.M., Hong, S, Farokhzad, OC, Margalit, R & Langer, R. Nanocarriers as an emerging platform for cancer therapy. *Nat. Nanotechnol.* **2**, 751-760 (2007).
2. Dancey, J.E., & Chen, HX. Strategies for optimizing combinations of molecularly targeted anticancer agents. *Nat. Rev. Drug Discov.* **5**, 649-659 (2006).
3. Marguet, M., Bonduelle, C., & Lecommandoux, S. Multicompartmentalized polymeric systems: towards biomimetic cellular structure and function. *Chem. Soc. Rev.* **42**, 512-529 (2013).
4. Mignani, S., Bryszewska, M., Klajnert-Maculewicz, B., Zablocka, M., & Majoral, J.P., Advances in combination therapies based on nanoparticles for efficacious cancer treatment: an analytical report. *Biomacromolecules.* **16**, 1-27 (2015).
5. Sng, W.J., & Wang, D.Y. Efficacy and side effects of antibiotics in the treatment of acute rhinosinusitis: a systematic review. *Rhinology.* **53**, 3-9 (2015).
6. Briones E., Colino C. I., Lanao J. M., Delivery systems to increase the selectivity of antibiotics in phagocytic cells. *J. Control. Release***125**, 210-227 (2008).
7. Spaniol V., Bernhard S., &Aebi C. Moraxella catarrhalis AcrAB-OprM efflux pump contributes to antimicrobial resistance and is enhanced during cold shock response. *Antimicrob Agents Chemother.* **59**, 1886-1894 (2015).
8. Sémiramoth N., et al. Self-assembled squalenoylated penicillin bioconjugates: an original

approach for the treatment of intracellular infections. *ACS Nano.* **22**, 3820-3831 (2012).

9. Scarano, W., de Souza, P., & Stenzel, M.H. Dual-drug delivery of curcumin and platinum drugs in polymeric micelles enhances the synergistic effects: a double act for the treatment of multidrug-resistant cancer. *Biomater. Sci.* **3**, 163-174 (2015).
10. Garbuzenko, O.B., Winkler, J., Tomassone, M.S., & Minko, T. Biodegradable Janus nanoparticles for local pulmonary delivery of hydrophilic and hydrophobic molecules to the lungs. *Langmuir* **30**, 12941-12949 (2012).
11. Meng, H. *et al*. Use of a lipid-coated mesoporous silica nanoparticle platform for synergistic gemcitabine and paclitaxel delivery to human pancreatic cancer in mice. *ACS. Nano.* **9**, 3540-3457 (2015).
12. Xie, H., She, Z. G., Wang, S., Sharma, G., & Smith, J. W. One-step fabrication of polymeric Janus nanoparticles for drug delivery. *Langmuir* **28**, 4459-4463 (2012).
13. Danhier, F., Messaoudi, K., Lemaire, L., Benoit, J. P., & Lagarce, F. Combined anti-Galectin-1 and anti-EGFR siRNA-loaded chitosan-lipid nanocapsules decrease temozolomide resistance in glioblastoma: in vivo evaluation. *Int. J. Pharm.* **481**, 154-161 (2015).
14. Hu, S. H. Chen, S. Y., & Gao, X. Multifunctional nanocapsules for simultaneous encapsulation of hydrophilic and hydrophobic compounds and on-demand release. *ACS. Nano.* **6**, 2558-2565 (2012).
15. Peters, R. J. *et al*. Cascade reactions in multi compartmentalized polymersomes. *Angew. Chem. Int. Ed. Engl.* **53**, 146-150 (2014).
16. Meng, H. *et al*. Use of a lipid-coated mesoporous silica nanoparticle platform for synergistic gemcitabine and paclitaxel delivery to human pancreatic cancer in mice. *ACS. Nano.* **9**, 3540-3457 (2015).
17. Ashley, C. A. *et al*. The targeted delivery of multicomponent cargos to cancer cells by nanoporous particle-supported lipid bilayers, *Nat. Mater.* **10**,389-397 (2011).
18. Poon, C., He, C., Liu, D., Lu, K., & Lin, W. Self-assembled nanoscale coordination polymers carrying oxaliplatin and gemcitabine for synergistic combination therapy of pancreatic cancer. *J. Control Release.* **201**, 90-99 (2015).
19. Horcajada, P. *et al*. Porous metal–organic-framework nanoscale carriers as a potential platform for drug delivery and imaging. *Nat. Mater.* **9**, 172-178 (2010).
20. Horcajada, P. *et al*. Metal-organic frameworks as efficient materials for drug delivery. *Angew. Chem. Int. Ed.* **45**, 5974-5978 (2006).
21. Baati, T. *et al*. In depth analysis of the in vivo toxicity of nanoparticles of porous iron(III)

metal–organic frameworks. *Chem. Sci.* **4**, 1597-1607 (2013).

22. Agostoni, V. *et al*. Towards an Improved anti-HIV Activity of NRTI via Metal-Organic Frameworks Nanoparticles. *Adv. Healthcare Mater.* **2**, 1630-1637 (2013).
23. Chalati, T. *et al*. Porous metal organic framework nanoparticles to address the challenges related to busulfan encapsulation. *Nanomedicine* **6**, 1683-1695 (2011).
24. Horcajada, P. *et al*. Flexible porous metal-organic frameworks for a controlled drug delivery. *J. Am. Chem. Soc.* **130**, 6774-6780 (2008).
25. di Nunzio, M. R., Agostoni, V., Cohen, B., Gref, R., & Douhal, A. A "ship in a bottle" strategy to load a hydrophilic anticancer drug in porous metal organic framework nanoparticles: efficient encapsulation, matrix stabilization, and photodelivery, *J. Med. Chem.* **57**, 411-420 (2014).
26. Horcajada, P. *et al*. Synthesis and catalytic properties of MIL-100(Fe), an iron(III) carboxylate with large pores. *Chem. Commun.* **27**, 2820-2822 (2007).
27. Agostoni, V. et al. Impact of phosphorylation on the encapsulation of nucleoside analogues within porous iron(III) metal-organic framework MIL-100(Fe) nanoparticles. *J. Materials Chemistry B* **1**, 4231-4242 (2013).
28. Fraunholz, M. & Sinha, B. Intracellular staphylococcus aureus: Live-in and let die. *Front. Cell. Infect. Microbiol.* **2,** 1–10 (2012).
29. Ramón-García, S. *et al.* Repurposing clinically approved cephalosporins for tuberculosis therapy. *Sci. Rep.* **6,** 34293 (2016).
30. Canton I,& Battaglia G. Endocytosis at the nanoscale. *Chem Soc Rev.* **41,** 2718-2739 (2012).
31. Kamaruzzaman, N. F., Kendall, S. & Good, L. Targeting the hard to reach: challenges and novel strategies in the treatment of intracellular bacterial infections. *Br. J. Pharmacol.* **174,** 2225–2236 (2017).
32. Li, X. *et al*. New insights into the degradation mechanism of metal-organic frameworks drug carriers. *Sci. Rep., in press.*
33. Briones, E., Colino C. I., & Lanao J. M. Delivery systems to increase the selectivity of antibiotics in phagocytic cells. *J. Control. Release* **125**, 210-227 (2008).
34. Lecaroz, C., Gamazo, C., Blanco-Prieto, & M. J. Nanocarriers with gentamicin to treat intracellular pathogens. *J. Nanosci. Nanotechnol.* **6**, 3296-3302 (2006).
35. Van Acker, H. *et al.* The role of reactive oxygen species in antibiotic-induced cell death in Burkholderia cepacia complex bacteria. *PLoS One* **11,** 1–20 (2016).

36. Ferrándiz, M. J., Martín-Galiano, A. J., Arnanz, C., Zimmerman, T. & De La Campa, A. G. Reactive oxygen species contribute to the bactericidal effects of the fluoroquinolone moxifloxacin in Streptococcus pneumoniae. *Antimicrob. Agents Chemother.* **60,** 409–417 (2016).

37. Agostoni, V. et al. 'Green' fluorine-free mesoporous iron(III) trimesate nanoparticles for drug delivery. *Green Materials*, **1**, 209-217 (2013).

38. Durga, M. R. T., & Singh, N. Development and Validation of Stability Indicating HPLC Method for Simultaneous Estimation of Amoxicillin and Clavulanic Acid in Injection. *American J. of Analytical Chemistry*, **1**, 95-101 (2010).

39. Düren, T., Millange, F., Férey, G., Walton, K.S., & Snurr, R.Q. Calculating Geometric Surface Areas as a Characterization Tool for Metal-Organic Frameworks *J. Phys. Chem. C*, **111**, 15350-15356 (2007).

40. Rappe, A.K., Casewit, C.J., Colwell, K.S., Goddard-III, W.A., & Skiff. W.M. UFF, a full periodic table force field for molecular mechanics and molecular dynamics simulations. *J. Am. Chem. Soc*., **114**, 10024 -10035 (1992).

41. Lastoskie C., Gubbins K.E., & Quirke, N. Pore Size Distribution Analysis of Microporous Carbons: A Density Functional Theory Approach. *J. Phys. Chem*. *97*, 4786-4796 (1993).

42. Férey, G., Serre, C., Mellot-Draznieks, C., Millange, F., Surble, S., Dutour J., & Margiolaki, I. A Hybrid Solid with Giant Pores Prepared by a Combination of Targeted Chemistry, Simulation, and Powder Diffraction. *Angew. Chem., Int. Ed.* **43**, 6296-6301 (2004).

43. Frost, H., Düren, T., & Snurr, R.Q. Effects of Surface Area, Free Volume, and Heat of Adsorption on Hydrogen Uptake in Metal-Organic Frameworks. *J. Phys. Chem. B* **110**, 9565-9570 (2006).

44. Yang, Q., & Zhong, C. Molecular Simulation of Carbon Dioxide/Methane/Hydrogen Mixture Adsorption in Metal-Organic Frameworks. *J. Phys. Chem. B* **110**, 17776- 17783 (2006).

45. Rappe, A. K., & Goddard, W. A. Charge equilibration for molecular dynamics simulations. *J. Phys. Chem.* **95**, 3358-3363 (1991). Wilmer, C. E., and Snurr, R. Q. Towards rapid computational screening of metal-organic frameworks for carbon dioxide capture: Calculation of framework charges via charge equilibration. *Chem. Eng. J.* **171**, 775 (2011).

46. Becke, A.D. Density-functional thermochemistry. III. The role of exact exchange. *J. Chem. Phys.* **98**, 5648-5652 (1993).

47. Schmidt, M.W., *et al*. General atomic and molecular electronic structure system. *J. Comput. Chem*. **14**, 1347-1363 (1993).

48. Wang, J., Wolf, R.M., Caldwell, J.W., Kollman, P.A., & Case, D.A. Development and testing of a general amber force field. *J. Comput. Chem.* **25**, 1157-1174 (2004).
49. Vlugt, T. J. H.; Garcia-Perez, E.; Dubbeldam, D.; Ban, S.; Calero, S., Computing the heat of adsorption using molecular simulations: The effect of strong Coulombic interactions. *J. Chem. Theory. Comput.* **4**, 1107-1118 (2008). *J. Phys. Chem. B* **110**, 17531-17538 (2006).
50. Sémiramoth, N. *et al*. Self-Assembled Squalenoylated Penicillin Bioconjugates: An Original Approach for the Treatment of Intracellular Infections. *ACS Nano,* **6**, 3820-3831 (2012).

Acknowledgments

This research was funded by European Union through Cyclon Hit project (People-2013-ITN), Grant Agreement 608407. We acknowledge support from the French ANR projects AntiTBnano (ANR-14-CE08-0017) and Virmil (ANR-2010-RMNP-004-01). We thank Dr. H. Willaime, Dr. P. Horcajada and Dr. C. Serre for helpful discussions. X. Li acknowledges support from China scholarship council (CSC, n° 201408330166). G.M. thanks Institut Universitaire de France for its support.

Author contribution statement

R.G. and X.L. wrote the main manuscript. N.S., X.L., D.F., N.G., L.M. and G.S. contributed to the nanoMOFs synthesis, characterization and drug loading. G.M. and S.H. performed the molecular modeling studies. N.S. and D.F. performed the cell culture studies and optical microscopy investigations. V.T., J.J. and F.L. performed cell toxicity studies and *in vitro* studies with infected cells. M.M.N. carried on the TEM studies. N.S., R.G., J.Z., X.L., P.C. and M.F.B.C. contributed to the analysis of the data. All authors reviewed the manuscript.

Additional information

Supplementary information is available. Correspondence and requests for materials should be addressed to R.G.

Competing financial interests

There is no competing financial interest.

Dedication

This paper is dedicated to the memory of Dr. Christian GREF.

Materials and Methods

I.1 Materials

Chemical materials. Iron (III) chloride hexahydrate (98%, Alfa Aesar, Schiltigheim, France), 1,3,5-benzenetricarboxylic acid (BTC, 95%, Sigma-Aldrich, Saint-Quentin-Fallavier, France) and absolute ethanol (99%, Carlo Erba, Val-de-Reuil, france) were used for the synthesis of nanoMOFs. AMOX and CL were purchased from Sigma-Aldrich. All the chemicals were used without further purification.

Cell culture. Murine macrophages J774 were grown in RPMI-1640 medium (BioWhittaker, Walkerville, MD, USA) supplemented with 10% v/v decomplemented fetal bovine serum (FBS) (Cambrex BioSciences, Verviers, Belgium) at 37°C in humidified air containing 5% CO_2. Lactate dehydrogenase leakage (LDH, Sigma-Aldrich) were used for toxicity evaluation of nanoMOFs.

NanoMOFs internalization assay. Cytochalasin D 5µg/mL, Latrunculine A 400 nM, Wortmannin 300 nM, Chlorpromazine 20 µM, Ikarugamycin 4 µM, methyl-β-cyclodextrin (Mβ-CD 1 mM, Genistein 100 µM, Fillipin III 1 µM (Sigma-Aldrich) were used as pharmacological inhibitors to investigate the nanoMOF mechanisms of cell internalisation. Tiron (Sigma-Aldrich) was used to inhibit the ROS effect. Prussian blue staining (Sigma-Aldrich) was used as Iron staining kit to visualise the intracellular nanoMOFs.

Bacterial culture. The beta-lactam sensitive *S. aureus* (ATCC55585) stock strains were maintained in 20% glycerol at -80°C. Before experiments, the bacteria were transferred onto fresh Brain Heart Infusion (BHI)/ agar (Difco, Invitrogen, Cergy-Pontoise, France) and incubated at 37°C for 24 h. For each experiment, bacteria were subcultured in BHI (medium) at 37°C for 18 h. The day of the experiment, the bacteria were washed twice with sterile PBS, counted in a Salumbini chamber, and adjusted to 5×10^6 bacteria/mL in RPMI-1640 medium supplemented with 10% v/v FBS.

I.2 MIL100 (Fe) nanoMOFs synthesis and characterization

NanoMOFs synthesis. MIL100 (Fe) iron trimesate nanoMOFs were synthesized by adapting a previously described method[26]. Briefly, nanoMOFs were obtained by microwave-assisted hydrothermal synthesis from a mixture of iron chloride (8.97 mmol) and BTC (4.02 mmol) in 20 mL of deionized water. The mixture was heated 6 min at 130°C under stirring. The power applied was 400 Watt (Mars-5, CEM, US) with a power maximum output 1,600 ± 240 Watts

and frequency at full power 2,450 mHz. The resulting nanoMOFs were recovered by centrifuging 10 min at 10,000 ×g and washed with absolute ethanol 6 times to remove the residual non reacted organic acid. A last centrifugation at 5500 ×g was performed during 1 min in absolute ethanol to sediment the largest particles and recover the supernatants as a suspension of monodisperse nanoparticles. NanoMOFs were stored wet in ethanol until final use.

NanoMOFs characterization. The cristallinity and purity of MIL-100 (Fe) nanoMOFs were assessed by X ray powder diffraction (XRPD) patterns which were collected in a conventional high resolution (θ-2θ) D5000 Bruker diffractometer (λ_{Cu} K_{α}, $K_{\alpha 2}$) from 1º to 20º (2θ) using a step size of 0.02º and 4° per step in continuous mode. The size distribution and Zeta potential of nanoMOFs were characterized by dynamic light scattering (DLS; Malvern® Nano-ZS) nanosight (NTA, LM10 Nanosight), and using a Zetasizer (Malvern® ZSP, UK) respectively.

Nanosight analyses combines a conventional optical microscope with a laser to illuminate nanoparticles in Brownian motion. Particles could be visualised one by one as moving point-scatters. Each measurement was repeated 5 times, at room temperature. The particle size distribution was determined using the NTA software.

Transmission electron microscopy (TEM) images were collected in a Darwin 208 Philips microscope (60-80-100 KV; Camera AMT). The nanoparticles porous surface was measured by nitrogen sorption experiments at -77 K on a ASAP 2020 (Micromeritics) after sample's outgassing at 150°C for 18 h under secondary vacuum.

I.3 Drug incorporation

Drugs were loaded within MIL-100 (Fe) nanoMOFs simply by impregnation of well defined amounts of nanoMOFs and drug(s) solutions in water. Practically, 1 or 4 mg of nanoMOFs were centrifuged for 10 min at 10,000 g and re-suspended in 1 mL of aqueous drug solutions (concentrations from 0.125 to 1 mg/mL) or water as a control. After incubation for 12 h under gentle stirring, the nanoMOFs were recovered by centrifugation (10,000×g, 10 min) and the non-encapsulated drug in the supernatant was quantified by adapting a previously described HPLC method[37]. Specifically, HPLC analysis was performed on a Waters™ system using a Waters™ 486 tunable UV absorbance detector. Eluant flowed at a rate of 0.5 mL/min through a C18 Silica 150 × 3.0 mm column (Interchim, Montluçon France) maintained at 30°C. The injection volume was 20 µL which ran for 8 min after each injection. The mobile phase consisted of 5.2 g/L of sodium dihydrogene phosphate monohydrate in 30% (v/v) methanol. The pH was adjusted to 5 using dilute ortho-phosphoric acid solution. CL and AMOX were

detected at 247 nm and retention times were 2.1 and 4.6 minutes, respectively.

The encapsulation efficiency (EE) was calculated as Equation (1):

$$EE\ \ (\%) = \frac{Encapsulated\ \ Drug\ (mg)}{Initial\ \ Drug\ (mg)} \times 100 \qquad (1)$$

where "encapsulated Drug" represents the amount (mg) of drug incorporated in nanoMOFs and "Initial drug" represents the amount (mg) of drug initially added in the experiment.

The drug payload was calculated as Equation (2):

$$Payload\ \ (\%) = \frac{Encapsulated\ \ Drug\ (mg)}{nanoMOFs\ (mg)} \times 100 \qquad (2)$$

Drug release was studied in different media (water, cell culture media). After incubation at 37°C during different lapses of time, nanoMOFs were recovered by centrifugation (10 min, 10000×g) and supernatants were assessed by HPLC to determine the amounts of released drug(s).

I.4 Molecular simulations

Simulation of the accessible surface area and free volume.

The accessible surface area and free volume were calculated using a geometric computational approach. Two cases were considered with the accessibility of (i) both small and large spherical mesoporous cages and (ii) only the large cages, the accessibility of the small cages being prohibited by the presence of a dummy atom with a van der walls radius which fits with the diameter of the small cage.

The theoretical accessible surface area of nanoMOFs powder was estimated using the method previously reported by Düren et al[38]. This surface was calculated from the center of a nitrogen probe molecule rolling across the surface. The diameters of each atom constituting the nanoMOFs were taken from the Universal Force Field (UFF)[39] whereas the diameter of the nitrogen probe molecule was considered to be 3.60 Å.[40] The calculations were performed using the crystal structure of MIL-100(Fe)[41] with 2 iron centers per trimer unsaturated and the third one coordinated by an -OH group with a corresponding bond length of 0.97 Å. Two cases were considered with the accessibility of (i) both small and large spherical mesoporous cages and (ii) only the large cages, the accessibility of the small cages being prohibited by the presence of a dummy atom with a van der walls radius which fits with the diameter of the small cage. These predicted accessible surface areas were then compared with the BET experimental values

obtained before and after encapsulation of AMOX and CL.

The free volume corresponding to the volume not occupied by the atoms of the MIL-100(Fe) nanoMOFs was also calculated using a similar method of trial insertions within the entire volume of the unit cell considering a probe size of 0 Å[42]. The experimental pore volume (0.66 cm^3/g) was lower than the theoretical free volume (0.99 cm^3/g) calculated using a perfect and infinite crystal. Indeed, small sized nanoMOF crystals are far from being perfect and the void space of the nanoMOFs is only partially available for the drugs. Therefore, a scaling factor of 1.5 was applied for the GCMC simulations, corresponding to the ratio (free volume/experimental pore volume).

Structural features were calculated using Materials Studio software. The predictions of the optimal encapsulation uptake for AMOX and CL as single component and binary encapsulation in the MIL-100(Fe) were performed using Grand Canonical Monte Carlo (GCMC) simulations at 303 K. The MIL-100(Fe)/drugs and drugs/drugs interactions were treated as a sum of a Lennard-Jones (LJ) and a coulombic contribution. The microscopic models selected for both the drugs and the MIL-100(Fe), the associated LJ parameters and partial charges are described in SI section I.4. Additional Monte Carlo simulations were conducted to reveal the preferential arrangements of both drugs in the pores of the MOFs. All the computational details are provided in SI section I.4.

Prediction of AMOX and CL loadings and energetic considerations. The predictions of the optimal encapsulation uptake for AMOX/CL in the MIL-100(Fe) were performed using Grand Canonical Monte Carlo (GCMC) simulations at 303 K with the CADSS software (Complex Adsorption and Diffusion Simulation Suite)[43]. The crystal structure of MIL-100(Fe) was considered with one iron metal per trimer coordinated by an –OH group while the two other metal sites are coordinated by water molecules, to mimic the fact that encapsulation is achieved in aqueous media. The partial charges carried by each atom of the frameworks were extracted as a first approximation using the qEq charge equilibration approach[44]. This protocol has been revealed to be sufficiently accurate for screening the properties of a series of MOFs for carbon dioxide capture[45]. The partial charges of AMOX and CL were extracted by DFT calculations using the B3LYP functional associated with the 6/311++G (d,p) basis set[46] as implemented in GAMESS[47]. The Lennard-Jones (LJ) parameters for all atoms of the MIL-100(Fe) frameworks and the drug molecules were taken from UFF[4] and the general Amber Force Field (GAFF)[48] respectively. The MIL-100(Fe)/drugs and drugs/drugs were treated as a sum of a LJ and a coulombic contribution. The Lorentz-Berthelot mixing rule was employed for all cross LJ terms

and a cut-off radius of 14 Å was used. The long-range electrostatic interactions were handled by the Ewald summation technique. The GCMC simulations were performed for a series of fugacity for the drug up to 5000 kPa in order to first estimate the saturation capacity for each single drug. The simulations consisted of 10^6 steps to ensure the equilibration, followed by 2×10^7 steps to calculate the ensemble averages. Additional GCMC calculations were performed to probe the co-encapsulation of the two drugs as well as their sequential uptakes. The predicted loadings were then converted into weight/weight encapsulation percentages for direct comparison with experimental DL values. The adsorption enthalpy for each drug was further calculated using the revised Widom's test particle insertion method. [49]

Further, additional Monte Carlo simulations were performed with a crystal structure of MIL-100(Fe) containing one iron metal per trimer coordinated by an –OH group while the two others are unsaturated to probe the preferential sitting sites of 1 molecule of AMOX and CL acid in the large and small cages respectively.

I.5 NanoMOFs toxicity assays

Cytotoxic effects of nanoMOFs were investigated using LDH assay. Following exposure to various concentrations of nanoMOFs as previously described, cells were washed and lysed. The activity of LDH was determined using a commercially available kit from Sigma. LDH reduces nicotinamide adenine dinucleotide (NAD), a coenzyme found in all living cells, to NADH, which is specifically detected by colorimetric (450 nm) assay. The absorbance was recorded using a microplate spectrophotometer reader system.

I.6 Internalization of nanoMOFs

Quantification of NanoMOFs internalized in the cells. J774 cells were seeded in 24-well-plates (3×10^5 cells/wheel) and then incubated with nanoMOFs at a final concentration of 100 µg/mL for 4 h in RPMI 1640 supplemented with 10% of FBS at 37°C, 5% CO_2. They were washed thrice with cell culture medium, dried at 60°C for 2 h. Subsequently, 300 µL of hydrochloric acid (5M) was added and then incubated for 2 h at 60°C. Afterwards, 100 µL of each well were withdrawn and mixed with 100 µL of 4% potassium ferrocyanide in a 96-well-plate and incubated at room temperature in the dark for 30 min. The absorbance was read at 690 nm to quantify the amounts of internalized nanoMOFs.

The absorbance was read at 690 nm to quatify the amounts of internalized nanoMOFs. NanoMOFs within cells were visualized by optical microscopy and TEM. Different pharmacological inhibitors (Cytochalasin D, Latrunculine, Wortmannin, Chlorpromazine,

Ikarugamycin, methyl-β-cyclodextrin) were used to investigate the nanoMOF cell internalisation mechanism (phagocytotic/endocytotic pathways). Practically, the cells were pre-incubated 1 h with the above mentioned inhibitors before further incubation with nanoMOFs.

Intracellular visualisation of nanoMOFs. NanoMOFs within cells were visualised by optical microscopy and TEM. Prussian blue staining (Sigma Iron staining kit) was applied for optical microscopy. After different incubation times with or without nanoMOFs, J774 cells were washed with complete medium and two times with PBS. Cells were fixed with 4% paraformaldehyde, washed and incubated for 10 minutes with 2% potassium ferrocyanide in 0.6 mM hydrochloric acid. Cells were washed again, counterstained with pararosaniline hydrochloride (0.02%) and evaluated for iron staining using light microscopy.

I.7 Intracellular antimicrobial activity of nanoMOFs.

Intracellular antimicrobial activity of nanoMOFs. The antimicrobial activity of nanoMOFs was investigated against *S. aureus* ATCC55585 and against a clinical penicillin-resistant *S. aureus*. It was carried out in a quantitative assay based on dilution method, using the Mueller-Hinton medium and the Minimum Inhibitory Concentration (MIC) was determined. Briefly, 2.5×10^5 J774 cells were seeded in 24 well plates and incubated overnight (37°C, 5% CO_2). The cells were washed with cell culture medium (RPMI 1640 containing 10% v/v decomplemented FBS) and then incubated for 2 h with or without different amounts of nanoMOFs, loaded or not with drugs. The cells were washed twice with complete cell culture media, to eliminate extracellular nanoMOFs and drugs. Then, they were infected with 500 µl of *S. aureus* suspension (ATCC55585) at 5×10^6 bacteria/mL (multiplicity of infection, MOI=10) and incubated for 2h. After washing the cells, gentamicin was added to kill extracellular bacteria. The ROS effect was inhibited at this moment with Tiron 10 mM. After 1, 6 and 24 h of incubation, cells were washed again with cell culture media and lysed by treatment with ice-cold water during 1 h. The lysates were plated at serial dilutions in sterile phosphate buffered saline (PBS, pH=7.4) on agar plates. The plates were incubated at 37°C overnight and the number of formed colonies (CFU) was evaluated[50].

Supplementary Information

Two drugs in two different mesoporous cages inside the same nanoparticle: design and applications

N. Semiramoth[1,&], X. Li[2,&], G. Maurin[3], J. Josse[4], V. Tafani[4], F. Laurent[4], G. Salzano[2], D. Foulkes[1], N. Ghermani[1], S. Hal[3], M. Moya-Nilges[5], P. Couvreur[1], L. Majlessi [6], M.F. Bernet-Camard[7], J. Zhang[8], R. Gref[2*].

[1] Institut Galien, Université Paris-Sud, UMR CNRS 8612, 92290 Chatenay Malabry, France.

[2] Institut de Sciences Moléculaires, UMR CNRS 8214, Université Paris-Sud, Université Paris-Saclay, 91405 Orsay Cedex, France.

[3]Institut Charles Gerhardt, Université Montpellier, UMR 5253 UM CNRS ENSCM, 34095 Montpellier Cedex 5, France.

[4] Centre International de Recherche en Infectiologie (CIRI), INSERM U1111, Hospices Civils de Lyon, Hôpital de la Croix-Rousse, 69004 Lyon, France.

[5]Imagopole, Ultrastructural Microscopy Platform, Institut Pasteur, 75724 Paris Cedex 15, France.

[6]Unit for Integrated Mycobacterial Pathogenomics, Institut Pasteur, 75015 Paris, France

[7]EA4043-Ecosystème Microbien Digestif et Santé, Université Paris-Sud, 92296 Châtenay-Malabry.

[8]Center for Drug Delivery Systems, Shanghai Institute of Materia Medica, Chinese Academy of Sciences, Shanghai 201203, China.

[&]Equally contributing first authors
Correspondence and requests for materials: Dr Ruxandra Gref

ruxandra.gref@u-psud.fr

I.1 X-ray powder diffraction (XRPD) characterization

XRPD experiments were performed to investigate the effect of drug loading and nanoMOF incubation in various media on their crystalline structures.

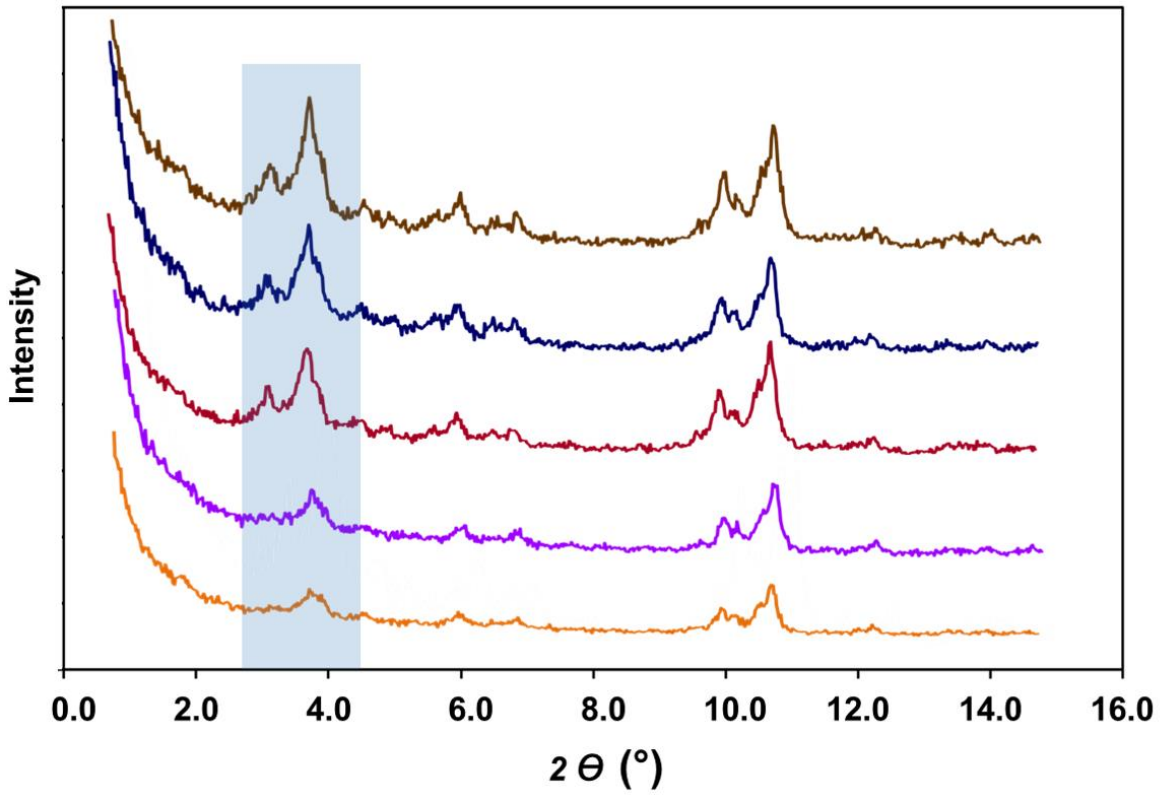

Fig. S1. X-ray powder diffraction (XRPD) patterns of empty and drug loaded nanoMOFs. Drug entrapment didn't modify the XRPD patterns of nanoMOFs (Brown: empty nanoMOFs in ethanol; Dark blue: empty nanoMOFs in water; Dark red: nanoMOFs loaded with 13 wt% AMOX and 22 wt% CL). Degradation was only observed when the nanoMOFs, loaded (purple) or not (orange) with drugs, were incubated in the cell culture media (RPMI, 2 h, 37 °C).

As shown in Fig. S1, the XRPD patterns of the drug loaded MOFs were very similar to the ones of empty nanoMOFs, suggesting that the incorporation of AMOX and CL didn't affect the crystallinity of the nanoMOFs. However, the incubation of nanoMOFs, containing or not drugs, in cell culture medium (RPMI) for 2 h lead to a diminution of the intensity of the peaks in the region 3°- 4°, showing nanoMOF degradation.

I.2 Effect of different pharmaceutical inhibitors on the internalisation of nanoMOFs in J774 cells

The cell viabilities were higher than 90% when the nanoMOFs concentration was lower than 50 μg/mL. A concentration of 12.5 μg/mL was chosen for the cell internalization studies.

Cytochalasin D, Latrunculine A Wortmannin, Chlorpromazine, Ikarugamycin, methyl-β-cyclodextrin (Mβ-CD), Genistein, and Fillipin III were used as pharmacological inhibitors to investigate the mechanisms of internalisation of nanoMOFs inside J774 cells. The inhibitors were incubated with the cells for 1 h, previously to adding the nanoMOF suspensions. Results are gathered in Fig. S2.

The internalization of nanoMOFs was reduced by 35% in the presence of Cytochalasin D[1] and Latrunculin A[2], which block actin polymerization and hence disrupt microfilament-mediated internalization, manifesting the role of phagocytosis. Wortmannin[1], Ikarugamycin[3], and Chlorpromazine[4], used as inhibitors of clathrin-dependent endocytosis, didn't significantly lessen the uptake of nanoMOFs, indicating that clathrin-pathway hardly played a part in the internalization. Genistein[4] and Filipin III[5], which block caveolin-mediated endocytosis, didn't significantly affect the internalisation. Mβ-CD, used in previous studies[4] to induce cholesterol depletion of cellular membrane, had no influence on the nanoMOF internalisation, neither. Furthermore, it was found that the nanoMOF incubation temperature plays a major role. The uptake of nanoMOFs was reduced by 60% when the temperature was decreased to 4°C, suggesting an energy-dependent internalization mechanism. As a conclusion, nanoMOFs were mainly internalised in J774 macrophages by phagocytosis.

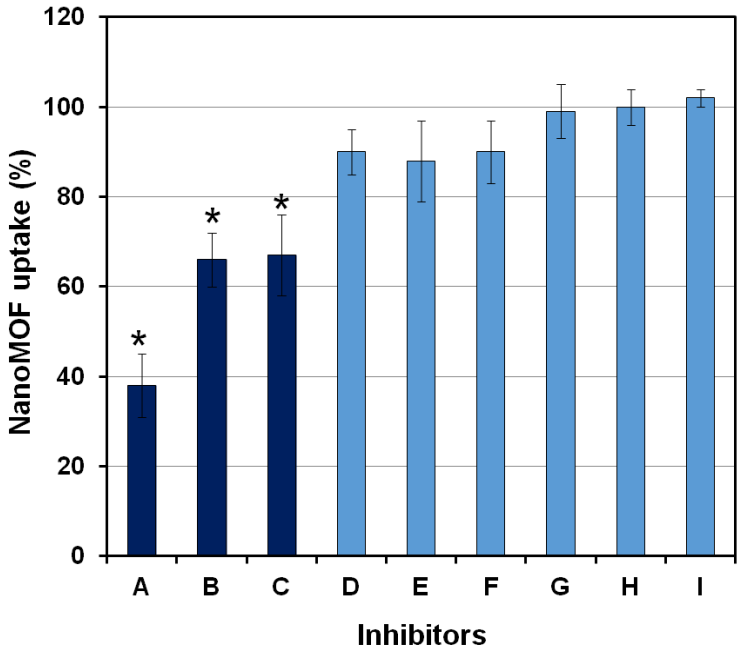

Fig. S2. Effect of different pharmaceutical inhibitors on the internalisation of nanoMOFs in J774 macrophages. The cells were pre-incubated for 1 h at 37°C with different inhibitors

(B: Cytochalasin D; C: Latrunculine A; D: Wortmannin; E: Chlorpromazine; F: Ikarugamycin; G: methyl-β-cyclodextrin; H: Genistein; I: Fillipin III) before further incubation with nanoMOFs. A: the cells were incubated with the nanoMOFs at 4°C instead of 37°C. All data are normalized as compared to the uptake of nanoMOFs at 37°C in the absence of any inhibitor.

I.3 Bactericidal effect of empty nanoMOFs

Interestingly, cell internalized empty nanoMOFs exhibited a bactericidal effect which was proportional both to the amount of nanoMOFs initially in contact with the cells and the incubation time (Fig.S4). A significant bactericidal effect of empty nanoMOFs was observed when the amount of nanoMOFs initially in contact with the cells was higher than 12.5 μg/mL and after 6 h of incubation.

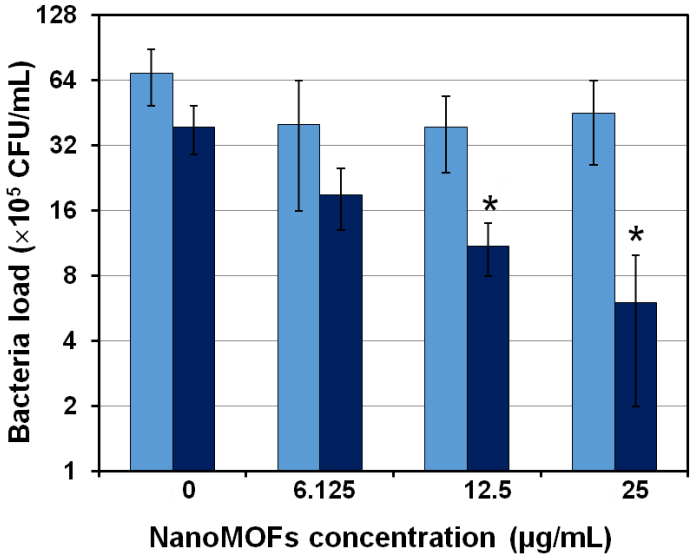

Fig. S3. Effect of nanoMOFs concentration on their bactericidal effect. (light blue: 1 h after infection; dark blue: 6 h after infection). There is a significant difference when the concentration of nanoMOFs is higher than 12.5 μg/mL ($P < 0.05$, *).

Supplementary References

1. Mäger I., Eiríksdóttir E., Langel K. E., Andaloussi S., & Langel U. Assessing the uptake kinetics and internalization mechanisms of cell-penetrating peptides using a quenched fluorescence assay, *Biochim. Biophys. Acta.*, **1798**, 338-343 (2010).
2. César P. G., *et al*. Microscopic analysis of the interaction of Gold nanoparticles with cells of the innate immune system. Sci. Rep. 3, 1-7 (2013). DOI: 10.1038/srep01326
3. Bannunah A.M., Vllasaliu D., Lord J., & Stolnik S. Mechanisms of nanoparticle internalization and transport across an intestinal epithelial cell model: effect of surface

charge. *Mol. Pharm.* **11**, 4363-4373 (2014).

4. Bandmann V., Homann U., & Plant J. Clathrin-independent endocytosis contributes to uptake of glucose into BY-2 protoplasts. *Plant J.* **70,** 578-584 (2012).
5. Veyrat D. C., Pomerleau L., Langlois D., & Gaudreau P. Internalization and trafficking of the human and rat growth hormone-releasing hormone receptor. *J. Cell Physiol.* **203,** 335-344 (2005).

General Discussion and Perspectives

Although people have already been using medicinal substances as far as there have been people, the history of pharmacy as an independent science dates back to the 19th century when chemical companies established their research labs for medical applications of their products. The last two centuries witnessed the outstanding progress of pharmaceutical science. In 1970s, microparticles (MPs) and NPs were applied as drug carriers, which are recognized as the first pioneering works for the further development of functionalized formulations. Recently, formulations for targeting [1] and personalized treatment [2] are attracting increasing attentions aiming to deliver the drug directly to the diseased cells and tissues of the body, and therefore enhance the drug's efficacies, decrease the treatment's side effects, and improve the patient's life quality.

The use of nanotechnologies for the treatment of diseases has led to new therapeutic strategies. Many functionalized NPs developed in the lab allow the efficient targeting, as well as the controlled drug release in these specific biological targets. However, the journey of a nanomedicine from lab to shelf is quite costly and time consuming [3]. Statistically, the research and development of a new drug to the market takes around 12 years and costs around £1.15 billion, while tens of thousands of candidate drugs fail. One of the main reasons that limits drug commercialization is the fact that their preparation needs to employ large amounts of potentially toxic organic solvents and surfactants, which is often not acceptable, at least for parenteral administration. For instance, a variety of polymer NPs were prepared by the well-known solvent evaporation method using volatile organic solvents to solubilize the polymer. Traces of solvents are very difficult to remove even using very complicated and time consuming methods such as ultradialysis, ultrafiltration or ultracentrifugation.

Therefore, there is an urgent need to develop particle preparation procedures avoiding the use of organic solvents and surfactants. Herein, CD-based NPs were prepared in pure water just by mixing two neutral polymers which instantaneously associate together by a "lock and key" mechanism (Chapter 2). In this chapter, we show not only the concept that host–guest interactions between hydrophobic molecules (Bz moieties) and the apolar cavities of CDs can be exploited for the formation of stable NPs, but also that this preparation can be successfully scaled up by microfluidics, an automatic technique. Briefly, two polymers for NPs preparation were firstly synthesized: i) a poly-CD polymer and ii) Dex-Bz polymer where Bz moieties were grafted with dextran. Bz acts as both the hydrophobic moiety that interacted with CDs and also

the active ingredient. By mixing the aqueous solutions of these two polymers with microfluidics, CD-NPs of around 100 nm were spontaneously formed with narrow size distribution. Although CD-NPs could also be prepared manually with pipette, it is very difficult to well control the procedure for NPs preparation, whereas the microfluidic chamber allows for exquisite control over the mixing profile of the solutions containing the NPs forming agents[4,5]. Parameters, including ratio between the different compounds, flow rate as well as temperature can be easily and accurately controlled, which make possible to prepare NPs in a well-controlled, reproducible and high-throughput manner. Moreover, the microfluidic device could allow a continuous NP production at a rate of tens to hundreds of microliters per minute. Studies in the literature [6] describe the utility of microfluidic devices to scale up the NP production.

The other novelty in this study is the use of NTA to evaluate the NPs' stability in terms of size distribution and concentration upon extremely dilution. As the inclusion complexes were formed by host-guest interaction, instead of covalent bonds, an equilibrium exists all the time between the components in the system, as described in introduction (section 1.3). When the system is extremely diluted, the equilibrium will shift to the disassociation of the inclusion complexes, which would induce the disassembly of the CD-NPs. NTA allows to measure the size distribution and concentration at extremely diluted condition by individually following the CD-NPs in their Brownian motions. Remarkably, CD-NPs were very stable even when their concentration was as low as 100 ng/mL.

The solvent-free "green" procedure and the remarkable stability of CD-NPs make them promising as drug carrier for hydrophobic drugs which fits with the cavity of CDs. However, considering the payload of active ingredient, which is normally less than 5 wt%, their application for many drugs is limited, especially when large doses are needed for the diseases, as it is the case with antibiotics. But they are still good candidates for drugs with small dosages such as anticancer drugs.

To improve the drug payload, the next strategy that we explored is to use "cage" porous particles. CD-MOFs were the first particles tried in this study since it is built with the "cage" molecules (CDs). The use of CD-MOF materials for biomedical applications requires them to have very homogeneous sizes. Before their applications as drug carriers, the optimization of the synthesis and the evaluation of their crystalline structure were performed. (Chapter 3.1). In this subchapter, a fast solvent evaporation approach was developed to synthesize and tailor the CD-MOFs to a controlled size, with the synthesis time shortened from the reported 26 h [7] to only 6

h. The size of CD-MOFs were well controlled by adjusting the reactant concentrations and molar ratios, temperature and reaction time, without any significant changes in crystallinity and porosity. A modified hydrothermal protocol has been established which produces efficiently at 50 °C in 6 h micron (5–10 μm) and nanometer (500–700 nm) diameter CD-MOF particles of uniform size with smooth surfaces and powder X-ray diffraction patterns that are identical with those reported in the literature [7].

CD-MOFs experienced degradation at high temperature (100 °C), high humidity (92.5%) and with polar solvents (methanol and DMF). More importantly, it was found that γ-CD was released and characteristic peaks in PXRD patterns disappeared when immersing the CD-MOFs in polar solvent whilst the morphology remained unchanged. After the stability study, the preliminary experiments on drug adsorption were performed with more than 20 drugs, the results shows that CAP has high affinity with CD-MOFs reaching payloads as high as 19.3 wt%, which corresponding to a molar ratio between CAP and γ-CD close to 1.6:1. These results confirm the high drug loading capacity of CD-MOFs.

LPZ was then used as drug of especial interest, as it is a proton-pump inhibitor used to reduce the production of acid in the stomach and recently identified as an antitubercular prodrug [8]. CD-MOFs of around 6 μm in diameter were used for LPZ encapsulation. LPZ-loaded CD-MOFs were successfully synthesized by a co-crystallization method, obtaining cubic crystals with the uniform size of around 6 μm. High drug payloads of 23.2 wt% were obtained, and calculations indicated that each CD in the CD-MOFs was able to host one LPZ molecule. Moreover, it was demonstrated that even after two years storage, the incorporated drug inside the CD-MOFs maintained its spectroscopic characteristics. Compared to other CD-based drug carriers, CD-MOF appears as one of the best systems in term of drug payload.

The CD-MOFs loaded or not with LPZ were fully characterized to gain a deep insight of the system. XRPD patterns of LPZ loaded CD-MOFs show that the peaks corresponding to the LPZ were not observed, indicating that LPZ was incorporated in CD-MOFs in amorphous state. As a crystalline drug, incorporation of LPZ is very challenging since the drug might form crystals which are not well encapsulated and difficult to be separated from the drug-loaded particles, hampering the medical applications. However, we demonstrated that in CD-MOF crystals, all the LPZ molecules located in each cavity of CDs, which possibly prevented the LPZ crystallization. Molecular modelling gave deeper insight into the interactions between LPZ and CD-MOFs showing that LPZ molecules preferred to insert in the γ-CD cavities of the CD-

MOFs instead of locating in the hydrophilic large pores. LPZ molecules were bended interacting strongly with the CD cavities mainly through their benzo imidazole and pyridine moieties. This result surprisingly indicated that the inclusion complexes formed between LPZ and CDs could self-assemble with coordinated K^+ ions into the cubic CD-MOF crystals.

Furthermore, we set up a novel characterization method based on Raman microscopy allowing to gain information on the structure and chemical composition of individual particles. Thistechnique combines the advantages of Raman spectroscopy and optical microscopy. Individual CD-MOF crystals could be analyzed in terms of morphology (particle size, shape) and chemical composition, enabling to confirm the homogeneity of the CD-MOF population. Morphologies of more than 2500 particles were analyzed, showing almost perfect cubes with diameters around 6 µm, before or after drug loading. Raman investigations confirmed the effective LPZ incorporation in CD-MOFs and suggested an interaction between γ-CD and LPZ, more specifically between the CDs and the benzo imidazole and pyridine moieties of LPZ, which agrees with the theoretical molecular modelling results. Of note, it was found that Raman spectra of different individual particles were the same, showing a remarkable homogeneity in terms of drug loading.

These results pave the way towards the use of CD-MOFs for drug delivery purposes, especially for pulmonary administration. Considering the size of CD-MOFs and the antitubercular effect of LPZ, the LPZ loaded CD-MOF crystals are quite promising as inhalation for tuberculosis, an infectious disease that occurs the lungs. Compared with other diseases caused by a single infectious agent, tuberculosis is the second biggest killer, globally. Pulmonary administration has recently gain more attention as it enables to deliver the drugs directly to lung both for local and systemic treatment [9]. For further study, the interactions between pulmonary surfactant and CD-MOFs would be interesting to investigate. Afterwards, *in vitro* evaluation of the drug loaded particles to kill tuberculosis could be performed in macrophage.

For other routes of administration except pulmonary inhalation, the drawback of CD-MOFs lies on the fact that they disassemble immediately in water, leading to burst release before the particles reach the target tissues or organs. In order to enlarge the scope of their application for more routes of administration, surface modification was designed to prepare CD-MOF/polymer composites, which are emerging as a new class of carriers for sustained drug delivery. In the literature, most of the MOFs and the polymers used so far in these composites are not pharmaceutically acceptable. Herein, biocompatible CD-MOFs were embedded inside

polyacrylic acid (PAA) polymer matrices by a solid in oil-in-oil emulsifying solvent evaporation method. Since the size of the solid dispersed in the internal phase needs to be as small as possible, hence, nanometer-sized CD-MOFs (around 650 nm in diameter) were selected in order to prepare CD-MOFs/PAA composite microspheres. Ibuprofen (IBU) and LPZ, both insoluble in water and lacking in stability, were entrapped with high drug loading in nano-scaled CD-MOFs by co-crystallization without causing MOF crystal degradation during the loading process. Nano-scaled CD-MOF crystals dispersed well inside PAA matrices leading to their uniform distribution in the microspheres, which further allowed the obtention of composite microspheres with spherical shapes. On the contrary, microspheres prepared with drug-γ-CD complexes have non spherical shapes since the size of the drug-γ-CD complexes was larger and not uniform when compared with the drug-loaded CD-MOF nanocrystals, even after sieving. Particle aggregation occurred during microsphere preparation with drug-γ-CD complexes.

Burst release is considered to be one of the main drawbacks hampering the NP applications. Achieving sustained drug release is important for drug formulations. *In vitro* cumulative drug release profiles showed sustained drug release from CD-MOF/PAA microspheres. IBU was released slowly over 48 h, whereas LPZ enabled a sustained release also during 48 h with an almost linear profile. However, microspheres containing IBU-γ-CD and LPZ-γ-CD complexes both showed a very fast burst and uncontrolled release – i.e., 70% in 30 min for IBU and 80% in 2 h LPZ. With no doubt, this observation reflected the good dispersion of drug-loaded CD-MOF nanocrystals in the microspheres and the homogeneous distribution of the drug molecules within these crystals, resulting from the efficient co-crystallization loading process.

Cytotoxicity is one of the most crucial parameters to evaluate the drug carrier. The cellular toxicity study showed that CD-MOFs were not toxic (cell viability > 90%) even at concentrations as high as 300 $\mu g \cdot mL^{-1}$. At concentrations up to 1.4 $mg \cdot mL^{-1}$, the cellular viability was still high (~ 80%). Interestingly, the toxicity of IBU loaded CD-MOF/PAA composite microspheres was reduced dramatically. The cell viability was around 90% even for samples at high concentrations of 17.5 $mg \cdot mL^{-1}$, corresponding to a CD-MOF nanocrystal concentration of 1.4 $mg \cdot mL^{-1}$ and IBU concentration of 0.2 $mg \cdot mL^{-1}$. These results showed that composite of CD-MOF nanocrystals in PAA microspheres could to be used as safe carriers for sustained drug delivery.

Taking into account the bio-adhesive properties of PAA and its excellent biocompatibility, the

composite microspheres have potential applications for biomedical applications and, in particular, for oral drug delivery. However, a limitation of the CD-MOF/PAA microspheres is that their drug loading is relatively low (about 1%, w/w) and so this system would be better adapted for the delivery of drugs requiring lower doses, such as anti-tumor drugs.

While CD-MOFs seem very promising for pulmonary administration, their applications for other routes of administration are limited by their physical frailness and their high solubility in aqueous media before surface modification or the low drug payloads after modification.In this context, our alternative strategy was to use stable porous particles to obtain both high payloads and high stability in water. However, although stability is very important, drug carriers need to be degraded inside the body for excretion. MIL-100 (Fe) MOFs are stable in water and could be degraded in a series of simulated physiological fluids. They are also considered among the most efficient materials for biomedical applications because of their unprecedented drug loading capability and biocompatibility [10]. In this view, MIL-100 (Fe) was chosen as the third drug delivery system.

Firstly, the degradation mechanism of MIL-100 (Fe) was investigated. As reported, MIL-100 (Fe) interacted efficiently with phosphate groups. Phosphated drugs, such as Gem-MP, were soaked from their aqueous solutions with high payloads (> 25wt%) and efficiencies (> 98%), and phosphated coatings, such as CD-P, were attached to the outer surfaces by incubation just in water. Unfortunately, MIL-100 (Fe) readily degraded in phosphate buffers leading sometimes to uncontrolled drug release. It is therefore necessary to have a deep understanding of the MIL-100 (Fe) degradation mechanism in complex media containing phosphates to be able to control it.

To better understand their degradation mechanism in PBS and the complex interactions taking place in the MOF/drug/coating systems, we developed a method based on Raman microscopy to track the morphology and chemical composition of individual particles. It was shown that MIL-100 (Fe) MOFs degraded in PBS releasing their constitutive trimesate linkers and leading to the formation of amorphous material, whereas the particle sizes remained unchanged. It was extremely interesting and fascinating to observe that despite the fact that more than 80% of the connective linkers were released, the particles perfectly maintained their initial morphology.

Remarkably, Raman spectra of different regions on the same particle could be recorded, evidencing the formation of an erosion front during MOF degradation. This front clearly separated an intact non eroded crystalline core from an amorphous shell made essentially of an

inorganic network. To gain a deeper understanding of the kinetics of the degradation process of single particles, automated imaging was used track the degradation process by capturing MOFs' images every half an hour during 8 days degradation.

Of interest, the method provided a direct measurement of the size, shape, color, surface area, and circularity of each particle. A fast degradation phase was observed in the first 6 hours with a rapid color change and increase of surface areas, which were too subtle to be observed by the naked eye. A second phase occurred in the following 8 days with the formation of an eroded zone with a clear color change (progressive phase). It can be speculated that in the first hours after incubation, a fast coordination reaction occurred between phosphates in the incubation medium and accessible iron sites at the MOF surface. This phase was followed by a slower diffusion of phosphates in the eroded region. The advancement of the degradation front was presumably limited by the diffusion of the reacting species (phosphates) from the media into the MOFs and by the diffusion of released trimesate out of the matrix.

To investigate the chemical composition of the eroded zone, ^{57}Fe Mössbauer spectrometry was applied to MIL-100 (Fe) particles before and after degradation. Before degradation, the spectrum was well described by means of 3 quadrupolar components, in agreement with the crystallographic MIL-100 (Fe) structure, while after degradation, quadrupolar doublets with broadened lines were observed. The best physical description requires a discrete distribution of quadrupolar doublets suggesting a structure close to that of a typical amorphous structure. Although the hyperfine structures of the nano-and microMOF samples after degradation was modified, the refined values of the isomer shift indicate unambiguously the presence of only Fe^{3+} species whatever the sample (nano-and microMOFs) and their degradation state. It could be concluded that no Fe reduction occurred during degradation. Taking into account the presence of phosphates in the media surrounding the MOF, it is plausible that a highly disordered Fe-P based skeleton phase was formed.

In contrast, neither drug entrapment nor particle coating did affected the integrity of the tridimensional MOF network. As descripted, MOFs degraded in PBS with kinetics dependent upon the amount of phosphates in the suspension media. When Gem-MP was loaded in MOFs, the equivalent amount of phosphates was up to 100 times lower than that in diluted PBS (1.19 mM), which could explain the reason why MOFs did not degrade during drug entrapment. When MOF particles were coated with CD-P, which could not penetrate inside the tridimensional MOF network, no degradation was induced. The good stability of the particles

after Gem-MP loading and CD-P coating offer promising possibilities to load drugs of interest and graft ligands for targeting purposes. These findings are of interest in the development of stable drug-loaded iron trimesate particles.

Combinatorial drug therapies are considered among the most effective strategies for the treatment of complex pathologies such as cancer and severe viral or bacterial infections involving multiple molecular and genomic pathways. However, co-administration of synergic drugs is challenging because of the differences in pharmacokinetics and biodistribution of each individual drug. Nanotechnology revolutionizes drug delivery in many aspects, but there are still few examples of NPs for drug co-encapsulation, such as Janus NPs, nanocapsules and polymersomes which are composed of several macroscopic compartments, each one being adapted to accommodate a specific drug. However, the preparation of anisotropic NPs are relatively complex and require the use of organic solvents and surfactants.

Taking advantage of the two types of "cages" present in MIL-100 (Fe) nanoMOFs, synergic antibiotics AMOX and CL were co-entrapped inside the porous "cage" nanoMOFs. AMOX and CL are typical drugs used in tandem to treat a variety of bacterial infections, mainly rhinosinusitis, ear infections, pharyngolaryngitis, tonsillitis, bronchitis and urinary tract infections. By using a simple "green" strategy consisting of incubating the nanoMOFs with aqueous solutions of both drugs, AMOX and CL were easily co-encapsulated. As a general trend, when drugs are co-encapsulated, one drug in the combination reduces the entrapment of another. Interestingly, the AMOX and CL were co-incorporated inside nanoMOFs without impeding each other. The combinational payload reached at maximum 35 wt%, including 22 wt% of CL and 13 wt% of AMOX. Molecular modelling gave a clear picture of location for the two drugs, showing that AMOX occupied mainly the large cages and CL the small cages.

Considering their excellent drug encapsulation properties, nanoMOFs were further studied *in vitro* on *S. aureus* infected cells. NanoMOFs were able to penetrate inside infected macrophages, whereas free drugs could poorly bypass cell membranes and/or are rapidly cleared off mainly because of efflux pumps. NanoMOFs, loaded or not with drugs, were non-toxic tested by MTT assays. Surprisingly, empty nanoMOFs co-localized with bacteria in macrophages and had bactericidal effect, proportional to the amount of nanoMOFs initially in contact with the cells. AMOX-loaded nanoMOFs were successful to show synergic effect with empty nanoMOFs, whereas no bactericidal effect was found with free AMOX, which is reasonable due to its poor intracellular penetration. When using a resistant *S. aureus* strain, the

bactericidal effect due to internalized nanoMOFs was so strong (85% bacteria were destroyed), that it was comparable to that of (co)encapsulated drugs. (Need to be adapted according to the ongoing study). In conclusion, intracellular nanoMOFs synergistically contribute with encapsulated drugs to eradicate intracellular bacteria. They are efficiently taken up inside macrophages essentially by phagocytosis and advantageously co-localize with bacteria, to eventually deliver their drug cargo. These results pave the way towards the design of engineered nanocarriers in which each component synergistically plays a role in fighting the disease.

For future study, it would be very interesting to deeply investigate the mechanism of antimicrobial effect of empty MIL-100 (Fe) nanoMOFs. The growing resistance of pathogens has become a public health problem. New effective antimicrobial materials are necessary and urgent for resistant pathogen treatment. It was discovered that nanoMOFs, entirely different to antibiotics, played a role as antibacterial materials providing promising novel solution to the problem of drug resistance. There are already some reports on antimicrobial MOFs based on Cu, Co, Zn, and Ag, but no reports on MOF based on Fe yet, to the best of our knowledge. Understanding their bactericidal mechanisms could help not only to explain the obtained results, but would be also beneficial to design new antimicrobial materials.

The current antibacterial mechanisms of reported MOFs involves [11]: 1) release of metal ions, such as Ag^{+} [12]; 2) reactive oxygen species (ROS) formed by metal oxides, especially ZnO, NiO, CoO, CuO, and Cu_2O [13]; 3) antibacterial autophagy [14]. It would be very interesting to understand the main antibacterial mechanisms for MIL-100 (Fe) nanoMOFs.

MOFs are an emerging class of materials suitable for infection treatment by encapsulation of antibiotics and their intrinsic antimicrobial properties. The two types of MOFs used in this study were able to efficiently load large amount of drugs for infection treatments. LPZ loaded CD-MOFs are very promising particles as pulmonary inhalation for tuberculosis treatment, whereas AMOX and CL loaded nanoMOFs could be used for many infections using different routes of administration.

Reference

1. Duncan, R., Pratten, M. K. & Lloyd, J. B. Mechanism of polycation stimulation of pinocytosis. *BBA - Gen. Subj.* **587,** 463–475 (1979).

2. Duffy, M. J. & Crown, J. A personalized approach to cancer treatment : how biomarkers can help. *Clin. Chem.* **54,** 1770-1779, (2008).

3. Room at the bottom: the technobureaucratic space of gold. *New Materials: Their Social and Cultural Meanings* **5,** 1-47 (2014).

4. Karnik, R. *et al.* Microfluidic platform for controlled synthesis of polymeric nanoparticles. *Nano Lett.* **8,** 2906–2912 (2008).

5. Shestopalov, I., Tice, J. D. & Ismagilov, R. F. Multi-step synthesis of nanoparticles performed on millisecond time scale in a microfluidic droplet-based system. *Lab Chip.***4,** 316–321 (2004).

6. Valencia, P. M., Farokhzad, O. C., Karnik, R. & Langer, R. Clinical translation of nanoparticles. *Nat. Publ. Gr.* **7,** 623–629 (2012).

7. Smaldone, R. A. *et al.* Metal-organic frameworks from edible natural products. *Angew. Chemie - Int. Ed.* **49,** 8630–8634 (2010).

8. Barradell, L. B., Faulds, D. & Mctavish, D. A Review of its pharmacodynamic and pharmacokinetic properties and its therapeutic efficacy in acid-related disorders lansoprazole. **44,** 225–250 (1992).

9. Yang, W., Peters, J. I. & Williams, R. O. Inhaled nanoparticles- a current review. **356,** 239–247 (2008).

10. Simon-Yarza, T. *et al.* In vivo behavior of MIL-100 nanoparticles at early times after intravenous administration. *Int. J. Pharm.* **511,** 1042–1047 (2016).

11. Wyszogrodzka, G., Marszałek, B., Gil, B. & Dorożyński, P. Metal-organic frameworks: mechanisms of antibacterial action and potential applications. *Drug Discov. Today* **21,** 1009–1018 (2016).

12. Berchel, M. *et al.* A silver-based metal–organic framework material as a 'reservoir' of bactericidal metal ions. **35**, 1000–1003 (2011).

13. Kandioller, W. *et al.* Organometallic anticancer complexes of lapachol: metal centre-dependent formation of reactive oxygen species and correlation with cytotoxicity. **49**, 3348–3350 (2013).

14. Jo, E., Yuk, J., Shin, D. & Sasakawa, C. Roles of autophagy in elimination of intracellular bacterial pathogens. **4,** 1–9 (2013).

General Conclusion

In this study, three different types of "cage" particles were prepared in view of possible biomedical application.

1. CD-NPs of around 100 nm were prepared by a "green" and simple preparation procedure consisting in mixing poly-CD aqueous solution and Dex-Bz aqueous solution using microfluidics or just pipettes. The host–guest interactions between β-CD in poly-CD polymer and Bz in Dex-Bz contributed to the spontaneous formation of stable CD-NPs. CD-NPs were instantaneously produced by mixing 2 aqueous solutions of neutral polymers. Despite their non-covalent nature, the CD-NPs were extraordinarily stable in terms of concentration and size distribution, even on extreme dilution (concentrations as low as 100 ng/mL).

2. In order to improve the drug loading in CD-based drug delivery systems, uniform cubic CD-MOFs were successfully synthesized. An optimized vapor diffusion method was developed at elevated temperature (50 °C) within 6 h, which is much shorter than the reported time (>24 h). Both microcrystals (~ 6 μm) and nanocrystals (~ 650 nm) were obtained by adjusting the amount of the pre-added methanol to the aqueous solution of γ-CD and KOH.

3. LPZ is a proton-pump inhibitor used to reduce the production of acid in the stomach and recently identified as an antitubercular prodrug. It was encapsulated in CD-MOF microcrystals (~ 6 μm) with payload up to 23.2 ±2.1% (wt) by co-crystallization method, where the drug was added during particle synthesis. The crystalline particles, loaded or not with LPZ, have almost perfect cubic morphologies with monodispersed size distributions. The interactions between LPZ and CD-MOF were revealed by molecular modelling. The formation of inclusion complexes within the tridimensional CD-MOF structures was confirmed by Raman spectra of individual particles, which also demonstrated that each individual particle had identical chemical composition, indicating a remarkable homogeneity in terms of drug loading. Moreover, the incorporated LPZ inside the CD-MOFs maintained its spectroscopic characteristics even after two years storage.
4. The drug loaded CD-MOF nanocrystals (~ 650 nm) were successfully embedded in polyacrylic acid (PAA) polymer matrices by a solid in oil-in-oil emulsifying solvent evaporation method. The composite microspheres exhibited spherical shapes and

sustained drug release over a prolonged period of time (over 48 h). No burst release of IBU (and LPZ) was observed from the CD-MOF/PAA composite microspheres, suggesting the homogeneous distribution of CD-MOF nanocrystals inside PAA matrices as well as strong drug carrier interactions inside the CD-MOF. Sustained release was achieved for IBU (and LPZ)-CD-MOF/PAA composite microspheres (ca. 50% in 24 h). The cellular toxicity study shows that IBU loaded MOF/PAA composite microspheres are not toxic (cell viability ~ 90%) even at very high concentrations of 17.5 $mg \cdot mL^{-1}$. In conclusion, MOF/PAA composite microspheres constitute an efficient and pharmaceutically acceptable MOF-based carrier for sustained drug release.

5. Biodegradable iron trimesate MOFs, MIL-100 (Fe), degraded in PBS losing their crystallinity and constitutive trimesate linkers, whereas, they kept their morphology intact. The degradation mechanism was revealed by Raman microscopy via recording spectra in different regions on the same particle, showing that intact cores were separated from the eroded regions by clearly visible erosion fronts. Mössbauer spectroscopy supported the hypothesis that Iron phosphates were formed in the eroded regions. In contrast, the integrity of the tridimensional MOF network was not affected by drug entrapment nor by particle coating.

6. Co-encapsulation of two synergic antibiotics (AMOX and CL) in MIL-100 (Fe) nanoMOFs was achieved following a simple and "green" procedure consisting of incubating the nanoMOFs with aqueous solutions of both drugs. Molecular modelling showed that each drug preferentially located in a separate compartment (large or small mesoporous cage) of nanoMOFs. Surprisingly, nanoMOFs were prone to co-localize with bacteria once internalized in infected macrophages. NanoMOFs acted synergistically with the entrapped drugs to kill intracellular *S. aureus, in vitro*. These results pave the way towards the design of engineered nanocarriers in which each component synergistically plays a role in fighting the disease.

These studies unravel the potential of "cage" nanoparticles for efficient drug entrapment and release. They open new routes of investigation especially in the field of the treatment of severe intracellular infections. Moreover, it was shown that "cage" particles are not just simple "carriers" but could play a role in killing bacteria.

Conclusion Générale

Les systèmes à délivrance de médicaments sont des technologies conçues pour administrer des molécules actives de façon optimisée afin d'améliorer leurs effets thérapeutiques tout en minimisant les effets secondaires. En effet, ces systèmes permettent une libération au niveau d'une cible thérapeutique. Les particules de type "cage" ont récemment attiré une attention particulière en raison de leur capacité accrue à (co)incorporer et à protéger des molécules actives vis-à-vis de dégradations *in vivo*.

Les cyclodextrines (CDs) sont des exemples type de molécules "cage", possédant une cavité hydrophobe et une surface extérieure hydrophile. Nous avons élaboré tout d'abord des assembages supramoléculaires à base de CDs d'environ 100 nm par une méthode douce consistant à mélanger deux solutions aqueuses de polymères neutres: 1) polymère de β-CD et 2) dextrane greffé avec la benzophénone (Bz), molécule invitée formant des complexes d'inclusion avec les CDs. La procédure de préparation "verte" en une seule étape rend la formulation attractive, malgré sa relativement faible capacité d'encapsulation (5% pds). Afin d'améliorer cete charge, nous avons élaboré des particules hybrides organiques-inorganiques (MOFs) à base de CDs (CD-MOFs). Avantageusement, les CD-MOF comportent non seulement des cavités de CD, mais aussi de larges pores engendrés lors l'auto-assemblage de CDs. Le lansoprazole (LPZ) a été incorporé avec sucès (23% pds) dans les CD-MOFs et nous avons montré que chaque CDs était capable d'accueillir une molécule de principe actif. Cependant, l'inconvénient majeur des CD-MOFs est leur faible stabilité en milieu aqueux, limitant leur domaine d'aplication.

Une modification de surface est apparue donc nécessaire pour améliorer leur stabilité. Notre statégie a été d'incorporer les CD-MOFs dans des matrices d'acide polyacrylique (PAA). Des microsphères composites d'environ 650 nm ont été élaborées avec succès et ont permis une bone stabilité et une libération prolongée sur plus de 48 h. Avantageusement, ces particules composites n'étaient pas toxiques in vitro même à des concentrations élevées.

Ces microsphères apparaissent comme des systèmes efficaces pour assurer une bonne stabilité dans de milieux biologiques et une libération prolongée, mais leur synthèse est laborieuse et leur taille ne peut pas être réduite en dessus de 50 nm.

Ainsi, nous nous sommes orientés vers l'étude comparative de MOFs plus stables dans l'eau, à base de trimesate de fer. Les MIL-100 (Fe) (MIL signifie Matériel of Institute Lavoisier) figurent parmi les premiers MOF étudiés en tant que nanomédicaments (nanoMOFs). Ces

particules, parfaitement stables dans l'eau, se dégradent dans des milieux contenant des phosphates (PBS) en perdant rapidement leur caractère cristallin et leurs ligands constitutifs. De façon étonnante, nous avons constaté que malgré leur dégradation, ces MOFs conservent leur taille intacte. Une analyse approfondie basée sur la microscopie de Raman a permis d'obtenir des informations pertinentes sur la morphologie et la composition chimique de particules individuelles. Ainsi, il a été montré qu'un front d'érosion délimitait nettement un cœur intact et une coquillé inorganique érodée. Cependant, ni l'encapsulation ni la modification de surface des MOFs n'altérait leur intégrité. Enfin, nous avons étudié la co-encapsulation de deux molécules actives utilisées en combinaison (Amoxicilline et Clavulanate de potassium) dans les nanoMOFs stables à base de MIL-100 (Fe). Les antibiotiques ont été incorporés par imprégnation et chaque molécule s'est localisée préférentiellement dans un compartiment (large ou petite cage) corroborant parfaitement les simulations par modélisation moléculaire. De plus, il a été découvert, de manière surprenante, qu'un grand nombre de nanoMOFs se localisait au voisinage des bactéries (Staphylococcus aureus) dans des cellules infectées. En se dégradant dans ces cellules, les nanoMOFs contenant les antibiotiques ont réduit de manière importante la charge bactérienne intracellulaire.

Ces études révèlent le potentiel des particules de type "cage" pour une incorporation efficace de molécules actives et leur libération contrôlée et ouvrent de nombreuses possibilités d'application.

Annex I: Evaluation of drug loading capabilities of γ-cyclodextrin-metal organic frameworks by high performance liquid chromatography

Journal of Chromatography A, 1488 (2017) 37–44

Contents lists available at ScienceDirect

Journal of Chromatography A

journal homepage: www.elsevier.com/locate/chroma

Evaluation of drug loading capabilities of γ-cyclodextrin-metal organic frameworks by high performance liquid chromatography

Xiaonan Xu[a,b,1], Caifen Wang[b,1], Haiyan Li[b,1], Xue Li[b,c], Botao Liu[b], Vikramjeet Singh[b], Shuxia Wang[b], Lixin Sun[a,***], Ruxandra Gref[c,**], Jiwen Zhang[a,b,*]

[a] Department of Pharmaceutical Analysis, School of Pharmacy, Shenyang Pharmaceutical University, Shenyang 110016, China
[b] Center for Drug Delivery Systems, Shanghai Institute of Materia Medica, Chinese Academy of Sciences, Shanghai 201203, China
[c] Institut de Sciences Moléculaires d'Orsay, Université Paris-Saclay, UMR CNRS 8214, 91400 Orsay Cedex, France

ARTICLE INFO

Article history:
Received 12 August 2016
Received in revised form 9 January 2017
Accepted 23 January 2017
Available online 24 January 2017

Keywords:
Metal-organic frameworks
γ-CD-MOFs
Retention
Drug loading efficiency

ABSTRACT

Drug loading into γ-cyclodextrin-metal organic frameworks (γ-CD-MOFs) using the impregnation approach is a laborious process. In this study, a γ-CD-MOF construct (2–5 μm particle diameter) was used as the stationary phase under HPLC conditions with the aim to correlate retention properties and drug loading capability of the CD-based structure. Ketoprofen, fenbufen and diazepam were chosen as model drugs with *m*-xylene as a control analyte to investigate the correlation of drug loading and their chromatographic behaviour in the γ-CD-MOF column. Furthermore, γ-CD itself was also prepared as the stationary phase by coupling with silica in the column to illustrate the enhanced interaction between drugs and γ-CD-MOF as a reference. The retention and loading efficiency of the drugs were determined with different ratios of hexane and ethanol (10:90, 20:80, 50:50, 80:20, 90:10, v/v) at temperatures of 20, 25, 30 and 37 °C. With the increment in hexane content, the loading efficiency of ketoprofen and fenbufen increased from 2.39 ± 0.06% to 4.38 ± 0.04% and from 5.82 ± 0.94% to 6.37 ± 0.29%, respectively. The retention time and loading efficiency of ketoprofen and diazepam were the lowest at 30 °C while those of fenbufen had the different tendency. The excellent relation between the retention and loading efficiency onto γ-CD-MOF could be clearly observed through mobile phase and temperature investigation. In conclusion, a highly efficient chromatographic method has been established to evaluate the drug loading capability of γ-CD-MOF.

1. Introduction

Metal-organic frameworks (MOFs), with the advantages of diverse structures, highly porous topologies, accessible cages and tunnels [1,2] have been applied in gas storage [3–5], separation [6,7] and drug delivery [8,9]. They are synthesized with organic and inorganic components under mild conditions via coordination-directed self-assembly processes to generate exceptional properties that exceed what would be expected for a simple mixture of the components [10,11]. Recently, environment-friendly γ-cyclodextrin metal-organic frameworks (γ-CD-MOFs) synthesized through coordination of γ-cyclodextrins (γ-CD) and potassium ions have been reported [12–16]. The γ-CD-MOFs are body-centered cubic extended structures with molecular apertures of 0.78 nm in the structure of γ-CD and have larger spherical voids of 1.7 nm formed by regular arrangements of CDs [13].

The γ-CD-MOFs had been demonstrated as potential carriers of Rhodamine B4-Phenylazophenol and N_2, H_2, CO_2 and CH_4 gases by adsorption within their pores. The intrinsic nature of γ-CD-MOFs is able to provide excellent biodegradability, biocompatibility, and high loading capability to the drugs [17]. Though efforts on other MOF carriers have been made to pave the way for medical applications [18,19], few papers have been devoted to drug loading into γ-CD-MOFs systems. In an MOF-based drug delivery system, the drug loading and releasing can be controlled by adjusting the ligand and length or the connectivity and functionality [19–21]. However, it is challenging to achieve high loading efficiency through com-

* Corresponding author at: Center for Drug Delivery System, Shanghai Institute of Materia Medica, Chinese Academy of Sciences, No. 501 of Haike Road, Shanghai 201203, China.
** Corresponding author at: Institut de Sciences Moléculaires d'Orsay, Université Paris Sud, Université Paris Saclay, UMR CNRS 8214, 91400 Orsay, France.
*** Corresponding author at: School of Pharmacy, Shenyang Pharmaceutical University, No 103 of Wenhua Road, Shenyang 110016, China.
E-mail addresses: slx04@163.com (L. Sun), ruxandra.gref@u-psud.fr (R. Gref), jwzhang@simm.ac.cn (J. Zhang).
[1] These authors contributed equally to the manuscript.

http://dx.doi.org/10.1016/j.chroma.2017.01.062
0021-9673/

mon methods such as time-consuming impregnation approaches that the mixture solution of the drug and γ-CD-MOF was shaken for 24–72 h to achieve maximum payload. Therefore, an efficient alternative is of interest to facilitate the evaluation of drug loading into γ-CD-MOF.

Information retrieved from the chromatographic data can indicate the interaction between the analytes and the solid phase materials. Therefore, measures of chromatographic retention have been employed as an approach to investigate the uptake of the analytes and the activity of drugs. Vanatta and Coleman [22] determined the role of HF, H_3PO_4, HNO_3 in their mixture equilibrium reaction by evaluating their retention in ion chromatography. Detroyer et al. [23] analyzed the contribution of different chromatography systems to obtain the pharmacological activities of 83 drugs, with the method of the combination of chromatographic behaviour and chemometrics. The γ-CD is well known to exhibit chiral recognition ability, a per(3-chloro-4-methyl) phenylcarbamate-β-CD clicked chiral stationary phase (CSP) in high-performance liquid chromatography has been explored for the enantioseparation of 39 model racemic pairs including aromatic alcohols, flavonoids, β-blockers and amino acids [24]. Additionally, the chromatographic retention behaviour of the solute also could be used to evaluate the thermodynamic and kinetic interaction between the solute and the stationary phase. Since the 1980s, Hage's group has employed chromatographic techniques based on High Performance Affinity Chromatography (HPAC) to study the drug-human serum albumin and antibody-antigen interactions [25–28]. Furthermore, our previous work also investigated the interaction kinetics between the drug and β-CD by HPAC with β-CD bonded silica as solid phase materials [29]. On the other hand, the γ-CD-MOFs showed the advantage of the extended framework to separate a widely various mixtures, such as alkylaromatic compounds, saturated and unsaturated alicyclic compounds, as well as chiral compounds, which is different from the γ-CD column [16,30]. Because γ-CD-MOFs represent an emergent class of materials to encapsulate drug molecules, it is essential to investigate the relationship between drug loading ability and the chromatographic retention characters on γ-CD-MOF column.

In this paper, we reported a novel high-efficiency chromatographic evaluation strategy for drug loading into γ-CD-MOF by measurement of drug retention on γ-CD-MOF columns, with γ-CD columns as comparators. Acidic and basic compounds were investigated to obtain the mechanism of interaction between drugs and γ-CD-MOF to result in complex interactions. In order to explain the mechanism, nonsteroidal anti-inflammatory drugs with similar structure were employed while some of them (such as ibuprofen, naproxen and indomethacin) possessed poor chromatographic peak shape on the γ-CD-MOF column. Therefore, ketoprofen, fenbufen, and diazepam were chosen as the model drugs to investigate chromatographic behaviours under different solvents and temperatures in the γ-CD-MOF and γ-CD columns and their efficiency for drug loadings. For the drugs, ketoprofen and fenbufen are structural isomers with the similar molecular sizes and functional groups, which are compared to explain the interaction between the MOF cavities and drugs. As for diazepam, with the larger molecular size (0.81 nm) to hardly pass through the cavities in the MOF (0.78 nm), it could be employed to analyze the interaction mechanism on the γ-CD-MOF surface. And the retentions of drugs under varied chromatographic conditions were evaluated as indication of the interaction between drugs and γ-CD-MOF or γ-CD in the columns. The drug loading conditions were also optimized to obtain the maximal drug loading efficiency. In summary, a new strategy for quick evaluation of drug loading into γ-CD-MOF using chromatography is demonstrated (Fig. 1).

2. Experimental

2.1. Materials

All chemicals and reagents were of high purity (analytical grades or higher). The ketoprofen, fenbufen and diazepam (>99.5% purity) were purchased from the Dalian Meilun Biotech Co.,Ltd. The *o*-xylene (>98.0% purity), *m*-xylene (>99.0% purity), *p*-xylene (>98.5% purity) were purchased from Sinopharm Chemical Reagent Co., Ltd. (Beijing, China). Ethanol (EtOH), *n*-hexane, and dichloromethane (DCM) used as mobile phase solvents were of chromatographic grade and purchased from Sinopharm Chemical Reagent Co., Ltd. (Beijing, China).

2.2. Apparatus

The chromatographic system consisted of a binary pump (G1311C), an autosampler (G1329B), a temperature controller (G1316A) and a diode-array detector (G4212B, Agilent, Palo Alto, USA). Chromatographic data were acquired using the workstation of Chemstation Rev.B.04.03 (Agilent, Palo Alto, USA). An SB-5200DT ultrasonic cleaner (Ningbo Scientific Biotechnology Co., Ltd, Zhejiang, China) was used.

2.3. Synthesis of γ-CD-MOF

The γ-CD-MOF was synthesized using a modified solvent evaporation method [15]. Briefly, the γ-CD (4.86 g, 3.75 mol) and KOH (1.68 g, 30 mol) were mixed in 150 mL aqueous solution. The solution was filtered through a 0.45 μm filter membrane into a glass tube, and 15 mL of methanol (MeOH) was added, followed by vapor diffusion of MeOH into the solution at 50 °C for 12 h. The supernatant was then transferred into another glass tube and cetyl trimethyl ammonium bromide (CTAB, 8 mg/mL) was added. After the dissolution of CTAB, the solution was incubated overnight at room temperature. The precipitates were collected by centrifuging and washing with isopropanol for three times, and dried at 37 °C overnight to produce γ-CD-MOF particles with the size of 2–5 μm.

2.4. Preparation of γ-CD-MOF packed column

The γ-CD-MOF HPLC column (100 mm × 4.6 mm i.d.) was prepared by a high-pressure slurry packing procedure [31]. Namely, the γ-CD-MOF powder (1.5 g) was suspended in 20 mL of methanol then the suspension was loaded into an empty column (100 mm × 4.6 mm i.d.) under 35 MPa using 80 mL of methanol as the slurry solvent. Performance evaluation of the prepared γ-CD-MOF column was necessary and the detailed method and results were elaborated in the Supporting Information. The mechanical stability and the separation ability were proved to be excellent. Furthermore, we also evaluated the column performance before and after the experiment.

The γ-CD column (4.6 × 100 mm, 5 μm) and silica gel column (4.6 × 100 mm, 5 μm) were kindly gifted by Professor Xinmiao Liang at the Key Lab of Separation Science for Analytical Chemistry, Dalian Institute of Chemical Physics, Chinese Academy of Sciences, China. A native γ-CD stationary phase was prepared by covalently coupling γ-CD on silica particles via Huisgen [3 + 2] dipolar cycloaddition between the organic azide and terminal alkyne, which was characterized by FT-IR, ^{13}C NMR and elemental analysis. The pore size and surface area of the γ-CD bonding silica were 10 nm and 300 m^2/g, respectively. And the content of γ-CD on the silica was 0.12 μmol/m^2. Then the γ-CD columns (4.6 × 100 mm, 5 μm) were fabricated using a similar procedure to that for the γ-CD-MOF column [32]. As for the evaluation of the column performance, the separation efficiency was about 75 000 plates per meter and the

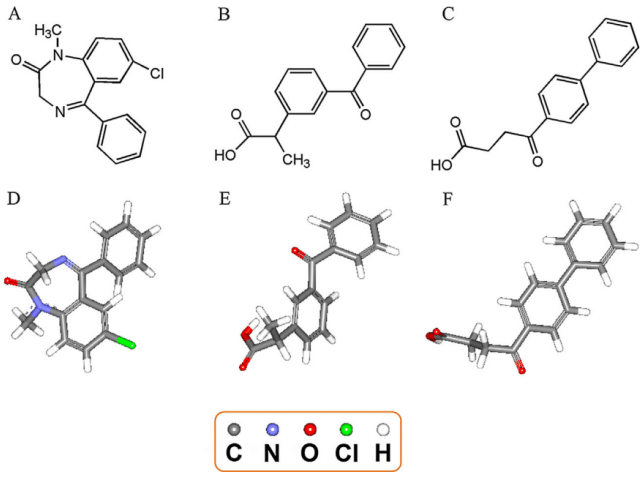

Fig. 1. The 2D and 3D images of the drug analytes. (A) 2D structure of diazepam, (B) 2D structure of ketoprofen, (C) 2D structure of fenbufen, (D) 3D structure of diazepam, (E) 3D structure of ketoprofen, (F) 3D structure of fenbufen.

asymmetry of peaks was 1.03 calculated from orotic acid on this column, the high column efficiency and good peak shape proved that the column was packed successfully.

2.5. Retentions of drugs in the γ-CD-MOF column and γ-CD column

The retention behaviours of drugs under different chromatographic conditions were studied on both γ-CD-MOF column and the γ-CD column in parallel. All drugs were dissolved by methanol to 10 mg/mL and diluted by isopropanol to 1 mg/mL, and 1,3,5-tri-*tert*-butylbenzene (TTBB, dissolved to 1 mg/mL by hexane) was used to determine the dead time. The determination was performed using hexane and ethanol as mobile phase. All the experiments were performed in duplicate for each set of test conditions.

2.6. The effects of mobile phase compositions

To study the impact of the mobile phase compositions, the retention profiles of the drugs on the γ-CD-MOF column and γ-CD column were characterized by retention factor (k) with mobile phase in different ratios of hexane and ethanol (10:90, 20:80, 50:50, 80:20, 90:10, v/v) at 30 °C. The sample concentration was set as 1 mg/mL with the injection volume of 10 μL at the flow rate of 0.8 mL/min.

2.7. The effects of the temperature

To investigate the temperature effects on the retention of the ketoprofen, fenbufen and diazepam in the γ-CD-MOF column and γ-CD column, the solutions of the drugs were injected to the column and eluted at temperatures of 20, 25, 30 and 37 °C with hexane and ethanol (80:20, v/v) as mobile phase at a flow rate of 0.8 mL/min. The sample concentration and injection volume were 1 mg/mL and 10 μL, respectively.

2.8. The determination of drug loading

The loading efficiency of drug with γ-CD-MOF and γ-CD was determined to compare the retention observed in γ-CD-MOF column and γ-CD column. Thus, the ketoprofen, fenbufen and diazepam were loaded in γ-CD-MOF and γ-CD by impregnation approach, which was carried out by soaking the dried γ-CD-MOF powder or γ-CD powder (30 mg) into 10.0 mL solution of drugs (2 mg/mL, with the specific solvents). The suspension was incubated at the defined temperature at least 24 h and shaken at 150 rpm. The drug loaded γ-CD-MOF deposits were collected by filtration and washed with equivalent volume of ethanol then the samples were dried under vacuum at 35 °C overnight. Impregnation conditions were further optimized by the chromatographic behaviour of drugs on the γ-CD-MOF column and γ-CD column under predefined chromatographic conditions.

The loading efficiency of drug adsorbed γ-CD-MOF was measured by dissolving 5 mg of dried samples in a certain amount of water and ethanol to solute all the samples and the drug content was determined by HPLC method with the Agilent C18 column (4.6 mm × 150 mm, 3.6 μm i.d.) at a flow rate of 0.6 mL/min on 25 °C column temperature. The mobile phase composed of 10% acetonitrile in 0.1% formic acid aqueous solution with gradient elution, changing linearly over 10 min to 90% acetonitrile then maintained for 3 min with the injection volume of 10 μL.

The drug loading (DL) was calculated according to Eq. (1), where m represented the amount of drug in γ-CD-MOF, M represented the total amount of the γ-CD-MOF.

$$\mathrm{DL}(\%) = \frac{m}{M} \times 100\% \quad (1)$$

3. Results and discussion

3.1. Characterization of γ-CD-MOF

The synthesized γ-CD-MOF particles were characterized by SEM, powder-XRD and the particle size distribution (Fig. 2). The shapes of γ-CD-MOF crystals were recorded as cubic and uniform by SEM with an average size of 3 μm. The crystalline characteristics of synthesized γ-CD-MOF particles were in agreement with that reported in literature [15] with the 2–5 μm particle size distribution.

As for the stability of the γ-CD-MOF, we have investigated the crystalline transformation of γ-CD-MOF in solvents

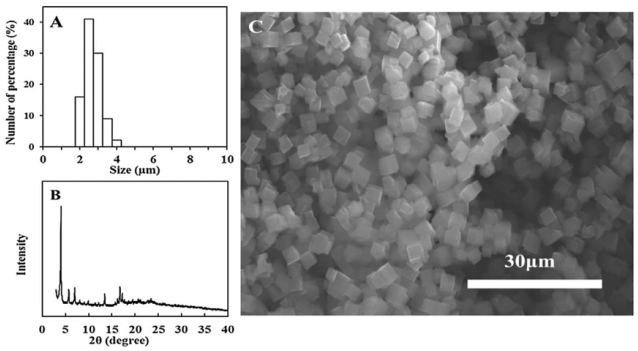

Fig. 2. The characterization of γ-CD-MOF showing (A) particle size distribution graph, (B) powder-XRD image and (C) the SEM image.

of dichloromethane, isopropanol, ethanol, acetone, methanol and N,N-dimethylformamide (DMF). The characterization of SEM and PXRD demonstrated the degradation in γ-CD-MOF crystals increases in parallel with solvent polarity. For example, major changes were noticed for crystalline stability in the case of methanol and DMF solvents at 70 °C after 1 d and there was no obvious change in other solvent during the whole stability experiment [33].

3.2. The mobile phase effects on the retentions of drugs in the γ-CD-MOF and γ-CD columns

The retention factors of the *m*-xylene, ketoprofen, fenbufen and diazepam on γ-CD-MOF column and γ-CD column presented significant diversity under different mobile phase compositions (Fig. 3). In the γ-CD column, with the increment of hexane in the mobile phase, the retention strength of the ketoprofen, fenbufen and diazepam increased. It may be due to the interaction between the hydroxyl groups in the γ-CD ring and the polar groups of the analytes, such as the carboxyl group of ketoprofen and the carbonyl group of diazepam. Thus, a slight change was observed in the *m*-xylene retention time (t_R = 1.58 min) which was similar to the non-retained material 1,3,5-tri-*tert*-butylbenzene (TTBB) (t_R = 1.45 min), due to the weak interaction between the nonpolar compound and the γ-CD. Furthermore, we also determined the retention factors of compounds in the silica column under the hexane/ethanol (90:10, v/v) in which the retention of drugs was stronger to clarify the influence of silica gel in the γ-CD column. The *k* values of fenbufen, ketoprofen (0.78 and 0.58, respectively) in silica gel column were much less than that in the γ-CD column (13.96 and 9.91, respectively), which indicated that the interaction between the fenbufen, ketoprofen and the silica gel of γ-CD was almost ignorable. However, the *k* values of diazepam (0.72 and 2.59 in the silica gel column and γ-CD column respectively) showed that the interaction of the polar groups with silica might also partly contribute to the retention in the γ-CD column.

For the γ-CD-MOF column, the retention of the analytes was more complicated. The retention factor of *m*-xylene in the γ-CD-MOF column decreased with the increment in hexane content. This might be due to that the nonpolar *m*-xylene can flow into γ-CD-MOF channels easily and was more likely soluble in the hexane, which lead to the downward trend of the retention with the increase of the hexane [30]. The retention factors of the ketoprofen (0.70 nm) and fenbufen (0.67 nm) increased with the increase in hexane content as shown in Fig. 3 which were different with that of *m*-xylene. The reasons might be that ketoprofen and fenbufen could both be absorbed into the pores due to the relative small kinetic diameter and the strong solubility in the ethanol. As for diazepam, the retention factor changed slightly in different mobile phase compositions owing to the size of the diazepam molecule (0.81 nm) which was too large to access the γ-CD-MOF cavities (0.78 nm). Specifically, the hydroxyl groups in the γ-CD ring took part in the coordination of potassium ion to construct the cubic space. The molecular apertures of 0.78 nm in the structure of CD and the larger spherical voids of 1.7 nm formed by regular arrangements of CDs provide more opportunities for compounds to pass through the cavities of the γ-CD-MOF.

3.3. Temperature effects on drug retention in γ-CD-MOF column and γ-CD column

The effect of the temperature on the interaction of the model drugs with γ-CD-MOF and γ-CD column was investigated by measuring the *k* at temperatures of 20, 25, 30 and 37 °C (Fig. 4). The retention factors of the analytes reduced except for *m*-xylene with the increment in column temperature of γ-CD column, suggesting an exothermic interaction in column. Whilst in the case of γ-CD-MOF column, the retention factors of analytes except for diazepam decreased with temperature increments suggesting exothermic interactions. However, the diazepam retention decreased with temperature reduction from 20 to 30 °C, then increased at 37 °C. Due to exothermic nature of the reaction, the affinity of γ-CD-MOF and γ-CD with drugs became significantly lower with the increase in temperature, leading to a decline in retention factors. The retention time of diazepam showed no correlation with temperature possibly due to its weak interaction with both γ-CD-MOF and γ-CD.

3.4. Correlation of drug loadings and chromatographic characteristics

The loading efficiencies of the γ-CD-MOF and γ-CD were determined under the same conditions mentioned in the chromatographic tests. Ketoprofen, fenbufen and diazepam were chosen as the model drugs to determine the loading efficiency. The different ratios of the hexane/ethanol (20:80, 50:50, 80:20, v/v) were used to verify the solvent effect on drug loadings. The results showed that the solvents significantly affected the retention and loading efficiencies of γ-CD-MOF and γ-CD (Fig. 5). The loading efficiency of γ-CD-MOF for ketoprofen and fenbufen were both higher than 2.39 ± 0.06%, suggesting a stronger interaction with γ-CD-MOF,

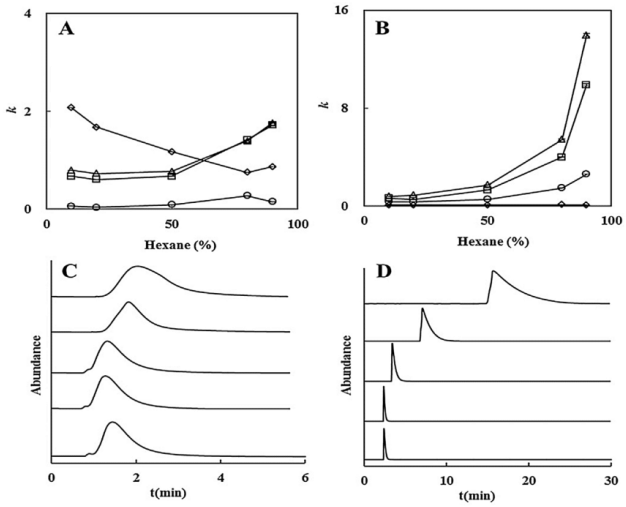

Fig. 3. The retention factors of the *m*-xylene, ketoprofen, fenbufen and diazepam at different mobile phase compositions in (A) γ-CD-MOF column and (B) the γ-CD column. (□: ketoprofen, △: fenbufen, ○: diazepam, ◊: *m*-xylene, error bars in these plots represented a range of ±SD for duplicate injection); effect of the mobile phase on the ketoprofen HPLC chromatograms in the (C) γ-CD-MOF column and (D) γ-CD column, from top to bottom, the ratio of hexane were 90%, 80%, 50%, 20% and 10%.

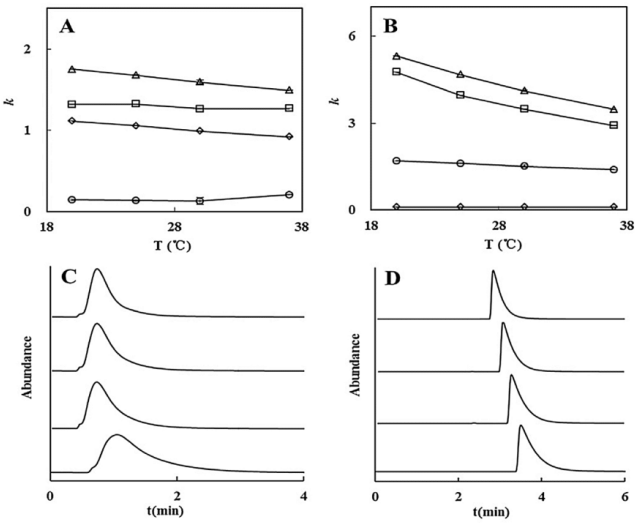

Fig. 4. The retention factors (*k*) of *m*-xylene, ketoprofen, fenbufen, and diazepam at different column temperature: (A) The γ-CD-MOF column, (B) The γ-CD column. (□: ketoprofen, △: fenbufen, ○: diazepam, ◊: *m*-xylene, error bars in these plots represent a range of ±SD for duplicate injection); effect of the temperature on the HPLC chromatograms of ketoprofen is shown in (C) the γ-CD-MOF column and (D) the γ-CD column, from top to bottom, at column temperatures of 37 °C, 30 °C, 25 °C, 20 °C.

while it showed weaker interaction of diazepam with the loading efficiency of only 0.05 ± 0.00%. Additionally, the loading efficiency of ketoprofen and fenbufen gradually increased with the increase of hexane content, in good agreement with the tendency of retention factors in HPLC columns. However, the diazepam exhibited a different tendency that a high content of hexane reducing the polarity of the solvent resulted in stronger interaction between drug and functional groups of CDs in γ-CD-MOF. For diazepam, its large molecular size (0.81 nm) might make it difficult to enter into the cavities of γ-CD-MOF (0.78 nm) leading to weak interactions between diazepam and γ-CD-MOF column.

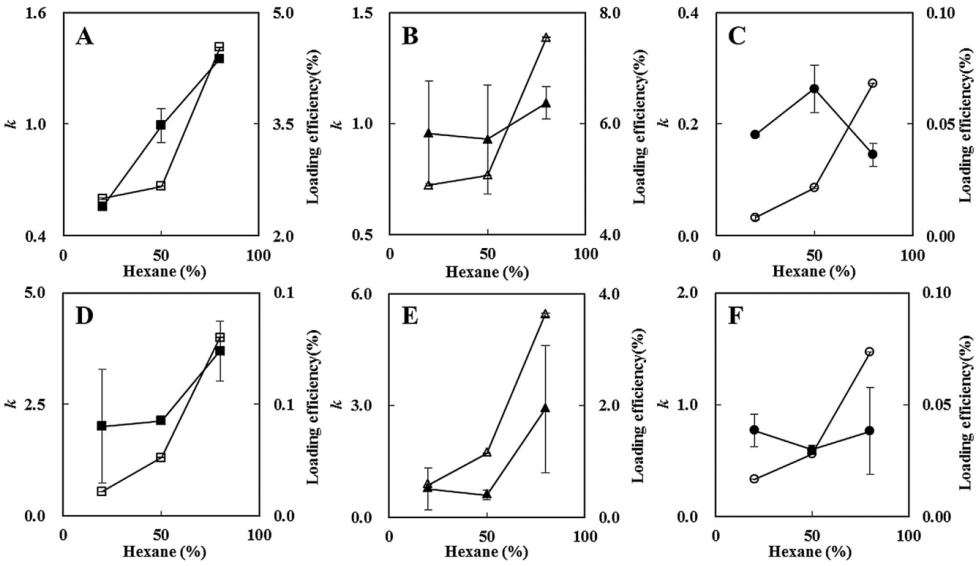

Fig. 5. Correlation of drug loadings and retention factor *k* value on γ-CD column and γ-CD-MOF column using different solvent at hexane/ethanol (20:80, 50:50, 80:20, v/v). (A) Ketoprofen on γ-CD-MOF, (B) Fenbufen on γ-CD-MOF, (C) Diazepam on γ-CD-MOF, (D) Ketoprofen on γ-CD, (E) Fenbufen on γ-CD, (F) Diazepam on γ-CD. (Solid points represent the loading efficiency, the hollow points represent the retention factor, error bars represented a range of ±SD for duplicate injections).

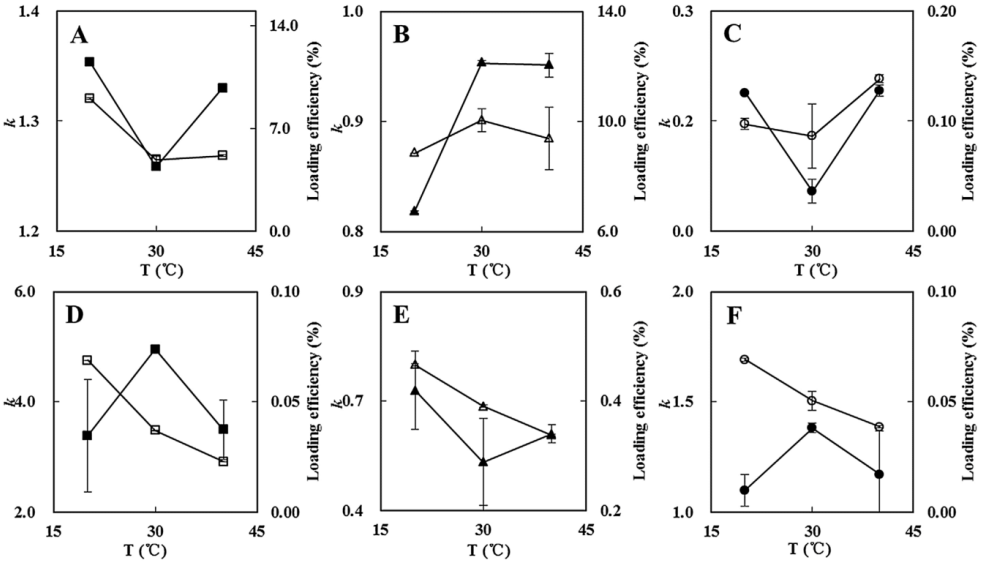

Fig. 6. Correlation of drug loadings and retention factor *k* value on γ-CD column and γ-CD-MOFs column at different temperature. (A) Ketoprofen on γ-CD-MOF, (B) Fenbufen on γ-CD-MOF, (C) Diazepam on γ-CD-MOF, (D) Ketoprofen on γ-CD, (E) Fenbufen on γ-CD, (F) Diazepam on γ-CD (solid points represent the loading efficiency, the hollow points represent the retention factor, error bars represented a range of ±SD for duplicate injections).

The temperature was also one of the most important factors to the loading efficiency. Therefore, experiments were performed at 20, 30 and 40 °C with hexane/ethanol (80:20, v/v) as the loading solvent except for fenbufen, for which the ratio of hexane/ethanol was 20:80 (v/v) due to its poor solubility at other ratios. The loading efficiencies obtained over the range from 20 to 40 °C showed a good correlation between the retention and loading efficiency on γ-CD-MOF (Fig. 6). The loading efficiencies for ketoprofen and diazepam

were recorded to be lowest at 30 °C, whilst the loading efficiency for fenbufen rapidly increased from 20 to 30 °C and then remained almost unchanged at 40 °C. Overall, the loading efficiencies of γ-CD for all drugs were recorded very low (<0.42 ± 0.07%). The loading efficiencies for ketoprofen and diazepam of γ-CD were higher at 30 °C than those at 20 and 40 °C, whilst the loading efficiency of fenbufen decreased from 20 to 30 °C. The exothermic interaction between ketoprofen and γ-CD-MOF resulted in the decline of loading efficiency with the increment in temperature from 20 to 30 °C. According to the Irene equation [34], although the temperature had little effect on the energy barrier of γ-CD-MOF inclusion decomposition, the concentration of the activated reactants increased which could make the k and loading efficiency large at 40 °C. However, this equation can't be applied to the drug loading for fenbufen with higher polarity of loading media.

The good consistency between the retention and loading efficiency was observed in γ-CD-MOF for solvent and temperature effects investigations. However, the fluctuation of retention and loading efficiency of drugs in γ-CD had no linear correlation. This might be due to the chemical bonding of γ-CD to silica gel which possibly changed the nature of γ-CD and generated additional interactions between the γ-CD and drugs. Thus, the retention was unable to reflect the real interactions between guest and host molecules for the γ-CD column. In this paper, γ-CD-MOF with its fine particle size distribution was used directly as the stationary phase for measurement of the host-guest interactions. Meanwhile, the drug loading characteristics of γ-CD-MOF were successfully evaluated due to consistency in retention behaviour and loading efficiency.

4. Conclusions

In this research, a high efficient chromatography evaluation methodology for drug loading to γ-CD-MOF was successfully established. For its uniformed size and shape, γ-CD-MOF had been directly used as stationary phase without conventional chemical modification on the silica. The novel strategy was proved to be efficient in the rapid evaluation of interactions between γ-CD-MOF and drugs. The solvent and temperature were identified as key factors to the correlation between retention and loading efficiency. The consistency of retention behaviour and drug loading efficiency further strengthened the utility of chromatographic evaluation as a new approach for drug loading optimization.

Acknowledgements

The authors are thankful to Prof. Xinmiao Liang and his group (the Key Lab of Separation Science for Analytical Chemistry, Dalian Institute of Chemical Physics, Chinese Academy of Sciences, China) for the preparation of columns. The financial support from the National Natural Science Foundation of China (No. 81573392, 81430087, 81373358) and National Science and Technology Major Project (2013ZX09402103) are gratefully acknowledged.

Appendix A. Supplementary data

Supplementary data associated with this article can be found, in the online version, at http://dx.doi.org/10.1016/j.chroma.2017.01.062.

References

[1] H. Furukawa, K.E. Cordova, M. O'Keeffe, O.M. Yaghi, The chemistry and applications of metal-organic frameworks, ChemInform 341 (2013).
[2] Y. Cui, B. Li, H. He, W. Zhou, B. Chen, G. Qian, Metal–organic frameworks as platforms for functional materials, Acc. Chem. Res. 49 (2016) 483–493.
[3] J.A. Mason, M. Veenstrab, J.R. Long, Evaluating metal–organic frameworks for natural gas storage, Chem. Sci. 5 (2014) 32–51.
[4] S. Ma, H.C. Zhou, Gas storage in porous metal-organic frameworks for clean energy applications, Chem. Commun. 46 (2010) 44–53.
[5] B. Li, H.M. Wen, W. Zhou, B. Chen, Porous metal-organic frameworks for gas storage and separation: what, how, and why? J. Phys. Chem. Lett. 20 (2014) 3468–3479.
[6] B. Chen, S. Xiang, G. Qian, Metal-organic frameworks with functional pores for recognition of small molecules, Acc. Chem. Res. 43 (2010) 1115–1124.
[7] J.R. Li, J. Sculley, H.C. Zhou, Metal-organic frameworks for separations, Chem. Rev. 112 (2012) 869–932.
[8] P. Horcajada, C. Serre, G. Maurin, N.A. Ramsahye, F. Balas, M. Vallet-Regí, M. Sebban, F. Taulelle, G. Férey, Flexible porous metal-organic frameworks for a controlled drug delivery, J. Am. Chem. Soc. 130 (2008) 6774–6780.
[9] R. Liu, T. Yu, Z. Shi, Z. Wang, The preparation of metal-organic frameworks and their biomedical application, Int. J. Nanomed. 11 (2016) 1187–1200.
[10] N. Stock, S. Biswas, Synthesis of metal-organic frameworks (MOFs): routes to various MOF topologies, morphologies, and composites, ChemInform 112 (2012) 933–969.
[11] Y. Sun, H.C. Zhou, Recent progress in the synthesis of metal-organic frameworks, Sci. Technol. Adv. Mater. 16 (2015).
[12] R.A. Smaldone, R.S. Forgan, H. Furukawa, J.J. Gassensmith, A.M. Slawin, O.M. Yaghi, J.F. Stoddart, Metal-organic frameworks from edible natural products, Angew. Chemie–Int. Ed. 49 (2010) 8630–8634.
[13] R.S. Forgan, R.A. Smaldone, J.J. Gassensmith, H. Furukawa, D.B. Cordes, Q. Li, C.E. Wilmer, Y.Y. Botros, R.Q. Snurr, A.M. Slawin, J.F. Stoddart, Nanoporous carbohydrate metal–organic frameworks, J. Am. Chem. Soc. 134 (2013) 406–417.
[14] J.J. Gassensmith, H. Furukawa, R.A. Smaldone, R.S. Forgan, Y.Y. Botros, O.M. Yaghi, J.F. Stoddart, Strong and reversible binding of carbon dioxide in a green metal-organic framework, J. Am. Chem. Soc. 133 (2011) 15312–15315.
[15] Y. Furukawa, T. Ishiwata, K. Sugikawa, K. Kokado, K. Sada, Nano- and microsized cubic gel particles from cyclodextrin metal-organic frameworks, Angew. Chemie – Int. Ed. 51 (2012) 10566–10569.
[16] K.J. Hartlieb, J.M. Holcroft, P.Z. Moghadam, N.A. Vermeulen, M.M. Algaradah, M.S. Nassar, Y.Y. Botros, R.Q. Snurr, J.F. Stoddart, CD-MOF: a versatile separation medium, J. Am. Chem. Soc. 138 (2016) 2292–2301.
[17] P. Horcajada, T. Chalati, C. Serre, B. Gillet, C. Sebrie, T. Baati, J.F. Eubank, D. Heurtaux, P. Clayette, C. Kreuz, J.S. Chang, Y.K. Hwang, V. Marsaud, P.N. Bories, L. Cynober, S. Gil, G. Férey, P. Couvreur, R. Gref, Porous metal-organic-framework nanoscale carriers as a potential platform for drug delivery and imaging, Nat. Mater. 9 (2010) 172–178.
[18] M.R. Di Nunzio, V. Agostoni, B. Cohen, R. Gref, A. Douhal, A ship in a bottle strategy to load a hydrophilic anticancer drug in porous metal organic framework nanoparticles: efficient encapsulation, matrix stabilization, and photodelivery, J. Med. Chem. 57 (2014) 411–420.
[19] P. Horcajada, R. Gref, T. Baati, P.K. Allan, G. Maurin, P. Couvreur, G. Férey, R.E. Morris, C. Serre, Metal-organic frameworks in biomedicine, Chem. Rev. 112 (2012) 1232–1268.
[20] R.C. Huxford, R.J. Della, W. Lin, Metal-organic frameworks as potential drug carriers, Curr. Opin. Chem. Biol. 14 (2010) 262–268.
[21] S. Keskin, S. Kızılel, Biomedical applications of metal organic frameworks, Ind. Eng. Chem. Res. 50 (2011) 1799–1812.
[22] L.E. Vanatta, D.E. Coleman, Ion-chromatographic study of interactions in $HF–H_3PO_4–HNO_3$ semiconductor etchants: systematic use of statistically designed mixture experiments, J. Chromatogr. A 804 (1998) 161–169.
[23] A. Detroyer, V. Schoonjans, F. Questier, H.Y. Vander, A.P. Borosy, Q. Guo, D.L. Massart, Exploratory chemometric analysis of the classification of pharmaceutical substances based on chromatographic data, J. Chromatogr. A 897 (2000) 23–36.
[24] J. Tang, L. Pang, J. Zhou, S. Zhang, W. Tang, Per(3-chloro-4-methyl)phenylcarbamate cyclodextrin clicked stationary phase for chiral separation in multiple modes high-performance liquid chromatography, Anal. Chim. Acta 946 (2016) 96–103.
[25] J.E. Schiel, C.M. Ohnmacht, D.S. Hage, Measurement of drug-protein dissociation rates by high-performance affinity chromatography and peak profiling, Anal. Chem. 81 (2009) 4320–4333.
[26] Z. Tong, J.E. Schiel, E. Papastavros, C.M. Ohnmacht, Q.R. Smith, D.S. Hage, Kinetic studies of drug-protein interactions by using peak profiling and high-performance affinity chromatography: examination of multi-site interactions of drugs with human serum albumin columns, J. Chromatogr. A 1218 (2011) 2065–2071.
[27] Z. Tong, D.S. Hage, Characterization of interaction kinetics between chiral solutes and human serum albumin by using high-performance affinity chromatography and peak profiling, J. Chromatogr. A 1218 (2011) 6892–6897.
[28] J. Chen, J.E. Schiel, D.S. Hage, Noncompetitive peak decay analysis of drug-protein dissociation by high-performance affinity chromatography, J. Sep. Sci. 32 (2009) 1632–1641.
[29] C. Wang, J. Ge, J. Zhang, T. Guo, L. Chi, Z. He, X. Xu, P. York, L. Sun, H. Li, Multianalyte determination of the kinetic rate constants of drug-cyclodextrin supermolecules by high performance affinity chromatography, J. Chromatogr. A 1359 (2014) 287–295.
[30] J.M. Holcroft, K.J. Hartlieb, P.Z. Moghadam, J.G. Bell, G. Barin, D.P. Ferris, E.D. Bloch, M.M. Algaradah, M.S. Nassar, Y.Y. Botros, K.M. Thomas, J.R. Long, R.Q. Snurr, J.F. Stoddart, Carbohydrate-mediated purification of petrochemicals, J. Am. Chem. Soc. 137 (2015) 5706–5719.

[31] S.M. Xie, M. Zhang, Z.X. Fei, L.M. Yuan, Experimental comparison of chiral metal-organic framework used as stationary phase in chromatography, J. Chromatogr. A 1363 (2014) 137–143.
[32] Z. Guo, Y. Jin, T. Liang, Y. Liu, Q. Xu, X. Liang, A. Lei, Synthesis, chromatographic evaluation and hydrophilic interaction/reversed-phase mixed-mode behavior of a click beta-cyclodextrin stationary phase, J. Chromatogr. A 1216 (2009) 257–263.
[33] B. Liu, H. Li, X. Xu, X. Li, N. Lv, V. Singh, J.F. Stoddart, P. York, X. Xu, R. Gref, J. Zhang, Optimized synthesis and crystalline stability of γ-cyclodextrin metal-organic frameworks for drug adsorption, Int. J. Pharm. 514 (1) (2016) 212–219.
[34] D. Todorova-Balvay, I. Stoilova, S. Gargova, M.A. Vijayalakshmi, An efficient two step purification and molecular characterization of β-galactosidases from Aspergillus oryzae, J. Mol. Recognit. 19 (2006) 389–407.

Supporting Information for

"Evaluation of drug loading capabilities of γ-cyclodextrin-metal organic frameworks by high performance liquid chromatography**"**

Xiaonan Xu[1,2,a], Caifen Wang[2,a], Haiyan Li[2,a], Xue Li[2,3], Botao Liu[2], Vikramjeet Singh[2], Shuxia Wang[2], Lixin Sun[1,*], Ruxandra Gref[3,*], Jiwen Zhang[1,2,*]

[1] Department of Pharmaceutical Analysis, School of Pharmacy, Shenyang Pharmaceutical University, Shenyang 110016, China;

[2] Center for Drug Delivery Systems, Shanghai Institute of Materia Medica, Chinese Academy of Sciences, Shanghai 201203, China;

[3] Institut de Sciences Moléculaires d'Orsay, Université Paris-Saclay, UMR CNRS 8214, 91400 Orsay Cedex, France

[a:] These authors contributed equally to the manuscript

***Corresponding Author:**

Prof. Jiwen Zhang

Center for Drug Delivery System, Shanghai Institute of Materia Medica, Chinese Academy of Sciences, No. 501 of Haike Road, Shanghai 201203, China; Tel/Fax +86-21-20231980; E-mail: jwzhang@simm.ac.cn;

Prof. Ruxandra Gref

Institut de Sciences Moléculaires d'Orsay, Université Paris-Sud, Université Paris-Saclay, UMR CNRS 8214, 91400 Orsay, France; Tel: +33 (1)69158234; E-mail: ruxandra.gref@u-psud.fr.

Prof. Lixin Sun

School of Pharmacy, Shenyang Pharmaceutical University, No. 103 of Wenhua Road, Shenyang 110016, China; Tel/Fax +86-24-23986365; E-mail: slx04@163.com.

S1. Methods of γ-CD-MOF column evaluation

The performance of γ-CD-MOF column was evaluated on an Agilent 1260 HPLC system with hexane-dichloride methylene (DCM) as mobile phase at 30 °C. In order to investigate the mechanical stability of the γ-CD-MOF composites packed column, the column pressure was measured at the flow rates of 0.2, 0.4, 0.6, 0.8 and 1.0 mL/min using different mobile phases of hexane/DCM (10:90, 30:70, 50:50, 70:30, 90:10, v/v). Precision was validated by the relative standard deviations (RSDs) of retention time, peak area, and half peak width of *o*-xylene, *m*-xylene, *p*-xylene and their mixture in five replicates with the hexane/DCM (95:5, v/v) as mobile phase at 0.4 mL/min. The mixture of xylene isomers was also employed to determine the resolution capability of γ-CD-MOF column with the mobile phase of the hexane/DCM (70:30, 80:20, 90:10, 95:5, v/v) and the flow rate of 0.4, 0.6, 0.8 and 1.0 mL/min. The detection wavelength and injection volume were 254 nm and 0.1 μL, respectively.

S2. Results of γ-CD-MOF column evaluation

The effects of flow rate and mobile phase on the column back pressure are shown in Fig. S1. The back pressure of the γ-CD-MOF packed column increased with the increment of flow rate and DCM content in the mobile phase. The maximum pressure of the column was only 48.55 bar using n-hexane/DCM (10:90, v/v) as the mobile phase at a flow rate of 1.0 mL/min. The precision was validated by the *o*-xylene, *m*-xylene, *p*-xylene and their mixture respectively in five replicates with the mobile phase of hexane/DCM (95:5, v/v) at 0.4 mL/min. The relative standard

deviations (RSDs) of *m*-xylene, *p*-xylene and *o*-xylene were 0.27%, 0.13%, 0.27% for the retention time, 2.51%, 4.23%, 3.94% for peak area, and 0.87%, 0.15%, 1.30% for half peak width, respectively. In addition, the resolutions of the *m*-xylene, *p*-xylene and *o*-xylene were 1.24 and 2.44, respectively. The results demonstrated that γ-CD-MOF as stationary phase could overcome the problem of high column pressure and with a satisfactory mechanical stability and reproducibility.

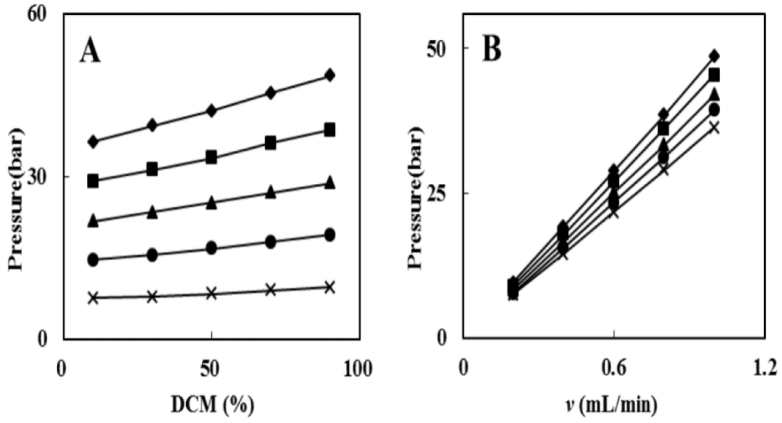

Fig. S1 Dependence of γ-CD-MOF packed column pressure on the flow rate and mobile phase composition. (A) The different flow rate.（×: 0.2 mL/min, ●: 0.4 mL/min, ▲: 0.6 mL/min, ■: 0.8 mL/min, ◆: 1.0 mL/min）, (B) The contents of DCM in the mobile phase. (×: 10%, ●: 30%, ▲: 50%, ■: 70%, ◆: 90%).

The xylene isomers were used to evaluate the HPLC separation ability of γ-CD-MOF composite packed column. As shown in Fig. S2, the xylene isomers were successfully eluted as the overlapped peak by γ-CD-MOF column. The retention of the xylene isomers became weak with the increment of DCM content in mobile phase and the flow rate increased. The xylene mixtures exhibited base-lined separation with the retention order ortho > meta > para in this study, which was consistent with that

reported in the literature [1]. At the flow rate of 0.4 mL/min, the excellent baseline separation of the xylene isomers could be achieved at the hexane/DCM (95:5, v/v). Thus, it was concluded that the basic separation could be achieved using γ-CD-MOF column for the xylene isomers. **Furthermore, as for the column efficiency of the γ-CD-MOF column, the theoretical plate number is about 12 000 plates/m calculated from *p*-xylene in this column.**

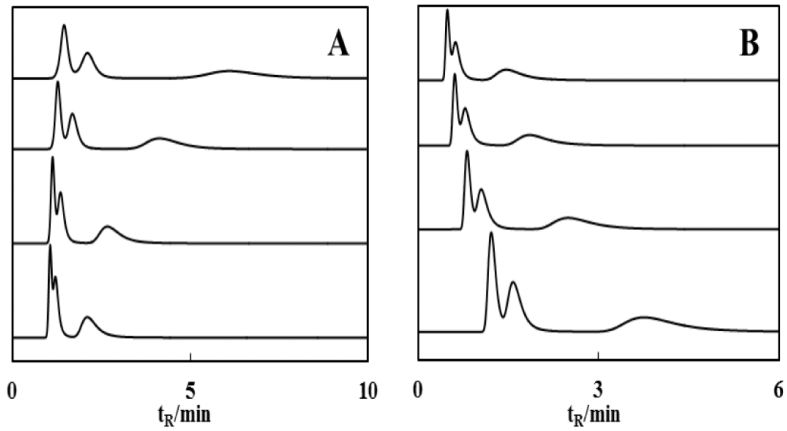

Fig. S2 The typical HPLC chromatograms of xylene isomers separation, (A) The different ratios of the mobile phase, from bottom to up, 70:30, 80:20, 90:10, 95:5, hexane/DCM, v/v at a constant flow rate of 0.4 mL/min, (B) The different flow rate, from bottom to up, 0.4, 0.6, 0.8 and 1.0 mL/min with the hexane/DCM (95:5, v/v) as the mobile phase.

S3. Crystallinity stability of the γ-CD-MOF column

We also ensure the crystallinity of the γ-CD-MOF during column preparation by simulating the preparation procedure, which was carried out by immersing the γ-CD-MOF powder in the methane for 72h, according to the amount needed in the packed method. The precipitates were collected by centrifuging and dried at 37 °C overnight to obtain γ-CD-MOF particles, and the powder-XRD and the SEM also

were characterized to demonstrate the excellent crystallinity (Fig.S3). The SEM and the powder-XRD both indicated that the γ-CD-MOF retain its crystallinity well. On the other hand, the packed γ-CD-MOF column still possessed excellent HPLC performance after 400 samples were injected into the column under the determination condition. The column pressure still behaved well showing linearity with flow rate and increasing DCM content, and the relative standard deviations (RSDs) of *m*-xylene for retention time and peak area were 0.43% and 3.55%, respectively. Furthermore, the ability of separating xylene isomers mixture still can achieve baseline resolution (resolution were 1.34 and 3.21, respectively), which represented the tolerant mechanical stability and column efficiency.

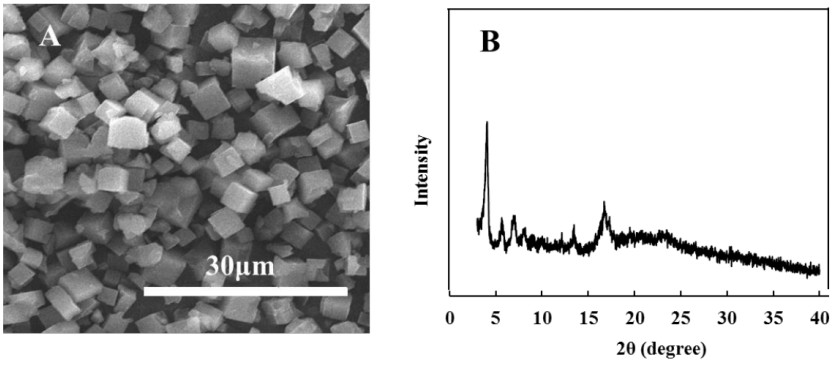

Fig. S3 The characterization of γ-CD-MOF during the column preparation, (A) the SEM image. and (B) the powder-XRD image.

References

[1] J.M. Holcroft, K.J. Hartlieb, P.Z. Moghadam, J.G. Bell, G. Barin, D.P. Ferris, E.D. Bloch, M.M. Algaradah, M.S. Nassar, Y.Y. Botros, K.M. Thomas, R. Long, R.Q. Snurr, J.F. Stoddart, Carbohydrate-Mediated Puri fi cation of Petrochemicals, J. Am. Chem. Soc. 137 (2015) 5706-5719.

Annex II: Improvement in thermal stability of sucralose by γ-cyclodextrin metal-organic frameworks

Pharm Res
DOI 10.1007/s11095-016-2059-1

RESEARCH PAPER

Improvement in Thermal Stability of Sucralose by γ-Cyclodextrin Metal-Organic Frameworks

Nana Lv[1,2] • Tao Guo[2] • Botao Liu[2,3] • Caifen Wang[2] • Vikaramjeet Singh[2] • Xiaonan Xu[1,2] • Xue Li[1,4] • Dawei Chen[1] • Ruxandra Gref[4] • Jiwen Zhang[1,2]

Received: 10 August 2016 / Accepted: 24 October 2016

ABSTRACT

Purpose To explain thermal stability enhancement of an organic compound, sucralose, with cyclodextrin based metal organic frameworks.

Methods Micron and nanometer sized basic CD-MOFs were successfully synthesized by a modified vapor diffusion method and further neutralized with glacial acetic acid. Sucralose was loaded into CD-MOFs by incubating CD-MOFs with sucralose ethanol solutions. Thermal stabilities of sucralose-loaded basic CD-MOFs and neutralized CD-MOFs were investigated using thermogravimetric analysis (TGA), differential scanning calorimetry (DSC) and high performance liquid chromatography with evaporative light-scattering detection (HPLC-ELSD).

Results Scanning electron microscopy (SEM) and powder X-ray diffraction (PXRD) results showed that basic CD-MOFs were cubic crystals with smooth surface and uniform sizes. The basic CD-MOFs maintained their crystalline structure after neutralization. HPLC-ELSD analysis indicated that the CD-MOF crystal size had significant influence on sucralose loading (SL). The maximal SL of micron CD-MOFs (CD-MOF-Micro) was 17.5 ± 0.9% (w/w). In contrast, 27.9 ± 1.4% of sucralose could be loaded in nanometer-sized basic CD-MOFs (CD-MOF-Nano). Molecular docking modeling showed that sucralose molecules preferentially located inside the cavities of γ-CDs pairs in CD-MOFs. Raw sucralose decomposed fast at 90°C, with 86.2 ± 0.2% of the compound degraded within only 1 h. Remarkably, sucralose stability was dramatically improved after loading in neutralized CD-MOFs, with only 13.7 ± 0.7% degradation at 90°C within 24 h.

Conclusions CD-MOFs efficiently incorporated sucralose and maintained its integrity upon heating at elevated temperatures.

Equally contributing authors (N.L. for drug loading, experiments other than HPLC and preparation of the manuscript; T.G. for molecular simulation; B.L. for CD-MOFs preparation; C.W. for HPLC method establishment and validation).

Nana Lv, Tao Guo, Botao Liu and Caifen Wang contributed equally to this work.

Electronic supplementary material The online version of this article (doi:10.1007/s11095-016-2059-1) contains supplementary material, which is available to authorized users.

✉ Dawei Chen
chendawei@syphu.edu.cn

✉ Ruxandra Gref
ruxandra.gref@u-psud.fr

✉ Jiwen Zhang
jwzhang@simm.ac.cn

[1] School of Pharmacy, Shenyang Pharmaceutical University, Shenyang 110016, China

[2] Center for Drug Delivery System, Shanghai Institute of Materia Medica, Chinese Academy of Sciences, No. 501 of Haike Road, Shanghai 201210, China

[3] School of Chemical and Environmental Engineering, Shanghai Institute of Technology, Shanghai 201418, China

[4] Institute of Moléculaires Sciences d'Orsay, UMR CNRS 8214, Université Paris Sud, Université Paris-Saclay, 91400 Orsay, France

Published online: 28 November 2016

KEY WORDS cyclodextrin metal-organic frameworks · sucralose · thermal stability

ABBREVIATIONS

CD-MOFs	Cyclodextrin metal organic frameworks
CTAB	Cetyl trimethyl ammonium bromide
DSC	Differential scanning calorimetry
EtOH	Ethanol
HPLC-ELSD	High performance liquid chromatography with evaporative light-scattering detection
MeOH	Methanol
PXRD	Powder X-ray diffraction
TGA	Thermogravimetric analysis
γ-CD	γ-cyclodextrin

INTRODUCTION

In recent years, inorganic–organic hybrid materials, especially metal-organic frameworks (MOFs) composed of metals and organic linkers, emerged as a new class of highly versatile porous materials (1). Due to their large surface areas, the possibility to tune their structure and porosity, as well as their high loading capacities, MOFs are well suited to serve as carriers for a variety of guest molecules. In particular, their use for drug delivery purposes attracted a great interest (2–10). However, the use of biocompatible materials is a prerequisite for biomedical applications. MOFs based on toxic metals (*e.g.*, Co, Ni, Cr,…) and/or non-pharmaceutical grade organic linkers are not suitable for healthcare applications (3). Many efforts have been carried on to synthesize biocompatible MOFs with endogenous linkers or pharmaceutical acceptable excipients (11–15). For instance, environmentally friendly and renewable MOFs were synthesized using γ-CD, a symmetrical cyclic oligosaccharide, as a ligand and potassium ion as the metal source (16–18). The resulting CD-MOFs are body-centered cubic structures with apertures of 7.8 Å and large spherical voids of 17 Å linked by coordination between the D-glucopyranosyl residues of γ-CDs and potassium cations. These cubic CD-MOFs with large surface areas of up to 1200 $m^2 \cdot g^{-1}$ were capable of storing gases (N_2, H_2, CO_2 and CH_4) and some small molecules (rhodamine B and 4-phenylazophenol) within their pores (19,20).

To the best of our knowledge, there are only few studies on MOFs applications as carriers or micro-containers to improve the stability of guest molecules (15,21). Moussa *et al.* have successfully encapsulated curcumin in the cavities of CD-MOFs, to better stabilize it for food applications (21). Sucralose is another example of compound unstable at elevated temperatures with formation of hazardous polychlorinated compounds. In this study, sucralose was selected as a model molecule to investigate its stability enhancement by confinement inside CD-MOFs. Sucralose, an artificial sweetener which was firstly synthesized by selectively substituting three hydroxyl groups of sucrose with chlorine atoms in 1976, has shown an increasing trend of consumption since its commercial development (22). Sucralose is a relatively new, non-nutritive sweetener with a 600 times higher sweetness than sucrose without bitter nor metallic taste (23). Because of these properties, sucralose is widely used in food products and pharmaceuticals (24). Although sucralose was initially considered safe, recently published data suggested that this molecule could be degraded even at mild temperatures with the generation of hazardous polychlorinated aromatic hydrocarbons (25). Various techniques were applied to improve the thermal stability of sucralose under hot and dry conditions, such as microencapsulation and the formation of co-crystallized complexes with γ-CDs (26). However, none of the above mentioned methods has been proven satisfactory and the resulting sucralose products continued to exhibit undesirable instability under hot and dry conditions.

We show here that CD-MOFs prepared from edible natural products can be used as carriers or containers to improve the stability of sucralose. The as-synthesized CD-MOFs were alkaline with a pH of about 12 when dissolved in water, and they were termed as basic CD-MOFs. Taking into consideration the weak acidity of sucralose with a pK_a of 2.52 ± 0.70 and its tendency to be hydrolyzed in the alkaline environment of basic CD-MOFs, neutralized CD-MOFs were obtained by treating basic CD-MOFs with glacial acetic acid. SEM, PXRD and gas adsorption were employed to characterize basic and the neutralized CD-MOFs. Sucralose was conveniently loaded into all the CD-MOFs by simply incubating them with sucralose solutions. The thermal stability of sucralose under the free and encapsulated form was investigated by a set of complementary techniques including TGA, DSC and HPLC-ELSD. In addition, molecular docking studies were performed to determine the sucralose location inside CD-MOFs and the mechanism by which these particles improve sucralose stability.

MATERIALS AND METHODS

Materials

Sucralose was purchased from Tate & Lyle Singapore Pte. Ltd. (batch number: JU1419427). γ-CD was purchased from MaxDragon Biochem Ltd (Guangzhou, China). Methanol (MeOH), potassium hydroxide (KOH), cetyl trimethyl ammonium bromide (CTAB), isopropanol, ethanol (EtOH), dichloromethane (DCM), acetone and other reagents of analytical grade were all purchased from Sinopharm Chemical Reagent Co., Ltd. (Shanghai, China) and used without further purification. Water was purified by Milli-Q system (Millipore).

Synthesis of Micron and Nanometer Sized Basic CD-MOFs

Basic CD-MOFs were synthesized according to a published procedure with the only difference that the temperature of MeOH diffusion was changed from 25°C to 50°C to improve the synthesis efficiency. In brief, γ-CD (162 mg, 0.125 mmol) was mixed with 8 equivalent moles of KOH (56 mg, 1 mmol) in 5 mL aqueous solution. The solution was filtered through a 0.45 μm filter membrane into a glass tube, and 0.5 mL of MeOH was added, followed by vapor diffusion of MeOH into the solution at 50°C. After 6 h, the supernatants (about 7 mL) were recovered and were transferred into another glass tube followed by addition of 56 mg CTAB and the solution was incubated at room temperature overnight. The precipitates were then harvested and washed with isopropanol three times, and dried at 37°C overnight to produce basic CD-MOFs with the size of about 5–10 μm (CD-MOF-Micro). The synthesis procedure of nanometer-sized CD-MOFs (CD-MOF-Nano) was the same as that for CD-MOF-Micro, except that 7 mL of MeOH was added into the supernatants previously to the addition of 56 mg of CTAB.

The basic CD-MOFs were neutralized with glacial acetic acid. In brief, 600 mg basic CD-MOFs in 20 mL EtOH and 2 mL glacial acetic acid, then CD-MOFs and acetic acid were well mixed under shaking (150 rpm) for 0.5 h. The precipitates were harvested by centrifugation, followed by washing with EtOH for three times, and vacuum dried at 50°C overnight.

Loading of Sucralose into Basic CD-MOFs

Sucralose was loaded into basic CD-MOFs by incubating CD-MOFs with sucralose solution. For this, 200 mg of dried basic CD-MOFs powders (micron or nanometer sized) were dispersed under ultrasonic bath into 4 mL EtOH solution of sucralose with a concentration of 41 $mg{\cdot}mL^{-1}$ (molar ratio of constitutive γ-CD in basic CD-MOFs to sucralose was 1:3) and impregnated at 37°C in an incubator with a speed of 50 rpm for 20 h. The precipitates were dried under vacuum overnight to obtain sucralose-loaded basic CD-MOFs. Sucralose-loaded neutralized CD-MOFs were obtained similarly. Two other concentrations of sucralose solutions, 69 and 96 $mg{\cdot}mL^{-1}$ were investigated on sucralose loading (SL), corresponding to molar ratios of γ-CD in basic or neutralized CD-MOFs to sucralose of 1:5 and 1:7, respectively.

Characterization of CD-MOFs and Sucralose Loaded CD-MOFs

Morphological characterizations of basic, neutralized CD-MOFs, and sucralose loaded CD-MOFs were conducted using an SEM (S3400, Hitachi). Specimens were immobilized on metal stubs with double-sided adhesive tape and coated with gold, then observed under definite magnification.

Crystallinity of the samples (basic or neutralized CD-MOFs and that loaded with sucralose) was characterized by PXRD. Diffraction patterns were detected with a Bruker D8 Advance diffractometer (Bruker, USA). Samples were irradiated with monochromatized CuKα radiation (λ = 1.54 Å) and analyzed over a 2θ angle range of 3-40° with a tube voltage of 40 kV, a tube current of 40 mA at a scan speed of 0.1 s/step.

Fourier-transform infrared spectroscopy (FT-IR) spectra of samples (basic or neutralized CD-MOFs and that loaded with sucralose) were obtained using an FT-IR spectrometer (Thermo Nicolet iS5, Thermo Scientific, USA). Briefly, sample was thoroughly mixed with potassium bromide at a ratio of 1:10 and compressed into a tablet. Each specimen was recorded with 16 scans at a resolution of 4 cm^{-1} in a wavenumber range of 400–4000 cm^{-1}.

Nitrogen adsorption-desorption isotherm of samples (basic or neutralized CD-MOFs and that loaded with sucralose) was measured at −196°C using a porosimeter (Micromeritics ASAP 2020, USA). In order to remove the interstitial solvents, the samples were activated by immersing in DCM for 3 days and dried under vacuum at 50°C for 12 h. Known amounts of CD-MOFs (e. g. 150–200 mg) were loaded into the sample tubes and degassed under vacuum (10^{-5} Torr) at 50°C for 6 h. BET and Langmuir models were applied to measure the specific surface areas of the prepared samples.

Sucralose loading was measured by dissolving 5 mg of a sample in 2 mL of water under sonication for 5 min and the solution was analyzed by HPLC-ELSD, as described in S1 of Supporting Information (SI). The SL was calculated according to the following equation (27).

$$\mathrm{SL}(\%) = \frac{\text{Sucralose determined in CD-MOFs}}{\text{Weight of sucralose loaded CD-MOFs}} \times 100 \quad (1)$$

Release of sucralose from sucralose loaded neutralized CD-MOF-Nano in EtOH was also performed. Sucralose loaded neutralized CD-MOF-Nano (wash or without wash with EtOH after sucralose loading) equivalent to 1 mg of sucralose (calculated on the basis of sucralose loading) were suspended in 5 mL EtOH and maintained at 25°C with a speed of 100 rpm. Samples of 200 μL were withdrawn at predefined time intervals (0, 0.1, 0.2, 0.3, 0.5, 1, 2, 4, 6, 20 and 24 h) and the same volume of fresh EtOH was added. The concentration of sucralose in each sample was determined and cumulative release percentage was calculated. More detailed methods and results were described in S4.

Thermal Analysis

TGA was performed using a thermal analysis system (NETZSCH 209 F3 240-20-382-L, USA) at a heating rate

of 10°C · min^{-1} under nitrogen. Samples were weighed (approximately 5 mg) in an aluminum crucible and the percentage weight loss of the samples was monitored from 30 to 400°C.

DSC was performed by differential scanning calorimeter (PerkinElmer DSC8500, USA) in the temperature range from 45°C to 230°C with a heating rate of 10°C · min^{-1} under constant nitrogen purging of 30 mL · min^{-1}. Samples were weighed (approximately 5 mg) in an aluminum crucible. The temperature and melting calibrations were performed with indium (mp = 156.6°C and ΔHm = 28.5 J · min^{-1}).

Thermal Stability Measured by HPLC-ELSD

Thermal stability of sucralose, sucralose loaded basic and neutralized CD-MOFs were investigated at elevated temperature. Briefly, samples of 300 mg were mounted in glass dishes, and then exposed to 90°C in an oven. Samples of 5 mg were withdrawn at predefined time intervals (0, 1, 2, 4, 8, 16, 24 h) and then dissolved in 2 mL of water. The concentration of sucralose in each sample was determined by HPLC-ELSD in triplicate. The methodology validation of HPLC-ELSD can be found in S1. The content of sucralose in the samples exposed at 90°C was calculated according to the following formula.

$$\text{Sucralose content (\%)} = \frac{\text{Content of sucralose after heating}}{\text{Content of sucralose before heating}} \times 100 \quad (2)$$

Molecular Docking of Sucralose and CD-MOFs

Crystal structures of basic CD-MOFs were extracted from the reported single crystal structure of CD-MOFs (20). In the docking, an expanded non-periodic structure of CD-MOFs was used, in which the K^+ ion was deleted and the OH^- ion was replaced by H_2O. The structure of sucralose molecule was built in Materials Studio 5.0 (MS, Accelrys Inc.). The Forcite module in MS was employed for minimization and molecular dynamics (MD) simulation. The docking program AutoDock Vina 1.1.2 was used to perform the automated molecular docking calculation (28). Details were described in S6.

RESULTS AND DISCUSSION

Synthesis and Characterization of CD-MOFs

Basic CD-MOFs crystals with micron and nanometer sizes were obtained by reacting γ-CD with 8.0 equivalents of KOH in aqueous solutions, followed by vapor diffusion of MeOH into the solution at ambient temperature (29). However, this method required more than 24 h for the reaction to be completed.

Therefore, in this study, a hydrothermal method was set up to reduce the reaction time to only 6 h, by using a higher temperature (50°C). Basic CD-MOFs with micron sizes (5–10 μm, CD-MOF-Micro) and nanometer sizes (200–500 nm, CD-MOF-Nano) were successfully synthesized. They were cubic crystals with smooth surfaces and uniform sizes (Fig. 1). The PXRD patterns of basic CD-MOF-Micro and CD-MOF-Nano were consistent with the previously reported ones (29). The SEM images showed that the neutralized CD-MOFs and basic CD-MOFs shared similar cubic structures, but a small fraction of CD-MOFs disintegrated into fine particles after neutralization. In contrast, basic CD-MOFs and neutralized CD-MOFs had very similar PXRD patterns, which showed that the crystallinity of basic CD-MOFs was unaffected by neutralization with glacial acetic acid. The N_2 adsorption-desorption isotherms were measured on activated basic CD-MOFs and neutralized CD-MOFs (Fig. 2). The typical isotherms exhibited steep N_2 uptake in the low-pressure areas, hence validating the micro-porosity of these materials. The BET (Langmuir) surface areas of basic CD-MOF-Micro and CD-MOF-Nano were 786 and 668 $m^2 \cdot g^{-1}$, respectively. The surface areas of neutralized CD-MOF-Micro and neutralized CD-MOF-Nano were 745 and 543 $m^2 \cdot g^{-1}$, respectively. The slight decreases in surface areas after neutralization could be attributed to possible local structure collapses or to the adsorption of acetic acid molecules in the cavities of the γ-CD-MOFs, leading to a partial pore filling and thus eventually to a decrease of the surface area.

In conclusion, there were no significant differences in terms of structure, crystallinity and porosity between basic CD-MOFs and neutralized ones.

Characterization of Sucralose Loaded CD-MOFs

The encapsulation of sucralose (molecular size of about 10.2 × 7.1 Å) into CD-MOFs was carried out by impregnation. Indeed, the dimensions of the windows (7.8 Å) of γ-CD and the internal pores (17 Å) in CD-MOFs are compatible with the molecular dimensions of sucralose molecules. After sucralose loading, the particles maintained their cubic structure and did not collapse (Fig. 3). Maximal payloads were obtained after 20 h incubation in sucralose solutions. The basic CD-MOF-Micro could maximally adsorb around 17.5 ± 0.9% (w/w) sucralose, whereas basic CD-MOF-Nano could adsorb 27.9 ± 1.4% (w/w) sucralose in the same experimental conditions. Noteworthy, maximal SL was obtained when increasing the molar ratio of γ-CD in basic CD-MOFs to sucralose to 1:7 in the incubation experiments (Fig. 4).

However, the PXRD patterns of sucralose-loaded basic or neutralized CD-MOFs showed the disappearance of the

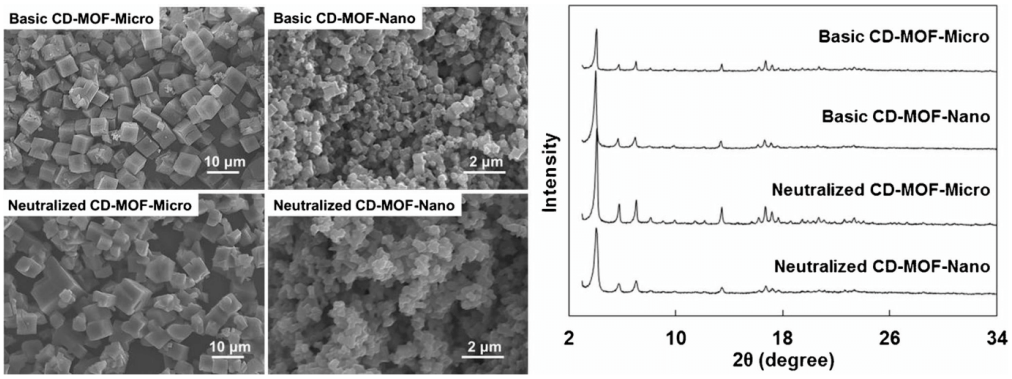

Fig. 1 SEM images and PXRD patterns of basic CD-MOFs and neutralized CD-MOFs.

characteristic peaks at 5.7° and 7.0° together with significant decrease of the intensity of the peaks at 16.7° (Fig. 5). This is an indication of the leakage of γ-CD from basic and neutralized CD-MOFs in EtOH. FT-IR investigations support this hypothesis. The characteristic wide band at 2926 cm^{-1} assigned to -CH- (ν_{CH}) vibrations in CD-MOFs was significantly reduced after impregnation (Fig. 6). In the solid state, sucralose presents a strong band at 891 cm^{-1} assigned to the vibration of O-C-C bonds (30). Interestingly, the intensity of this band strongly decreased when sucralose was incorporated inside CD-MOF-Nano, as compared to free sucralose and to a physical mixture of sucralose and basic CD-MOF-Nano (Fig. 6). This is an indication that sucralose was loaded in a molecular state strongly interacting with the CD-MOFs.

The adsorption of sucralose led to a significant decrease in N_2 uptake (Fig. 2), which was a further proof of the interaction taking place between sucralose and the CD-MOFs, with sucralose occupying the empty interconnected pores. There was almost no residual porosity in the basic CD-MOF-Micro and basic CD-MOF-Nano samples after the inclusion of sucralose

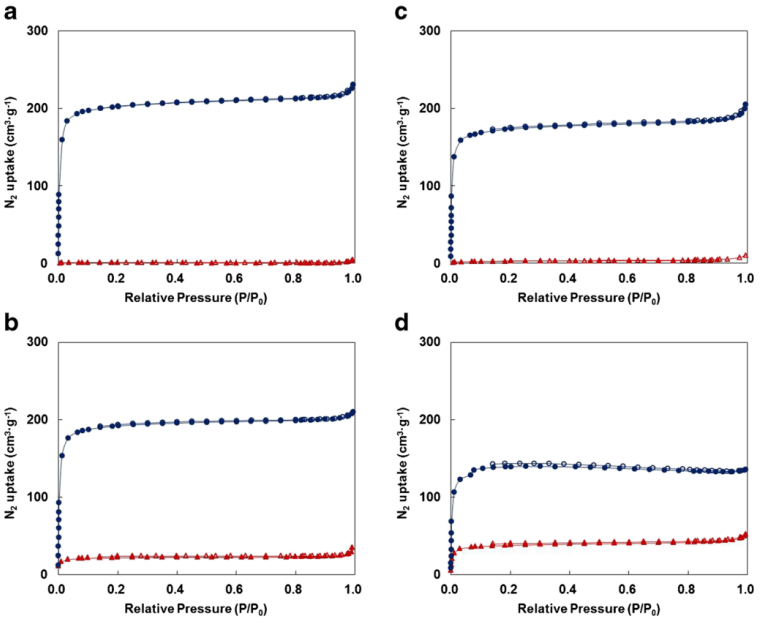

Fig. 2 N_2 adsorption isotherms of CD-MOFs (blue circles: filled adsorption, empty desorption) and sucralose loaded CD-MOFs (red triangles: filled adsorption, empty desorption) for basic CD-MOF-Micro (**a**), neutralized CD-MOF-Micro (**b**), basic CD-MOF-Nano (**c**) and neutralized CD-MOF-Nano (**d**), where sucralose loaded CD-MOFs were obtained by impregnation (molar ratio of constitutive γ-CD in CD-MOFs to sucralose was 1:7 in the initial impregnation system).

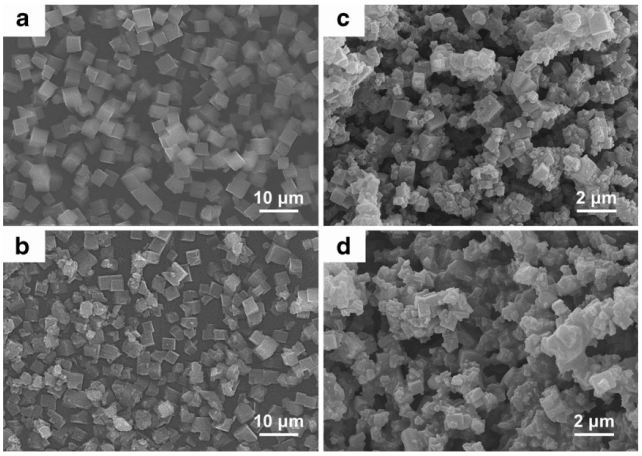

Fig. 3 SEM images of sucralose loaded basic CD-MOF-Micro (**a**), sucralose loaded neutralized CD-MOF-Micro (**b**), sucralose loaded basic CD-MOF-Nano (**c**) and sucralose loaded neutralized CD-MOF-Nano (**d**).

molecules in their pores. For neutralized CD-MOF-Micro and neutralized CD-MOF-Nano, the decrease in BET surface areas was 88.6% and 77.3%, respectively.

Thermal Analysis

The thermal behaviors of sucralose, neutralized CD-MOF-Nano and sucralose loaded neutralized CD-MOF-Nano were studied by TGA and DSC (Fig. 7). Free sucralose typically presents a significant weight loss starting at 123°C. The inclusion complexes with γ-CDs allowed to shift the sucralose decomposition to higher temperatures (173°C) as compared to free drug. This clearly indicates a stabilization of the drug by γ-CDs. More interestingly, when sucralose was loaded in neutralized CD-MOF-Nano, decomposition started at 205°C.

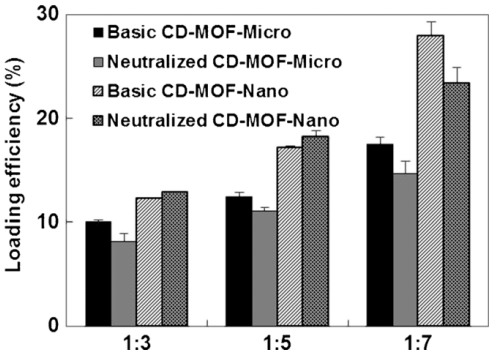

Fig. 4 Loading efficiency of sucralose in basic or neutralized CD-MOFs in sized of micron or nanometers, where the molar ratio of γ-CD in CD-MOFs to sucralose were 1:3, 1:5 and 1:7 in the initial impregnation system

These results were consistent with DSC investigations (Fig. 7b). Sucralose presents an endothermic peak at 124°C in agreement with previously reported data (31). This transition corresponds to sucralose fusion followed by its decomposition, releasing water and hydrogen chloride. This peak completely disappeared when sucralose was incorporated in neutralized CD-MOF-Nano. In this case, the drug was stable up to 200°C. Only the oxidative degradation of γ-CD led to the decomposition of the framework from 200 to 400°C. However, an endothermic peak was detected at 212°C in the case of sucralose-loaded neutralized CD-MOF-Nano, which clearly indicated that decomposition of sucralose was delayed of about 88°C as compared to the free form. In contrast, only about 49°C delay in sucralose decomposition was observed in the case of sucralose inclusion complexes with γ-CD. As control samples, the physical mixture of sucralose with neutralized CD-MOF-Nano and γ-CD were also analyzed under identical conditions, but no delay in decomposition temperature of sucralose was observed (Figure S2). This clearly shows that sucralose needs to be incorporated inside a device to protect it from decomposition.

In conclusion, neutralized CD-MOFs were the most effective systems to stabilize sucralose against degradation upon heating.

Thermal Stability Measured by HPLC-ELSD

The thermal stabilities of free sucralose and sucralose in basic or neutralized CD-MOFs were investigated at 90°C, for which discoloration of sucralose could be observed after only 10 min. Remarkably, after being loaded in the CD-MOFs,

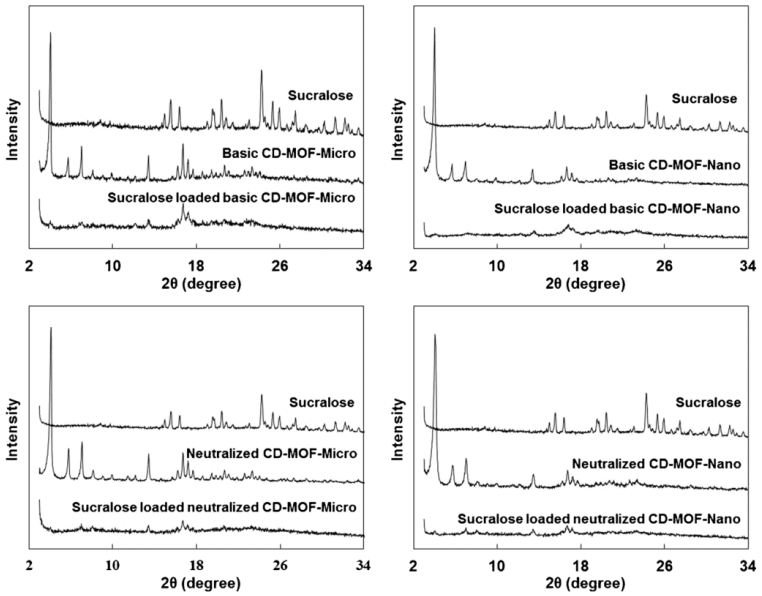

Fig. 5 PXRD patterns of sucralose, basic or neutralized CD-MOFs and sucralose loaded basic or neutralized CD-MOFs.

there were no obvious color changes for all samples of sucralose loaded basic or neutralized CD-MOFs, even after 8 h exposure at 90°C (Table S1). Decomposition of sucralose during the heating process was quantitatively analyzed by HPLC-ELSD. A fast degradation was observed at 90°C, with 86.2 ± 0.2% of sucralose degraded within 1 h. However, sucralose loaded in CD-MOFs was significantly more stable in comparison with free sucralose (Fig. 8). SL dependent degradations were observed for sucralose loaded basic or neutralized CD-MOFs. Sucralose-loaded basic CD-MOFs with SL of 27.9 ± 1.4% degraded much slower than free sucralose. However, still 39.9 ± 4.4% of sucralose decomposed within 1 h. Then, degradation was slower with 52.7 ± 3.1% of sucralose losing its integrity within 24 h. As a control, the thermal stabilities of the physical mixtures of sucralose and basic or neutralized CD-MOFs were also investigated. As expected, no delay of degradation was observed. The different degradation profiles may be ascribed to the existence of two states of sucralose in CD-MOFs, namely, (i) sucralose adsorbed on the surface of CD-MOFs and (ii) sucralose molecules included in the cavities of CD-MOFs. In the latter case, CD-MOFs play a role as drug delivery systems possibly protecting sucralose against degradation at elevated temperatures. Since there was no sucralose-carrier interaction in the physical mixtures, no delay in degradation or protection was recorded.

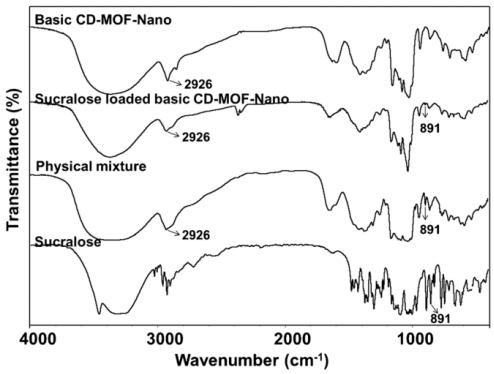

Fig. 6 FT-IR spectra of sucralose, basic CD-MOF-Nano, sucralose loaded basic CD-MOF-Nano and the physical mixture of sucralose with basic CD-MOF-Nano.

It was very interesting to note that the neutralized form of CD-MOFs was much effective for the stability improvement compared to the ones without neutralization. As shown in Fig. 8b and d, there were only 26.7 ± 0.5% and 13.7 ± 0.7% of sucralose degraded under 90°C within 24 h from sucralose loaded neutralized CD-MOF-Micro (SL, 14.7 ± 1.2%) and neutralized CD-MOF-Nano (SL, 23.4 ± 1.6%), respectively. Sucralose is a weak acid with a pK_a value of 12.52 ± 0.70 and can be easily hydrolyzed in alkaline environment. This could explain its fast degradation in basic CD-MOFs and its protection inside neutralized CD-MOFs.

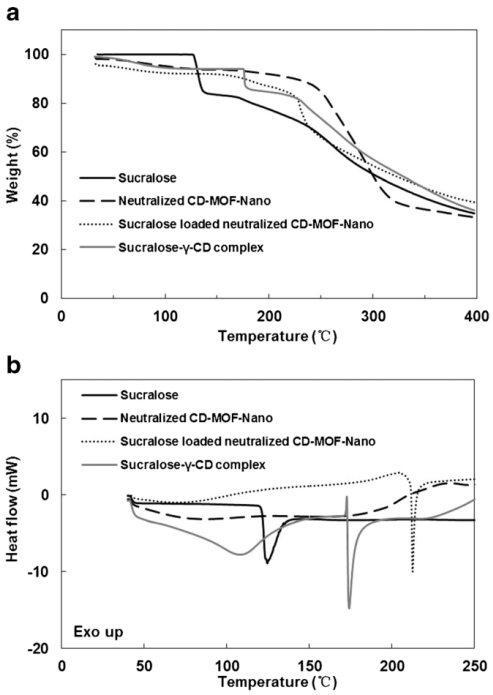

Fig. 7 TGA and DSC characteristics (A and B, respectively) of sucralose, neutralized CD-MOF-Nano, sucralose loaded neutralized CD-MOF-Nano and sucralose-γ-CD inclusion complex.

Molecular Docking of Sucralose and CD-MOFs

From a thermodynamic point of view, the stable conformations have the lowest free energy. Therefore, docking with relatively low energy was used for energy optimization and molecular dynamics (MD). Molecular docking results showed that sucralose molecule preferentially located in the cavities formed by γ-CD pairs inside basic CD-MOFs (docking free energy of −7.1 kcal·mol^{-1}) than in the hydrophilic chamber surrounded by γ-CDs in CD-MOFs (Fig. 9). The detailed molecular docking results were described in S6.

Presumably, the highly porous CD-MOFs crystals provide a confined microenvironment for sucralose, offering numerous interactions with this drug. The resulting stabilizing effect delayed sucralose decomposition and significantly improved its thermal stability at elevated temperatures. The high efficacy of CD-MOFs to improve the thermal stability of sucralose is derived mainly from the special architectures of these particles, allowing to confine sucralose and offering numerous steric hindrances. It has been shown previously that the confinement of sucralose in γ-CDs, when forming inclusion complexes, protects this compound from oxidation. Noticeably, the crystalline CD-MOFs studied here allowed even a higher protection. The simulation result in Fig. 9 showed that the sucralose mainly located in the cavities of γ-CD pairs. These cavities of γ-CD pairs are also the channels for the destructive molecules (such as oxygen gas) into the CD-MOFs. The special complex structure of CD-MOFs could impede the entry of the oxidizing molecules.

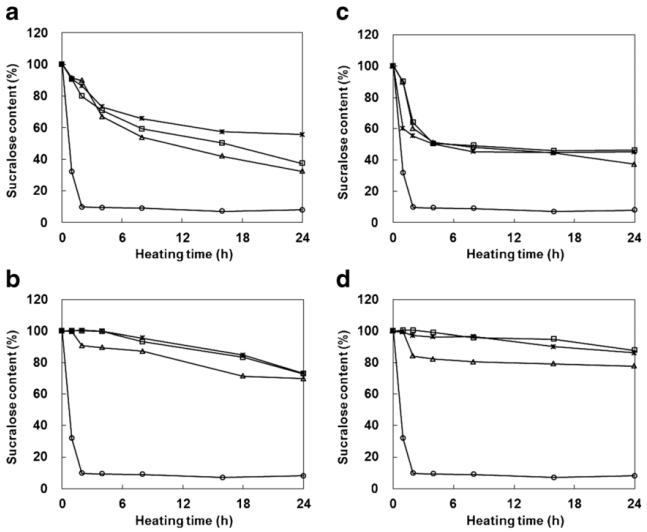

Fig. 8 Sucralose content profiles during stability test at 90°C of sucralose (○), sucralose loaded basic CD-MOF-Micro (**a**), sucralose loaded neutralized CD-MOF-Micro (**b**), sucralose loaded basic CD-MOF-Nano (**c**), and sucralose loaded neutralized CD-MOF-Nano (**d**), in which samples were prepared by incubating CD-MOFs with different concentration of sucralose, wherein the molar ratio of carriers to sucralose were 1:3 (Δ), 1:5 (□) and 1:7 (▯) in the impregnation system.

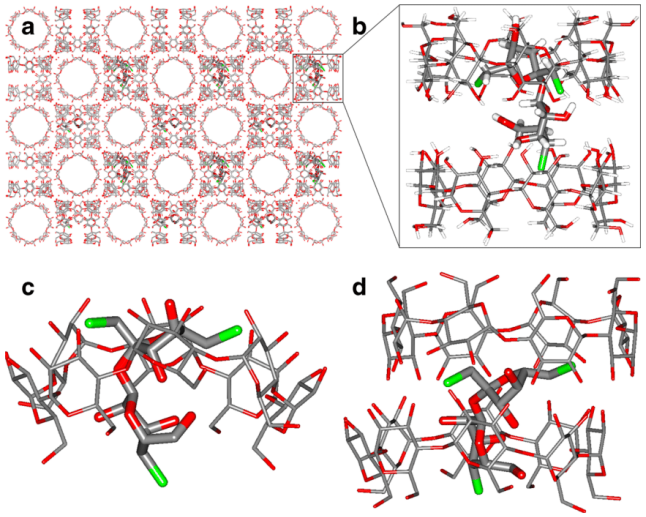

Fig. 9 The molecular model after docking and optimization of sucralose with CD-MOFs in sucralose loaded CD-MOFs (a and b), in comparison with sucralose in complex one molecule of γ-CD or two molecules of γ-CD in aqueous solution (c and d, respectively).

CONCLUSIONS

Micron and nanometer sized basic CD-MOFs were successfully synthesized by a modified hydrothermal method, exhibiting good purity and high production yield. Neutralized CD-MOFs were obtained by treating basic CD-MOFs with glacial acetic acid. Sucralose was successfully loaded in basic or neutralized CD-MOFs by impregnation and showed significant improvement in thermal stability at elevated temperatures. Neutralized CD-MOFs were more effective than basic CD-MOFs to protect sucralose, possibly because of the fast hydrolyzation of sucralose in alkaline environment. Molecular docking showed that sucralose molecules preferentially locate in the cavities of γ-CDs inside CD-MOFs. Presumably, the highly porous CD-MOFs crystals provide a confined microenvironment for sucralose, offering numerous interactions with this drug. The resulting stabilizing effect delayed sucralose decomposition and significantly improved its thermal stability at elevated temperatures. Industrial uses of sucralose face problems related to sucralose oxidation and corrosive effects upon heating. In this study, biodegradable CD-MOFs were shown to decrease the amounts of toxic side products of sucralose, which potentially opens a field of applications in food industry. Besides, it would be of great interest to further investigate the potential application of CD-MOFs for loading and improving thermal stability of other unstable compounds.

ACKNOWLEDGMENTS AND DISCLOSURES

The authors are grateful for the financial support from the National Natural Science Foundation of China (No. 81430087) and National Science and Technology Major Project (2013ZX09402103).

REFERENCES

1. Horcajada P, Gref R, Baati T, Allan PK, Maurin G, Couvreur P, *et al.* Metal-organic frameworks in biomedicine. Chem Rev. 2012;112(2):1232–68.
2. Lin WB. Nanoscale metal-organic frameworks for biomedical imaging and drug delivery. Abstr Papers Am Chem Soc. 2014;248.
3. Sun CY, Qin C, Wang XL, Su ZM. Metal-organic frameworks as potential drug delivery systems. Expert Opin Drug Deliv. 2013;10(1):89–101.
4. Horcajada P, Serre C, Vallet-Regi M, Sebban M, Taulelle F, Ferey G. Metal-organic frameworks as efficient materials for drug delivery. Angew Chem Int Ed. 2006;45(36):5974–8.
5. Horcajada P, Chalati T, Serre C, Gillet B, Sebrie C, Baati T, *et al.* Porous metal-organic-framework nanoscale carriers as a potential platform for drug delivery and imaging. Nat Mater. 2010;9(2):172–8.
6. Chalati T, Horcajada P, Couvreur P, Serre C, Ben Yahia M, Maurin G, *et al.* Porous metal organic framework nanoparticles to address the challenges related to busulfan encapsulation. Nanomedicine. 2011;6(10):1683–95.
7. Kundu T, Mitra S, Patra P, Goswami A, Diaz DD, Banerjee R. Mechanical downsizing of a gadolinium(III)-based metal-organic framework for anticancer drug delivery. Chem Eur J. 2014;20(33):10514–8.
8. Sun CY, Qin C, Wang CG, Su ZM, Wang S, Wang XL, *et al.* Chiral nanoporous metal-organic frameworks with high porosity as materials for drug delivery. Adv Mater. 2011;23(47):5629.
9. Ananthoji R, Eubank JF, Nouar F, Mouttaki H, Eddaoudi M, Harmon JP. Symbiosis of zeolite-like metal-organic frameworks

(rho-ZMOF) and hydrogels: composites for controlled drug release. J Mater Chem. 2011;21(26):9587–94.
10. Taylor-Pashow KML, Della Rocca J, Xie ZG, Tran S, Lin WB. Postsynthetic modifications of iron-carboxylate nanoscale metal-organic frameworks for imaging and drug delivery. J Am Chem Soc. 2009;131(40):14261.
11. Smaldone RA, Forgan RS, Furukawa H, Gassensmith JJ, Slawin AMZ, Yaghi OM, *et al.* Metal-organic frameworks from edible natural products. Angew Chemie Int Ed. 2010;49(46):8630–4.
12. Su H, Sun F, Jia J, He H, Wang A, Zhu G. A highly porous medical metal-organic framework constructed from bioactive curcumin. Chem Commun. 2015;51(26):5774–7.
13. Sontz PA, Bailey JB, Ahn S, Tezcan FA. A metal organic framework with spherical protein nodes: rational chemical design of 3D protein crystals. J Am Chem Soc. 2015;137(36):11598–601.
14. Yin F, Chen J, Liang Y, Zou Y, Yinzhi J, Xie J. Syntheses, structures, and properties of Co(II)/Zn(II) mixed-ligand coordination polymers based on 4-[(3,5-dinitrobenzoyl)amino]benzoic acid and 1,4-bis(1-imidazolyl) benzene. J Solid State Chem. 2015;225:310–4.
15. Agostoni V, Horcajada P, Noiray M, Malanga M, Aykaç A, Jicsinszky L, *et al.* A "green" strategy to construct non-covalent, stable and bioactive coatings on porous MOF nanoparticles. Sci Rep. 2014;5:7925.
16. Han SB, Wei YH, Valente C, Forgan RS, Gassensmith JJ, Smaldone RA, *et al.* Imprinting chemical and responsive micropatterns into metal-organic frameworks. Angew Chemie Int Ed. 2011;50(1):276–9.
17. Gassensmith JJ, Kim JY, Holcroft JM, Farha OK, Stoddart JF, Hupp JT, *et al.* A metal-organic framework-based material for electrochemical sensing of carbon dioxide. J Am Chem Soc. 2014;136(23):8277–82.
18. Yoon SM, Warren SC, Grzybowski BA. Storage of electrical information in metal-organic-framework memristors**. Angew Chemie Int Ed. 2014;53(17):4437–41.
19. Gassensmith JJ, Furukawa H, Smaldone RA, Forgan RS, Botros YY, Yaghi OM, *et al.* Strong and reversible binding of carbon dioxide in a green metal-organic framework. J Am Chem Soc. 2011;133(39):15312–5.
20. Forgan RS, Smaldone RA, Gassensmith JJ, Furukawa H, Cordes DB, Li QW, *et al.* Nanoporous carbohydrate metal-organic frameworks. J Am Chem Soc. 2012;134(1):406–17.
21. Moussa Z, Hmadeh M, Abiad MG, Dib OH, Patra D. Encapsulation of curcumin in cyclodextrin-metal organic frameworks: dissociation of loaded CD-MOFs enhances stability of curcumin. Food Chem. 2016;212:485–94.
22. Sharma VK, Oturan M, Kim H. Oxidation of artificial sweetener sucralose by advanced oxidation processes: a review. Environ Sci Pollut Res. 2014;21(14):8525–33.
23. Rocha-Selmi GA, Theodoro AC, Thomazini M, Bolini HMA, Favaro-Trindade CS. Double emulsion stage prior to complex coacervation process for microencapsulation of sweetener sucralose. J Food Eng. 2013;119(1):28–32.
24. Quinlan ME, Jenner MR. Analysis and stability of the sweetener sucralose in beverages. J Food Sci. 1990;55(1):244–6.
25. de Oliveira DN, De MM, Catharino RR. Thermal degradation of sucralose: a combination of analytical methods to determine stability and chlorinated byproducts. Scientific Reports. 2015;5.
26. Cherukuri SR, Wong LL. Stabilized sucralose complex. In.: US; 1990.
27. Alai MS, Lin WJ. A novel nanoparticulate system for sustained delivery of acid-labile lansoprazole. Colloids Surf B: Biointerfaces. 2013;111:453–9.
28. Trott O, Olson AJ. Trott, O and Olson, AJ. AutoDock Vina: improving the speed and accuracy of docking with a new scoring function, efficient optimization, and multithreading. J Comput Chem. 2009;31(2):455–61.
29. Furukawa Y, Ishiwata T, Sugikawa K, Kokado K, Sada K. Nano- and microsized cubic Gel particles from cyclodextrin metal-organic frameworks. Angew Chemie Int Ed. 2012;51(42):10566–9.
30. Beatriz Brizuela A, Beatriz Raschi A, Victoria Castillo M, Leyton P, Romano E, Antonia BS. Theoretical structural and vibrational properties of the artificial sweetener sucralose. Comput Theor Chem. 2013;1008:52–60.
31. Oliveira DND, Menezes MD, Catharino RR. Thermal degradation of sucralose: a combination of analytical methods to determine stability and chlorinated byproducts. Scientific Reports. 2015;5.

Supporting Information

Improvement in thermal stability of sucralose by γ-cyclodextrin metal-organic frameworks

Authors:

Nana Lv[1,2,#], Tao Guo[2,#], Botao Liu[2,3,#], Caifen Wang[2,#], Vikaramjeet Singh[2], Xiaonan Xu[1,2], Xue Li[1,4], Dawei Chen[1,*], Ruxandra Gref[4,*], Jiwen Zhang[1,2*]

Affiliations:

[1] School of Pharmacy, Shenyang Pharmaceutical University, Shenyang 110016, China;

[2] Center for Drug Delivery System, Shanghai Institute of Materia Medica, Chinese Academy of Sciences, Shanghai 201210, China;

[3] School of Chemical and Environmental Engineering, Shanghai Institute of Technology, Shanghai 201418, China;

[4] Institute of Moléculaires Sciences d'Orsay, UMR CNRS 8214, Université Paris Sud,Université Paris-Saclay, 91400 Orsay, France.

[#] The authors contribute equally. N.L. for loading, measurement other than HPLC and preparation of manuscript; T.G. for molecular simulation; B.L. for CD-MOFs preparation; C.W. for HPLC method establishment and validation.

Corresponding Authors:

Prof. Jiwen Zhang

Center for Drug Delivery Systems, Shanghai Institute of Materia Medica, Chinese Academy of Sciences, No. 501 of Haike Road, Shanghai 201210, China; Tel: +86-21-20231980; E-mail: jwzhang@simm.ac.cn.

Prof. Ruxandra Gref

Institut Sciences Moléculaires Sciences d'Orsay, (UMR CNRS 8214), Universite´ Paris-Sud, Université Paris-Saclay, 91400 Orsay, France; Tel: +33 (1)69158234; E-mail: ruxandra.gref@u-psud.fr.

Prof. Dawei Chen

School of Pharmacy, Shenyang Pharmaceutical University, Shenyang 110016, China; Tel: +86-24-23986306; E-mail: chendawei@syphu.edu.cn.

S1. Determination of the sucralose by HPLC-ELSD

The amount of sucralose was determined by high performance liquid chromatography with evaporative light-scattering detection (HPLC-ELSD). Analysis was carried out with the Phenomenex C18 column (4.6 mm×150 mm, 5 μm i.d.), under the flow rate of 1.0 $mL \cdot min^{-1}$, the injection volume of 20 μL, and the column temperature of 35°C. The mobile phase was composed of acetonitrile and water (20:80, v/v). Sucralose were detected with an evaporative light-scattering detector, the temperature of drift tube was set as 70°C, the pressure of carrier gas (high purity nitrogen) was 3.3 bar and the gain was 6.

The results showed that reasonable linearity was achieved for all of the analytes over the range of 50-1000 $\mu g \bullet mL^{-1}$ with the correlation coefficients (R) greater than 0.998. The precision for sucralose were 5.39% and the recoveries of sucralose ranged from 94.6 to 101.8% at three spiked concentrations with the relative standard deviations (RSDs) lower than 4.9%. This method was fast, simple, sensitive and low cost, and has been successfully used to determine sucralose in our study. Sucralose and γ-CD released in the water solution while sucralose loaded CD-MOFs were dissolved, and they were completely separated using the HPLC-ELSD described above (Figure S1).

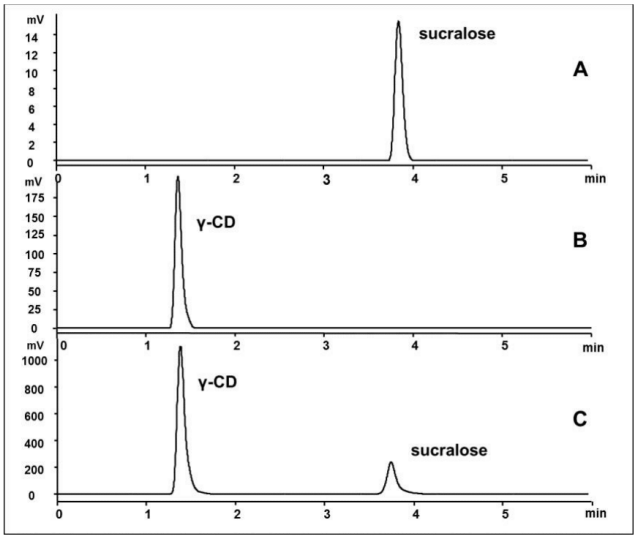

Figure S1. HPLC chromatograms of sucralose (A), γ-CD (B) and sucralose loaded CD-MOFs (C).

S2. Preparation of sucralose-γ-CD inclusion complex

Sucralose of 397 mg was dissolved in 15 mL of ethanol and then added to the stirred γ-CD aqueous solution (γ-CD of 1297 mg dissolved in pure water) drop by drop, with the temperature being maintained at 40 °C, wherein the molar ratio of sucralose to γ-CD was 1.0. The drug solution was then stirred continuously for 4 h. Ethanol in the resulting clear solution was removed by rotary evaporation at 45 °C for 1 h, the remaining liquid was pre-frozen under -80 °C for 4 h and then lyophilized to obtain sucralose-γ-CD inclusion complex. The loading efficiency of sucralose in S-CD was21.8±1.3 %.

S3. DSC curves of physical mixtures

Differential scanning calorimetry (DSC) was detected for physical mixtures of sucralose and neutralized CD-MOF-Nano or γ-CD, in which the sucralose content were the same as that for sucralose loaded neutralized CD-MOF-Nano or

sucralose-γ-CD inclusion complex. The decomposition temperature for sucralose in physical mixtures was observed around 124°C, no delay of decomposition temperature was detected (Figure S2).

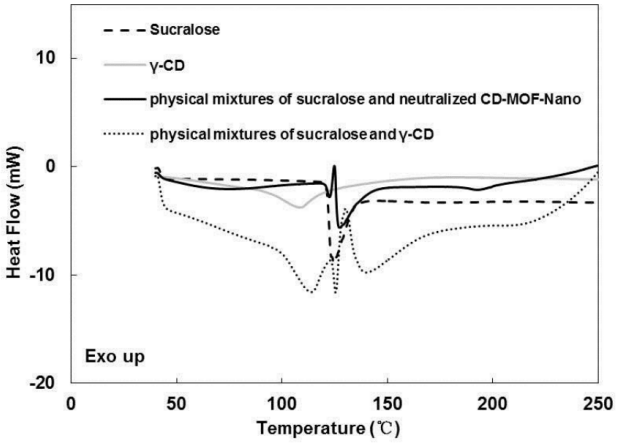

Figure S2. DSC curves of sucralose, γ-CD and physical mixtures of sucralose with neutralized CD-MOF-Nano or γ-CD.

Table S1. Color changes of sucralose, CD-MOFs and sucralose loaded CD-MOFs when exposed at 90°C for different time

Sample/Time	0 min	10 min	8 h
Sucralose	White	Dark brown	Dark brown
CD-MOFs	White	White	Light yellow
Sucralose loaded CD-MOFs	White	White	Light yellow

S4. Release of sucralose from sucralose loaded neutralized CD-MOF-Nano in ethanol

Sucralose loaded neutralized CD-MOF-Nano (wash or without wash) equivalent to 1 mg of sucralose were suspended in 5 mL of ethanol and maintained at 25 °C with

a shaking rate of 100 rpm. Samples of 200 μL were withdrawn at predefined time intervals (0, 0.1, 0.2, 0.3, 0.5, 1, 2, 4, 6, 20 and 24 h) and the same volume of fresh EtOH was added. The concentration of sucralose in each sample was determined by HPLC-ELSD method described in section 2.5.4 and cumulative release percentage was calculated. Experiments were performed in triplicate.

For sucralose loaded neutralized CD-MOF-Nano without wash, about 65% of sucralose released within 1 h, for sucralose loaded neutralized CD-MOF-Nano washed with ethanol, only 30% of sucralose released under the same condition. The release kinetics of sucralose loaded neutralized CD-MOF-Nano (wash or without wash) satisfied the pseudo-second order model. Pseudo-second order kinetic equation(1) is as follows:

$$\frac{t}{q_t} = \frac{1}{k_2 q_e^{\ 2}} + \frac{1}{q_e} t$$

Wherein, t represents time, q_t represents the release amount at time t, qe represents equilibrium release amount, k_2 represents kinetic constant of pseudo-second order release.

The linear fitting equation and kinetic constant for sucralose loaded neutralized CD-MOF-Nano without wash and the samples washed with ethanol were t/q_t = 0.0014t + 0.0001 (R^2 = 0.9989), k_2 = 0.0196 and t/q_t = 0.0022t + 0.0007 (R^2 = 0.996), k_2 = 0.0069, respectively. The fast release of the sucralose from sucralose loaded neutralized CD-MOF-Nano without wash might be due to the large fraction of sucralose adsorption on the surface of CD-MOFs. However, for sucralose loaded neutralized CD-MOF-Nano washed with ethanol, the majority of sucralose located in

the interior of CD-MOFs, which may account for its relatively slow release in ethanol.

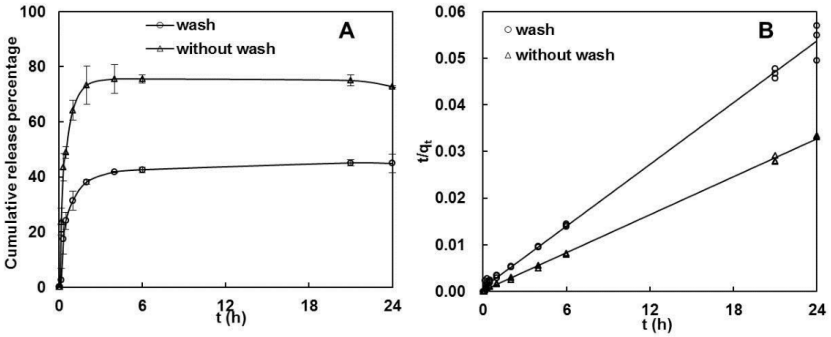

Figure S3. Cumulative release curves (A) of sucralose loaded neutralized CD-MOF-Nano (wash, without wash) in EtOH, and pseudo-second order kinetic fitting of the release parameters (B).

S5. Solid-state nuclear magnetic resonance (SSNMR)

Solid-state ^{13}C cross-polarization/magic angle spinning (CP/MAS) spectra were collected on Agilent 600 MHz DD2 solid system, equipped with a 3.2 mm double-resonance MAS probe. The Hartmann-Hahn conditions of the CP experiment for acquiring ^{13}C spectra were optimized by using adamantane. ^{13}C NMR spectra were obtained at 6 kHz MAS spinning speed with a contact time of 1.0 ms. Recycle delay time for sucralose and γ-CD are 2 and 120 s, respectively. The ^{13}C chemical shifts were externally referenced to tetramethylsilane (δ = 0.0 ppm).

No signal of sucralose was observed in sucralose loaded neutralized CD-MOF-Nano wash (surface located sucralose were removed, sucralose weight content was 4.6%) and the NMR spectra of which was almost similar to the neutralized CD-MOF-Nano (Figure S4). Whereas, the chemical shift of sucralose at chemical shifts (δ) of 93.3 was detected in physical mixture sample, wherein the

weight content was also 4.6% (same as loaded one). The NMR spectra of sucralose loaded neutralized CD-MOF-Nano without wash was similar to that of neutralized CD-MOF-Nano, however, the characteristic chemical shifts (δ) of sucralose at 91.4 ppm and 43.6 ppm were detected in loaded neutralized CD-MOF-Nano without wash.

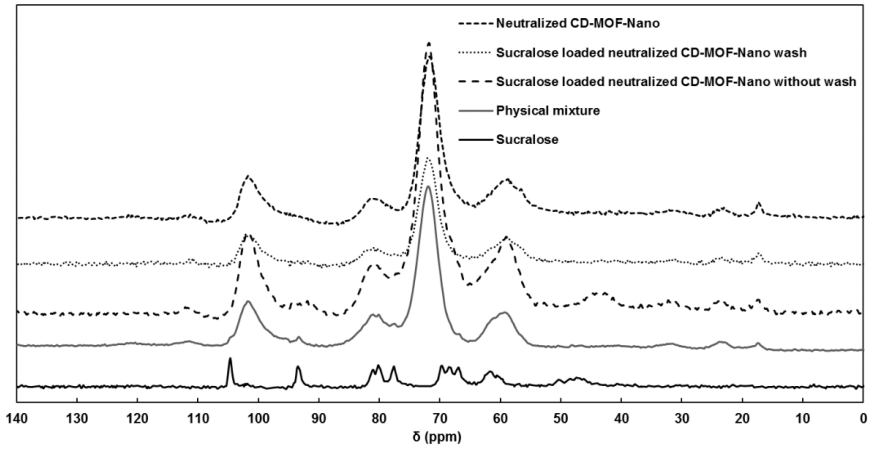

Figure S4. ^{13}C MAS NMR spectra of sucralose, neutralized CD-MOF-Nano, sucralose loaded CD-MOF-Nano with wash, sucralose loaded neutralized CD-MOF-Nano without wash and physical mixture of sucralose with neutralized CD-MOF-Nano.

S6. Molecular docking of sucralose and CD-MOFs

Docking protocol was executed to the prepared sucralose model and CD-MOFs model. Then the docking with relatively low energy was used for energy optimization and molecular dynamics (MD), in which CD-MOFs model was fixed and all models were put in vacuum. In the MD protocol, the COMPASSII force field was adopted, and the NVT ensemble and the Berendsen temperature control method was employed for a total time of 50 ps. The nonbond cut-off distance of 18.5 Å, spline width of 1.0

Å and buffer width of 0.5 Å were used. In the task of minimization, a smart algorithm was employed with the total energy of the system converged to less than 2.0×10^{-5} kcal·mol^{-1}, the residual force to less than 0.001 kcal·mol^{-1}·Å^{-1}, the displacement of atoms to less than 1×10^{-5} Å. In the Vina, a Lamarckian genetic algorithm (LGA) in combination with a grid-based energy evaluation method were used for pre-calculating grid maps according to the interatomic potentials of all atom types present in the host and guest molecules, including the Lennard-Jones potentials for van der Waals interactions and Coulomb potentials for electrostatic interactions. A grid map of dimensions 70×70×70 Å, with a grid spacing of 0.375 Å, was placed to cover the CD-MOFs structure. With the help of AutoDockTools(2), the atomic partial charges were calculated by the Gasteiger–Marsili method(3). The parameters used for the global search were an initial population of 50 individuals, with a maximal number of energy evaluations of 1,500,000 and a maximal number of generations of 50,000 as an end criterion and other docking parameters were set as default.

For the docking of sucralose to one mole of γ-CD, the sucralose molecule was almost entirely included in γ-CD (docking free energy of -5.3 kcal·mol^{-1}), based on which, the second CD was docked (docking energy of -5.9 kcal·mol^{-1}) in the same pattern as that for sucralose in CD-MOFs. However, the distance between two γ-CDs were closer than that in CD-MOFs due to the stagger of γ-CDs in aqueous solution. The sucralose molecule still stayed in the first γ-CD, and hardly entered the second γ-CD, the docking interaction mainly derived from the electrostatic effect between the hydroxyls in γ-CDs. It can be estimated that sucralose was generally included in one

γ-CD in diluted solution, and more γ-CDs would be required for sucralose to be enclosed by two γ-CDs.

References

1. Ho YS, McKay G. Pseudo-second order model for sorption processes. Process Biochemistry. 1999;34(5):451-465.
2. Institutions OOS, Jolla L. The Scripps Research Institute. Molecular Medicine. 1997;3(12):1359.
3. Belik AV, Potyomkin VA, Krasil'Nikov VB. Conmutación a cero voltaje y cero corriente de un convertidor AC-DC trifásico que utiliza una sola etapa controlada de procesamiento de potencia. Revista Técnica De La Facultad De Ingeniería Universidad Del Zulia. 2007;30(2):190-198.

Title : "Cage" nano and micro-particles for biomedical applications

Keywords : “cage” particles; drug carrier; degradation; antibiotic

Abstract : Drug delivery systems are engineered technologies to administer pharmaceutical ingredients to improve their therapeutic effects, aiming at minimizing their side effects by means of targeted delivery and/or controlled release. “Cage” particles recently drew special attention since they could act as “drug containers” which potentially load large amount of drugs, improve their stability and offer the possibilities to co-encapsulate synergetic drugs.

Cyclodextrins (CDs) are typical “cage” molecules with a hydrophobic cavity and a hydrophilic outer surface. Taking advantage of the host-guest interactions between β-CD and benzophenone (Bz), CD based nanoparticles (CD-NPs) were the first formulation investigated. CD-NPs of around 100 nm were instantaneously produced by mixing two aqueous solutions of neutral polymers : 1) poly-CD containing β-CDs, and 2) Bz grafted Dex (Dex-Bz). The “green” and facile preparation procedure makes it attractive formulation, whereas its limitation lies on the low drug payloads (~ 5 wt%).

In order to improve the drug loading capacity of CDs, porous CD based metal orgainc frameworks (CD-MOFs) were synthesiezed, which contain not only CD cavities, but also large pores built up by CDs self-assembly. Lansoprazole (LPZ) was incorporated in CD-MOF microcrystals (~ 6 µm) reaching payloads as high as 23.2 ± 2.1% (wt). Remarkably, each CD cavity was able to host a drug molecule, offering new opportunities for the use of CD-MOFs for drug delivery purposes. However, these particles disassembled in aqueous media, which limits their application for oral and intravenous administration.

Surface modification is therefore necessary to improve their stability in water. The drug loaded CD-MOF nanocrystals (~ 650 nm) were successfully embedded in polyacrylic acid (PAA) polymer matrices. The composite microspheres exhibited spherical shapes and sustained drug release over a prolonged period of time (over 48 h). Drug loaded MOF/PAA composite microspheres were not toxic *in vitro* (cell viability ~ 90%) even at very high concentrations up to 17.5 mg/mL. MOF/PAA composite microspheres constitute an efficient and pharmaceutically acceptable MOF-based carrier for sustained drug release. However, the process of surface modification was complicated and lead to larger particles and reduced drug payloads.

Water-stable MOFs are a novel type of hybrid particles, showing a high potential as drug carriers. Iron trimesate MOFs, namely, MIL-100 (Fe) (MIL stands for Material of Institute Lavoisier) was among the first nano-scaled MOFs used for drug delivery. These particles were stable in water but degraded in phosphate buffer saline (PBS) losing their crystallinity and constitutive trimesate linkers. However, it was discovered that they kept their morphology intact. A thorough analysis based on Raman microscopy was carried on to gain insights on both the morphology and chemical composition of individual particles. It was evidenced the formation of a sharp erosion front during particle degradation. Noteworthy, the MOFs did not degrade during drug loading nor surface modification.

Co-encapsulation of two synergic antibiotics (amoxicillin and potassium clavulanate) in MIL-100 (Fe) nanoMOFs was achieved following a “green” procedure by soaking nanoMOFs in aqueous solutions of both drugs. Molecular modelling showed that each drug preferentially located in a separate nanoMOF compartment. Surprisingly, nanoMOFs were prone to co-localize with bacteria once internalized in infected macrophages. NanoMOFs acted synergistically with the entrapped drugs to kill intracellular S. aureus, *in vitro*. These results pave the way towards the design of engineered nanocarriers in which each component synergistically plays a role in fighting the disease.

These studies unravel the potential of “cage” particles for efficient drug entrapment and controlled release and open numerous possibilities for applications.

Université Paris-Saclay
Espace Technologique / Immeuble Discovery
Route de l’Orme aux Merisiers RD 128 / 91190 Saint-Aubin, France

Titre : Particules de type “cage” pour des applications biomédicales

Mots clés : particule "cage"; MOF ; médicament; dégradation; antibiotique

Résumé: Les systèmes à délivrance de médicaments sont des technologies conçues pour administrer des molécules actives de façon optimisée afin d’améliorer leurs effets thérapeutiques tout en minimisant les effets secondaires. En effet, ces systèmes permettent une libération au niveau d’une cible thérapeutique. Les particules de type «cage» ont récemment attiré une attention particulière en raison de leur capacité accrue à (co)incorporer et à protéger des molécules actives vis-à-vis de dégradations *in vivo*.

Les cyclodextrines (CDs) sont des exemples type de molécules "cage", possédant une cavité hydrophobe et une surface extérieure hydrophile. Nous avons élaboré tout d’abord des assembages supramoléculaires à base de CDs d'environ 100 nm par une méthode douce consistant à mélanger deux solutions aqueuses de polymères neutres: 1) polymère de β-CD et 2) dextrane greffé avec la benzophénone, molécule invitée formant des complexes d’inclusion avec les CDs. La procédure de préparation «verte» en une seule étape rend la formulation attractive, malgré sa relativement faible capacité d’encapsulation (5%pds). Afin d'améliorer cete charge, nous avons élaboré des particules hybrides organiques-inorganiques (MOFs) à base de CDs. Avantageusement, les CD-MOF comportent non seulement des cavités de CD, mais aussi de larges pores engendrés lors l’auto-assemblage de CDs. Le lansoprazole a été incorporé avec sucès (23%pds) dans les CD-MOFs et nous avons montré que chaque CDs était capable d’accueillir une molécule de principe actif. Cependant, l’inconvénient majeur des CD-MOFs est leur faible stabilité en milieu aqueux, limitant leur domaine d’aplication.

Une modification de surface est apparue donc nécessaire pour améliorer leur stabilité. Notre statégie a été d’incorporer les CD-MOFs dans des matrices d'acide polyacrylique (PAA). Des microsphères composites d’environ 650 nm ont été élaborées avec succès et ont permis une bone stabilité et une libération prolongée sur plus de 48 h. Avantageusement, ces particules composites n’étaient pas toxiques *in vitro* même à des concentrations élevées. Ces microsphères apparaissent comme des systèmes efficaces pour assurer une bonne stabilité dans de milieux biologiques et une libération prolongée, mais leur synthèse est laborieuse et leur taille ne peut pas être réduite en dessus de 50nm.

Ainsi, nous nous sommes orientés vers l’étude comparative de MOFs plus stables dans l’eau, à base de trimesate de fer. Les MIL-100 (Fe) (Material of Institute Lavoisier) figurent parmi les premiers MOF étudiés en tant que nanomédicaments (nanoMOFs). Ces particules, pafaitement stables dans l'eau, se dégradent dans des milieux contenant des phosphates (PBS) en perdant rapidement leur caractère cristallin et leurs ligands constitutifs. De façon étonnante, nous avons constaté que malgré leur dégradation, ces MOFs conservent leur taille intacte. Une analyse approfondie basée sur la microscopie de Raman a permis d’obtenir des informations pertinentes sur la morphologie et la composition chimique de particules individuelles. Ainsi, il a été montré qu’un front d'érosion délimitait nettement un coeur intact et une coquillé inorganique érodée. Cependant, ni l’encapsulation ni la modification de surface des MOFs n’altérait leur intégrité. Enfin, nous avons étudié la co-encapsulation de deux molécules actives utilisées en combinaison (amoxicilline et clavulanate de potassium) dans les nanoMOFs stables à base de MIL-100 (Fe). Les antibiotiques ont été incorporées par imprégnation et chaque molécule s’est localisée preferentiellement dans un compartiment (large ou petite cage) corroborant parfaitement les simulations par modélisation moléculaire. De plus, il a été découvert, de manière surprenante, qu’un grand nombre de nanoMOFs se localisait au voisinage des bactéries (S.aureus) dans des cellules infectées. En se dégradant dans ces cellules, les nanoMOFs contenant les antibiotiques ont réduit de manière importante la charge bactérienne intracellulaire.

Ces études révèlent le potentiel des particules de type «cage» pour une incorporation efficace de molécules actives et leur libération contrôlée et ouvrent de nombreuses possibilités d’application.

Université Paris-Saclay
Espace Technologique / Immeuble Discovery
Route de l’Orme aux Merisiers RD 128 / 91190 Saint-Aubin, France